PREPARATION AND CHARACTERISATION OF GLASS FIBRE/NANOCLAY/POLYPROPYLENE NANOCOMPOSITES

NOR MAS MIRA BINTI ABD RAHMAN

FACULTY OF SCIENCE
UNIVERSITY OF MALAYA
KUALA LUMPUR

2013

PREPARATION AND CHARACTERISATION OF GLASS FIBRE/NANOCLAY/POLYPROPYLENE NANOCOMPOSITES

NOR MAS MIRA BINTI ABD RAHMAN

**THESIS SUBMITTED IN FULFILLMENT
OF THE REQUIREMENTS
FOR THE DEGREE OF DOCTOR OF PHILOSOPHY**

**DEPARTMENT OF CHEMISTRY
FACULTY OF SCIENCE
UNIVERSITY OF MALAYA
KUALA LUMPUR**

2013

UNIVERSITI MALAYA

ORIGINAL LITERARY WORK DECLARATION

Name of Candidate: **NOR MAS MIRA BINTI ABD RAHMAN** …(Passport/I.C. No: 851026-11-5136)

Registration/Matric No: SHC090055

Name of Degree: Doctor of Philosophy

Title of Project Paper/Research Report/Dissertation/Thesis ("this Work"):

PREPARATION AND CHARACTERISATION OF GLASS FIBRE/NANOCLAY/POLYPROPYLENE NANOCOMPOSITES

Field of Study: **ADVANCED MATERIAL**

I do solemnly and sincerely declare that:

(1) I am the sole author/writer of this Work;
(2) This Work is original;
(3) Any use of any work in which copyright exists was done by way of fair dealing and for permitted purposes and any excerpt or extract from, or reference to or reproduction of any copyright work has been disclosed expressly and sufficiently and the title of the Work and its authorship have been acknowledged in this Work;
(4) I do not have any actual knowledge nor do I ought reasonably to know that the making of this work constitutes an infringement of any copyright work;
(5) I hereby assign all and every rights in the copyright to this Work to the University of Malaya ("UM"), who henceforth shall be owner of the copyright in this Work and that any reproduction or use in any form or by any means whatsoever is prohibited without the written consent of UM having been first had and obtained;
(6) I am fully aware that if in the course of making this Work I have infringed any copyright whether intentionally or otherwise, I may be subject to legal action or any other action as may be determined by UM.

Candidate's Signature Date

Subscribed and solemnly declared before,

Witness's Signature Date

Name:

Designation:

ABSTRACT

Hybrid composites of glass fibre/nanoclay/polypropylene (PP) were prepared by extrusion and injection moulding. Fibre length distribution (FLD), Fourier-transform infra-red (FTIR), X-ray diffraction (XRD), scanning electron microscopy (SEM) and transmission electron microscopy (TEM) together with characterisation of thermal, dynamic mechanical and mechanical properties were carried out on moulded specimens. FLD analyses revealed that composites with relatively high glass fibre loading exhibited low number average fibre length (L_n) and weight average fibre length (L_w) values than those containing relatively low glass fibre content. Due to the presence of added functional groups, a difference in the FTIR spectra for treated and untreated nanoclay powder was observed. XRD analyses showed that the interaction between nanoclay and PP matrix resulted in the intercalation of the polymer chains, which increased the nanoclay interlayer distance, as the TEM micrographs showed intercalated morphologies. Thermogravimetric analysis (TGA) revealed that the incorporation of untreated nanoclay into the glass fibre composite improved the thermal stability of the material. Further enhancement of this property was observed with the presence of treated nanoclay. Differential scanning calorimetric (DSC) study showed that the incorporation of untreated clay into glass fibre composite shifted the melting and crystallisation temperatures to higher values. Furthermore, the degree of crystallinity was strongly influenced by the presence of glass fibre and nanoclay in the matrix. Dynamic mechanical analysis (DMA) showed an increase in the storage modulus, indicating higher stiffness in case of the hybrid composites when compared to the clay nanocomposite, glass fibre composite and pure PP matrix. Glass fibre and nanoclay content showed a strong influence on the magnitude of *tan* δ. Incorporation of glass fibre into the PP matrix reduced the tensile strength of the binary composites, indicating

a poor fibre-matrix interfacial adhesion. However, by introducing the untreated nanoclay in the glass fibre composite, the strength of the ternary hybrid composites increased. In addition, tensile modulus was enhanced with incorporation of glass fibre and further increased with an introduction of untreated nanoclay. On the other hand, the flexural modulus and strength were found to increase with glass fibre and nanoclay loadings. Further enhancement in tensile and flexural properties was observed with the presence of treated nanoclay. For glass fibre composite and clay nanocomposite, the peak load (P) and critical stress intensity factor (K_c) increased with filler contents. By contrast, the fracture energy (W) and critical strain energy release rate (G_c) decreased with the addition of nanoclay in the hybrid composites. Incorporation of maleic anhydride grafted polypropylene (MAPP) into the composites, led to improvement in the thermal and mechanical properties to various extents. In the hybrid composites, incorporation of 8 wt% MAPP provided the highest tensile and flexural properties (strength and modulus).

ABSTRAK

Komposit hibrid gentian kaca/tanah liat/polipropilena disediakan dengan menggunakan kaedah ekstrusi dan acuan suntikan. Sampel komposit dikaji menggunakan teknik pengukuran taburan panjang gentian (FLD), Fourier-transform infra merah (FTIR), pembelauan sinar-X (XRD), mikroskopi pengimbasan electron (SEM) dan mikroskopi pancaran electron (TEM) bersama dengan pencirian terhadap sifat terma, mekanikal dinamik dan mekanikal. Analisis FLD menunjukkan bahawa nilai nombor purata panjang gentian (L_n) dan berat purata panjang gentian (L_w) didapati semakin menurun dengan peningkatan komposisi gentian kaca di dalam bahan komposit. Pemerhatian mendapati terdapat perbezaan dalam spektrum FTIR untuk tanah liat yang dirawat berbanding dengan yang tidak dirawat, disebabkan kehadiran kumpulan berfungsi tambahan. Analisis XRD menunjukkan interaksi antara tanah liat dan PP matriks menyebabkan berlakunya interkalasi rantaian polimer ke dalam lapisan tanah liat yang meningkatkan jarak antara lapisan di dalam tanah liat. Keputusan TEM menunjukkan ciri morfologi bersifat interkalasi. Analisis termogravimetri (TGA) menunjukkan penambahan tanah liat yang tidak dirawat ke dalam komposit yang mengandungi gentian kaca memperbaiki kestabilan terma bahan tersebut. Di samping itu, dengan menggunakan tanah liat yang dirawat, peningkatan kestabilan terma bahan komposit adalah semakin ketara. Ujian kalorimetri pengimbasan pembezaan (DSC) menunjukkan penambahan tanah liat yang tidak dirawat ke dalam komposit gentian kaca meningkatkan suhu lebur dan penghabluran kepada nilai yang lebih tinggi. Selain itu, penambahan gentian kaca dan tanah liat ke dalam PP matriks amat mempengaruhi darjah penghabluran dalam bahan komposit. Analisis mekanikal dinamik (DMA) menunjukkan komposit hibrid mempunyai modulus penyimpanan yang lebih tinggi berbanding dengan komposit tanah liat, komposit gentian kaca dan PP matriks.

Komposisi gentian kaca dan tanah liat juga didapati sangat mempengaruhi nilai *tan δ*. Selain itu, penambahan gentian kaca ke dalam PP matriks menyebabkan penurunan nilai kekuatan tegangan bahan komposit binari. Hal ini menunjukkan lekatan antara muka di antara gentian kaca dan PP matriks adalah lemah. Walaubagaimanapun, dengan kehadiran tanah liat yang tidak dirawat di dalam komposit gentian kaca, peningkatan dalam kekuatan tegangan dalam komposit hibrid ternari diperolehi. Selain itu, penambahan gentian kaca dan tanah liat yang tidak dirawat meningkatkan modulus tegangan bahan komposit. Selain itu, kekuatan dan modulus lenturan bahan komposit juga didapati meningkat dengan peningkatan komposisi gentian kaca dan tanah liat. Dengan menggunakan tanah liat yang dirawat, sifat tegangan dan lenturan bahan komposit menunjukkan peningkatan yang lebih ketara. Nilai beban puncak (P) dan faktor intensiti tekanan kritikal (K_c) bagi bahan komposit menunjukkan peningkatan dengan penambahan komposisi gentian kaca dan tanah liat. Namun demikian, nilai tenaga pematahan (W) dan kadar lepas tenaga kritikal (G_c) didapati berkurangan dengan penambahan tanah liat ke dalam sistem komposit hibrid. Penambahan polipropelina maleik anhidrida (MAPP) ke dalam komposit membawa kepada peningkatan dalam sifat terma dan mekanikal pada tahap yang berbeza. Penambahan sebanyak 8 wt% MAPP menghasilkan komposit hibrid dengan sifat tegangan dan lenturan yang maksimum (kekuatan dan modulus).

ACKNOWLEDGEMENTS

First and foremost, gratitude and praises go to Allah, in whom I have put my faith and trust. During the course of this study, my faith has been tested countless times and with the help of the Almighty, I have been able to overcome the obstacles that stood in my way.

I also will like to take this opportunity to express my profound gratitude to my supervisors Prof. Dr. Aziz Hassan and Prof. Dr. Rosiyah Yahya for their noble guidance and valuable advices throughout the period of study. Their patience, time and understanding are highly appreciated. I must thank Prof. Peter R. Hornsby from the School of Mechanical and Aerospace Engineering, Queen's University, Belfast, United Kingdom, for his help and support during my short term attachment.

Thanks to the staff members of the Chemistry Department especially Mr. Zulkifli Abu Hasan, Ms. Ho Wai Ling, Ms. Nisrin and Mr. Hafizi for providing assistance in many ways. I am also grateful to all the members of the polymer and composite research group for the many ways they have contributed to the completion of this study.

I am thankful to the University of Malaya for funding this research from grant numbers PS230/2008B, PS376/2009B and PS504/2010B. I also want to show my gratitude to the Ministry of Higher Education, Malaysia and University of Malaya for sponsoring my studies with SLAB/SLAI scholarship.

Finally, I am eternally grateful to my family members, especially my father, Mr. Abd. Rahman Embot, my mother, Mrs. Mawan Serah and my husband, Mr. Abdul Hafiz Muhammad, whom I owe a debt of gratitude for their prayers, sacrifices, encouragement and moral support throughout the duration of my study.

TABLE OF CONTENTS

Page

CHAPTER TWO: LITERATURE REVIEW

CHAPTER THREE: EXPERIMENTAL

CHAPTER FOUR: RESULTS AND DISCUSSION

CHAPTER FIVE: CONCLUSION AND RECOMMENDATIONS FOR FURTHER WORK

RESEARCH OUTPUT

LIST OF FIGURES

Page

LIST OF TABLES

Page

LIST OF SYMBOLS AND ABBREVIATIONS

AE	Acoustic emission
ASTM	American Society for Testing and Materials
ATR	Attenuated total reflectance
a/D	Notch (or crack length) to depth ratio
B	Thickness of specimen
D	Depth of specimen
DSC	Differential scanning calorimetry
DMA	Dynamic mechanical analysis
DTG	Derivative weight change thermogram
DT_p	Derivative peak temperature
E	Tensile modulus
E'	Storage or elastic modulus
$E'_{25°C}$	Storage modulus value at 25°C
$E'_{100°C}$	Storage modulus value at –100°C
E''	Loss or viscous modulus
E''_{max}	Maximum magnitude of loss modulus in α-transition region
$E''_{25°C}$	Magnitude of loss modulus at 25°C
FLD	Fibre length distribution
FOD	Fibre orientation distribution
FTIR	Fourier transform infra-red
FIB-SEM	Focused ion beam scanning electron microscope
G_c	Critical strain energy release rate
GPa	Gigapascal

GF	Glass fibre
K_c	Critical stress intensity factor
L	Fibre length
L_c	Critical fibre length
LEFM	Linear elastic fracture mechanics
L_n	Number average fibre length
L_w	Weight average fibre length
MA	Maleic anhydride
MAPP	Maleic anhydride grafted polypropylene
MFI	Melt flow index
MMT	Montmorillonite
$M_{447°C}$	The amount of matrix remaining at 447°C
NC	Nanoclay
NCUT	Nanoclay (untreated)
NCST	Nanoclay (surface treated)
P	Peak load
PCN	Polymer-clay nanocomposites
phr	Parts per hundred parts of resin
PP	Polypropylene
rpm	Revolutions per minute
S	Span of specimen
SEM	Scanning electron microscopy
SEN	Single edge notch
S/D	Span to depth ratio

$T_{\alpha}^{E''}$	Temperature at the maximum value of E'' in the α–transition region
tan δ	Tan delta
tan δ_{max}	Maximum magnitude of *tan* δ at T_g
tan $\delta_{25°C}$	Magnitude of *tan* δ at 25°C
T_c	Crystallisation temperature
TEM	Transmission electron microscopy
T_g	Glass transition temperature
TGA	Thermogravimetric analysis
T_m	Melting temperature
T_{onset}	Onset temperature
$T_{5\%}$	Temperature at 5% degradation / weight loss
$T_{10\%}$	Temperature at 10% degradation / weight loss
$T_{50\%}$	Temperature at 50% degradation / weight loss
V	Impactor velocity
V_f	Fibre volume fraction
W	Fracture energy (energy to failure)
W_f	Fibre weight fraction
W_m	Matrix weight fraction
W_{MAPP}	MAPP weight fraction
w/w	Weight per weight
wt%	Weight percent
X_c	Degree of crystallinity
XRD	X-ray diffraction

Y	Geometry correction factor
Z	Straining rate of the outer fibre
3-PB	Three point bending
ΔH_c	Enthalpy heat of crystallisation
ΔH_m	Enthalpy heat of melting
ΔH_m^*	Enthalpy heat of melting of an "ideally" fully crystalline polymer
ρ	Density
δ	Phase angle
σ	Tensile strength
ε	Tensile strain
Φ	Correction factor

LIST OF APPENDICES

CHAPTER ONE

1 Introduction

1.1 Background

A range of materials may be classed as composites [1] because they are characterised by being made from two, or more, constituent materials [2], comprising of strong load bearing material, known as the reinforcement, embedded in a weaker material, known as the matrix [3]. However, the modern definition of a composite material is more refined. The modern definition assumes that the constituent materials are present in reasonable quantities [2], with the properties of the composite significantly different from the constituents and that the reinforcement is typically made from some high performance fibre.

Composites can be found in almost every aspect of modern materials and are useful in everyday life. They depend primarily, on the use of strong, stiff fibres to upgrade the performance of traditional bulk materials. Reinforced plastics are the most highly developed class of composite materials and an attempt is made to illustrate their wide variety of applications. Composite materials are chosen over traditional material for its good corrosion resistance, greater design flexibility and ability to produce complex parts, coupled with their good electrical and thermal insulating properties. Therefore, composites are widely used in automotive and aircraft parts, industrial storage tank, sport equipment and textile spinning machinery.

The matrix constituent is made from a continuous material. Some of the functions of the matrix are to transfer the load to the reinforcement [1, 3], to protect the reinforcement, *e.g.*, from environmental degradation, to disperse the reinforcement and to maintain the position and orientation of the reinforcement as well as to provide shape and form to the structure. The three major classes of matrix materials, are: ceramic, metallic and polymeric, with polymeric resins being the most widely used matrix

material. The addition of any type of reinforcement to a polymer matrix is expected to result in a composite with improved mechanical properties compared to the pure matrix. Additionally, since the processing temperatures are reasonably low, the mechanical properties of the reinforcement will not be affected, negatively.

The reinforcement material contained in a composite is to support the structural load carried by the component and hence to provide strength and stiffness to the structure [3]. To achieve these goals, the reinforcement is typically made from discontinuous material that is stiffer and stronger than the matrix. The reinforcement also tends to possess high elastic modulus and strength, low density and is often anisotropic in nature. These criteria allow composite materials to be "tailored" to the required application.

1.2 Justification

The incentive for thermoplastic composites research and development activities is huge, given the very large commercial and engineering sectors it attracts. There are wide ranges of existing thermoplastic polymers [4], such as: polyamide (PA), acrylics, polyethylene (PE) and polypropylene (PP). PP (commonly reinforced with calcium carbonate ($CaCO_3$), talc, glass fibre (GF) and organic fillers) is one of the most exploited thermoplastic resins in the composites, alloy and blends industries. As early as 1869, propylene was polymerised by Berthelot by reaction with concentrated sulphuric acid [5]. Its industrial importance results in the development of the high molecular weight crystalline PP, which was first polymerised in separate effort by Edvin Vandenberg [6] and Guilio Natta [7]. The homopolymer PP can exist in isotactic, syndiotactic or atactic forms, depending on the orientation of the pendant methyl groups attached to the alternating carbon atoms. The moderate cost and favourable properties of PP contribute to its strong growth. It has the lowest density among all thermoplastics

(~0.8–0.9 g cm^{-3}) and a higher strength than other polyolefins. PP has the highest melting temperature (~165°C – 175°C) and better heat resistance than other low-cost commodity thermoplastics. PP also possesses outstanding properties like sterilisability, good surface hardness, scratch resistance, good abrasion resistance and excellent electrical properties. Unlike PE, PP is usually not susceptible to environmental stress cracking and has greater clarity than PE. Because of its hydrophobicity, PP is resistant to attack by polar chemical agents, but can undergo extensive swelling, softening and surface crazing in the presence of liquid hydrocarbons, chlorinated solvents, or very strong oxidising agents [8].

In order to improve PP competitiveness in engineering applications, there is an important objective to simultaneously increase the dimensional stability, stiffness, strength and impact resistance. This goal can be achieved either by producing PP composites containing fibre reinforcement, through special processing technology involving fibre impregnation and pre-preg formation or by developing new grades of filled PP which is produced by means of conventional melt processing technology [9].

GF reinforced PP composite is quite attractive as it offers a number of distinct advantages over more conventional engineering materials, such as: high specific modulus, specific strength, superior corrosion resistance, improved fatigue properties, and low manufacturing cost. In spite of their advantages, GF reinforced PP however has limited performance due the chemical incompatibility of the non-polar PP with the GF. This results in the inability of the composites to take full advantage of the reinforcement potential, due to the poor adhesion between the matrix and fibre [10].

In the context of plastics, a nanocomposite is a near-molecular blend of resin molecules and nanoscale particles. A nanoscale particle is a material with at least one dimension in the nanometre range. Conventional plastic composites can now contain functional fillers of around 0.5 μm in size. A nanoparticle is 500 times smaller in, at

least, one dimension. In this case size does matter. Many physical and gas barrier properties are greatly enhanced when these infinitesimal particles interact at the molecular level. Achieving the near-molecular blending is one of the principal aims, at the moment, for scientists

A relatively new development in polymer-clay nanocomposites (PCN) has attracted great interest, in industry and academia, because they exhibit remarkable improvement in material properties when compared to virgin polymer or conventional micro and macro composites. PCN is a new class of material with ultrafine phase dimension, typically in the order of a few nanometres. This material is produced from crossbreeding between a polymer and unique multilayer-structured clay. This multilayered clay is conventionally termed, layered-silicate and its crystal structure consists of periodical atomic-scale layers of extremely large surface area, fused together into a micron-size pack by interlayer molecular forces. The physical origin of its extraordinary property is derived mainly from delamination and dispersion of the clay multilayer, technically termed as exfoliation, or diffusion and swelling of the multilayered structure by polymer chain, termed as intercalation. Exfoliation and intercalation of these clay particles give rise to nanoscale molecular interaction between the polymer and clay layers, which are responsible for the dramatic property enhancement not experienced in conventional polymer composite materials. More spectacularly, the improvement is usually achieved with the incorporation of as low as 1 to 5 *wt%* clay particles when compared to a typical 20 to 40 *wt%* filler loading for most conventional composites.

Recently, it has been observed [11, 12] that by incorporating nanoparticles into the matrix of fibre-reinforced polymer (FRP), synergistic effect may be achieved. Hybrid composites are those composites which have a combination of two or more reinforcement fibres in a pre-determined geometry and scale; making them suitable to

serve specific engineering purpose. The length scale of the property improvement in the FRP composites and nanocomposites are very different. For example, the thickness of an exfoliated silicate sheet is 10,000 times smaller than that of the diameter of a typical GF. Therefore, the two materials can be combined in a new type of a three-phase hybrid composite. In this new composite system, the main reinforcing phase is the discontinuous fibres. The matrix itself is supposedly a composite too, containing particles on the nanometre length scale. A schematic drawing of this concept has been explained by Vlasveld *et al.* [13] The particles in the matrix material fit between the fibres, without reducing the fibre volume fraction. The matrix-dominated properties of the fibre composite can benefit from the improved properties imparted by the nanoparticles.

These hybrid composites often exhibit remarkable improvement in materials properties when compared with the conventional micro- and macro-composites [14]. It has been observed that by incorporating filler particles into the matrix of fibre-reinforced composites, synergistic effects can be achieved in the form of reduction in material costs, increased modulus, heat resistance and biodegradability (of biodegradable polymers), decrease gas permeability, and flammability. However, due to stress concentration, agglomeration, and confinement of matrix molecular mobility around the rigid filler phase, the impact toughness is reduced [15]. The most prominent effect of particulate fillers on the crystalline structure of semi-crystalline thermoplastics is their ability to work as nucleation agents.

However, hybrid-reinforced composites form a complex system and there is inadequate data available about the phenomena behind the property changes due to the addition of particulate fillers to the fibre reinforced thermoplastic composites. Thus, this study is an attempt to clarify the properties of hybrid composites based on: PP matrix, GF reinforcement and nanoclay particulate filler. PP/clay nanocomposite systems were

prepared for use as a matrix material for GF composites. An experimental study was carried out to exploit the functional advantages and potentially synergistic effect of GF and NC, in order to enhance the overall properties of PP.

1.3 Research objectives

This research is aimed at enhancing the properties of hybrid composites by incorporating GF, nanoclay and compatibiliser. Other specific objectives are to:

(i) Investigate the effects of chemical surface treatment on the nanoclay the micro- and nano-structure of the resultant nanocomposites.

(ii) Evaluate the effects of hybridisation between GF, untreated and surface treated nanoclay on the thermal degradation and crystalline behaviour of the resultant composites.

(iii) Assess the effects of GF, nanoclay and compatibiliser on the dynamic mechanical and mechanical properties of hybrid composites over a range of compositions and compatibiliser concentrations.

(iv) Study the effects of compounding screw speeds on the thermal, dynamic mechanical and mechanical properties of hybrid composites

(v) Elucidate the failure mechanisms through fracture surfaces of hybrid composites.

1.4 Scope of work

This thesis will discuss the relationship between the hybridisation of GF with untreated and surface treated nanoclay and the properties of the resulting hybrid composites, to be determined through a series of systematic studies. First, composites were compounded and injection moulded under specified conditions. The effects of the compounding screw speeds, nanoclay surface treatment, GF and nanoclay loadings as

well as compatibiliser concentration on the morphology, thermal, dynamic mechanical and mechanical properties of composites will be discussed.

1.5 Thesis outline

This thesis is arranged in the following chapters;

Chapter one presents an overall introduction to hybrid composites, the background and its technology. Justification, research objectives and scope of work are also presented.

Chapter two provides a review of literature on nanoclay, GF and their modifications and also describes the various techniques on the synthesis and production of nanocomposites. It then proceeds to examine the market and applications of composites before reviewing the processing routes that can be employed to manufacture the hybrid composite. This chapter ends by discussing the structure-property relationship of the hybrid composite materials.

In Chapter three, the materials and methods are highlighted, including detailed testing methods employed in this research.

Chapter four focuses on the presentation of results and its discussion on the influence of nanoclay surface treatment and its concentration as well as GF on the properties of the hybrid composites.

Finally, Chapter five presents the general conclusions and recommendations for the further work.

CHAPTER TWO

2 Literature review

2.1 Polymer-clay nanocomposite

2.1.1 Structure and modification of clay

Clays can be divided into four different main groups, namely; kaolinite, smectite, illite and chlorite. The constitution of common clays is subjected to natural variability since they are naturally occurring minerals; besides their purity can affect the final polymer-clay nanocomposites (PCN) properties. However, many varieties of clay are aluminosilicates with a layered structure which consists of silica (SiO_4^{4-}) tetrahedral sheets bonded to alumina (AlO_6^{9-}) octahedral ones. These sheets can be arranged in a variety of ways; in smectite clays a 2:1 ratio of the tetrahedral to the octahedral is observed. Montmorillonite (MMT) is the most common of the smectite clays [16].

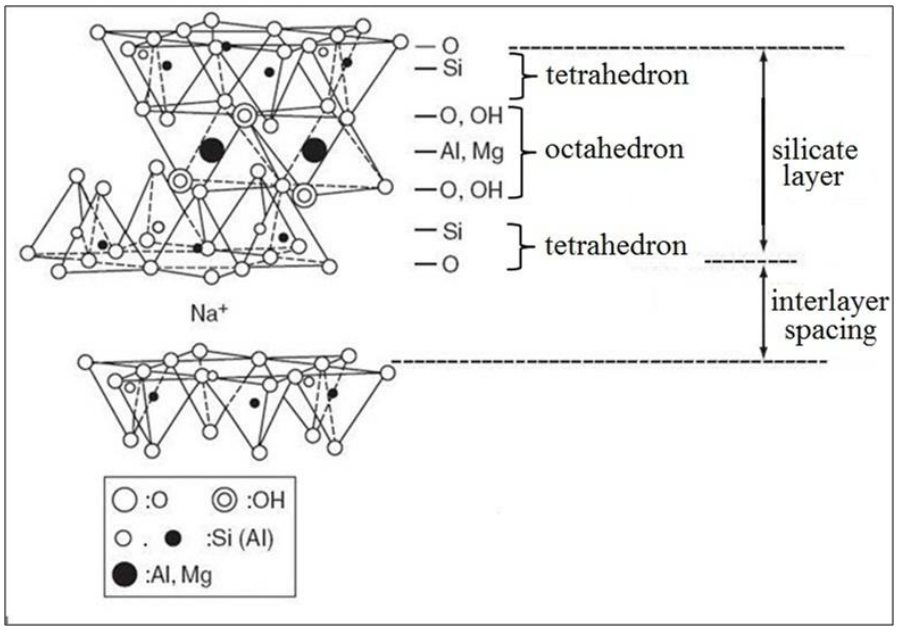

Figure 2.1: Schematic illustration of atoms arrangement in a typical MMT layer [17]

As shown in Figure 2.1, the montmorillonite group comprises a number of clay mineral with alumina octahedral and silica tetrahedral sheets in three layered structures.

The thickness [18] of the layers is of the order of 1 nm and the aspect ratios are high, typically 100 – 1,500. These layers are in turn linked together by van der Waals forces and organised in stacks with a regular gap between them called interlayer d-spacing. Within the layers, isomorphic substitution of atoms, such as Al^{3+} with Mg^{2+} or Fe^{2+} can occur thereby generating an excess of negative charge, the amount of which characterises each clay type and is defined through the charge exchange capacity (CEC). The CEC value for MMT depends on its mineral origin, however it is typically between 0.9 – 1.2 meq g^{-1}. In natural clays, ions such as Na^{+}, Li^{+} or Ca^{2+} in their hydrated form, balance this excess negative charge. One important consequence of the charged nature of the clays is that they are generally highly hydrophilic species, therefore naturally incompatible with a wide range of polymer types, except only with hydrophilic polymers like polyethylene oxide and polyvinyl alcohol [19 – 21].

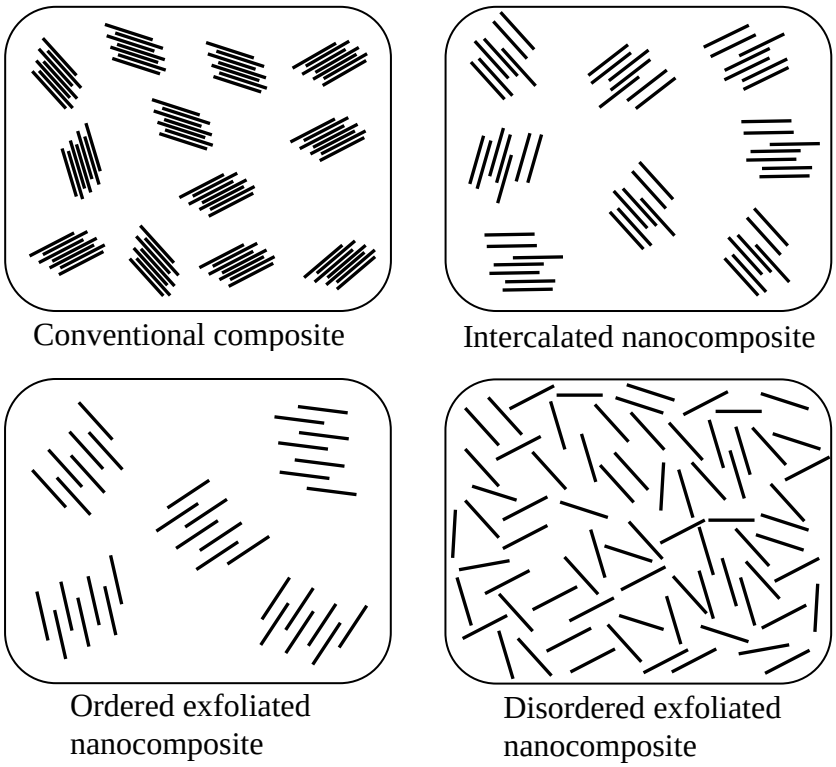

Figure 2.2: Schematic representation of different nanoclay particles structure in polymer matrix [22]

It is possible to have different clay dispersion levels in the composite, as illustrated in Figure 2.2. The ultimate platelet configuration is when the mineral is completely dispersed (exfoliated) and the specific surface is at its maximum, which will result in a high possibility of attaining the greatest advantages from nanoclay [22]. Depending on the physical and chemical properties of the matrix, to completely exfoliate the mineral can be a real challenge. In many cases part of it remains intercalated or even aggregated.

Prior to production, it is often necessary to tailor the chemical characteristic of the inorganic (organophobic) clay surfaces in order to improve their miscibility with the organic polymer. Modification is typically achieved by the introduction of a suitable organic alkyl-surfactant (of similar chemical structure to the polymer system) into the clay interlayer d-spacing, in order to impart organic characteristic (organophilic) to the clay surface [23]. The organically modified clay is usually referred to as organoclay or organosilicate. For example, in montmorillonite, the sodium ions in the clay can be exchanged [18] for an amino acid, such as 12-aminododecanoic acid (ADA):

$$Na^{+}\text{-CLAY} + HO_2C\text{-R-}NH_3^{+}\ Cl^{-} \rightarrow HO_2C\text{-R-}NH_3^{+}\text{-CLAY} + NaCl \quad (2.1)$$

It is not only the chemical product used as treating agent, but the way in which this substitution is performed has an effect on the formation of particular nanocomposite product forms. However, the laboratory route commonly used to introduce alkyl ammonium ions in the interlayer is an ion exchange reaction which promotes the formation, in solution, of the desired ion dissolving either the related amine together with a strong acid [24] or a salt which has long alkyl chain cation linked to counter-ions as chloride or bromide [25] (schematically illustrated in Figure 2.3) in hot water (about 80°C). Such solution has to be poured into MMT previously dispersed in hot water as well. A vigorous stirring with a homogeniser is required in order to yield white precipitates which have to be collected, washed and eventually dried.

It is important to note that surface treatment not only to renders the clay an organoclay, improves the wetting characteristic with the non-polar polymer, but it also increases the interlayer distance. Indeed, surface treated clay is used even in case of polar polymers in which the modification of clay polarity is not fundamental for the PCN production. Clearly, as the amount of carbon atoms in the tail of the ammonium ion increases, the clay becomes more organophilic. Furthermore, the introduction of a longer organic molecule in the clay structure helps to increase the interlayer distance as well. For this reason, hexadecyl-trimethyl-ammonium ion [24] or dioctadecyl-dimethyl-ammonium ion [25], can be used. Some experimentation has been done in order to improve the surface treatment efficiency because silicate layers, modified by non-polar long alkyl groups, are still polar and thermodynamically incompatible with polyolefin.

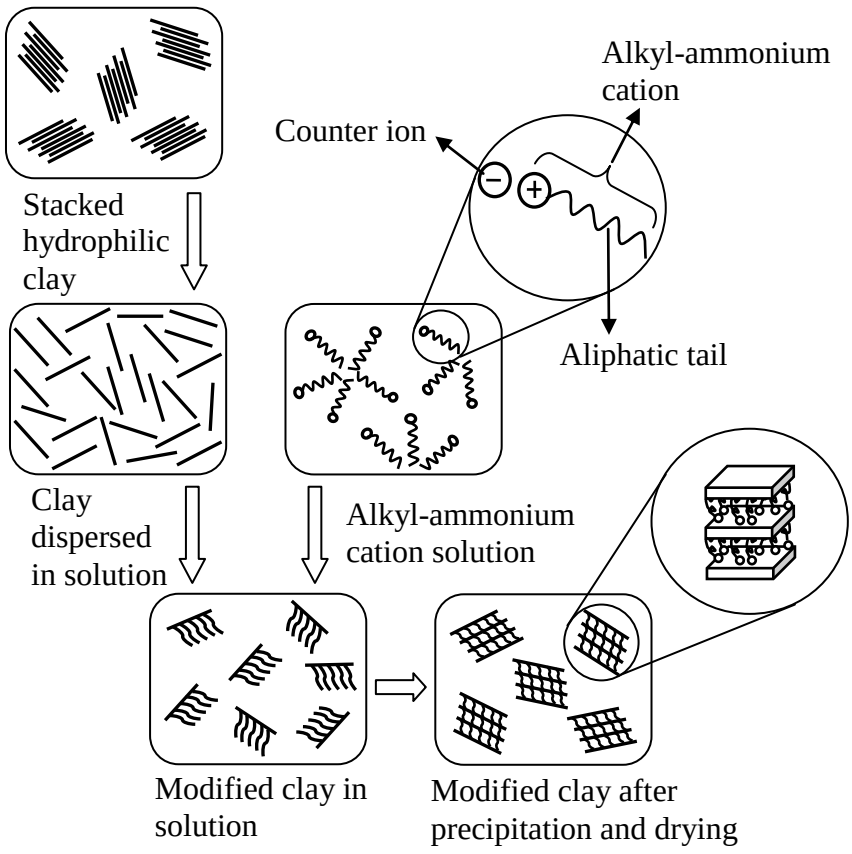

Figure 2.3: Schematic representation of clay surface treatment [25]

An alternative route to the ordinary organophilic clay has been suggested by Liu *et al.* [25] and it consists of co-intercalating in clay stacks, an unsaturated monomer which promotes the larger interlayer d-spacing and the possibility for the monomer to bind on the PP backbone by grafting reaction. Although the organic pre-treatment adds to the cost of the clay, clays are, nonetheless, relatively cheap feed stocks with minimal limitation on supply.

2.1.2 Synthesis and production of clay nanocomposites

Filling polymers with clays (either synthetic or natural, with appropriate modification) is not a completely new subject [26, 27]. Nonetheless, in the last decade, there are two reports that initiated the revitalisation of these materials. The first work is the report of a clay/nylon 6 from Toyota Group research in 1993 [28, 29]. The PCN obtained, contained clay layers that were homogeneously dispersed throughout the nylon matrix. Significant enhancements in the thermal and mechanical properties, were observed in spite of a very moderate inorganic loading. This notwithstanding, PCN did not gain applicative success owing to a very long preparation method, which hugely increased the final material cost.

Generally, low concentrations of clay ($\leq$ 5 *wt%*) are incorporated in these nanocomposites, partly because this is often sufficient to modify the desired properties significantly. The higher levels of clay can also adversely increase the system viscosity leading to poor processability, although the viscosity increase is shear rate dependent.

The second work that boosted the subject was from Giannelis *et al.* [30] who found a procedure leading to PCN by melt mixing of polymers with clays (intercalated with organic cations), without using organic solvents [31, 32]. Unfortunately, this technique was fruitfully applicable, only to polymers with polar groups in their backbone and not to non-polar polymers such as, polyolefin in general and PP in

particular [33]. Ever since, a lot of new techniques were tested in order to find a feasible route leading to the production or preparation PCNs without increasing the process complexity and, consequently, the cost. However, it is possible to distinguish four distinct strategies which can be used to prepare PCNs.

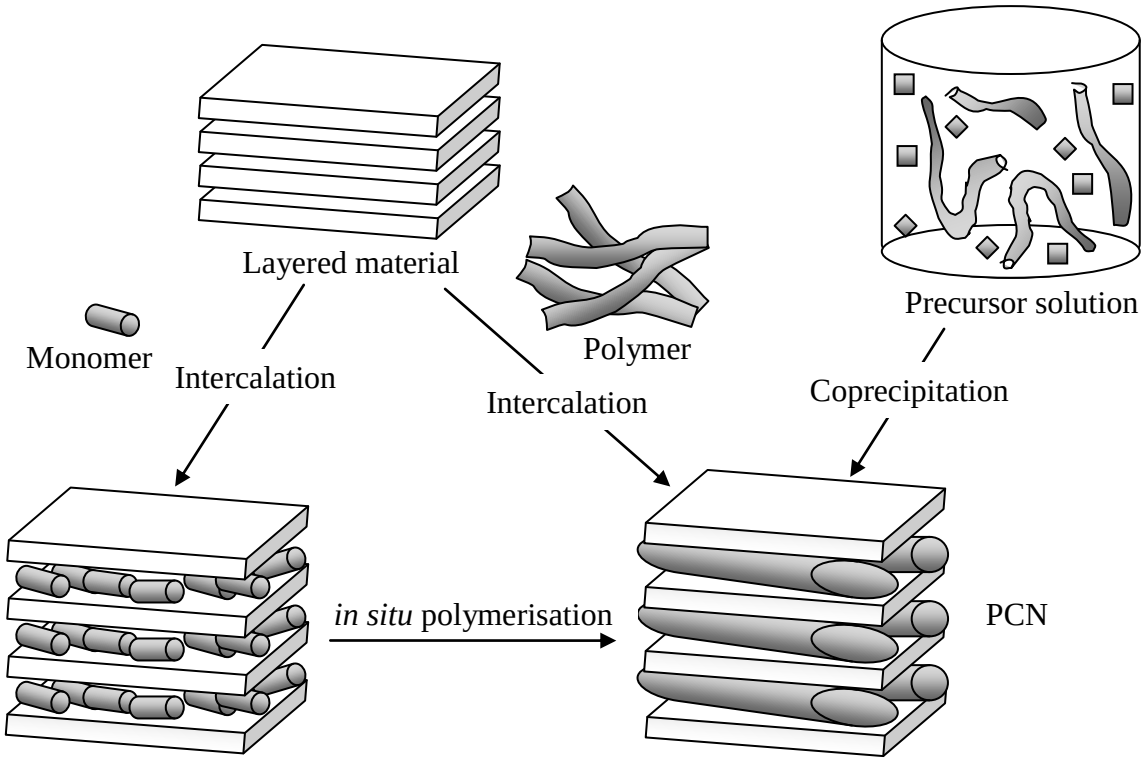

Figure 2.4: Schematic representations of the different preparation routes for PCN [34]

The four mainstream techniques used for synthesis of PCNs are (i) *in-situ* polymerisation, (ii) solvent intercalation, (iii) solution-gel intercalation and (iv) melt intercalation (Figure 2.4).

2.1.2.1 *In-situ* polymerisation

Early PCN researches utilised the *in-situ* polymerisation route that produced the first successful PCN based on polyamide 6. This method was first filed in a U.S patent by Okada *et al.* [35] from the Toyota Motor Company, Japan in 1988. To facilitate the polymerisation reaction and intercalation, a mixture of silicate layers with the monomer

[28, 36, 37] and polymerization initiator [38 – 40] is then polymerised in a high pressure autoclave to obtain a polymer-clay nanocomposite. In-situ polymerisation permits the possibility to have PCNs with tailored physical properties while avoiding nanoparticle clustering. At the same time, it improves the interfacial adhesion between the inorganic clay and organic polymer phases. Recent variations to this technique include insertion of protonated species, such as amino lauric acid, laurolactam, amines, *etc.* into the clay interlayer through rigorous solution mixing prior to the polymerisation step.

By this method, the formation of PCN with non-polar polymers is also possible. Starting from monomers, a more favourable thermodynamic for non-polar polymers/silicate miscibility occurs. Actually, the non-polar monomers can penetrate more easily than their respective polymers in the interlayer gallery because of a smaller entropic loss in intercalating. Although PCNs synthesised through *in-situ* polymerisation have shown promising property improvement, the batch size achieved by this route in the laboratory is limited due to very small reactor scale. Additionally, this technique has suffered from a high production cost, requirement of suitable monomer co-solvent, cost of solvent waste management, high level of expertise and is economically less adaptable to smaller scale manufacturers.

2.1.2.2 Solvent intercalation

For solvent intercalation, the polymer is initially solubilised into an excess amount of suitable organic solvent, followed by rigorous stirring with the clay particles, for an extended period. PCNs are obtained upon either through the evaporation of the solvent or precipitation of the polymer [41 – 43]. The disadvantages of this technique, which limit their potential only to laboratory scale, are: the requirement of a suitable solvent, high cost associated with solvents, their disposal and environmental impact, long processing time and the resultant PCNs requiring further purifications [44].

2.1.2.3 Solution-gel intercalation

Solution-gel intercalation consists of direct crystallisation of layered-silicate by hydrothermal treatment of a gel/polymer/clay suspended solution, using a solvent precursor. On removal of the solvent, uniform mixed PCNs are obtained. This technique has the potential of promoting a high degree of clay dispersion in a one-step process without the need of clay surface modification [44]. Other variations of this solution-gel mediated technique include emulsion or suspension polymerisations, in which the layered-silicates are suspended in an aqueous phase and a monomer is polymerised in a second phase within the suspension.

2.1.2.4 Melt intercalation

Melt intercalation synthesis of PCNs can be achieved via processes involving the annealing of a polymer melt together with the clay, statically or under shear [45]. During the shearing process, polymer chains diffuse from the bulk polymer melt into the clay multilayer. Progressive polymer diffusion results in finite expansion of the clay multilayer. Depending on the degree of penetration, PCN hybrids are obtained with structures ranging from intercalated to exfoliated. In general, the successful preparation of PCNs through melt intercalation is determined by (i) thermodynamic conditions, which involves the interplay of entropic and enthalpic effects between the clay and the polymer and (ii) kinematic factors, which involve the physical control of polymer rheology in order to achieve an optimum distributive and dispersive mixing condition.

In order for this method to be effective, though, the silicates needed to be previously surface treated through an organo-modification process. The melt intercalation technique is more flexible and '*green*' than the previous three routes, due to the absence of solvent [46] and chemical reaction; besides, its testing with nylon-6, polysiloxane and even polystyrene yielded noteworthy results. On the other hand, when

non-polar matrices are involved [31, 47 – 49], a third component, such as maleic anhydride grafted polymer has to be added to the PCN system, even though the clay was already organically modified. The aim of this new constituent is to improve the matrix filler interactions [24, 50] by reducing the interfacial tension between them [51].

Although the incorporation of particulate material into polymers generally results in an increased melt viscosity, nanocomposite formulations exhibit even a greater reduction in viscosity with shear rate than their unfilled counterparts. This results in insignificant differences in viscosity at the shear rates frequently encountered in commercial melt fabrication processes. In addition, due to the substantially lower loading level required to achieve the same property levels obtainable via conventional filler materials, the viscosity increases with nanoclay formulations are obviously low in comparison to their more conventionally filled counterparts. Furthermore, lower loading levels of particulate material will also be advantageous in minimising the abrasive effects on processing equipment [18].

2.2 Production and modification of glass fibre

Glass fibre is one of the most common types of reinforcement used for thermosetting and thermoplastic composite applications [52]. Manufacturing glass reinforcement starts with the molten glass being extruded, under gravity, through a number of orifices to form GF. The fibres are combined into glass strands which are treated with starch oil emulsion, in order to protect them. This process is known as sizing. Once treated, the strands are processed into the appropriate type of reinforcement and then treated with coupling agents in order to improve their wetting and bonding characteristics [2]. The glass fibres can be processed in many different forms, such as: continuous fibres, woven fabrics, chopped strand mat and it is very cheap when

compared with other types of reinforcement. Glass fibres do not burn and they are generally resistant to moisture and corrosion. The fibres are also isotropic.

The physical and chemical properties of GF depend on its composition. The sodalime-silica glass, known as A-glass (A for alkali) is the original type of GF. This is a high alkali content material, with a chemical composition similar to that of window glass. It has been used as plastic reinforcement in small quantity. The C-glass (C for chemical) is a grade with improved resistance to chemical attack. This material is more chemically resistant than E-glass, especially against acidic solution. This type of GF is mainly used in surfacing mats for corrosion resistance purposes. Many other glass compositions are commercially produced for special applications. The D-glass (D for dielectric) is rich in boric oxide and has lower dielectric constant. Due to its superior electrical properties, D-glass is widely used in the electronics industry. The E-glass (E for electrical), is a calcium alumino-borosilicate composition and has a low content of alkali ions. It is known for its excellent electrical resistance, which is an important property for the textile glass yarns. It also has a good tensile and compressive (strength and stiffness) properties, stronger than A-glass and relatively low cost, but low in impact strength. This GF is the most widely used in the general purpose composite system [53]. The AR-glass (AR for alkali resistance) is rich in zirconium oxide content. This material improves the alkali resistance of the glass and widely used for the reinforcement of concrete. Two high-strength glasses, the R- and S-glasses have a different chemical composition. S-glass from Owens Corning and R-glass from Vetrotex International, have higher tensile strength and modulus and better wet strength retention. They were developed to meet the demand for higher technical performance from the aerospace and defence industries [52]. Hollow S-glass filaments are also available to further increase the strength-to-weight ratio. The chemical composition of each type of glass is given in Table 2.1

Table 2.1: Typical composition (*wt%*) in various commercially produced glass fibres [54]

Compound	Type of glass fibre					
	A	C	D	E	R	S
SiO_2	71.8	65.0	74.5	55.2	60.0	65.0
CaO	8.8	14.0	0.5	18.7	25.0	
Al_2O_3	1.0	4.0	0.3	14.8		25.0
B_2O_3			22.0	7.3		
MgO	3.8			3.3	6.0	10.0
Na_2O	13.6	11.0	1.0	0.3	9.0	
K_2O	0.6		0 – 1.3	0.2		
Fe_2O_3	0.5			0.3		Trace
F_2				0.3		
ZrO_2						
Li_2O_3						
SO_3			0.1			

Glass is an inorganic material, whereas the polymer is organic. These two materials are naturally incompatible and do not form hydrolytically stable bonds. A coupling agent is necessary for a chemical reaction to occur between the two materials. Coupling agents contain chemical functional groups that can react with silanol groups on glass. At the other end of the coupling agent, the organofunctional group is to react with the polymer. Covalent bonds, which are assumed to have been formed, lead to the strongest interfacial bond.

Various silanes were developed for specific resin systems (with excellent and superior composite properties) meant to replace the chromium complex Volan, which was proven to be the most effective coupling agent in the GF-reinforced plastics industry. Since all GF sizes are water based, alkoxysilanes have to be hydrolyzed before being applied to glass surfaces to function as coupling agents. The hydrolysis is for trialkoxysilanes to react with excess water to form silane triols [54] as shown in equation (2.2):

$$R'Si(OR)_3 + \text{excess } H_2O \rightarrow R'Si(OH)_3 + 3ROH \qquad (2.2)$$

The thickness of the silane layer on the glass surface also depends on the concentration of the silane solution [55]. At concentrations between 1 *wt%* to 30 *wt%*,

the thickness of the aminosilane increased between 1.0 mm to 4.8 mm on a 200 mm GF. This implied that even at very low silane concentrations, not all silane molecules were chemically bounded to the glass surface. Although it has been proven that silane forms a covalent bond to the glass surface and provides the interfacial strength to the composites, many other ingredients must be used in size formulations of the GF. The adhesion between the size on the glass surface and the resin matrix is also maximized when the solubility parameters of the two are matched. It is sometimes described as 'like dissolves like'.

GF has a high tensile strength combined with low extensibility giving exceptional tensile, compression and impact properties, with a relatively high modulus of elasticity and good flexural strength. It also has high temperature resistance, good dimensional stability and improves the creep performance considerably. Its low moisture absorption, makes it possible to produce mouldings with good electrical properties, even under extreme weather condition [56]. Engineering polymers are often reinforced with GFs in order to obtain increased mechanical stiffness and strength; however, it leads to reduced ductility and impact resistance. In some cases, it is useful to combine reinforcement with rubber toughening to balance end use performance of final product [57].

2.3 Compatibiliser

All composite materials, whether fibrous or particulate, require good bonding between the matrix and the reinforcement. This is needed for mechanical reasons, to ensure effective load transfer through the reinforcing phase and for long-term integrity, since an unbonded interface provides a possible route for corrosive attack of the reinforcement. Since many polymer systems do not naturally form strong chemical

bonds with inorganic surfaces, compatibiliser must be employed to provide the required chemical interface between the polymeric and non-polymeric phases.

The use of a compatibiliser, (usually a chemical that is able to render some degree of compatibility between two different materials), made it possible for the melt intercalation technique to be accepted as the most promising approach to composite formation. In this way, the use of solvents and dedicated processes could be avoided providing a formation procedure which is environmentally- and user friendly. It is important, at this point, to clarify that the surface treatment and the compatibilisation are two different, independent and complementary ways adopted to solve the problem of poor miscibility between PP and fillers. They act on parallel levels to overcome the same difficulty. The incompatibilities between PP, GF and nanoclay are, indeed of thermodynamic and of physical nature. The first kind of obstacle for a successful hybrid formation is the fact that the stacks of layers in nanoclay form, are very stable and unwilling to reach the state of disorder required for a well formed hybrid composite. The second impediment to the desired exfoliated structure is the chemical unsuitability of the non-polar PP to be bonded, in any way, to the polar GF and nanoclay platelets, at least to hold them in a non-thermodynamically favourable arrangement.

Through surface treatment, it is possible to change the interlayer structure of nanoclay by increasing the gallery gap and modifying the silicate surface in an organic fashion, but this ingenuity is not enough to render compatible, the matrix and filler, therefore the ‘polarising’ compatibiliser needs to be introduced in the PP. For example, nanocomposites with host polymers containing polar components, such as styrene acrylic acid copolymer already showed remarkable improvement of mechanical properties [50, 58].

The polar group introduced in the hydrophobic PP backbone to make it hydrophilic, is maleic anhydride, which has been shown, from a study conducted by

Kawasumi *et al.* [50], to be crucial in promoting the desired phase structure [58]. The repeating unit is to represent the resulting polymer chain (Figure 2.5). From the figure, the maleic anhydride (MA) groups should be randomly grafted or block copolymerised in the PP chain. Nevertheless, this kind of product is usually made by reactive extrusion with a peroxide initiator, which causes a free radical formation via the scission of the PP chain. Such radical is the reactive site to which the MA group attaches. It is suggested that the compatibiliser more than one group can react with a broken PP chain leading to a dimer or even trimer formation. This means that a maleic anhydride grafted PP (MAPP) can act as a 'surfactant', where a polar head is attached to an aliphatic tail.

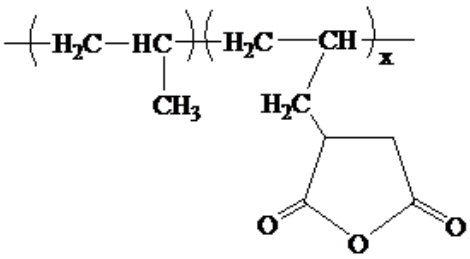

Figure 2.5: Schematic illustration of MAPP

Hence, in simple ternary mixtures of PP, GF and nanoclay, the task of MAPP is to establish a bond between these three different materials: the hydrocarbon part of the molecule tends to be kept in the PP matrix, while the oxygen atoms in the maleic anhydride ring can be linked to the hydroxyl groups of the GF and nanoclay by electrostatic attraction, thereby generating a strong hydrogen bonding between them, which is expected to help the exfoliation process [24] (Figure 2.6). There is an optimum level of MAPP loading in the composite system. The compatibilising technique will not be effective if the amount of MAPP used is too little, however, excessive compatibiliser content results in immiscibility between the matrix and MAPP, due to large polarity difference [58].

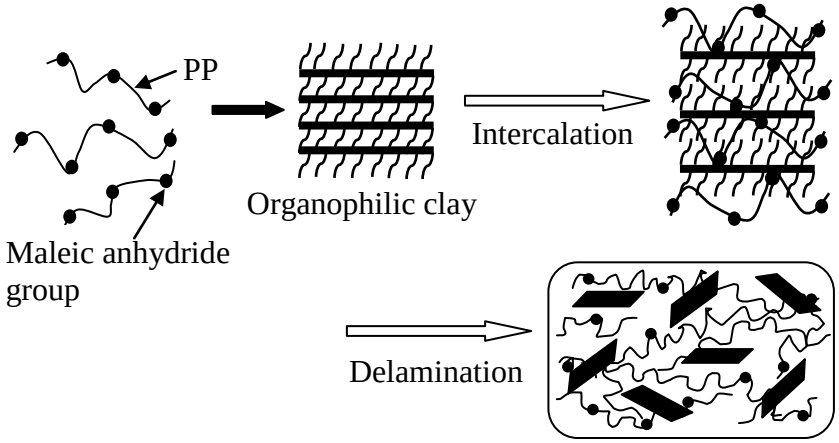

Figure 2.6: Schematic representation of the clay dispersion process [59]

2.4 Market and applications of composites

2.4.1 Polymer-clay nanocomposites

Polymer-clay nanocomposites (PCN) have often been shown to yield remarkable improvements in mechanical properties, flame retardancy, thermal, dimensional stability, antibrasiveness and anticorrosiveness, electrolyte properties, chemical resistance, barrier properties, optical characteristics, tuneable biodegradability, processability and recyclability [23, 30, 60 – 62]. For the first time, there is an opportunity to design materials without the compromises, typically found in conventionally reinforced polymer composites. From commercial and military perspectives, the value of PCN technology is not based on mechanical enhancements of the neat resin. Rather, it comes from providing value-added properties not present in the neat resin, without sacrificing the inherent processability and mechanical properties of the resin and the nanoclay. Traditionally, blend or composite attempts at multifunctional materials require a trade-off between the desired performances, mechanical properties, density, cost and processability.

As a consequence, the packaging applications become the ‘natural’ field of use for such materials. The advantage is evident, the currently adopted addition of higher barrier plastics in multilayer structures or surface coatings, necessarily increases the cost

of the usually cheap polymers utilised for packaging manufacturing, whereas the PCN option would be, a rather cost effective choice because of the ease of incorporation of the filler into resin systems. In fact, nylon 6 and PP are already used for packaging and injection moulded articles, whereas semi-crystalline nylon finds application for ultra-high barrier containers and fuel systems [63] in vehicle piping and in storage devices. The enhanced optical clarity and reduced haze which PCNs films exhibit (in comparison with the conventionally filled polymers), encourages even more of their use in packaging: films, bottles, boil-in bags, vacuum packs and blister packs. At the same time, it can be a completely transparent and an effective barrier to gas and water permeation. Indeed, the use of nanocomposite formulations would be expected to enhance considerably the shelf life of many types of food, just as studies are being conducted by the U.S. Army, in order to investigate the possibility of using PCNs as food packaging materials for soldiers.

The ability of nanoclay incorporation to reduce the flammability of polymeric materials was a major theme of the paper presented by Gilman *et al.* [61]. In this work, the extent to which flammability behaviour could be restricted in polymers, such as PP, with as little as 2 *wt%* of nanoclay loading was demonstrated. In particular heat release rates, as obtained from cone calorimetry experiments, were found to diminish substantially, following nanoclay incorporation. Although conventional micro particle filler incorporation, together with the use of flame retardant and intumescent agents would also minimise flammability rate, this is usually accompanied by reductions in various other important properties. With the nanoclay approach, this (flame retardancy) is usually achieved whilst maintaining or enhancing other properties and characteristics [18].

Lightness is another interesting aspect of PCNs. Their reduced particle size leads to high elements concentration, allowing very low loading levels, which indeed, rarely

exceed 5 *wt%*. On the contrary, currently the most used glass or mineral filled systems for automotive and appliance applications have loading levels ranging from 15 *wt%* to 50 *wt%*, leading inevitably to heavier products [60]. A light-weight material is typically appreciated when used on vehicles because it means less fuel consumption. For this reason unsaturated polyester based PCNs are already used for watercraft lay-ups and potential utilisation can be as mirror housings, door handles, engine covers and timing belt covers. A classical example of PCN material is the polyamide 6 nanocomposite timing belt cover produced in 1993 [29] by Toyota Motor Co. Kojima *et al.* [29] and Zanetti *et al.* [44] reported an improvement, (when compared to the neat resin), of 40% higher tensile strength, 68% higher tensile modulus, 60% higher flexural strength, 45% decrease in the coefficient of thermal expansion, 41% decrease in water absorption, with loss in impact strength of only < 10%, using just 4.7 *wt%* of layered-silicate loading.

In the medical industry, polyamide 12 nanocomposite catheters were commercialised by Foster Corp. in 2002 [64] and an artificial heart, based on polyurethane nanocomposites has been developed by researchers in the College of Medicine at Penn State University [65]. In pharmacology, cutting edge development in control drug release using polyvinyl-alcohol (PVA) and ethylene-vinyl-acetate (EVA) polymer nanocomposites has recently been introduced by a group of researchers led by Giannelis [66]. Mobile devices can take advantage from a low density material, such as the cover for portable electronic equipment (mobile phones, laptops, pagers *etc.*). The possibility to improve the flame retardance of the pristine polymer is an attractive characteristic of nano-fillers: the resulting PCNs, in fact, have been shown to be potent char formers and thus suitable to be used in fire retardant cabling, electrical enclosures and housings [63]. Other ongoing developments by the U.S. Army Research Laboratory include nanocomposite-based ballistic resistant wear and military packaging [67, 68] and epoxy-based nanocomposites for anticorrosive aerospace applications [69]. Other

general applications currently being considered include usage as impellers and blades for vacuum cleaners, power tool housings, mower hoods and outdoor advertising panels [18].

2.4.2 Polymer-glass fibre composites

Many of our modern technologies require materials with unusual combinations of properties that cannot be met by the conventional metal alloys, ceramics and polymeric materials. This is true especially for materials that are required for aerospace, underwater and transportation applications. For example, aircraft engineers are increasingly searching for structural material that have low densities, strong, stiff, high impact resistance and are not easily corroded. Thus, fibre reinforced polymer composites are designed with high strength and stiffness as well as light weight in order to meet these new applications.

In order to realize the greatest improvement in composite toughness, reinforcement with short fibres is very important for thermoplastic and thermoset materials. Glass fibres provide the stiffest and strongest reinforcing materials and for this reason they are the most commonly used reinforcing agent. The introduction of fibres into the matrix induces directionality (or anisotropy) to the material and for this reason, the properties are, therefore, highly dependent on the alignment of the fibres [70]. In some cases, toughness is enhanced, but in others where tougher resins are used, impact strength may be compromised, especially with shorter GF [71]. Currently, it is now possible to obtain commercially almost any thermoplastic resin reinforced with GF.

Glass fibre reinforced polypropylene (GFRP) is one of the fastest growing materials for automotive interior applications, due to the low overall material cost and also the ease of UV stabilization in the PP parts. This improves the recyclability of

vehicle parts and greatly reduces the costs of components by eliminating the painting process. GFRP materials can often be found in structural parts throughout the vehicle. Armrest substrates and console substrates are often injection moulded with 20 *wt%* – 30 *wt%* GF. These products offer a good combination of stiffness and impact, while maintaining the low specific gravity characteristics of PP [54].

Whereas fibre glass insulation is used to control heat loss and excessive noise in appliances and equipment, moulded composite parts are used for housing and bases. The use of GF composite for frames, time-share terminal units, calculator, television sets, air conditioning units and similar appliances is also well established.

Numerous adaptations of GF composites, in all type of construction, have taken place. The list includes: interior and exterior building components for residential, commercial, industrial and farm construction. Also important are the well-accepted tub and shower units and other ancillary equipment such as patio covers and garage doors.

Consumer products fabricated in GF composites are generally related to home leisure or recreational activities. Home products include basic frames for furniture as well as the finished items (traditional and modern). The controllable flexibility of GF composites that allows the production of varying stiffnesses required in vaulting poles, golf club shafts etc., plus the combination of high mechanical strength, lightness of weight, easy formability and resistance to corrosion and wear are all viable properties which favour the use of this material for consumer products [72].

2.5 Processing of hybrid composites

2.5.1 Extrusion/compounding

The production of composites through a compounding process has become mainstream approach for most industrial resin producers and in academic research. Extrusion/compounding refer to the method that is used to introduce fillers into the

polymer matrix, prior to moulding of a component. The polymer chains diffuse into the fibres and nanoparticles galleries, which involves annealing, above the softening or melting point of the polymer [45]. The ultimate criterion of success for any compounding method is whether the final moulded component has the desired properties. For this to be achieved, the following requirements normally have to be met [73]:

a) The fillers have to be 'wetted-out' where each filler must be totally encapsulated by the matrix.

b) The fillers should be uniformly dispersed throughout the matrix, with an absence of undispersed fibre bundles or particulate agglomerates, which might otherwise lead to variable strength of the composite.

c) The fibres should be of sufficient length when compared to their diameter in order to ensure an effective transfer of stress from the matrix to the fibres.

This route involves the use of three different possible types of compounder which are single screw extruder, twin screw extruder and co-kneader. Single screw extruder is still very widely used and with a properly designed screw profile, can produce compound with an acceptably low level of fibre degradation. It has the lowest capital cost of the three different types of compounder but is not very versatile if required to work with a variety of different types of compound [5]. Twin screw extruder is more expensive but is frequently built in a modular format, which allows different geometries of mixing and compounding regions to be used for different materials [74]. Generally, it is acknowledged that a twin screw extruder is preferred over a single screw for the formation of nanocomposites material. This is because of its more intense dispersive mixing mechanism [75, 76], mainly derived from the design (space between the pushing flight flank and the barrel is wedge shaped) that creates superior elongational flow as the material is forced through the flight clearance [77]. Since there

is no rotation in pure elongational flow, the deformation stress of the polymer is effectively transferred to the particle agglomerates in the melt, thus resulting in tensile forces acting to pull apart the clusters into smaller aggregates.

The screw design is of paramount importance and since one of the major sources of fibre breakage occurs at the feed section, it is usual to have deep flights in order to minimise this. In a twin screw extruder, the mixing is effected almost entirely by the action of the screws. There is a possibility to introduce the fibres or particulate fillers at some point along the barrel where the polymer is already fully or partially molten. The addition of fibres to a pre-melted polymer has the advantage that less fibre breakage occurs together with an improvement in dispersion [73]. Generally, for the thermoplastic-nanoparticle blends, a non-intermeshing arrangement tends to yield the best exfoliation property [76] and co-rotating screw is preferred over counter-rotating due to its rather balanced mixing force and residence time [78].

2.5.2 Injection moulding

The principal method for the production of components in polymer composites is injection moulding. The normal moulding cycle that is used for unfilled polymers is also used for the reinforced material, but the detailed processing condition employed maybe rather different. Since the properties of composites are highly dependent on the length and orientation of the fillers, it is important that these parameters should be controlled in the final moulding, by an appropriate choice of processing conditions. The problem is aggravated by the fact that when fillers are introduced into the polymer matrix, the rheological properties of the melt are significantly modified. Furthermore, the thermal conductivity of the melt is usually increased by the presence of fillers. Hence, the flow field and thermal conditions will be quite different when compared to unfilled polymer [79].

During the moulding of polymer composites, the following processing conditions are recommended for the production of good quality parts:

a) High injection speed should be used in order to achieve a good surface finish and to prevent premature solidification of the melt, either in the cavity or at the gate.

b) The screw speed and back pressure must be kept to a minimum, even though a homogenous melt is required, fibre breakage may become excessive.

c) The melt temperature used for polymer composites is usually at the upper end of the range recommended for the polymer matrix counterpart. This is chosen to reduce the viscosity of the melt and partly to assist in preventing premature solidification in the cavity.

d) After the cavity is filled, a long hold time is needed. This is required, not only to ensure that the moulding dimensions are correct, but to minimize the ever present problem of voiding observed in the core of moulded components [80].

Typically, melt temperature for moulding reinforced PP is in the range of 220°C to 240°C and mould temperature in the range from ambient up to 80°C may be used [5].

2.6 Structure-property relationships

2.6.1 Structural orientation

Recent studies mentioned that in addition to dispersion, orientation of the clay platelets plays a major role in tuning some property enhancements in PCN systems. Early study by Kojima *et al.* [81] concluded that the orientation of the clay platelets affected the strength of the nanocomposite along different sample directions. Lew *et al.* [82] demonstrated that silicate layers orientation followed an inter-dependent relationship between the degree of exfoliation, processing shear and mixing time. Krishnamoorti *et al.* [83] proposed that the orientation of the clay platelets could affect the viscoelastic properties of the nanocomposite.

Recently, an increasing number of studies started to focus on the effect of shear on the orientation of the clay platelets and the polymer unit cells in PCN systems. Kojima *et al.* [81] studied the effect of shear on the orientation of clay platelets as a function of depth in a 3 mm thick injection moulded polyamide 6 nanocomposites samples. Depending on the level of the shear involved, the clay platelets and the unit cell (020) or (110) lattice planes are oriented in different directions. Due to the high shear involved in the region of the sample close to the surface of the mould, the clay platelets and polymer unit cell (020) or (110) lattice planes were found to orient along the flow direction. On the other hand, in the bulk of the sample, the clay platelets and polymer unit cell (020) or (110) lattice planes were found to orient perpendicular to each other, due to the lower shear rate. The clay platelets were found to govern the orientation of the polymer unit cells due to hydrogen bonding between the alkylammonium cations at the end of polyamide 6 molecules and the ionic sites on the montmorillonite monolayer.

Fong *et al.* [84] studied clay dispersion and orientation in nylon-clay nanocomposite films and fibres using XRD and TEM. Films were cast and fibres were electrospun from solution. The effect of shear on the orientation of clay platelets and polymer unit cells in electrospun nylon-clay nanocomposite fibres was also studied. The authors found that the fibres had layered silicates crystallite (020) planes aligned with their vortices parallel to the fibre axis, implying orthogonal orientation between clay platelets and polymer crystallite (020) planes.

2.6.2 Thermal properties

Zanetti *et al.* [85] investigated the degradation behaviour of PP-clay nanocomposites. An increment of about 50°C in the onset degradation temperature was observed when compared to neat the homopolymer. A decrease in the rate of

degradation was also observed. The improvement in the thermal stability is believed to be due to the reduction in the transportation rate of the volatile products in and out of the sample. This phenomenon may be due to (i) the labyrinth effect (complex arrangement of the silicate layers which increases the tortuous path) that increases the barrier to flow of the degradation volatiles and (ii) physical adsorption of the volatile products on the surface of the silicate layers.

The thermal properties of PP/clay/wood flour hybrid composites prepared by melt compounding were reported by Lee *et al.* [86]. In thermogravimetric analysis (TGA), the addition of clay (1 phr to 5 phr), compatibiliser (5 phr to 10 phr) and wood flour (10 phr to 20 phr) considerably increased the decomposition temperature. Meanwhile, the melting and crystallisation temperatures obtained from differential scanning calorimetry (DSC) measurement were also improved with the use of clay and wood flour when compared to that of neat PP. However, the enthalpy heat of crystallisation largely decreased due to the increase in viscosity of the polymer and the decrease of clay, compatibiliser and wood flour dispersion in the polymer.

2.6.3 Dynamic mechanical properties

Dynamic mechanical analysis (DMA) is a powerful tool, used to study the various phase transition (molecular relaxation) behaviours of polymer and composite samples. The various phase transition temperatures were identified by the dissipation (damping) factor peaks (*tan δ*) of the thermograms. *Tan δ* is defined as the ratio of loss (or viscous) modulus (*E″*) to the storage (or elastic) modulus (*E′*).

In a viscoelastic experiment, an imposed stress or strain gives a response which is somewhat retarded by the viscous component of the polymer, its fluid-like behaviour, and because the polymer has solid-like behaviour, there is also an elastic response. DMA separates these two responses into separate moduli components: *E′* and *E″*. *E′*

represents the elastic response which is in-phase with the imposed deformation $(E' = (stress/strain)\cos\delta)$ and an indicator of elasticity, while the viscous damping, E'' is out-of-phase with the signal input $(E'' = (stress/strain)\sin\delta)$. The overall lag of the system from the input signal is the phase angle, δ. The tangent of the phase angle, *tan* δ, is a valuable indicator of the relative damping ability of the polymer. Any peak in the *tan* δ corresponds to a region where the polymer properties are changing very rapidly, or undergoing a transition.

Bozkurt *et al.* [87] studied the effect of clay on the mechanical and thermal properties of non-crimp GF reinforced epoxy nanocomposites. XRD results obtained from natural and modified clays indicated that intergallery spacing of the layered clay increases with surface treatment. DMA test was conducted on the specimens with multi-frequency strain mode using dual cantilever clamp. Incorporation of surface treated clay particles improved the dynamic mechanical properties of nanocomposite laminates. An increase of about 51% and 76% in the storage and loss moduli, respectively, of the composite were obtained with the addition of 6 *wt%* treated clay which is due to the restricting effect of the molecular motions.

The mechanical and dynamic mechanical properties of hybrid composites of PP reinforced with bamboo and GFs, compatibilised with MAPP, were studied by Samal *et al.* [88]. The DMA result showed an increase in storage modulus (*E'*), indicating higher stiffness of the hybrid composites as compared with untreated composites and virgin matrix. Incorporation of 2 *wt%* of MAPP resulted in an increase in *E'* as compared with the uncompatibilised system, due to the formation of ester linkage between the fibre surface and the compatibiliser tail, resulting in a stiffer combination. The *tan* δ spectra presented a strong influence of fibre content and coupling agent on the α– and γ– relaxation processes of PP. The damping properties of the composites, however,

decreased with the addition of the fibres and MAPP, indicating an improvement in the interfacial bonding in the composites.

2.6.4 Mechanical properties

2.6.4.1 Tensile properties

Under tension, tensile properties (modulus, strength and strain) are all important properties both commercially and theoretically [89]. Tensile strength is important in many applications; ranging from engineering to films, giving information on the maximum allowable load without plastic deformation occurring. Conversely and of similar importance, the tensile strain is the elongation allowable before plastic deformation occurs.

In the case where the fibres run from end to end of a long sample, the two components will be constrained to deform equally, provided the fibre/matrix bonding is good. Then the load carried by the composite as a whole, will be distributed between them in proportion to their relative cross-sectional areas. The rule of mixture, as previously explained by Thomason [90], is strictly valid only for composites in which fibres and matrix have identical Poisson's Ratio and equation of the rule of mixture, usually gives a good estimation of composite strength.

The significant enhancement in the tensile modulus often obtained in PCNs, originates from the formation of hydrogen bonds between the hydrophilic polymer (or compatibiliser) and the silicate layers. The extent of improvement is directly related to the average surface area to thickness (aspect ratio) of the dispersed layered-silicates. In a review done by Ray and Okamoto [91], the authors suggested that an exfoliated silicate structure, given by its greater aspect ratio, enhances the modulus more than an intercalated structure. Their suggestion was substantiated by the predictive model developed by Brune *et al.* [92] and based on the Halpin-Tsai equation, by assuming a

pseudo-particle (filler) character for the intercalated layered-silicate stacks with a decreased aspect ratio and elastic modulus. Due to the decrease in the aspect ratio and elastic modulus of the filler, the relative modulus of nanocomposite that has pseudo-particles component, of exfoliated silicate structure, is lower. This theoretical model thus supports most experimental observations in the literature which often reported the attainment of greater modulus in predominantly an exfoliated morphology rather than a predominantly intercalated morphology. Recent modelling by Luo and Daniel [93], based on the Mori-Tanaka method, also arrived at a similar conclusion.

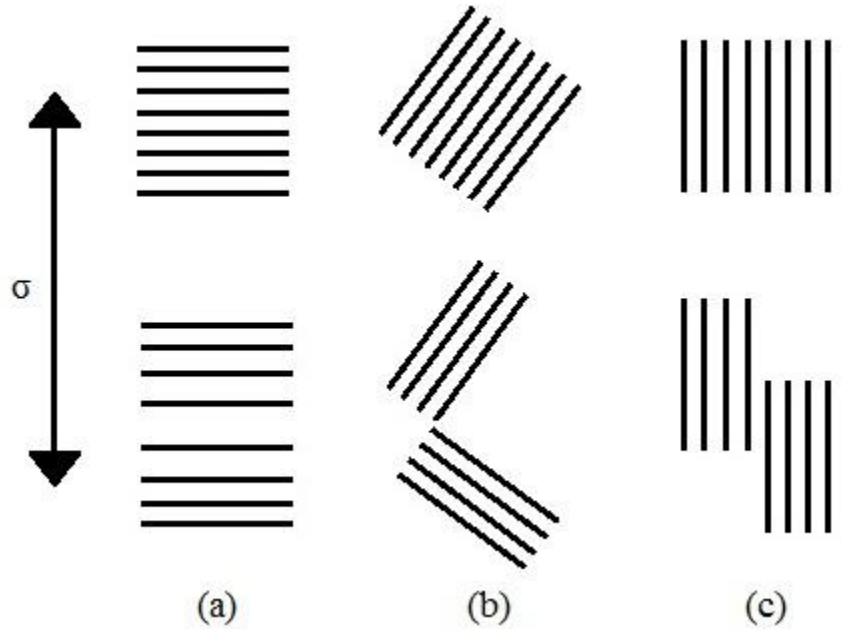

Figure 2.7: Schematic models of micromechanical deformation processes of stacked silicate layer, depending on the orientation (arrow indicates the load direction): (a) splitting mode, (b) opening mode and (c) sliding mode [94]

Kim *et al.* [94] carried out an in-situ high resolution transmission electron microscope **(**HRTEM) tensile deformation study of polyamide 12 nanocomposites. Based on the results obtained, the authors proposed that the improvement in toughness was attributed to a mechanism that slow down the matrix deformation process, by the tilting of the partially separated silicate stacks, perpendicular to the direction of applied

load. Depending on the orientation of the stacked layers, some amount of applied energy is dissipated by splitting, sliding or opening the separated bundles in the stacked layers (Figure 2.7). Due to the micro-environments of layered-silicates (well organised structures), they could function as microvoid initiation sites, which are necessary for high toughness. The silicate layers, bounded at the fringes of microvoids, are load-bearing and therefore enhance the stiffness of the nanocomposite matrix by resisting the microvoids/cavities from growing further [94, 95]. The results indicate that an intercalated structure is a more effective reinforcement for stiffness and toughness.

Hemmasi *et al.* [96] studied the effect of nanoclay on the mechanical and morphological properties of wood polymer nanocomposites. Hybrid composite with lower clay loading exhibited better dispersion of the clay layers within the polymer matrix, as confirmed by the increment in the d-spacing from XRD measurement. They observed a significant improvement in the tensile modulus by the addition of 3 phr of nanoclay. However, the tensile modulus levelled off, as higher content of clay was used, due to the agglomeration of the nanoparticles. The reinforcing efficiency of the nanoclay was reported to be further enhanced with the presence of compatibiliser in the system.

The effects of nanoclays on short GF reinforced PP composites were examined by Mohan and Kanny [97], with special emphasis on the processing parameter on the structure, tensile and wear properties of the materials. Improved tensile properties were observed in nanoclay filled GF composites, due the intercalated and exfoliated nanocomposite structure. An enhancement in the tensile modulus of about 21%, was observed with the addition of 5 *wt%* of nanoclay. However, at clay concentration higher than 3 *wt%*, a reduction in the tensile strength of the hybrid composite was obtained, due to the agglomeration of the nanoclay.

The effect of fibre treatments and matrix modification on the mechanical properties of flax fibre/glass fibre/polypropylene hybrid composites was reported by Arbelaiz *et al.* [98]. Treatments using chemicals, such as; maleic anhydride (MA), vinyltrimethoxy silane (VTMO), MAPP copolymer *etc.* were carried out. VTMO and MA treatments applied to flax fibres showed no effect on the mechanical properties, while MAPP-treated fibres increased tensile and flexural strengths of the composite. Matrix modification with VTMO and MA in the presence of dicumyl peroxide, increased the composites tensile strength and modulus by 77% and 31%, respectively, when compared to composites based on untreated flax fibre bundles.

2.6.4.2 Impact properties

Nowadays, there has been an increasing interest in instrumented impact-testing machines, especially in industrial laboratories. For many years, Charpy and Izod tests [99] have been commonly used to evaluate the impact resistance of polymers and their composites, due to their simplicity. Most of the investigations of the impact behaviour have been with pendulum impact tests. Unfortunately, impact pendulum tests give results that are very sensitive to sample dimension and difficult to relate with service condition. Therefore, instrumented drop weight impact tests are widely used among the different types of impact tests due to its capability of testing materials at a wide range of velocities.

Very frequently, impact test involve notched samples. The geometry of the notch plays a major role in determining the type and energy of fracture. Sharp notches produce plane-strain conditions and accentuate brittle failures and are now generally favoured over blunt notches, which allow for crazing and shear yielding mechanisms. Another variable is whether the notch is moulded into the specimen or machined into it. Sometimes the notch is positioned on the same side as the striker and sometimes on the

opposite side. Orientation of polymer and filler particles during processing affect impact properties and often specimens are cut from a product with across flow [89].

Impact resistance can be defined as the ability of a material and its structure to survive impact induced damages during an impact event. The impact performance of composite materials depends on many factors, including the nature of the fibre, matrix, interface, geometry and testing conditions [100]. Matrix ductility, fibre type and content, as well as void content of the composites are the main structural parameters which significantly affect the impact behaviour [101]. Basically, under impact loading materials tend to behave in a brittle manner before fracture.

Traditionally, it is believed that the addition of a rigid filler to a thermoplastic results in a decreased plastic's toughness, as measured by impact strength, while its rigidity is increased [102]. The greater the increase in rigidity, the lower is the impact strength. However, as research efforts on the use of mineral-filled thermoplastics have increased, it has been established that while this rule is true for many composites, reduction in impact strength is not an inevitable consequence of filling. It is, however, a very complicated picture with filler size, shape, loading, interfacial adhesion, polymer type, glass transition temperature and even type of impact test, all playing a role [89].

Bramuzzo *et al.* [103] reported that a stearate-coated calcium carbonate increased fracture toughness of PP, reaching a maximum at about 40 *wt%* loading. Using SEM, plastic deformation was found to have occurred around the calcium carbonate particles, giving rise to the toughening effect.

It has been suggested that increases in toughness can be due to crack pinning, with the particles inhibiting its propagation. Sizes and numbers of particles will affect the entent of pinning [104]. The relative contribution of pinning to crack growth depends on the strength of the filler-polymer interaction and the toughness of the

matrix. Increasing matrix toughness or reducing filler-polymer interaction will reduce composite toughness.

Notched and unnotched impact strengths of china-clay and calcined-clay filled PP have similarly been found to be independent of particle size [89]. In the latter case, treatment of the calcined clay with stearic acid gave a small improvement, probably because its dispersion was improved.

The relationship between structure and the fracture behaviour of PP, reinforced with long GF and particulate $CaCO_3$, prepared by melt processing was reported by Hartikainen *et al.* [12]. Fibre orientation, fibre length distribution and impact properties of hybrid composites, as well as crystallinity changes of PP upon filler addition, were reported. Furthermore, acoustic emission (AE) analysis was applied to get information about the fracture mode during the loading. It was found that the filler addition had little effect on the fibre orientation and crystallisation behaviour of the composites, but average fibre length decreased. AE analysis showed that the addition of filler caused early stage debonding of the hybrid composite, resulting in a reduction of fracture toughness.

CHAPTER THREE

3 Experimental

3.1 Materials

Commercially available PP (Propelinas H022), supplied by Petronas Malaysia, was used as the matrix. Chopped E-glass fibre, surface-treated with silane and having a density of 2,550 kg m^{-3}, diameter of 14 µm and length of 6 mm was obtained from KCC Corporation, Korea and used as the principal reinforcement. The untreated natural montmorillonite nanoclay (type PGV) and the surface modified nanoclay (type 1.44 PS), containing dimethyl dialkyl amine, was obtained from Nanocor USA. Maleic anhydride grafted PP, MAPP (Polybond 3200) was supplied by Chemtura Corporation, USA (formerly Crompton Corporation) and used as the compatibiliser. Tables 3.1 and 3.2 show the properties of the raw materials.

Table 3.1: Properties of PP and MAPP

Property	Unit	PP	MAPP [105]	ASTM test method
Melt flow index (2.16 kg load at 190°C)	g/10 min	11	115	D-1238 [106]
Density	kg m^{-3}	910	910	D-1505 [107]
Tensile strength at yield	MPa	35.3	-	D-638 [108]
Elongation at yield	%	8	-	D-638
Flexural modulus	GPa	1.67	-	D-790 [109]
Notched izod impact strength (at 23°C)	kJ m^{-2}	3	-	E-23 [99]
Heat deflection temperature (at 4.6 kg cm^{-2})	°C	90	-	D-648
Rockwell hardness	R scale	93	-	D-785A
Maleic anhydride grafting level (w w^{-1})	%	-	1	-

Table 3.2: Properties of untreated (PGV) and treated (1.44 PS) nanoclays

Property	Unit	Nanoclay PGV [110]	Nanoclay 1.44 PS [111]
Surface modification	-	Untreated	Contains 35 – 45 *wt%* dimethyl dialkyl (C14 – C18) amine
Appearance	-	Beige powder	Off–white powder
Weight loss (drying at 105°C for 1 hour)	%	10.6	1
Bulk density	kg m^{-3}	776	273
Average particle size	µm	16	12
Cation exchange capacity (CEC) ±10%	(meq/100 g)	145	–
Aspect ratio	-	150 – 200	–

3.2 Processing

3.2.1 Compounding

Nanoclay (NC) and GF were dried in a vacuum oven at 95°C for 24 hours to a moisture content of less than 1% and stored in sealed plastic bags over dried silica gel in desiccators for not more than 24 hours prior to compounding.

In order to prepare PP/NC nanocomposites, different compositions of PP, MAPP and NC powder in 200 g portions were compounded using the co–rotating twin screw extruder (Brabender KETSE 20/40, Germany), with the screw diameter and screw aspect ratio of 20 mm and 40, respectively. Figure 3.1 shows the extruder's screw configuration used for the compounding. The temperature profile from the hopper to the die was set at: 185°C, 185°C, 180°C, 180°C, 185°C and 185°C for 6 different heating zones. The screw speeds used were 100 rpm, 300 rpm, 500 rpm and 800 rpm, as detailed in Table 3.3. The melt pressure varied between 20 bar and 25 bar (2.0 MPa – 2.5 MPa), while the die temperature was measured between 197°C to 203°C.

On the other hand, in order to prepare PP/GF composites, PP, MAPP and GF were pre-mixed in different compositions in 500 g portions and compounded using the same extruder. The temperature profile along the barrel from the hopper to the die was

set at 185°C, 185°C, 185°C, 185°C, 190°C and 190°C for heating zone 1 to 6, respectively, and the screw speed of 50 rpm, 100 rpm and 150 rpm were used. The melt pressure varied between 16 bar and 18 bar (1.6 MPa – 1.8 MPa) depending on the GF content, while the die temperature was measured between 195°C to 198°C.

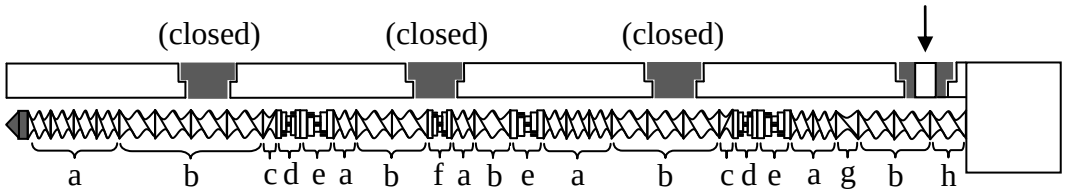

(a) SE-20/20R
(b) SE-30/30R
(c) SE-20/10L
(d) KBW-45/5/20/L
(e) KBW-45/5/30/R
(f) KBW-45/5/20/R
(g) SE-30/15R
(h) SE-30/30A

Figure 3.1: Extruder's screw configuration

In order to produce the PP/GF/NC hybrid composites, the different ratios of the corresponding PP/NC composite in pellets form and GF were physically mixed and re-compounded in a twin screw extruder, using the same temperature profile and the screw speed used in the preparation of PP/GF composites, as mentioned earlier.

Vacuum venting was used to ventilate out the volatile compounds. The samples were extruded out through a circular die of 3 mm in diameter. The extruded strand was cooled in a water bath and pelletised into lengths of about 6 mm using a pelletiser. Extruded pellets were vacuum oven dried at 95°C for 24 hours and stored in sealed plastic bags not more than 24 hours before injection moulding. The list and abbreviation of specimens prepared are given in Table 3.3. It should be noted here that due to the difference in the density of nanoclay untreated (NCUT) and nanoclay surface treated (NCST), the amount of clay used were not the same, in order to maintain the same filler volume fraction (V_f) for each type of nanocomposite. For example, 2 phr of treated clay nanocomposite has the same V_f as 6 phr of untreated clay nanocomposite.

Table 3.3: Formulations of PP/NC nanocomposites, PP/GF composites and PP/GF/NC hybrid composites

Sample code	Matrix weight fraction W_m (%)	MAPP weight fraction W_{MAPP} (%)	Fibre weight fraction W_f (%)	Fibre volume fraction V_f (%)	Clay content (phr)	Screw speed (rpm)
PP	100	-	-	-	-	-
Clay nanocomposites						
PP100/NCUT3	100	-	-	-	3	800
PP100/NCUT6	100	-	-	-	6	800
PP100/NCUT9	100	-	-	-	9	800
(PP100:C0)/$NCST2_{800}$	100	-	-	-	2	800
(PP92:C8)/$NCST2_{100}$	92	8	-	-	2	100
(PP92:C8)/$NCST2_{300}$	92	8	-	-	2	300
(PP92:C8)/$NCST2_{500}$	92	8	-	-	2	500
(PP92:C8)/$NCST2_{800}$	92	8	-	-	2	800
(PP95:C5)/NCUT3	95	5	-	-	3	800
(PP98:C2)/NCUT6	98	2	-	-	6	800
(PP95:C5)/NCUT6	95	5	-	-	6	800
(PP92:C8)/NCUT6	92	8	-	-	6	800
(PP95:C5)/NCUT9	95	5	-	-	9	800
(PP98:C2)/NCST2	98	2	-	-	2	800
(PP95:C5)/NCST2	95	5	-	-	2	800
(PP92:C8)/NCST2	92	8	-	-	2	800
Glass fibre composites						
PP85/G15	85	-	15	6	-	100
PP70/G30	70	-	30	14	-	100
PP55/G45	55	-	45	23	-	100
$PP85/G15_{50}$	85	-	15	6	-	50
$PP85/G15_{100}$	85	-	15	6	-	100
$PP85/G15_{150}$	85	-	15	6	-	150
(PP83:C2)/G15	83	2	15	6	-	100
(PP80:C5)/G15	80	5	15	6	-	100
(PP77:C8)/G15	77	8	15	6	-	100
(PP65:C5)/G30	65	5	30	14	-	100
(PP50:C5)/G45	50	5	45	23	-	100
Glass fibre/ nanoclay hybrid composites						
(PP85)/G15/NCUT3	85	-	15	6	3	100/800
(PP85)/G15/NCUT6	85	-	15	6	6	100/800
(PP85)/G15/NCUT9	85	-	15	6	9	100/800
(PP70)/G30/NCUT3	70	-	30	14	3	100/800
(PP70)/G30/NCUT6	70	-	30	14	6	100/800
(PP70)/G30/NCUT9	70	-	30	14	9	100/800
(PP55)/G45/NCUT3	55	-	45	23	3	100/800
(PP55)/G45/NCUT6	55	-	45	23	6	100/800
(PP55)/G45/NCUT9	55	-	45	23	9	100/800

Table 3.3, continued

Sample code	W_m (%)	W_{MAPP} (%)	W_f (%)	V_f (%)	(phr)	(rpm)
(PP83:C2)/G15/NCUT6	83	2	15	6	6	100/800
(PP80:C5)/G15/NCUT6	80	5	15	6	6	100/800
(PP77:C8)/G15/NCUT6	77	8	15	6	6	100/800
(PP83:C2)/G15/NCST2	83	2	15	6	2	100/800
(PP80:C5)/G15/NCST2	80	5	15	6	2	100/800
(PP77:C8)/G15/NCST2	77	8	15	6	2	100/800

Note:
NCUT: Nanoclay untreated (PGV)
NCST: Nanoclay surface treated (1.44 PS)
phr: parts per hundred parts of resin

3.2.2 Injection moulding

(a)

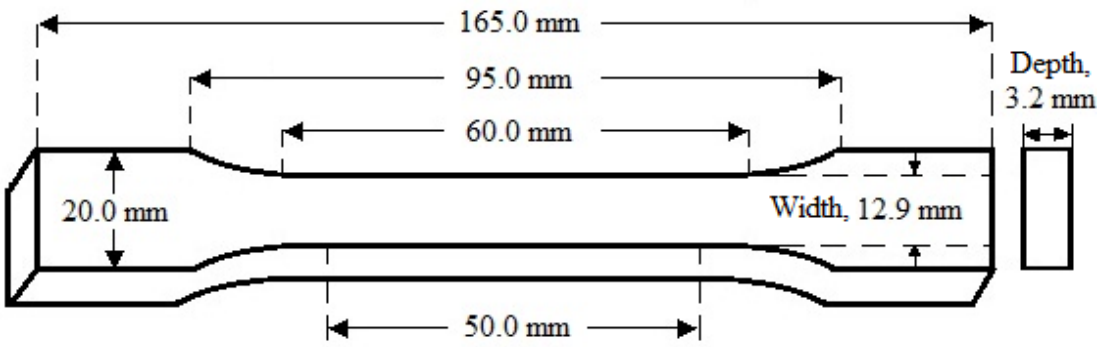

(b)

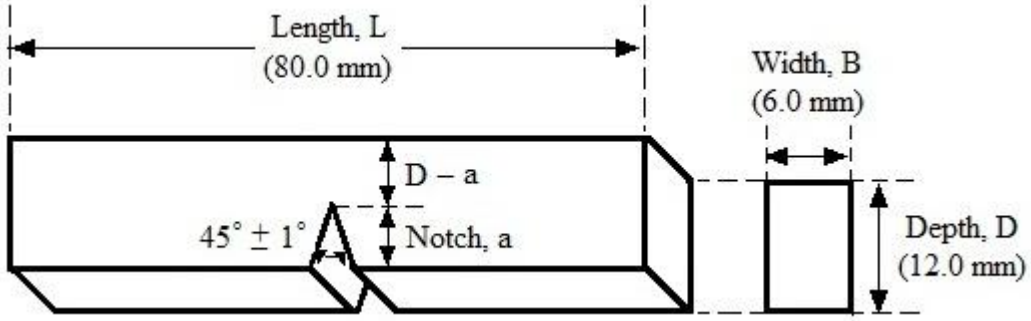

Figure 3.2: Dimension of: (a) the dumb-bell shaped tensile test specimen and (b) the single edge notch (SEN) impact test specimen

The dumb-bell shaped tensile and rectangular bar impact test specimens (Figure 3.2), according to ASTM D-638 standard [108] and ASTM E-23 standard [99], respectively, were then injection moulded using a Boy® 55M (Germany), with a 55–

tonne clamping force injection moulding machine. The processing temperature profile along the barrel from the hopper to the nozzle was set at 180°C, 195°C, 195°C and 195°C for the heating zone 1 to 4, respectively and the mould temperature was set at 25°C with the cooling time of 20 s. The screw speed was maintained between 30 rpm – 50 rpm, with the injection pressure and the holding pressure of between 60 bar – 120 bar and 50 bar – 100 bar, respectively.

3.3 Characterisations

3.3.1 Determination of fibre volume fraction (V_f)

For the determination of fibre volume fraction, V_f, samples from the central portion of the injection moulded tensile test piece were cut and the polymer matrix was removed by heating a composite specimen in a muffle furnace at a temperature of up to 700˚C for a period of about 6 hours. Fibres were then weighted [112].

3.3.2 Determination of fibre length distribution (FLD)

The isolation of fibres from the composite material was done by burning about 1 cm of specimens taken from the middle section of the tensile test bar at 700˚C in a muffle furnace for not less than 6 hours. The fibres were then dispersed in a beaker containing water, glass microscope slide and a small amount of detergent to reduce surface tension. In order to ensure uniform mixing of fibres, the beaker containing fibres was placed in an ultrasonic water bath for a period of about 2 minutes.

The slides with fibres on one side were then dried in an oven. The glass slide were then placed on the observation stage of a Zeiss Primo Star microscope (Leco, Model IA-32, USA) image analyser and viewed in dark field transmission mode with resolution of 4X. A video camera was attached to the microscope transmitted live fibre images to the image analyser. Dedicated software automatically digitised the fibre

image and enhanced the contrast between foreground (fibres) and background. Lengths of not less than 500 fibres were measured.

3.3.3 Fourier-transform infra-red (FTIR) spectroscopic analysis

FTIR-ATR spectra of samples were recorded using the FTIR spectrophotometer (Spotlight 400, Perkin Elmer, USA), combined with a universal attenuated total reflectance (ATR) accessory at a resolution of 4 cm^{-1} for 64 scans in the range of 650 – 4000 cm^{-1}. Samples were pressed against the diamond crystal of the ATR unit. A pressure applicator with a torque knob ensured that the applied pressure was uniform for all measurements. A background spectrum of the clear window was recorded, prior to sample spectra acquisition. The spectrum of the background was subtracted from that of the sample before conversion into transmittance units.

3.3.4 Microstructural characterisation

3.3.4.1 X-ray diffraction (XRD)

Neat clay, PP/NC nanocomposites and PP/GF/NC hybrid composites were analysed using the Philips-binary XRD diffractometer, with CuK_{α} radiation. Clay powder and nanocomposites tensile specimen were scanned over an interval of $2\theta = 2°$ – 30° at 40 kV and 30 mA. Using XRD, intercalation behaviour of clay particles (in the composites) with different concentration was analysed.

3.3.4.2 Focused ion beam scanning electron microscope (FIB-SEM)

The nanoclays powder and the fracture surface of the various nanocomposites were examined using a focused ion beam scanning electron microscope (FIB-SEM), model Auriga® Zeiss (Germany). The samples were adhered to the aluminium stub using conductive carbon tape. The stub was then mounted on the stub holder and loaded

into the chamber. The air evacuation in the chamber was performed before analysis. SEM micrographs were taken at an accelerating voltage of 10 keV at various magnifications. The samples were sputter-coated with a thin layer of gold to a thickness of 0.014 μm in order to improve the sample conductivity and to avoid electrical charging during examination.

3.3.4.3 Transmission electron microscope (TEM)

The microstructure of the PP/NC and PP/GF/NC were analysed with a Hitachi H-600 (Japan) transmission electron microscope (TEM). The samples were ultra-microtomed with a diamond knife on a Leica Ultracut UCT (UK) microtome at room temperature to obtain section with a nominal thickness of 200 nm. Sections were transferred to a 400 mesh Cu grids. Bright-field TEM images of the composites were obtained at 300 kV under low-dose conditions.

3.3.5 Thermal analysis

3.3.5.1 Thermogravimetric analysis

Thermogravimetric analysis (TGA) was carried out in order to investigate the thermal decomposition behaviour of the composite materials by using the Perkin Elmer TGA 6 (USA) on samples of between 10 mg – 15 mg in weight of the composites, in a ceramic crucible, over a programmed temperature range of 50^{o}C to 850^{o}C at a scan rate of 10°C min^{-1}. The tests were conducted under nitrogen environment with the nitrogen flow rate of 20 mL min^{-1}. Samples were taken from the injection moulded tensile test specimens. From each specimen, samples were taken from the nearest, middle and farthest portion from the gate of the mould cavity and subjected to TGA analyses. The percentage weight change over the programmed temperature range was analysed by using Pyris software.

3.3.5.2 Differential scanning calorimetry

Differential scanning calorimetry (DSC) experiments were performed with a Perkin-Elmer Hyper Diamond DSC (USA). Each sample was subjected to heating, cooling and second heating cycles at a scanning rate of 10°C min^{-1}, under nitrogen atmosphere at a flow rate of 20 ml min^{-1}, in order to prevent oxidation. The test sample weight of between 5 mg – 10 mg, was crimped in an aluminium pan and tested over a temperature range of between -50°C to 190°C. The endothermic and exothermic curves were obtained by using Pyris software.

3.3.6 Dynamic mechanical analysis

The dynamic mechanical analysis of specimens was performed using the Thermal Analysis Instrument, TAI Q800 (USA) dynamic mechanical analyser. Test specimens were taken from the middle section of the injection moulded dumb-bell test bar with average dimensions of 60.0 mm x 13.0 mm x 3.3 mm (length x width x thickness). Specimens were subjected to a three-point bending mode with a support span of 50 mm. Measurements were conducted over a temperature range of –100°C to 110°C, with a heating rate of 3°C min^{-1} at a constant frequency and amplitude of 1.0 Hz and 15 μm, respectively. The storage modulus, loss modulus and tan delta peaks were obtained using the TA universal analysis software.

3.3.7 Mechanical testing

3.3.7.1 Tensile testing

Tensile tests were carried out using the universal testing machine (Instron 5569, USA) equipped with a load-cell of 50 kN and a mechanical extensometer, according to the ASTM D-638 standard [108], at a constant cross-head speed of 5 mm min^{-1} at 25˚C. Injection moulded dumb-bell shaped specimens were used for the tests (Figure 3.2(a)).

The gauge length for the extensometer and the grip distance between the jaws of the clamp was fixed at 50 mm and 95 mm, respectively. The averages of at least five reproducible results were reported. The tensile modulus was calculated at 0.5% strain. Specimen arrangement during tensile testing is shown in Figure 3.3.

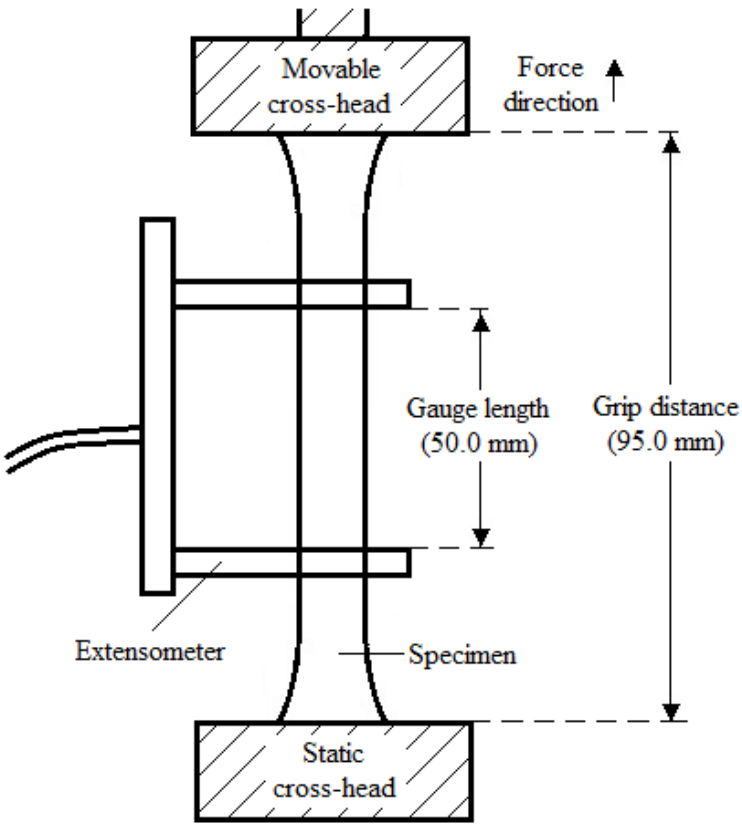

Figure 3.3: Setup for tensile testing

3.3.7.2 Flexural testing

The same instrument used for tensile testing was used for the flexural testing but on a three point bending mode according to ASTM D-790 standard [109]. Injection moulded dumb-bell shaped specimens (Figure 3.2(a)) were used with a span of 50 mm. Maximum deflections of 30 mm and a cross-head speed of 1.28 $mm.min^{-1}$ were maintained throughout the experiment. The speed of the cross-head, R, was calculated using the following equation:

$$R = \frac{ZL^2}{6d} \qquad (3.1)$$

where L and d are the specimen support span distance and depth respectively. The specimen thickness became the depth because the specimens were mounted in the flat position. Z is the straining rate of the outer fibre (equal to 0.01). L was fixed at 50 mm. A minimum of seven samples were tested and the values of at least five best results were recorded. Figure 3.4 shows the arrangement of the specimen during the test.

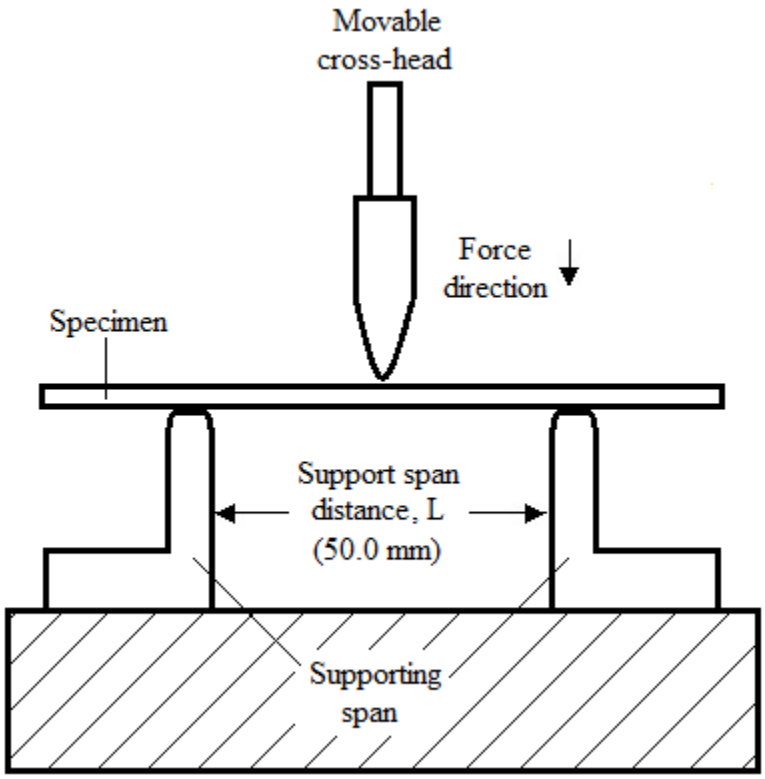

Figure 3.4: Setup for flexural testing

3.3.7.3 Impact testing

The charpy impact test measures the energy absorbed by a standard notched bar specimen, while breaking the specimen under an impacting load. The impact test bars of 60 mm x 12 mm x 6 mm (length x depth x width) dimensions were notched at the centre of one edge to produce a single edge notch (SEN) impact test specimen. The impact test specimen dimension is shown in Figure 3.2 (b).

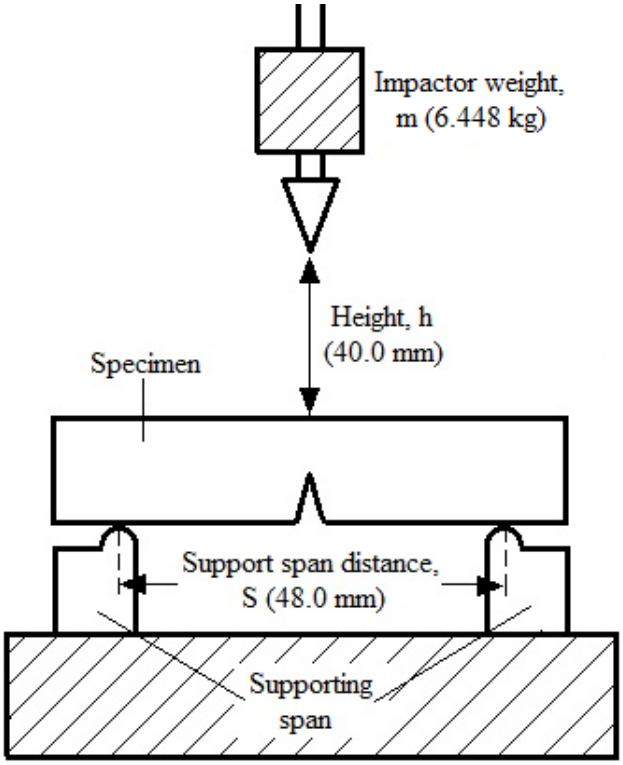

Figure 3.5: Setup for impact testing

The notch angle was set at 45°. Each batch was notched with four different notch-to-depth (*a/D*) ratios of 0.1, 0.2, 0.3 and 0.4 using a Ray-Ran notch cutting machine. The support span-to-depth ratio (*S/D*) was maintained at 4 throughout the experiment. The impact test was run under charpy mode using an Instron Dynatup 9210 (USA) instrumented falling weight impact tester with a V-shaped impactor tup (Figure 3.5). The test was carried out at 25°C, with fixed impactor weight (*m*) of 6.448 kg, height (*h*) of 40 mm, impactor velocity (*v*) of 0.9238 m s^{-1} and impact energy of 2.7512 J. The impactor tup struck the specimen midway between the supports. For each batch, a minimum of 10 specimens were tested and the results presented were taken from the average of at least 8 reproducible data. ASTM E-23 standard [99] was used as a standard, in calculating the impact properties.

CHAPTER FOUR

4 Results and discussion

4.1 Fibre volume fraction, V_f

Fibre volume fraction, V_f of composite specimens were calculated using standard equations [113]. The fibre volume fractions (V_f) and fibre weight fractions (W_f) were evaluated for each composite by using the density (ρ) values of PP, glass fibres, untreated and treated clays as previously mentioned in Tables 3.1 and 3.2. However, there is always a strong possibility that the resin has been modified by the presence of the fillers and the density of the matrix might be different from the pure resin because of fibre nucleating effect, molecular conformation effects of polymer chains at interface, dissolutions effects and reaction of the sizing.

Table 4.1: Fibre volume fraction of composites

Sample	Intended W_f (%)	Average experimental W_f (%)	Intended V_f (%)	Average experimental V_f (%)
PP100/NCUT3	2.9 (≈ 3 phr)	2.8	3.4	3.3
PP100/NCUT6	5.7 (≈ 6 phr)	5.6	6.6	6.5
PP100/NCUT9	8.3 (≈ 9 phr)	8.1	9.6	9.4
PP100/NCST2	2.0 (≈ 2 phr)	1.9	6.4	6.1
PP85/G15	15.0	15.0	6.0	6.0
PP70/G30	30.0	30.0	14.0	14.0
PP55/G45	45.0	45.0	23.0	23.0
(PP85)/G15/NCUT3	17.9	16.8	9.6	8.2
(PP85)/G15/NCUT6	20.7	20.7	13.2	13.2
(PP85)/G15/NCUT9	23.3	23.2	16.4	16.3
(PP70)/G30/NCUT3	32.9	31.8	17.3	15.8
(PP70)/G30/NCUT6	35.7	35.2	21.3	20.6
(PP70)/G30/NCUT9	38.3	38.0	24.9	24.4
(PP55)/G45/NCUT3	47.9	46.5	27.1	24.9
(PP55)/G45/NCUT6	50.7	50.2	31.5	30.7
(PP55)/G45/NCUT9	53.3	53.1	35.5	35.2

Table 4.1 shows the experimental values of V_f and the values obtained are as expected. As previously mentioned, in section 3.2.1, a precaution should be taken in preparing the materials before feeding into the compounding machine. The glass fibre

composite and clay nanocomposite blends were prepared in batches with a total weight of 500 g and 200 g, respectively. If a large quantity of blend is used, the fillers tend to settle down in the feed hopper of the extruder and leaving the polymer matrix at the top and could result in inconsistency of the composites composition.

4.2 Fibre length distribution (FLD)

The FLD data obtained from fibres extracts from the tensile test specimen are summarised in Table 4.2. The plots of FLD are shown in Figures 4.1 – 4.6.

Table 4.2: The fibre characteristic of injection moulded glass fibre composites

Sample	Percentage of fibre with length, L (%)			L_n	L_w
	L < 0.3 mm	L < 0.6 mm	L < 0.9 mm	(mm)	(mm)
PP85/G15	50.2	89.2	98.8	0.33	0.46
PP70/G30	72.0	96.2	100.0	0.24	0.35
PP55/G45	91.0	98.8	99.8	0.16	0.24
$PP85/G15_{50}$	45.0	87.0	98.0	0.37	0.49
$PP85/G15_{100}$	50.2	89.2	98.8	0.33	0.46
$PP85/G15_{150}$	73.8	94.8	99.4	0.25	0.37

Note: For specimen coding, for instance $PP85/G15_{50}$, the subscript refers to the extrusion screw speed.

4.2.1 Effect of glass fibre loading

It is generally known that the mechanical properties of injection moulded short glass fibre reinforced polymer (SFRP), such as: strength, stiffness and modulus are strongly dependent on the fibre length distribution (FLD) and fibre orientation distribution (FOD) of the final composites. It is also highly dependent on the critical fibre length and the shear strength at the fibre-matrix interface. Therefore, it is greatly important to study the effects of the FLD and FOD, due to the fact that both parameters depend on the fibre volume fraction, the gate geometry and the processing conditions [114]. From Figure 4.1, it can be seen that for all specimens, fibre distributions are quite

normal, tailing-off towards the longer fibre length. The same observation was reported by Hassan *et al*. [112].

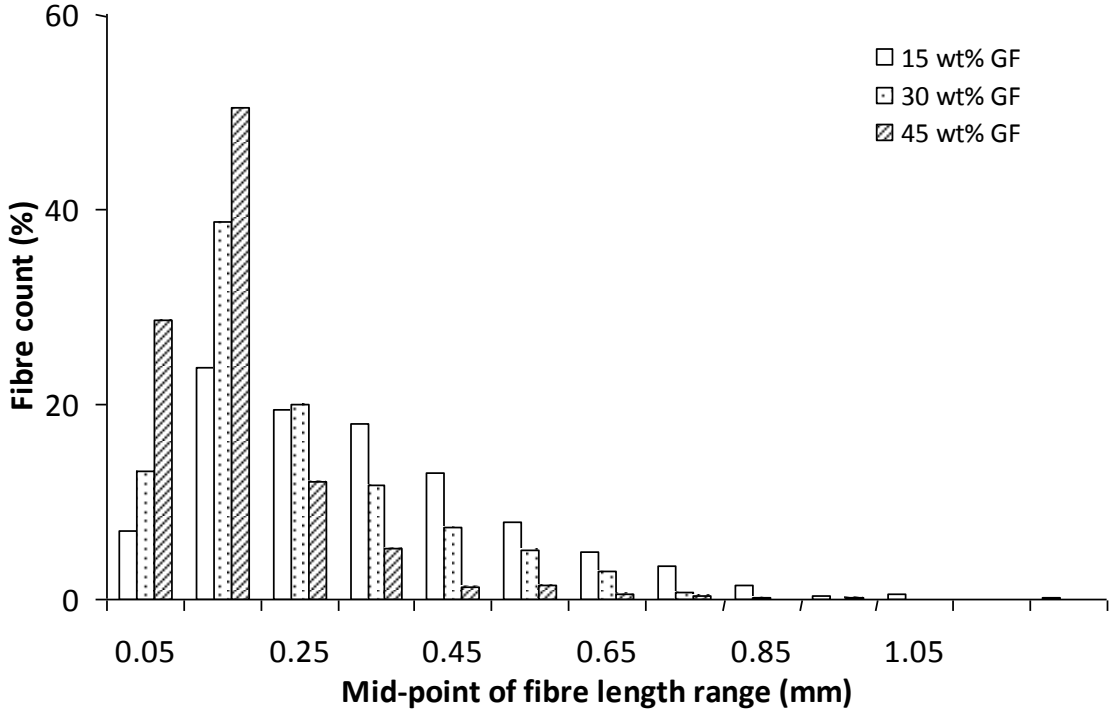

Figure 4.1: Fibre length distribution of injection-moulded glass fibre composites

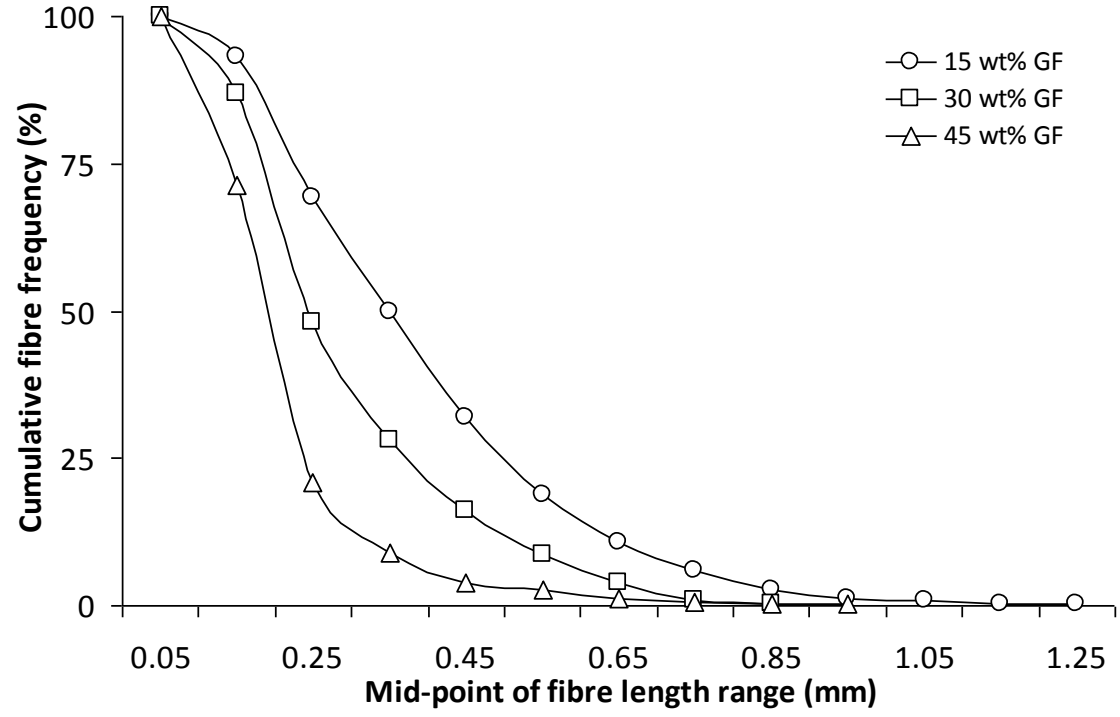

Figure 4.2: Cumulative fibre frequency of injection-moulded glass fibre composites

The plots in Figure 4.2 (cumulative FLD) also show that more fibre population with shorter length occurred in composites with higher fibre loading, whereas the composites with lower fibre loading have more fibre population with longer length. This indicates that more fibre degradation has taken place during compounding and moulding of composites with high fibre loading, probably due to fibre-fibre, fibre-matrix and fibre-machinery surface friction. In addition, high melt viscosity and increased tendency for high fibre contact are probably responsible for the higher fibre breakage in this category of composites [113, 115]. This type of behaviour can also be seen from the calculated values of the percentage of fibre with length, L less than 0.3 mm, 0.6 mm and 0.9 mm (Table 4.2). It can be seen that for PP/G45 composite, 91% of the fibre population is located in the category L < 3 mm, whereas for PP/G15 composite, only 50% of the fibre population is found to be in the same category. Again, this observation proved that composite with lower fibre loading tends to retain high fibre length. The same trend is observed for L < 6 mm and L < 9 mm.

The number average fibre length (L_n) that presents a measure of fibre ends density and weight average fibre length (L_w) which gives a greater importance to the proportion of long fibres in the distribution were also calculated using equation (4.1) and (4.2) respectively:

$$L_n = \Sigma\left(f_i L_i\right)/\Sigma f_i \qquad (4.1)$$

$$L_w = \Sigma\left(f_i L_i^2\right)/\Sigma\left(f_i L_i\right) \qquad (4.2)$$

where f_i is the number of fibre count (frequency) of fibres of species i with length L_i. A midpoint of fibre length ranges, each at 0.1 mm interval, was taken as an average value of fibre length, L_i in the calculation. L_n reflects the level of fibre damage during processing, whereas, L_w corresponds to the volume fraction of fibres that is useful to represent the composite mechanical properties, which are mainly related to volume fractions [116].

The effect of fibre weight fractions on L_n and L_w are presented in Figure 4.3. Generally, L_n and L_w decrease with an increase in fibre loading (Table 4.2). The L_n value reduces from 0.33 mm for PP/G15 to 0.24 mm and 0.16 mm for PP/G30 and PP/G45, respectively. Furthermore, L_w value also reduces from 0.46 mm for PP/G15 to 0.35 mm and 0.24 mm for PP/G30 and PP/G45, respectively. These results are in agreement with earlier report which suggested more fibre degradation occurred with increase in fibre loading [112].

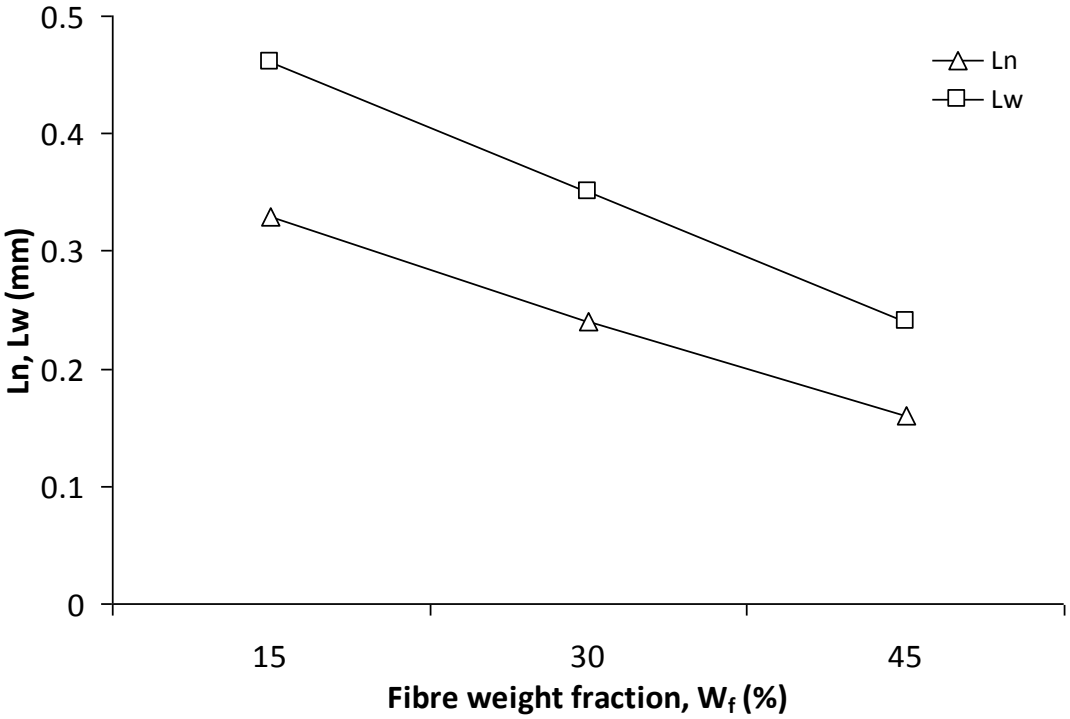

Figure 4.3: Average residual fibre length vs. fibre weight fraction of injection-moulded glass fibre composites

4.2.2 Effect of extrusion screw speed

From Table 4.2, it is evident that at the same glass fibre loading, increasing the screw speed from 50 rpm to 150 rpm caused an increase in the extent of fibre degradation. Plot of FLD in Figures 4.4 and 4.5 shows that more fibre population with shorter length has occurred in composite compounded with higher screw speed when

compared with lower screw speed. A similar trend has been reported by Lunt and Shortall [117].

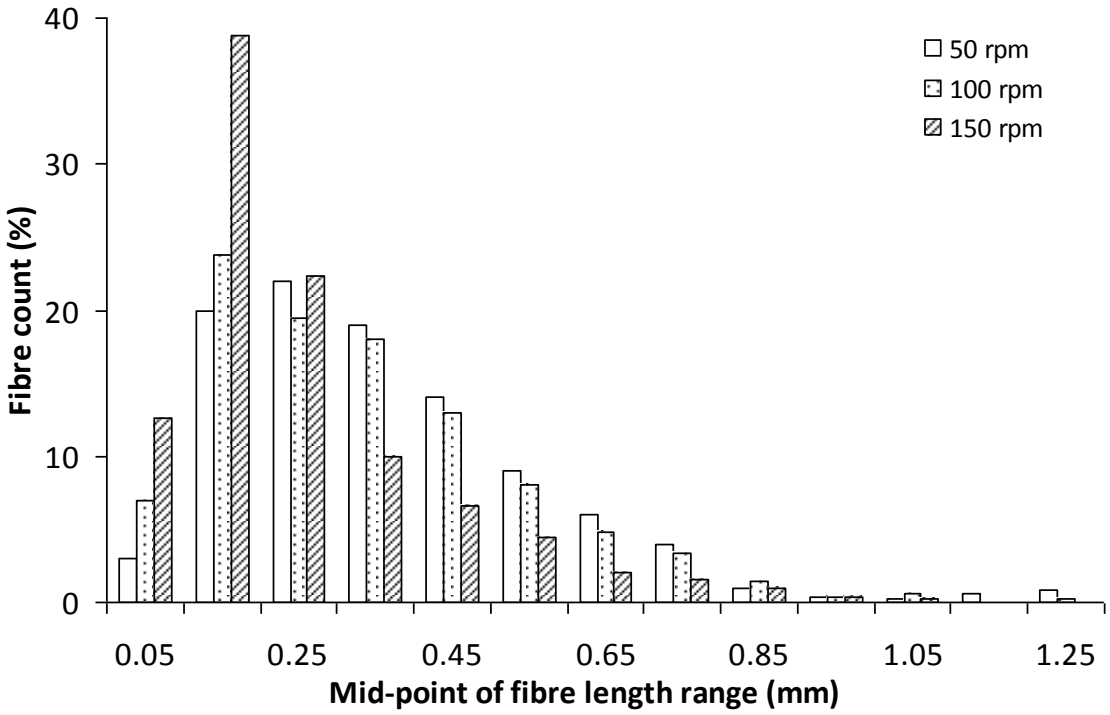

Figure 4.4: Fibre length distribution of PP/G15 composites compounded at different screw speeds

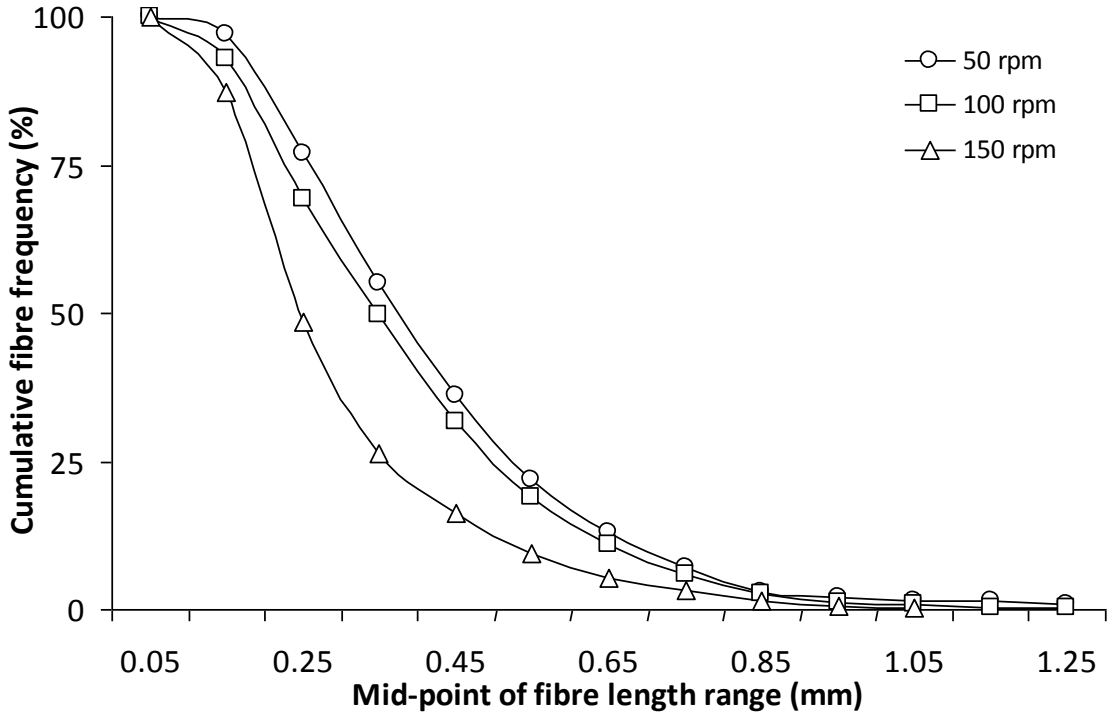

Figure 4.5: Cumulative fibre frequency of PP/G15 composites compounded at different screw speeds

Furthermore, it has been shown in Figure 4.6 that L_n value reduced from 0.37 mm for composite compounded with 50 rpm screw speed to 0.33 mm and 0.25 mm for composites compounded with 100 rpm and 150 rpm screw speeds, respectively. The same trend was obtained for L_w. It has been suggested that increasing the extruder screw speed would be expected to increase the level of dispersive and distributive mixing, leading to an over-all increase in the fibre breakage [117].

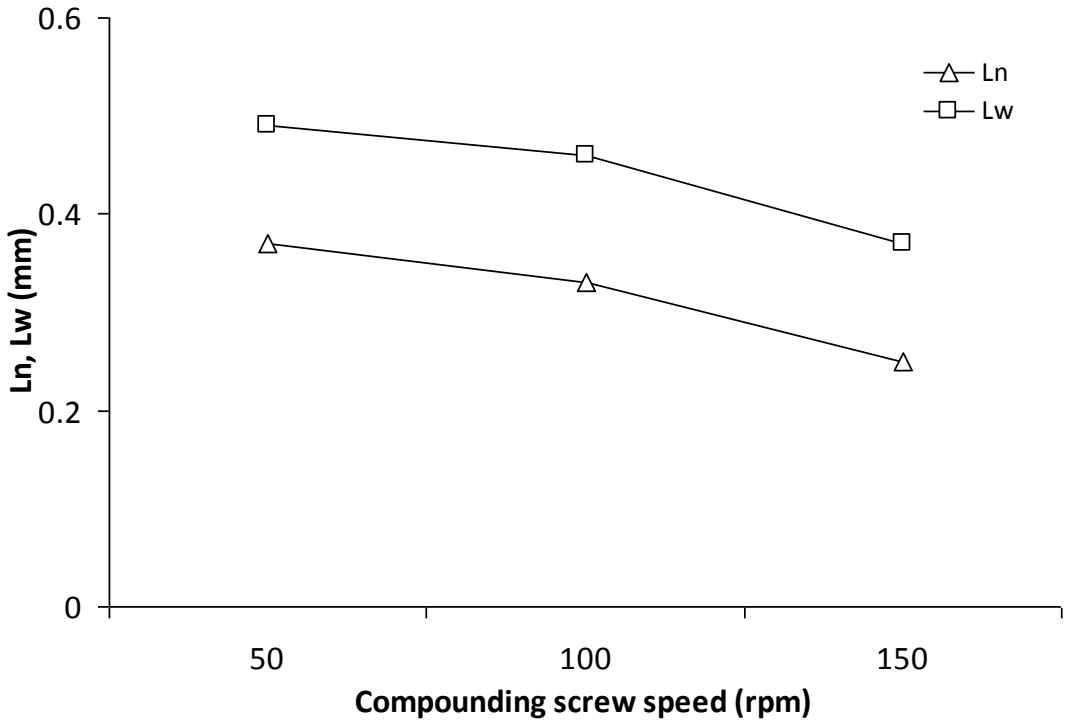

Figure 4.6: Average residual fibre length and fibre weight fraction of PP/G15 composites compounded at different screw speeds

4.3 Fourier-transform infra-red properties (FTIR)

FTIR spectroscopic analysis was used to confirm the presence of functional groups in the composite systems. Results from the FTIR analyses of composite specimens are shown in Figures 4.7 and 4.8. The FTIR spectra of the PP matrix, MAPP, untreated and treated nanoclays, in the region of 650 cm^{-1} to 4000 cm^{-1}, are given in Figure 4.7. The bands at 1375 cm^{-1} and 1451 cm^{-1} are characteristic of PP. In the case of MAPP, absorption bands at 1700 cm^{-1} and 1750 cm^{-1} were observed, which are assigned

to the absorption of the carbonyl groups (C=O) of maleic anhydride [118]. Therefore, it is confirmed that maleic anhydride was grafted onto the PP backbone.

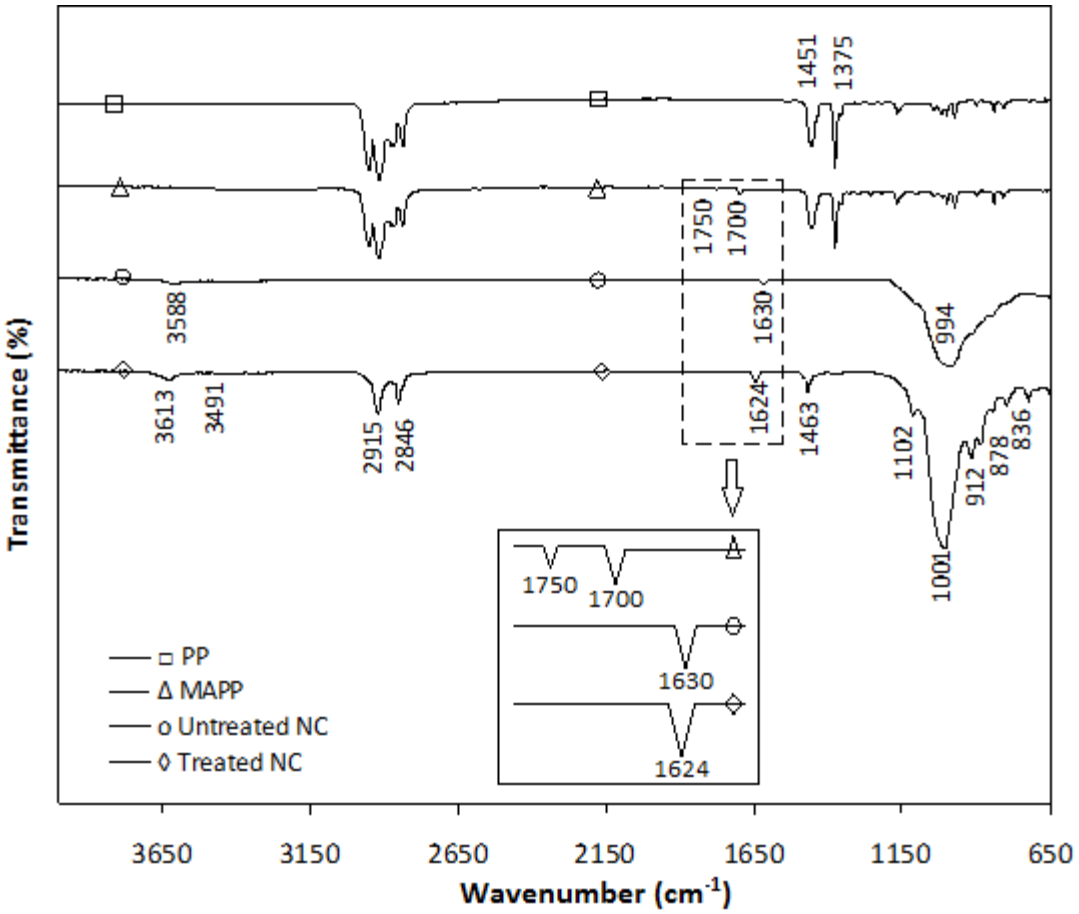

Figure 4.7: FTIR spectra of PP matrix, MAPP, untreated and treated nanoclays

Meanwhile, for the untreated and treated nanoclays (Figure 4.7), the bands at 3588 cm^{-1} and 3613 cm^{-1} are attributed to the hydroxyl stretching of Al-OH and Si-OH [119]. The broad band appearing between 700 cm^{-1} to 1100 cm^{-1}, is mainly due to the contribution of several structural –OH groups in the clay [120]. Due to the presence of added functional groups (dimethyl dialkyl amine), a difference is observed between the FTIR spectrum of untreated and treated clays. For the treated clay, the bands at 3491 cm^{-1} as well as 2846 cm^{-1} and 2915 cm^{-1} are assigned to the hydroxyl hydration stretching for interlayer water [120] and amino (N-R) groups, respectively. Moreover, the absorption in the regions of 1630 cm^{-1} and 1624 cm^{-1}, respectively for the untreated

and treated clay are assigned to the –OH bending mode in adsorbed water. The band at 1102 cm^{-1} is due to Si–O stretching (out-of-plane) for treated montmorillonite. Meanwhile, the band at 1001 cm^{-1} is attributed to the Si – O stretching (in-plane) vibration of layered clays. The bands at 912 cm^{-1}, 878 cm^{-1} and 836 cm^{-1} are attributed [120] to the AlAlOH, AlFeOH and AlMgOH bending vibrations, respectively.

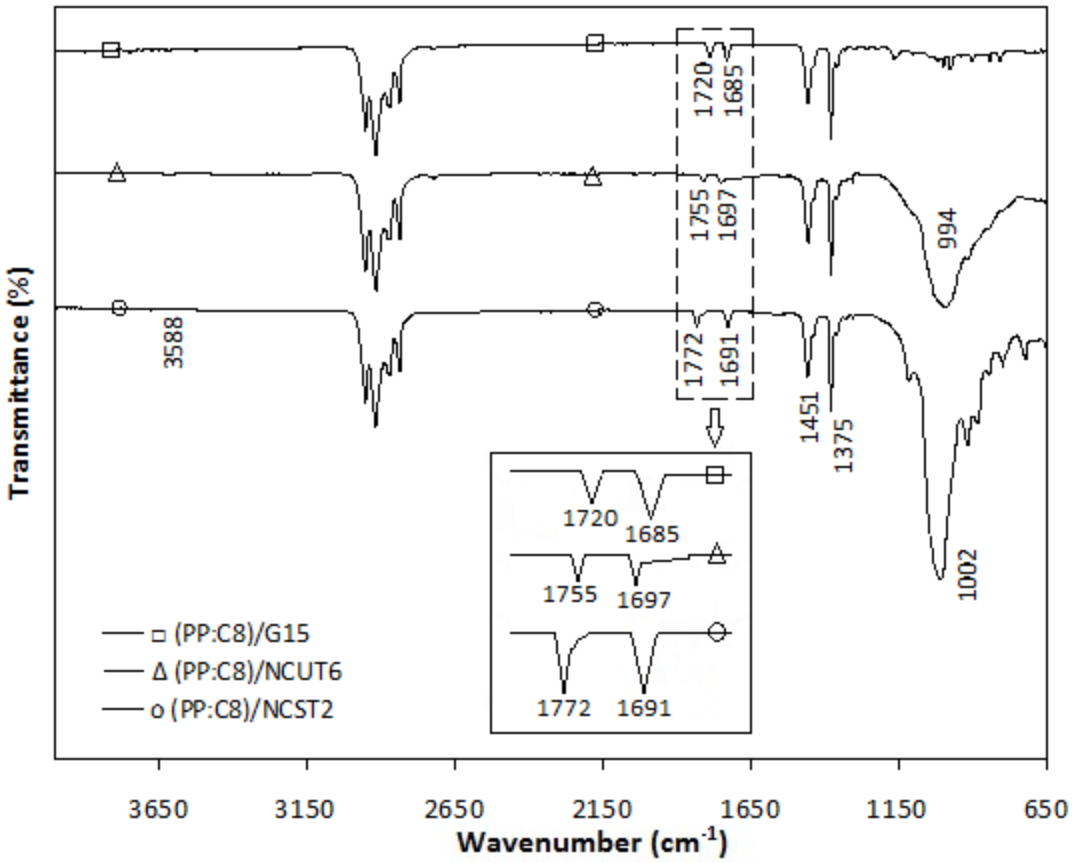

Figure 4.8: FTIR spectra of glass fibre composite, untreated and treated clay nanocomposites

Figure 4.8 shows the FTIR spectra for glass fibre composite, untreated and treated clay nanocomposites. All composites have been compatibilised with 8 *wt%* MAPP. The characteristic absorption bands of carbonyl groups of MA can be seen at 1720 cm^{-1} and 1685 cm^{-1} , 1755 cm^{-1} and 1697 cm^{-1} and 1772 cm^{-1} and 1691 cm^{-1} for the compatibilised glass fibre composite, clay nanocomposite and hybrid composite, respectively. Again, as mentioned before, a broad band in the region between 700 cm^{-1}

to 1100 cm^{-1}, observed for clay nanocomposites, are related to the characteristic absorption of nanoclay.

4.4 X-ray diffraction properties

Table 4.3: XRD data of nanoclay and composites

Sample	*2θ* (°)	Interlayer d-spacing (nm)	Peak intensity (counts s^{-1})
Nanoclay, untreated (NCUT)	8.86	1.00	127
Nanoclay, surface treated (NCST)	*a) 3.85	2.51	3178
	*b) 7.09	1.24	353
PP/NCUT3	6.97	1.27	251
PP/NCUT6	7.04	1.25	320
PP/NCUT9	7.04	1.25	362
(PP92:C8)/$NCST2_{100}$	a) 2.56	3.45	1486
	b) 6.59	1.34	491
(PP92:C8)/$NCST2_{300}$	a) 2.41	3.66	729
	b) 6.66	1.33	349
(PP92:C8)/$NCST2_{500}$	a) 2.32	3.81	1739
	b) 6.75	1.31	884
(PP92:C8)/$NCST2_{800}$	a) 2.33	3.79	1051
	b) 6.68	1.32	494
(PP98:C2)/NCUT6	6.85	1.29	467
(PP95:C5)/NCUT6	6.60	1.34	370
(PP92:C8)/NCUT6	6.61	1.34	357
(PP85)/G15/NCUT3	7.08	1.25	99
(PP85)/G15/NCUT6	7.09	1.25	121
(PP85)/G15/NCUT9	7.46	1.19	133

Note:
* a) Characteristic diffraction peaks for NCST
b) Non-characteristic diffraction peak for NCST
For specimen coding, for instance (PP92:C8)/$NCST2_{100}$, the subscript refers to the extrusion screw speed.

It has been shown by several researchers [121, 122] that X-ray diffraction method can be used to observe how layered nanoparticles are distributed in a polymer and it has been employed to characterise their degree of dispersion. Bragg's equation is typically employed to measure the interlayer distance, using the diffraction peak and its

position in the XRD patterns [123]. Bragg's equation is given as $n\lambda=2d\sin\theta$, where n, λ, d and θ are: integer, wavelength (1.54 Å), interlayer d-spacing and the diffraction angle, respectively. Results from the XRD analyses of composite specimens together with the supporting images from SEM and TEM are shown in Figures 4.9 – 4.17 and the data extracted from XRD patterns are tabulated in Table 4.3.

4.4.1 Clay nanocomposites

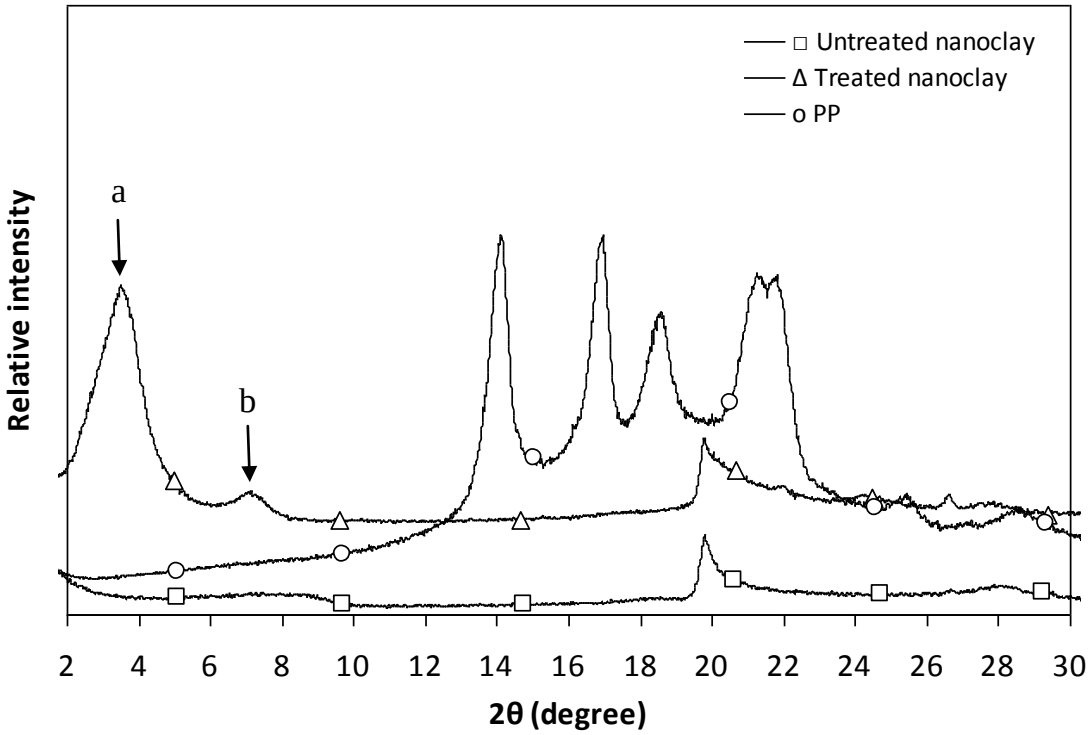

Figure 4.9: The XRD patterns of PP matrix, untreated and treated nanoclays

In Figure 4.9, the XRD data of PP matrix, untreated (NCUT) and treated (NCST) nanoclays are displayed as the relative intensity of the reflections versus the scattering angle, 2θ. The characteristic diffraction peak of untreated nanoclay with peak intensity of 127 counts s^{-1} is located at around 8.86°, corresponding to a basal interlayer d-spacing of 1.00 nm, using the Bragg's equation. Meanwhile, the characteristic and the non-characteristic diffraction peaks for treated nanoclay are located at: (a) 3.85° and (b)

7.09°, equivalent to basal interlayer d-spacing of 2.51 nm and 1.24 nm, respectively. The SEM images for untreated (NCUT) and treated (NCST) clay powders are shown in Figure 4.10. From this figure, it can be seen that at the same magnification, the NCST powder size (Figure 4.10 (b)) is finer than the NCUT powder (Figure 4.10 (a)).

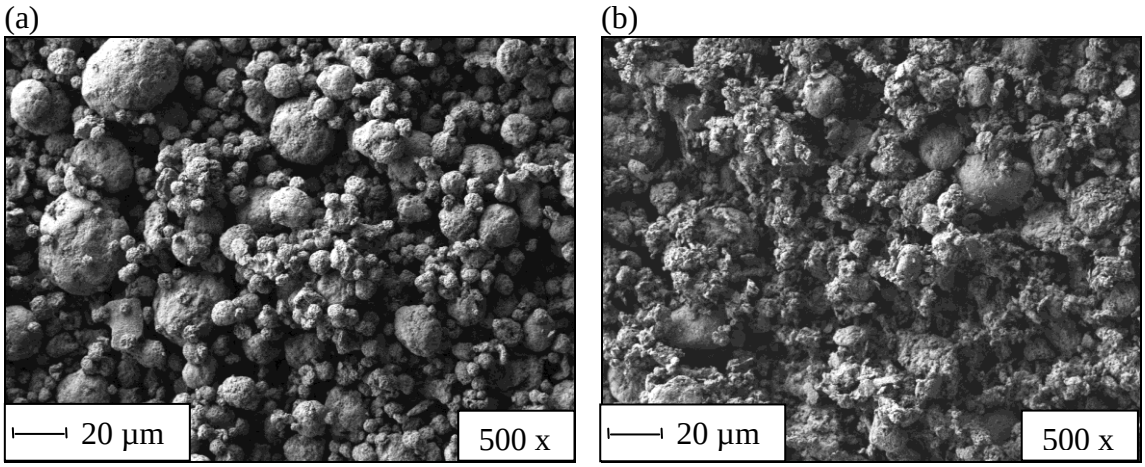

Figure 4.10: The SEM images of: (a) untreated and (b) treated nanoclays

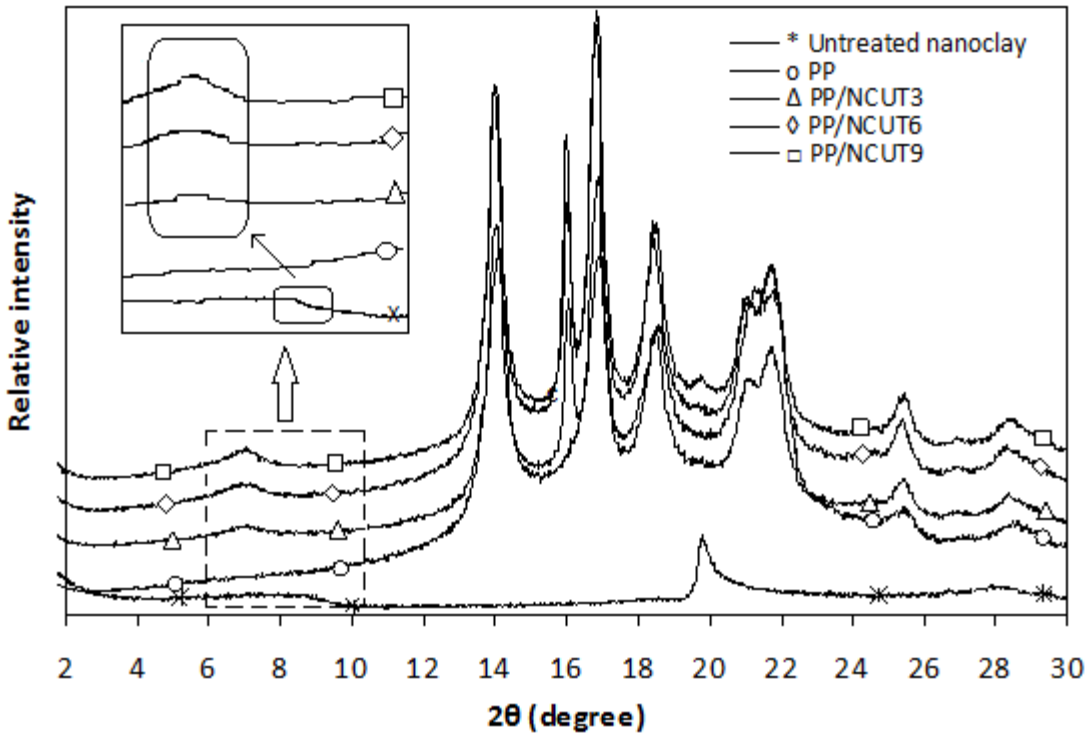

Figure 4.11: The XRD patterns of PP, untreated nanoclay and nanocomposites

Figure 4.11 displays the XRD patterns of PP, untreated nanoclay and nanocomposites made by direct melt intercalation with varying nanoclay contents. As shown in this figure, the characteristic peak of clay in the composites system is shifted to lower diffraction angle when compared with the NCUT clay powder (8.86°), which indicate that the basal interlayer d-spacing of clay has been increased. It is suggested that this increment is due to the diffusion of the polymer chains between the nanoclay layers, resulting in the expansion of the clay interlayer distance. The interlayer distances of nanoclay increased from the original 1.00 nm for NCUT powder to 1.27 nm for PP/NCUT3 and 1.25 nm for both PP/NCUT6 and PP/NCUT9 nanocomposites (Table 4.3).

Although intercalation had occurred, it is evident that some long-range stacking order still remained, as explained by Timmerman *et al.* [124]. Even though clay layers in the composites were expanded to a larger extent when compared to neat clay, its diffraction characteristic (peak) still existed, which means that some clay layers still retained in their original crystal structure and existed as primary particles [125]. The XRD data show that the characteristic diffraction peak of the nanocomposites was almost similar for all systems (3, 6 and 9 phr). Further incorporation of clay into the system, only affected the width and intensity of the diffraction peak, with the diffraction angles remaining almost the same. The peak intensity increased by 28% and 44% for 6 phr and 9 phr nanocomposites, respectively, relative to 3 phr nanocomposite. This observation suggests that as the concentration of the clay increased (from 3 phr to 9 phr), more ordered structures were obtained, resulting in a relatively higher fraction of clay agglomeration [11]. As indicated above, the amount of matrix in the composites was constant for all compositions prepared (PP/NCUT3–9). As the clay content increased, the amount of available matrix for clay intercalation reduced. As a result, a decrease in the basal interlayer d-spacing was observed (Table 4.3).

To evaluate the tendency of clay particles to agglomerate, SEM images from the fractured surfaces from tensile specimen of clay nanocomposites were taken, as shown in Figure 4.12. Figures 4.12 (a), (b) and (c) illustrate the microstructure of the 3 phr, 6 phr and 9 phr untreated clay nanocomposites, respectively, where the clay is shown as the bright spots in the images (highlighted in Figure 4.12). At higher clay content (9 phr), a relatively larger clay agglomeration is observed, when compared with the 3 phr and 6 phr clay nanocomposites.

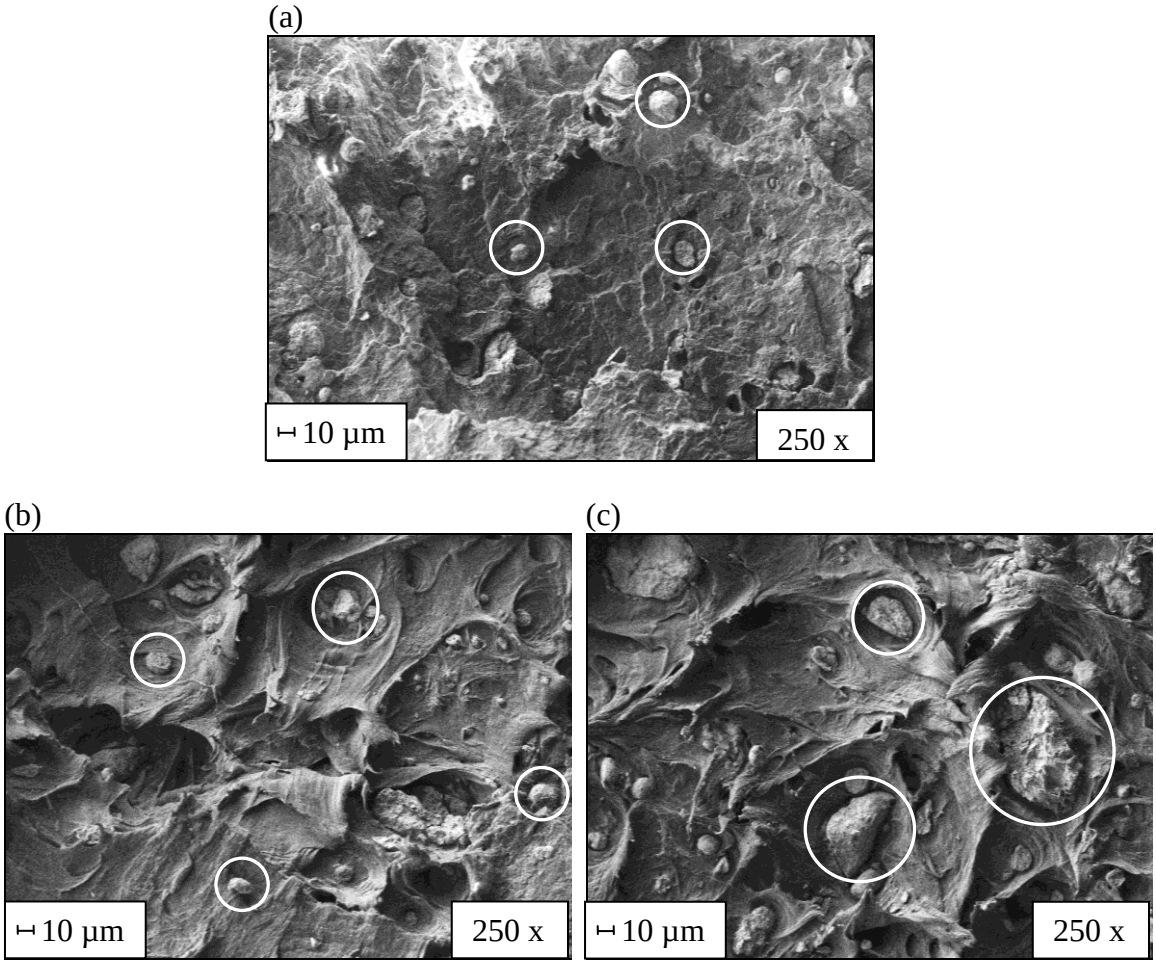

Figure 4.12: SEM images of tensile fracture surfaces of: (a) PP/NCUT3, (b) PP/NCUT6 and (c) PP/NCUT9

Figure 4.13 shows the effect of processing screw speed, varying from 100 rpm to 800 rpm for the PP/NCST2 nanocomposites. XRD pattern shows that the characteristic (3.85°) and non-characteristic (7.09°) diffraction peak positions of the

nanocomposites shifted towards the lower diffraction angle, as the screw speed increased, indicating a better dispersion of clay in the system. The interlayer distances of treated nanoclay powder increased from the original 2.51 nm and 1.24 nm for characteristic and non- characteristic peaks, to 3.45 nm and 1.34 nm, 3.66 nm and 1.33 nm, 3.81 nm and 1.31 nm, and 3.79 nm and 1.32 nm, for the nanocomposites processed at 100 rpm, 300 rpm, 500 rpm and 800 rpm compounding screw speeds, respectively (Table 4.3).

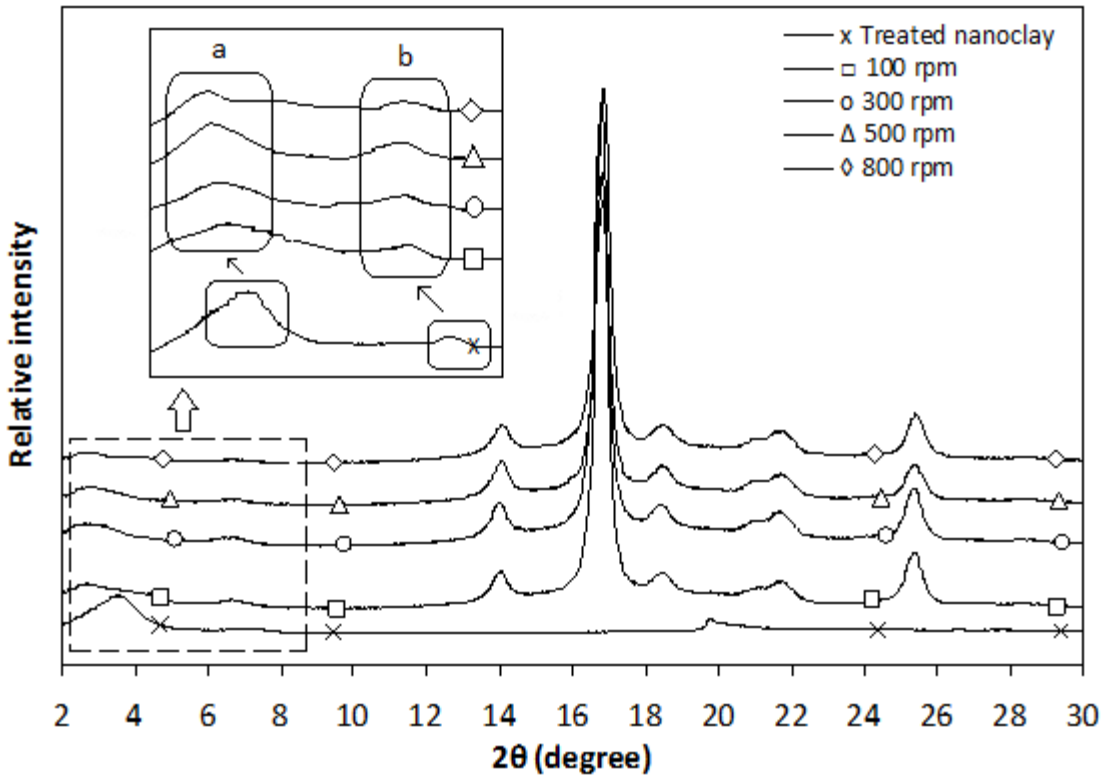

Figure 4.13: The XRD patterns of treated nanoclay and PP/NCST2 nanocomposites at different processing screw speeds

As can be seen from Table 4.3, the intensity of the characteristic diffraction peak for NCST powder is 3,178 counts s^{-1}. This value reduced by about 67% to 1,051 counts s^{-1} when the highest screw speed, 800 rpm was used to compound the nanocomposites material. It is suggested that a high shear stress is created when a higher screw speed was used during melt mixing. It is possible that the shear stress forced the polymer to

infuse and intercalate between the intergallery spacing of the layered silicates and hence gradually separated the clay layers. Lertwimolnun and Vergnes [122] in their study, also found that the degree of exfoliation was increased with increasing rotor speed.

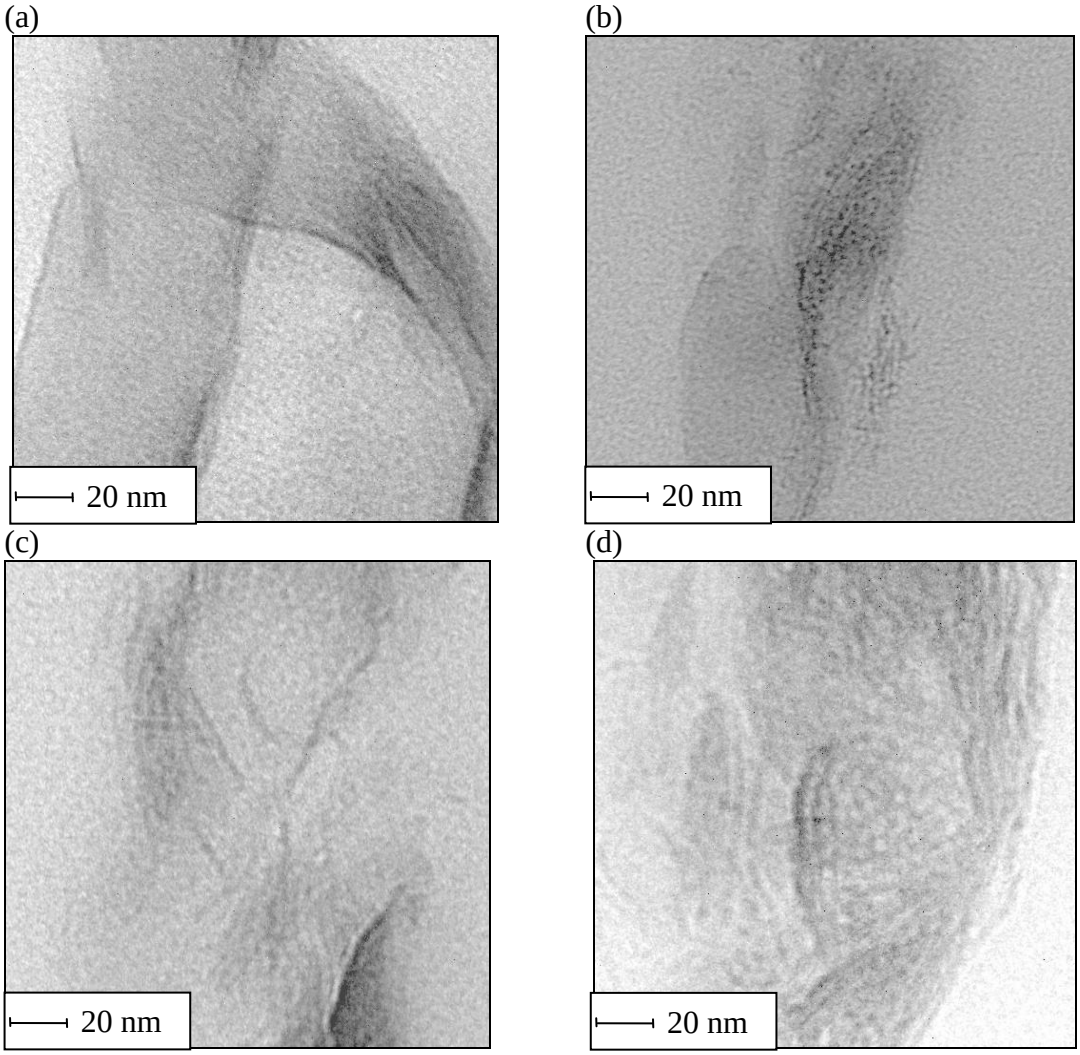

Figure 4.14: TEM images of PP/NCST2 nanocomposites at different processing screw speeds: (a) 100 rpm (b) 300 rpm (c) 500 rpm and (d) 800 rpm

This behaviour can be confirmed by analysing the transmission electron micrographs. Transmission electron microscope (TEM) images were taken on nanocomposite samples processed at different screw speeds (Figure 4.14) in order to compare with the XRD pattern (Figure 4.13). In the analysis of the nanocomposite compounded with lowest screw speed (100 rpm), the clay platelets are closely packed, which resembles intercalated structure (Figure 4.14 (a)). Meanwhile, nanocomposite

compounded with the highest screw speed (800 rpm) displays a different behaviour. The TEM image shows that the nanoclay dispersed well and the clay platelets were regularly intercalated and exfoliated (Figure 4.14 (d)). This confirms that the use of higher screw speed in processing the nanocomposite, led to the formation of intercalated and exfoliated nanocomposites while only intercalated structure was produced with lower processing screw speed.

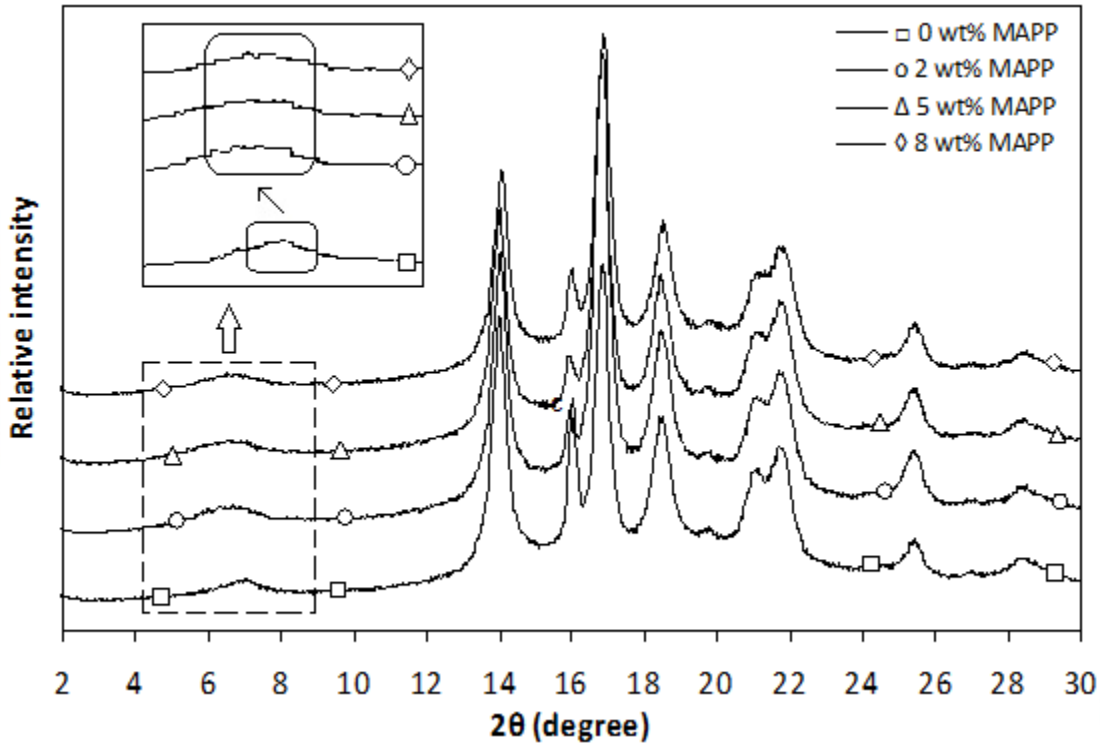

Figure 4.15: The XRD patterns of untreated clay nanocomposites with variation MAPP loadings

Figure 4.15 shows the series of XRD spectra of untreated clay nanocomposites, in which the concentration of MAPP varied from 0 *wt%* to 8 *wt%*. The nanoclay concentration in the composite was kept constant (6 phr) and the interlayer d-spacing of untreated clay powder was 1.00 nm (Table 4.3). For the uncompatibilised system (PP/NCUT6), the XRD pattern exhibited a significant increase in interlayer d-spacing to 1.25 nm after compounding (Figure 4.11 and Table 4.3). This indicates that with higher

processing screw speed, the PP was able to intercalate into the interlayer, even with poor compatibility between matrix and the nanoparticles.

Furthermore, for compatibilised systems, XRD peaks continually shifted to lower angles, indicating an increase in interlayer d-spacing by the diffusion of polymer chains (Figure 4.15). The interlayer d-spacing increased from 1.29 nm for 2 *wt%* of MAPP to 1.34 nm for 5 *wt%* of MAPP (Table 4.3). Further addition of 8 *wt%* of MAPP resulted in no significant change in this value. Nevertheless, it should be noted that even though a similar interlayer d-spacing values were obtained for the 5 *wt%* and 8 *wt%* MAPP loadings, there was a decrement in the peak intensity at higher MAPP content. The peak intensity for nanocomposite with 5 *wt%* of MAPP was recorded at 370 counts s^{-1} and the intensity reduced to 357 $\text{counts}\,\text{s}^{-1}$ with 8 *wt%* of MAPP. Lertwimolnun and Vergnes [122] suggested that the decrease in intensity and the broadening of peaks indicate that the stacks of layered silicates become more disordered, while maintaining a periodic distance. In addition, the decrease in intensity could be the result of a partial exfoliation of layered silicates.

4.4.2 Glass fibre/nanoclay hybrid composites

Figure 4.16 illustrates the XRD diffractograms for PP/G15 hybrid composites with 3–9 phr untreated clay loading. The interlayer d-spacing of nanoclay reduced from 1.25 nm for PP/G15/NCUT3 and PP/G15/NCUT6, to 1.19 nm for PP/G15/NC9 composite (Table 4.3). A reduction in this value with the addition of 9 phr of nanoclay loading indicates the presence of agglomerated nanoclay layers in the hybrid composite with higher clay content. Furthermore, as the clay loading increased, a noticeable increment in the peak intensity of the hybrid composites was also observed. In addition, the peak intensity of PP/G15/NCUT3 was slightly lower than that of PP/G15/NCUT6, even though these composites shared the same d-spacing value. It can be suggested that

the nanoclay in both composites partially kept the original crystal structure and existed as primary particle; however, due to the higher amount of PP in the PP/G15/NCUT3 composite, the clay particles in this system could have been partially exfoliated from the stacks of silicate layers. SEM images of the fracture surfaces from the PP/GF/NC composites are shown in Figure 4.17. A better dispersion of clay in the hybrid system was expected at lower clay loading.

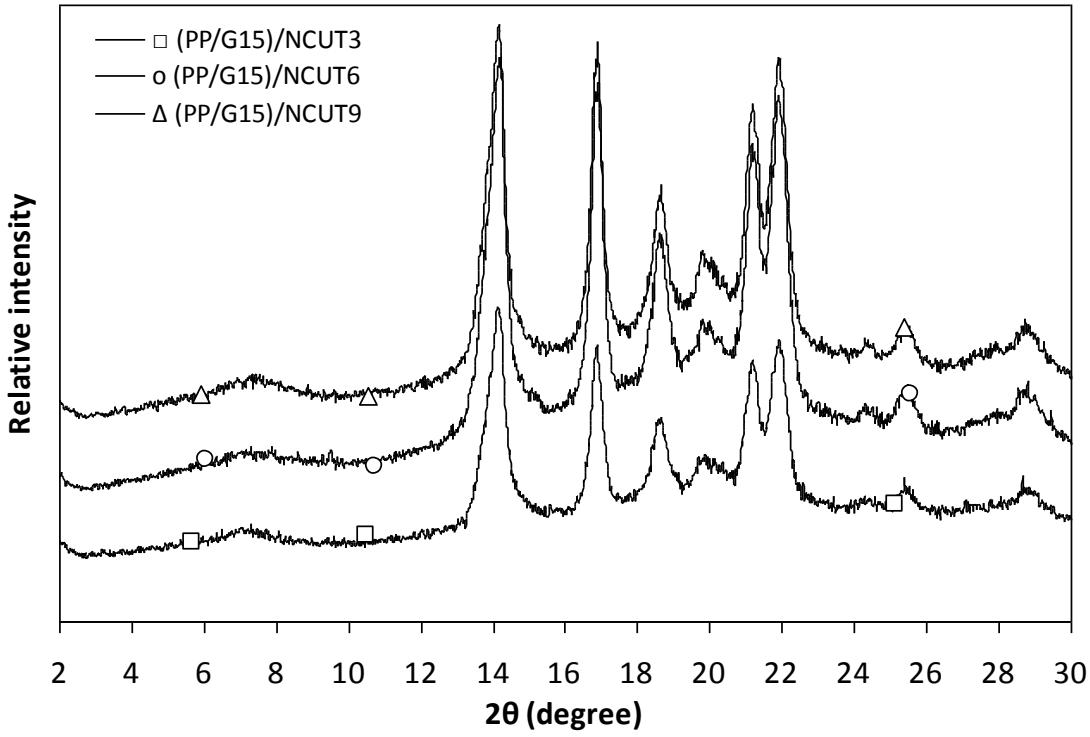

Figure 4.16: The XRD patterns of glass fibre/nanoclay hybrid composites

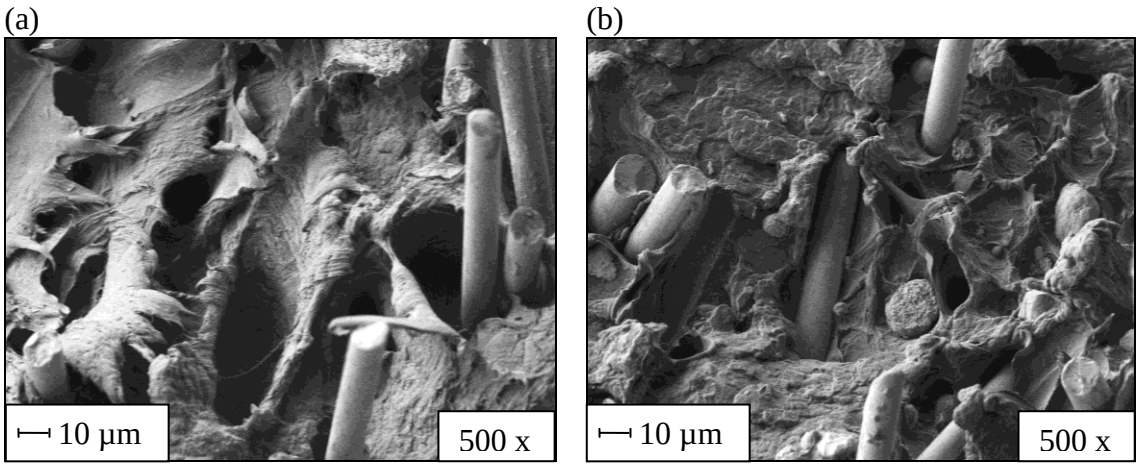

Figure 4.17: SEM images of tensile fracture surfaces of: (a) PP/G15/NCUT3 and (b) PP/G15/NCUT9 hybrid composites

4.5 Thermal properties

4.5.1 Thermogravimetric analysis (TGA)

The thermal stability of nanocomposites was studied by the thermogravimetric analysis (TGA). When heating under inert N_2 gas flow, a non-oxidative degradation occurs, while the use of air or oxygen allows oxidative degradation of the samples [126]. Figures 4.18 to 4.27 show the TGA scans in the form of weight change and derivative weight change (DTG) versus temperature, together with the supporting images from TEM characterisation for PP, PP/GF composites, PP/NC nanocomposites and PP/GF/NC hybrid composites. The TGA scan for PP matrix, untreated and treated clays can been seen in Appendix 4.1. Table 4.4 presents the quantitative values of the onset temperature, derivative peak temperature and the temperatures at 5%, 10% and 50% of weight loss, which are referred to as: T_{onset}, DT_P, $T_{5\%}$, $T_{10\%}$ and $T_{50\%,}$ respectively.

Table 4.4: TGA data of PP, PP/GF, PP/NC and PP/GF/NC composites

Sample	Range of decomposition (°C)	T_{onset} (°C)	$T_{5\%}$ (°C)	$T_{10\%}$ (°C)	$T_{50\%}$ (°C)	DT_p (°C)
PP	228.3 - 465.7	356.9	306.7	327.0	397.6	430.5
PP100/NCUT3	223.2 - 459.1	367.1	303.1	328.4	401.3	428.2
PP100/NCUT6	215.2 - 468.6	360.4	309.4	334.8	406.8	429.0
PP100/NCUT9	217.6 - 468.6	360.4	309.4	334.8	407.6	428.2
(PP100:C0)/NCST2$_{800}$	335.2 - 457.3	426.8	413.1	422.9	435.6	440.8
(PP92:C8)/NCST2$_{100}$	360.7 - 459.0	421.3	412.5	417.9	428.8	431.9
(PP92:C8)/NCST2$_{300}$	337.2 - 453.7	420.8	411.1	417.0	429.0	432.0
(PP92:C8)/NCST2$_{500}$	339.2 - 454.8	426.1	413.8	422.0	434.3	436.8
(PP92:C8)/NCST2$_{800}$	340.0 - 457.5	427.1	415.0	422.4	435.1	438.8
(PP95:C5)/NCUT3	251.5 - 446.8	380.0	337.5	359.2	410.3	423.5
(PP98:C2)/NCUT6	240.0 - 441.4	374.9	324.3	347.2	402.9	416.0
(PP95:C5)/NCUT6	239.6 - 445.0	374.4	327.2	351.3	408.6	422.6
(PP92:C8)/NCUT6	241.3 - 444.3	375.5	322.5	345.5	405.9	419.5
(PP95:C5)/NCUT9	249.3 - 443.0	387.2	334.5	358.5	413.5	428.2
(PP98:C2)/NCST2	264.2 – 459.7	422.3	384.5	403.1	439.5	449.6
(PP95:C5)/NCST2	268.3 – 462.0	426.4	395.7	415.3	442.6	449.6
(PP92:C8)/NCST2	285.5 – 463.9	428.6	400.0	417.9	443.7	449.9
PP85/G15	250.1 - 525.4	423.3	368.0	396.4	471.7	480.7
PP70/G30	250.1 - 530.7	435.4	385.9	415.0	488.9	491.1
PP55/G45	246.4 - 538.1	430.3	392.6	423.2	507.5	494.8
(PP77:C8)/G15$_{50}$	247.7 - 468.1	380.8	343.9	365.6	420.0	426.9
(PP77:C8)/G15$_{100}$	254.3 - 465.0	387.7	347.2	368.2	421.3	429.9
(PP77:C8)/G15$_{150}$	255.4 - 469.8	392.2	353.6	374.7	427.7	433.9

Table 4.4, continued

Sample	Range of decomposition (°C)	T_{onset} (°C)	$T_{5\%}$ (°C)	$T_{10\%}$ (°C)	$T_{50\%}$ (°C)	DT_p (°C)
(PP83:C2)/G15	249.1 - 472.9	385.0	345.8	368.8	422.9	428.6
(PP80:C5)/G15	202.3 - 450.7	373.4	331.9	351.5	408.1	420.4
(PP77:C8)/G15	237.9 - 447.2	357.5	320.1	341.8	339.2	409.2
(PP65:C5)/G30	243.6 - 446.4	367.8	343.4	361.2	413.9	423.9
(PP50:C5)/G45	242.3 - 436.0	377.5	339.2	362.4	418.2	417.4
(PP85)/G15/NCUT3	299.5 - 491.8	431.5	405.9	423.2	457.9	460.3
(PP85)/G15/NCUT6	310.5 - 492.6	433.2	420.1	430.3	458.7	459.5
(PP85)/G15/NCUT9	346.0 - 494.2	436.3	424.0	434.3	460.3	459.5
(PP70)/G30/NCUT3	303.5 - 492.6	432.3	413.0	429.5	463.4	458.7
(PP70)/G30/NCUT6	336.5 - 493.4	439.2	423.2	435.8	465.0	462.6
(PP70)/G30/NCUT9	310.5 - 495.0	441.3	428.0	439.0	466.6	462.6
(PP55)/G45/NCUT3	300.3 - 495.0	430.3	419.3	433.5	476.8	461.1
(PP55)/G45/NCUT6	302.7 - 495.0	435.5	427.7	439.0	478.4	461.9
(PP55)/G45/NCUT9	290.1 - 495.0	437.2	423.2	438.2	476.0	463.4
(PP83:C2)/G15/NCUT6	291.3 - 469.2	427.9	401.1	417.4	447.5	452.2
(PP80:C5)/G15/NCUT6	205.5 - 467.7	403.7	354.7	381.0	435.2	444.5
(PP77:C8)/G15/NCUT6	249.6 - 463.8	397.8	352.4	378.7	432.9	445.2
(PP82:C2)/G15/NCST2	238.7 - 471.5	424.5	377.2	401.1	446.0	453.0
(PP80:C5)/G15/NCST2	262.9 - 468.4	427.6	393.0	417.8	446.0	450.5
(PP77:C8)/G15/NCST2	247.6 - 471.0	427.0	384.0	408.2	447.7	454.0

4.5.1.1 Clay nanocomposites

The TGA and DTG curves in Figure 4.18 demonstrate that the incorporation of clay in PP matrix gave a significant improvement in the thermal stability of the material. The neat matrix completely decomposed within a temperature range of 228.3°C and 465.7°C, with maximum (% min^{-1}) rate at 430.5°C. Incorporation of untreated clay into the PP matrix widened the range of decomposition temperature, as the initial and the final decomposition temperatures shifted to lower and higher temperatures, respectively (Table 4.4).

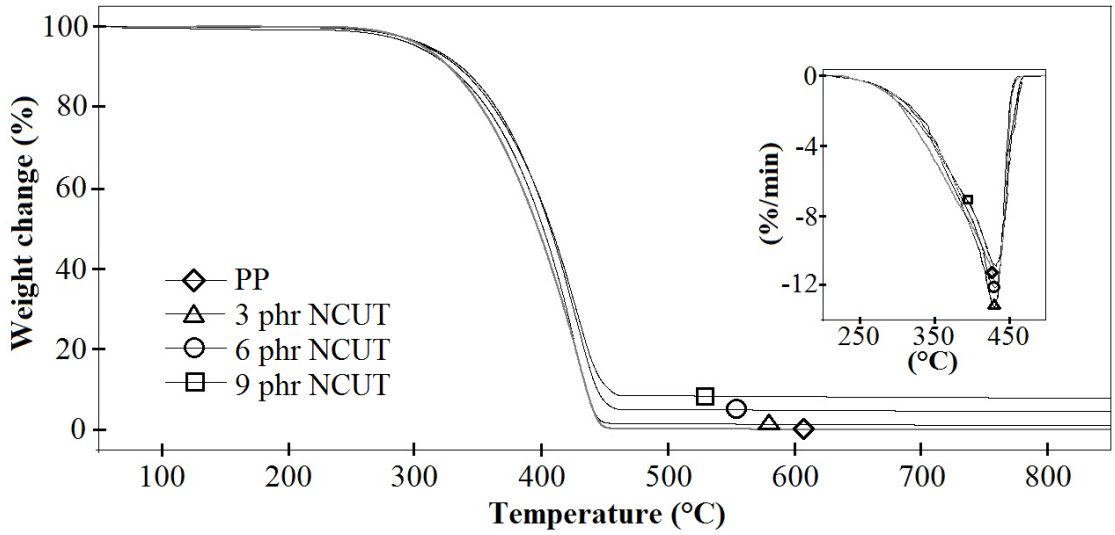

Figure 4.18: TGA and DTG thermograms of PP and PP/NCUT nanocomposites

The intersection point between the initial slope and that after the actual decomposition, basically provides primary onset of decomposition temperature, T_{onset}. The T_{onset} of PP matrix was recorded at 356.9°C. Incorporation of 3, 6 and 9 phr of untreated clay into the composites increased the T_{onset} values to 367.1°C, 360.4°C and 360.4°C, respectively. This behaviour could be explained by the diffusion effect experienced when clay is present, which limits the emission of the gaseous degradation products, resulting in an increased thermal stability of the material [86, 127 – 129]. The initial thermal stability was characterised by the temperatures at 5% and 10% weight

change ($T_{5\%}$ and $T_{10\%}$). It can be seen that these initial thermal decomposition temperatures are enhanced by the addition of clay into the PP matrix (Table 4.4).

The same trend has been observed for $T_{50\%}$. In the present study, $T_{50\%}$ is considered as an indicator for structural destabilization of the system [130 – 132]. In Table 4.4, it is clearly seen that the neat PP is stable up to 397.6°C, whereas with the incorporation of 9 phr of clay into the PP matrix, the thermal stability of the material is increased by 10.0°C, to 407.6°C. By contrast, DT_P values remained essentially unchanged was clay is added to the PP matrix.

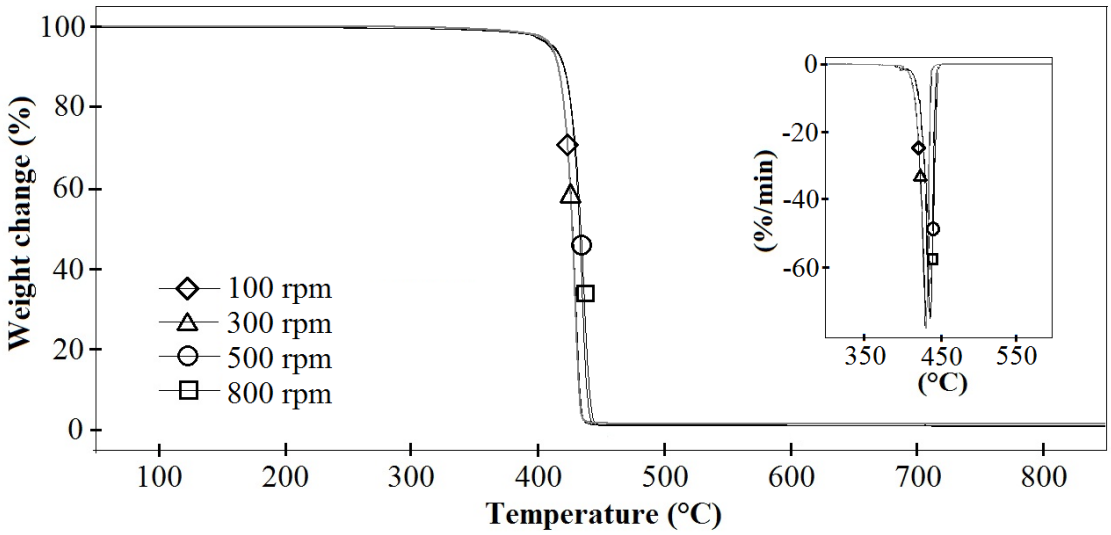

Figure 4.19: TGA and DTG thermograms of PP/NCST2 nanocomposites compounded at different screw speeds

Figure 4.19 shows the TGA and DTG curves of the PP/NCST2 nanocomposites compounded at different screw speeds. The TEM images, as shown in previous section (Figure 4.14), illustrate that the dispersion of silicates layers improved as the screw speed increased. The intimate contact between the polymer molecules and the lamella of silicates in nanocomposites compounded with 800 rpm screw speed was more extensive than that of other nanocomposites compounded with lower screw speed. Most of the quantitative values measured from this characterization such as: T_{onset}, DT_P, $T_{5\%}$, $T_{10\%}$ and $T_{50\%}$, showed improvements as the screw speed increased.

The T_{onset} value shifted to a higher temperature from 421.3°C to 427.1°C, as the processing screw speed increased from 100 rpm to 800 rpm, respectively. The same behaviour was observed for the initial degradation temperatures. The $T_{5\%}$ and $T_{10\%}$ values for nanocomposite processed with 100 rpm compounding screw speed are 412.5°C and 417.9°C, respectively and these values increased to 415.0°C and 422.4°C, respectively, as the highest compounding screw speed, 800 rpm was used. A remarkable effect was observed for the well dispersed nanocomposites at high processing screw speed which is likely to be due to an ablative reassembling of the silicate layers which could have occured on the surface of the exfoliated nanocomposites, creating a physical protective barrier on the surface of the material [133, 134]. Volatilization might also be delayed by the labyrinth effect of the individual silicate layers dispersed in the nanocomposites.

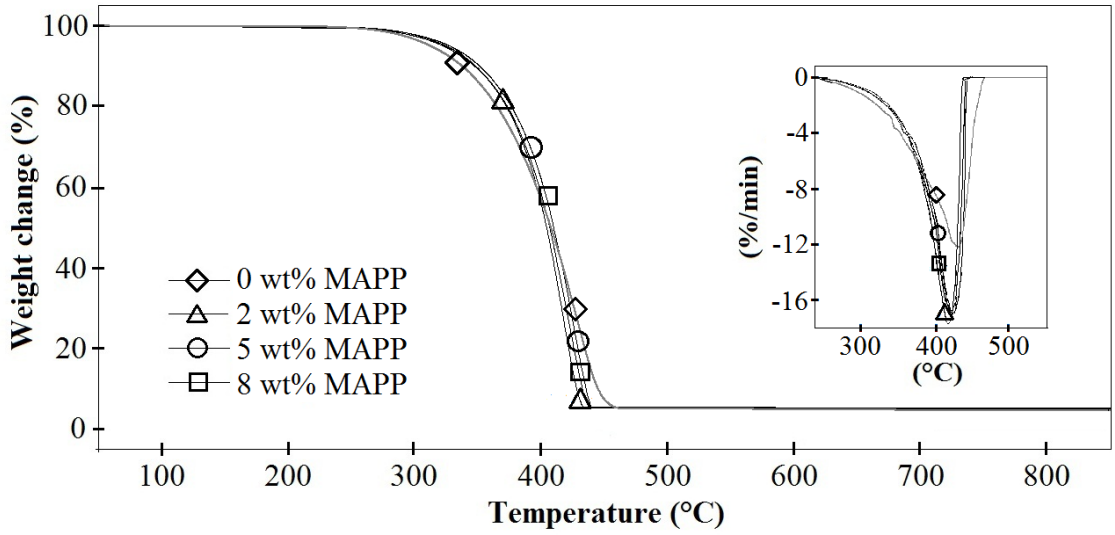

Figure 4.20: TGA and DTG thermograms of PP/NCUT6 nanocomposites with 0 *wt%* to 8 *wt%* of MAPP

Figure 4.20 shows the TGA and DTG curves of the PP/NCUT6 composites, with and without compatibiliser. With the addition of 2 *wt%* – 8 *wt%* of MAPP in the nanocomposites system, an increase of about 14.5°C to 15.1°C in the T_{onset} were observed when compared with the uncompatibilised PP/NCUT6 nanocomposites. This

improvement is probably due to the physico-chemical adsorption of the volatile products on the clay which indicate that the dispersion of clay is improved by the addition of the compatibiliser in the clay nanocomposites [85, 86].

It can also be seen that the initial thermal decomposition temperatures were enhanced by the addition of MAPP into the PP/NCUT6 nanocomposite. At 5% weight change, the $T_{5\%}$ increased from 309.4°C for uncompatibilised PP/NCUT6 nanocomposites to 324.3°C, 327.2°C and 322.5°C for PP/NCUT6 nanocomposites containing 2 *wt%*, 5 *wt%* and 8 *wt%* of MAPP, respectively. The same trend was observed at 10% weight change (Table 4.4). It is possible that at this initial degradation event, incorporation of MAPP improved the compatibility and homogeneity between the matrix and the nanoclay, which resulted in a more thermally stable nanocomposite. It is also believed that the bond breaking event during material degradation, which was affected by the changes in the chemical structure of the system due to the presence of compatibiliser is also important in determining the thermal stability of the composites. By contrast, the $T_{50\%}$ and DT_p values decreased slightly with the incorporation of MAPP into the PP/NC6UT system.

On the other hand, incorporation of MAPP into PP/NCST2 nanocomposites showed a different trend from the previously observed for PP/NCUT6 nanocomposites (Appendix 4.2, Table 4.4). The addition of 2 *wt%* of MAPP into PP/NCST2 nanocomposites resulted in a reduction in the initial thermal stability values by 4.5°C, 28.6°C and 19.8°C for T_{onset}, $T_{5\%}$ and $T_{10\%}$, respectively, relative to the uncompatibilised PP/NCST2 nanocomposite. As the MAPP contents in the system increased to 5 *wt%* and 8 *wt%*, an improvement in these values were observed. Meanwhile, the $T_{50\%}$ and DT_p values increased with increase in the MAPP loading.

4.5.1.2 Glass fibre composites

Figure 4.21 shows the TGA scans in the form of weight change and derivative weight change versus temperature for PP and composites with different glass fibre contents. The TGA curves demonstrated that the incorporation of GF in PP matrix improved the thermal stability of the material. The presence of the glass fibre caused apparent alterations in the starting decomposition temperature of the composite, from 228.3°C for PP, to 250.1°C for PP/G15 and PP/G30 composites, as similarly observed by other researchers [135, 136]. The T_{onset} values were also increase from 356.9°C for PP to 423.3°C, 435.4°C and 430.3°C, for PP/G15, PP/G30 and PP/G45 composites, respectively. The same behaviour has been observed for the $T_{5\%}$, $T_{10\%}$, $T_{50\%}$ and DT_p values.

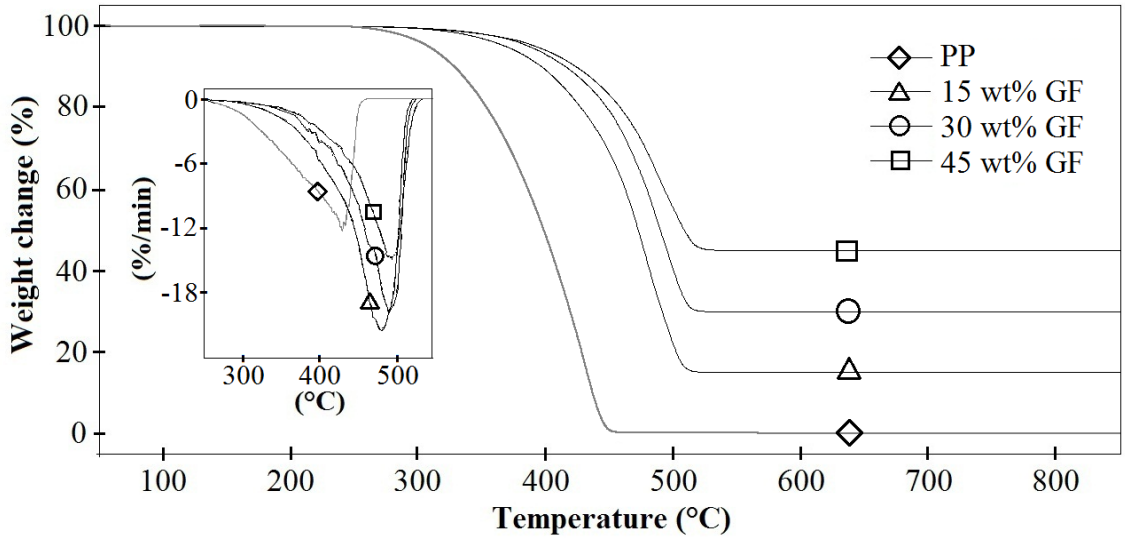

Figure 4.21: TGA and DTG thermograms of PP and PP/GF composites

According to the data presented in Table 4.4, it can be seen that generally, the thermal stability of composites increased with increase in GF loading. This is due to the fact that the heat absorption capacity of GF is higher than PP. As the content of fibres increased, the higher amount of fibres in the composites absorb more heat, thus higher temperature is therefore required to achieve the threshold energy for the commencement

of the degradation process [137]. Thus, as GF loadings are increased, there was an upward shift in the degradation temperature. According to Bryk [138], the introduction of fillers into polyalkanes resulted in an increase of the thermal stability of the polymer.

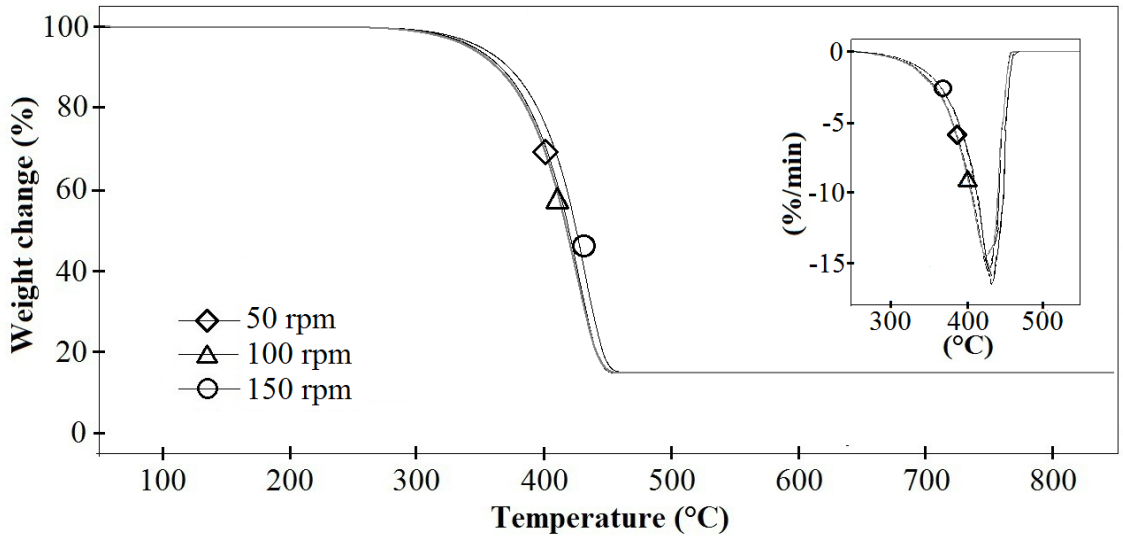

Figure 4.22: TGA and DTG thermograms of PP/G15 composites compounded at different screw speeds

It is observed that the thermal stability of PP/C8/G15 composites increased steadily with increasing screw speed, from 50 rpm to 150 rpm (Figure 4.22 and Table 4.4). PP/C8/G15 compounded with 150 rpm screw speed showed the highest T_{onset}, $T_{5\%}$, $T_{10\%}$, $T_{50\%}$ and DT_p values, relative to the material compounded with lower screw speed. It is likely that the improvement in the thermal properties of the PP/GF composite at high screw speed is due mainly to the fact that well dispersed structures were achieved for the composite system. Better dispersion of fibre in the polymer matrix will led to the fibre strengthening effect which consequently enhanced the thermal stability of the material.

Figure 4.23 shows the TGA and DTG thermograms of PP/G15 composite as a function of MAPP content. It is observed that the thermal stability of the composites generally reduced with increasing in MAPP content. It is possible that better compatibility between PP and GF, expected by the incorporation of MAPP into the

composites, might not be the criterion for improvement in the thermal stability of the glass fibre composite system.

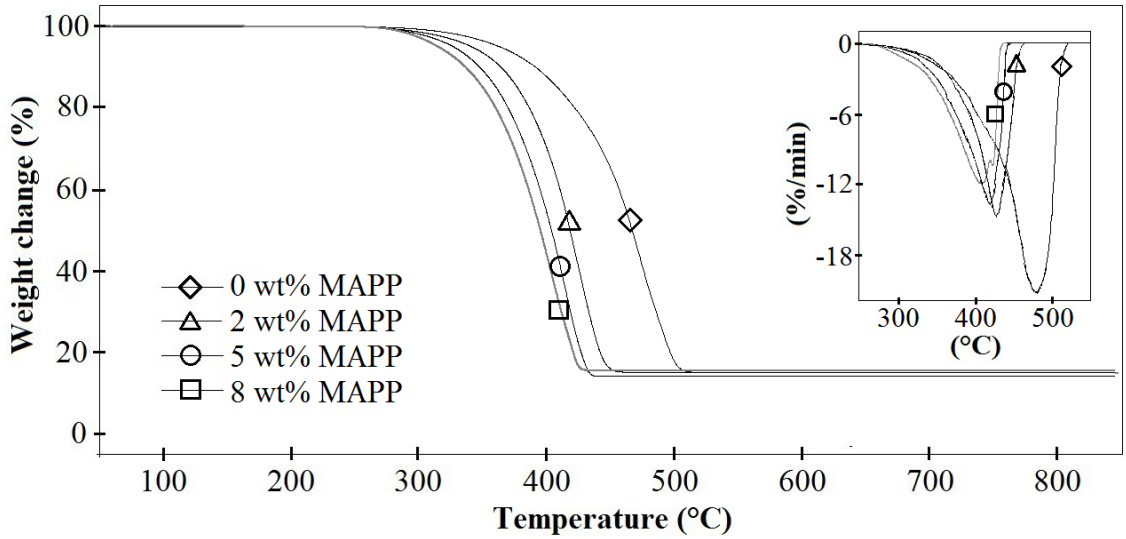

Figure 4.23: TGA and DTG thermograms of PP/G15 composites with 0 *wt%* to 8 *wt%* of MAPP

4.5.1.3 Glass fibre/nanoclay hybrid composites

Figure 4.24 shows TGA scans in the form of weight change and derivative weight change versus temperature for PP/G15 composites containing various amounts of untreated clay nanoparticles (0 – 9 phr). This provides information about the thermal stability of PP/GF/NC hybrid composites when compared to the corresponding PP/GF composites. The TGA curves demonstrate that the incorporation of clay in GF composites improved the thermal stability of the material. Degradation took place at a higher temperature in the presence of clay. The T_{onset} of PP/G15 was recorded at 423.3°C. Incorporation of 3 phr, 6 phr and 9 phr of clay into the composites increased T_{onset} of (PP/G15)/NC to 431.5°C, 433.2°C and 436.3°C, respectively. The improvement in the thermal stability can be ascribed to the hindered diffusion of the volatile decomposition products caused by the clay particles [118, 129]. The multi-layered silicate structure might have acted as an excellent insulator and mass transport barrier, slowing the escape of the volatile products generated during decomposition. It has also

been reported that the thermal stability of clay nanocomposite is due not only to its different structure but also to restricted thermal motion of the polymer molecules in the gallery [118, 139].

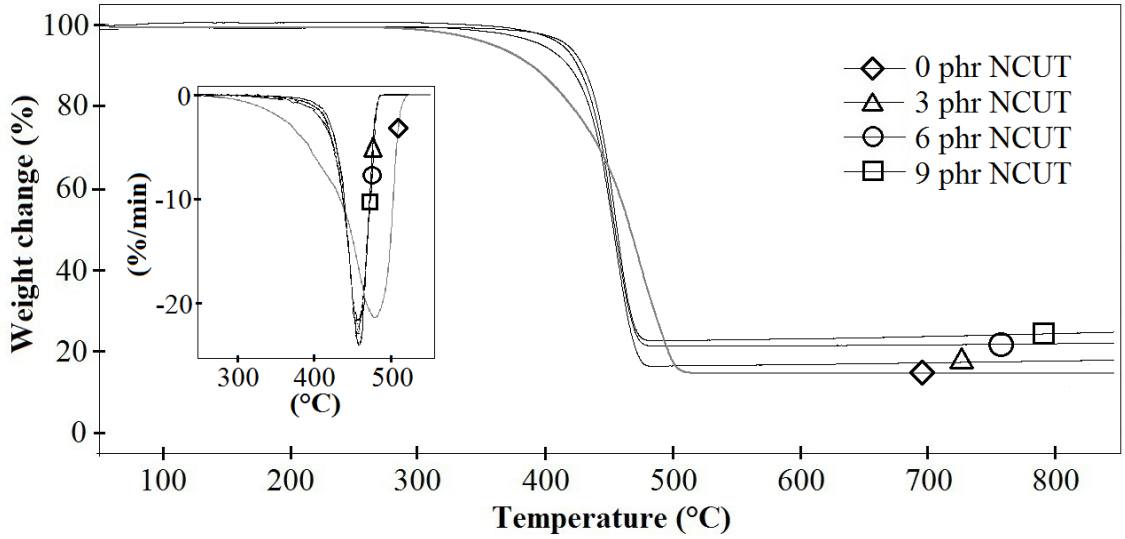

Figure 4.24: TGA and DTG thermograms of PP/G15/NC hybrid composites with 0 phr to 9 phr of NCUT

It can be seen from Figure 4.24 that these initial thermal decomposition temperatures ($T_{5\%}$ and $T_{10\%}$) were enhanced by the addition of clay into the GF composite. At 5% weight change, the $T_{5\%}$ increased from 368.0°C for PP/G15 to 405.9°C, 420.1°C and 424.0°C for composites containing 3 phr, 6 phr and 9 phr NC, respectively. The same trend was observed at 10% weight change. At this initial degradation event, it is possible that the polarity of PP in the PP/GF composites was enhanced by the incorporation of NC. This synergy led to better compatibility, resulting in the observed trend (Figure 4.24). In addition, it is believed that the homogenous dispersion of clay platelet acted as a barrier, trapping the volatilizing matrix from escaping into the atmosphere.

It should be noted from Table 4.4 and Appendix 4.1, that the degradation of PP was completed at about 465.7°C. It is evident in Figure 4.24 that there was a cross-over between degradation curves for PP/G15 and (PP/G15)/NC, occurring at 447°C. For

comparison, the amount of matrix remaining at this temperature has been calculated for the whole range of specimens, designated as $M_{447°C}$. Below the cross-over temperature, composites with clay (PP/GF/NC) were more stable compared to those without clay (PP/G15). From the degradation curve of PP (Appendix 4.1), it can be observed that at temperature of 447°C, only 1% of PP remained. By contrast, at the same temperature, with incorporation of clay into the system, after subtracting the GF and clay content, there was still a large amount of the matrix present, 52% for both (PP/G15)/NC3 and (PP/G15)/NC6 composites and 53% for (PP/G15)/NC9 composite.

It is well accepted that the improved thermal stability of the polymer/clay nanocomposites is mainly due to the formation of char which hinders the diffusion of the volatile decomposition products, as a direct consequence of the decrease in permeability usually observed in exfoliated nanocomposites [140, 141]. Furthermore, at temperatures higher than 447°C, the thermal behaviour of GF became predominant and an increase in thermal stability of the GF composite (PP/G15) was observed [11]. This may explain why the values of DT_p and $T_{50\%}$ for PP/G15 were higher than that of composites with increasing clay loading (Table 4.4). The same behaviour has been observed for the (PP/G30)/NC and (PP/G45)/NC hybrid composites (Table 4.4 and Appendices 4.3 and 4.4).

The thermal stability of treated clay hybrid composite increased when compared with hybrid composites using untreated clay (Figure 4.25). TEM images in Figure 4.26 show that there were completely delaminated sheets of treated clay (Figure 4.26 (a)) in the hybrid composites. Meanwhile, in untreated NC hybrid composites, the presence of clay aggregates was observed (Figure 4.26 (b)). As previously discussed in XRD section, the interlayer d-spacings of the clay in PP/GF/NCST composites were higher, when compared with the PP/GF/NCUT composites, which indicated that good dispersion of clay was achieved for the treated clay hybrid composites.

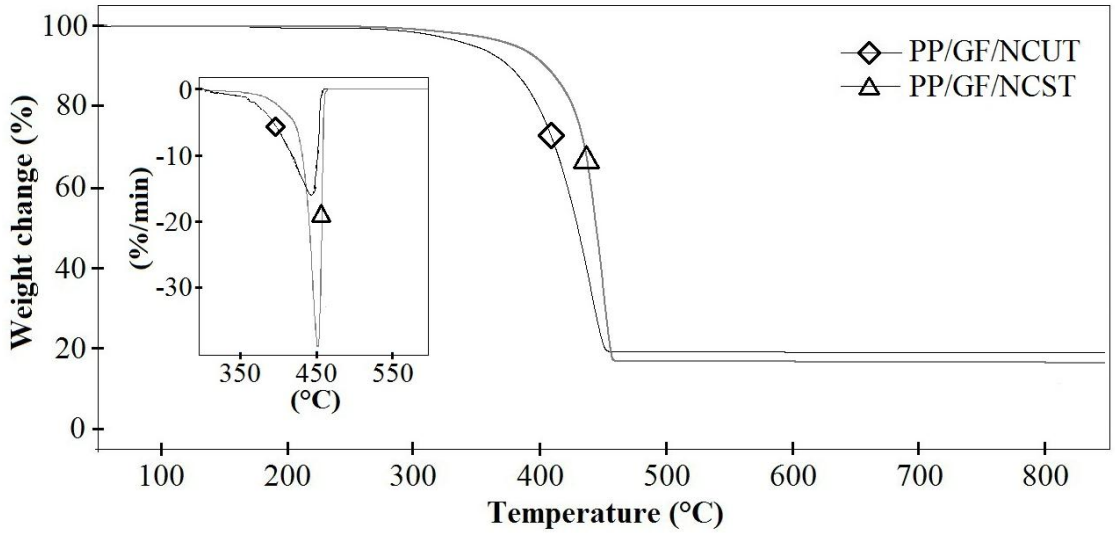

Figure 4.25: TGA and DTG thermograms of (PP:C8)/G15 with treated (NCST) and untreated (NCUT) clay composites

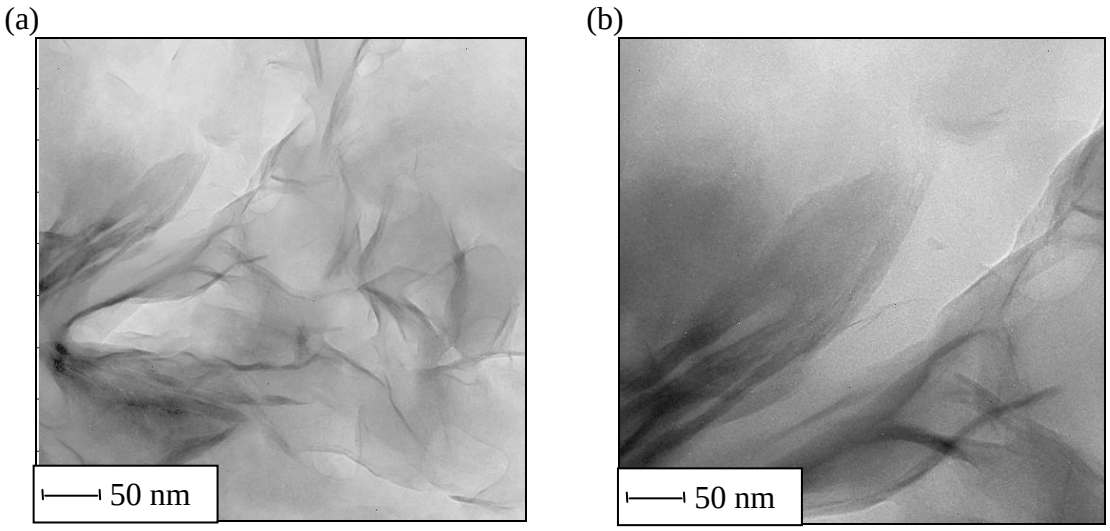

Figure 4.26: TEM images of hybrid composites with: (a) treated and (b) untreated nanoclays

By acting as a heat barrier, these high aspect ratio fillers, not only enhanced overall thermal stability of the system, but also promoted char formation, resulting in a high performance carbonaceous silicate layer, thereby insulating the underlying matrix material [142]. This phenomenon is usually observed in well dispersed nanocomposites. The significant increase in thermal stability resulting from the exfoliated clay platelets, may be due to the kinetic effects, with the platelets retarding the diffusion of oxygen into the polymer matrix [91].

Figure 4.27 shows the TGA thermographs of PP/G15/NCUT6 hybrid composite as a function of MAPP contents. As previously observed for PP/GF composites, the thermal stability of the hybrid composites generally reduced with increasing MAPP content. Better compatibility between PP, GF and NC, expected by the incorporation of MAPP into the hybrid composites may not be the criterion for the improvement of the thermal stability. By contrast, a different trend was obtained for PP/GF/NCST2 hybrid composites with incorporation of different MAPP contents (Appendix 4.5). It can be seen that the initial thermal decomposition temperatures (T_{onset}, $T_{5\%}$ and $T_{10\%}$) were enhanced by the addition of MAPP into the hybrid composite. However, $T_{50\%}$ and DT_P values showed insignificant improvement with MAPP content.

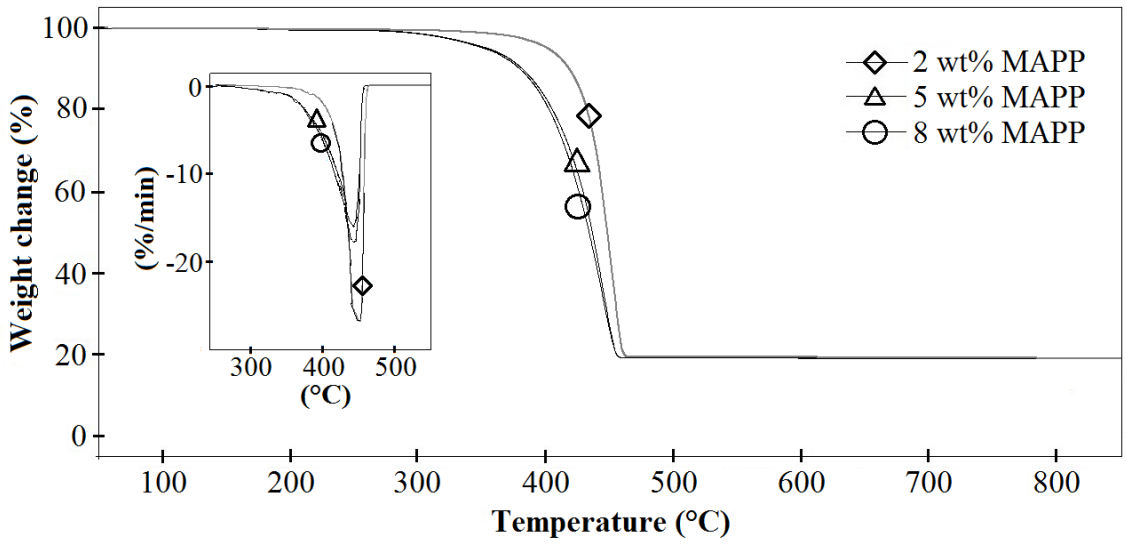

Figure 4.27: TGA and DTG thermograms of PP/G15/NCUT6 hybrid composites with 2 *wt%* to 8 *wt%* of MAPP

4.5.2 Differential scanning calorimetry (DSC)

The DSC thermograms provide information on the melting temperature (T_m), crystallisation temperature (T_c), enthalpy heat of melting (ΔH_m) and the enthalpy heat of crystallisation (ΔH_c). The degree of crystallinity (X_c) of the specimens was calculated [10] using equation (4.3):

$$X_c(\%) = \Delta H_m / \Delta H_m^* \quad (4.3)$$

where ΔH_m^* is enthalpy heat of fusion [14] of an "ideally" fully crystalline PP, taken as 209.0 J g^{-1}. The ΔH_m, ΔH_c and X_c values of PP, PP/GF, PP/NC and PP/GF/NC have been normalised and computed according to the actual PP content in the composites, as tabulated in Table 4.5.

Table 4.5: DSC data of PP, PP/GF, PP/NC and PP/GF/NC composites

Sample	T_m (°C)	ΔH_m (J g^{-1})	X_c (%)	T_c (°C)	ΔH_c (J g^{-1})
PP	163.7	86.5	41.4	121.7	91.9
PP100/NCUT3	162.0	63.2	30.3	121.4	68.3
PP100/NCUT6	163.5	93.0	44.5	121.6	93.5
PP100/NCUT9	163.6	93.1	44.5	122.8	93.7
(PP100:C0)/$NCST2_{800}$	155.9	88.3	42.2	116.7	89.5
(PP92:C8)/$NCST2_{100}$	156.3	86.9	41.6	116.0	89.1
(PP92:C8)/$NCST2_{300}$	155.3	88.0	42.1	116.7	87.6
(PP92:C8)/$NCST2_{500}$	156.3	87.1	41.7	116.1	87.1
(PP92:C8)/$NCST2_{800}$	155.8	85.5	40.9	116.6	88.8
(PP95:C5)/NCUT3	157.4	95.2	45.6	118.2	92.7
(PP92:C2)/NCUT6	157.7	95.6	45.8	118.9	94.5
(PP95:C5)/NCUT6	157.1	94.7	45.3	118.6	93.8
(PP92:C8)/NCUT6	156.6	94.7	45.3	118.0	92.3
(PP95:C5)/NCUT9	157.3	93.4	44.7	118.7	94.1
(PP98:C2)/NCST2	160.4	107.3	51.3	121.5	101.0
(PP95:C5)/NCST2	160.2	102.5	49.0	121.5	101.6
(PP92:C8)/NCST2	160.2	105.9	50.7	120.9	97.1
PP85/G15	161.6	87.7	42.0	121.7	94.1
PP70/G30	162.6	85.4	40.9	121.6	94.8
PP55/G45	161.4	87.5	41.9	121.2	95.4
(PP77:C8)/$G15_{50}$	159.2	107.6	51.5	118.6	98.8
(PP77:C8)/$G15_{100}$	159.2	104.7	50.1	117.9	99.1
(PP77:C8)/$G15_{150}$	159.1	106.7	51.1	117.6	97.4
(PP83:C2)/G15	158.3	98.6	47.2	125.0	92.3
(PP80:C5)/G15	157.8	97.2	46.5	123.7	91.8
(PP77:C8)/G15	157.3	92.6	44.3	121.4	91.9
(PP65:C5)/G30	158.3	97.4	46.6	123.8	91.5
(PP50:C5)/G45	157.4	89.5	42.8	122.5	90.3

Table 4.5, continued

Sample	T_m (°C)	ΔH_m (J g^{-1})	X_c (%)	T_c (°C)	ΔH_c (J g^{-1})
(PP85)/G15/NCUT3	163.8	91.4	43.8	125.5	96.9
(PP85)/G15/NCUT6	165.5	105.3	50.4	130.3	96.0
(PP85)/G15/NCUT9	164.9	104.4	49.9	129.7	100.9
(PP70)/G30/NCUT3	162.5	95.4	45.6	121.0	94.5
(PP70)/G30/NCUT6	165.1	103.2	49.4	129.9	101.3
(PP70)/G30/NCUT9	165.4	102.2	48.9	129.9	101.7
(PP55)/G45/NCUT3	161.3	98.1	46.9	119.1	94.8
(PP55)/G45/NCUT6	165.0	104.9	50.2	129.6	99.2
(PP55)/G45/NCUT9	165.2	105.3	50.4	129.3	99.7
(PP83:C2)/G15/NCUT6	160.4	104.5	50.0	121.0	97.3
(PP80:C5)/G15/NCUT6	160.2	103.1	49.3	120.6	97.8
(PP77:C8)/G15/NCUT6	159.7	106.6	51.0	120.5	96.4
(PP82:C2)/G15/NCST2	160.4	101.2	48.4	121.6	98.3
(PP80:C5)/G15/NCST2	160.3	101.6	48.6	121.3	98.9
(PP77:C8)/G15/NCST2	160.1	100.0	47.9	121.3	101.1

For the DSC analysis, all the samples were subjected to first heating, cooling and second heating cycles. However, only the results from the cooling and second heating are displayed and taken into consideration in the discussion. Ozdilek *et al.* [143] reported that the results from the second heating cycle is useful for the analysis, as the first heating results may be influenced by the sample history, such as preparation and storage conditions. DSC thermograms show the presence of single peak for the heating and cooling scans of the composites (Figures 4.28 – 4.36).

4.5.2.1 Clay nanocomposites

The melting temperature of pure PP is 163.7°C. DSC thermograms from Figure 4.28 and Table 4.5 show that increasing the clay loading in PP/NCUT (3 – 9 phr) had insignificant effects on the melting temperature of the nanocomposites. The same behaviour was also reported by Sharma *et al.* [142]. The ΔH_m is an important parameter since its magnitude is directly proportional to the overall level of X_c possessed by the polymer [10]. The ΔH_m of unreinforced PP was 86.5 J g^{-1} and decreased to 63.2 J g^{-1} for

the PP/NCUT3 nanocomposite. However, further addition of clay in the system increased the ΔH_m to 93.0 J g^{-1} for PP/NCUT6 and PP/NCUT9 nanocomposites. As expected, the values of X_c for the nanocomposites followed the same trend as previously stated for ΔH_m. The X_c value of PP/NCUT3 was reduced, relative to that of neat PP. Meanwhile, further addition of 6 and 9 phr of clay in the PP matrix increased the X_c values to 44.5%. It has been suggested that the presence of NC platelets dispersed in PP promotes heterogeneous nucleation of matrix, thus increasing the degree of crystallinity [11, 144]. As for T_c, no significant changes in its values were observed with the incorporation of clay into the PP matrix. On the other hand, the values of ΔH_c for PP/NCUT nanocomposites showed a similar trend, as was measured for X_c. The presence of 3 phr NCUT reduced the ΔH_c value when compared with PP matrix, however, this value shows an increment with further addition 6 phr and 9 phr NCUT into the system.

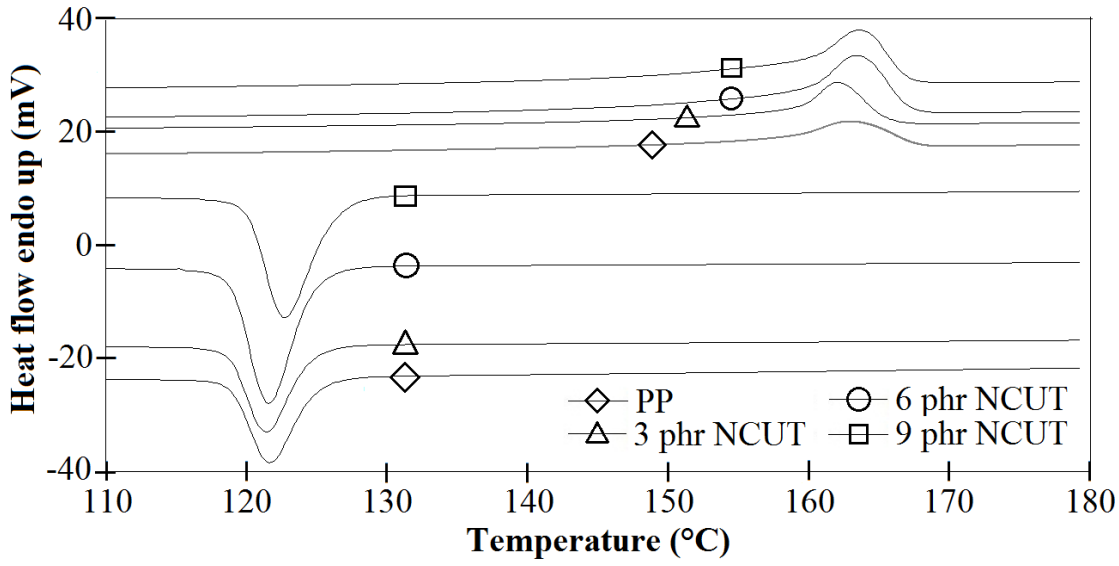

Figure 4.28: The DSC thermograms of PP and clay nanocomposites (the curves were shifted vertically for clarity)

The addition of treated NC showed marginal effect on the melting temperature of the composite, relative to the untreated clay composite (Figure 4.29). The melting point of PP/NCUT6 was recorded at 163.5°C and this value reduced by about 7.6°C to 155.9°C when treated NC was used in the composite system. The ΔH_m of unreinforced PP/NCUT6 was 93.0 J g^{-1} and decreased to 88.3 J g^{-1} for the PP/NCST2 nanocomposite. As expected, the values of X_c for the nanocomposites followed the same trend as previously stated for ΔH_m. The X_c value of PP/NCUST2 reduced to 42.2% relative to that of PP/NCUT6 (44.5%). T_c and ΔH_c for PP/NCST2 also showed some reductions in their values when compared with PP/NCUT6. However, Mohan and Kanny [97] obtained a reversed trend in the study of PP filled with untreated and treated Cloisite clay.

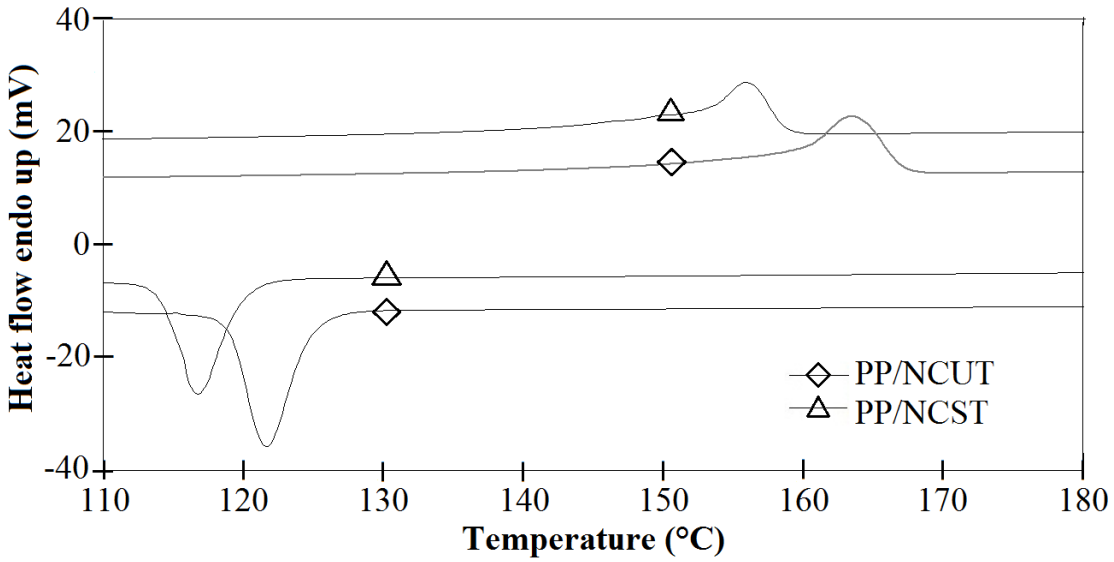

Figure 4.29: The DSC thermograms of untreated and treated clays nanocomposites

The effect of processing screw speed on the thermal properties of PP/NCST2 nanocomposites is illustrated in Appendix 4.7. Data extracted from this figure and shown in Table 4.5 reveal that the difference in the processing screw speed (100 rpm – 800 rpm) showed no significant effect on the thermal properties of the nanocomposites.

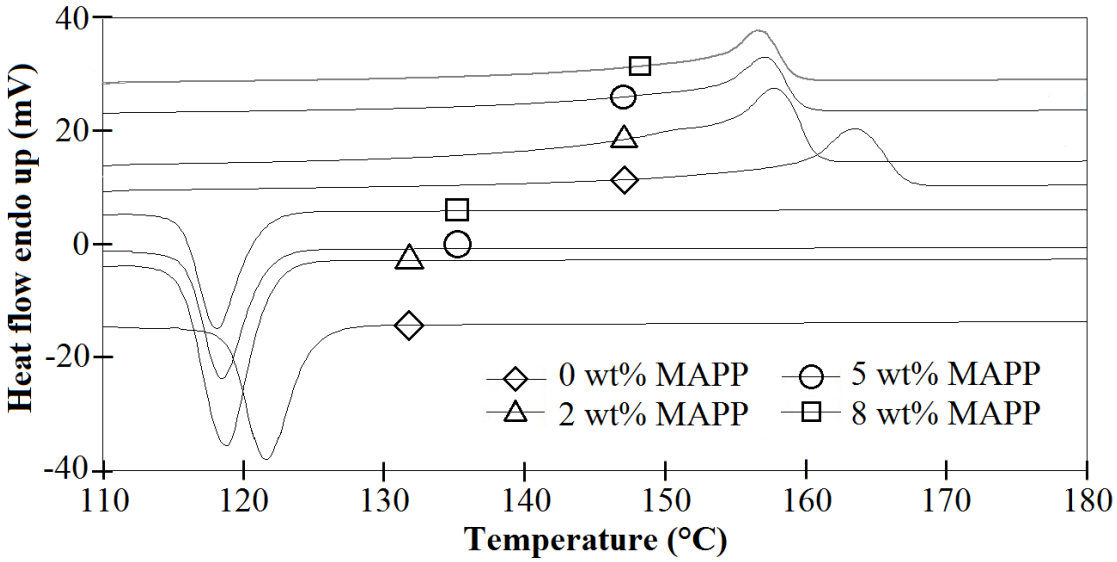

Figure 4.30: The DSC thermograms of injection-moulded PP/NCUT6 nanocomposite with different MAPP content

DSC thermograms of PP/NCUT6 with various contents of MAPP are shown in Figure 4.30. The T_m value of the nanocomposites showed a very slight decrement with increasing in MAPP loading. This might be caused by MAPP which interfered with the crystal integrity of PP, consequently decreasing the melting point of the nanocomposites, as similarly observed by Zhang *et al.* [145]. The authors also suggested that the reduction in T_m value might be due to the introduction of MAPP which has a lower melting point. As previously discussed in earlier section, the incorporation of 6 phr of NCUT in PP matrix increased the X_c value from 41.4% for PP to 44.5% for PP/NCUT6 nanocomposites. As observed in Table 4.5, the incorporation of 2 *wt%* of compatibiliser resulted in a slight increment in this value to 45.8%. This result indicated that the presence of compatibiliser in PP/NCUT system plays a role in enhancing the action of nanoclay as a nucleating agent in the crystallisation of the PP matrix [146]. However, further addition of both 5 *wt%* and 8 *wt%* of MAPP resulted in a lower magnitude of increment in X_c to 45.3%. On the other hand, a decrement of about 2°C in T_c values was observed with the incorporation of MAPP (2 *wt%* – 8 *wt%*) in PP/NCUT6 nanocomposites. The ΔH_c values in this system followed the same trend as

discussed for X_c. Except with the addition of 8 wt% of MAPP, this value slightly reduced from 93.5 J g^{-1} for uncompatibilised PP/NCUT6 nanocomposites to 92.3 J g^{-1} (Table 4.5).

DSC thermograms of PP/NCST2 with various contents of MAPP are shown in Figure 4.31. The addition of compatibiliser into treated clay nanocomposites showed greater influence in the thermal behaviour of the corresponding nanocomposites as compared with untreated clay nanocomposites. The T_m values of the nanocomposites shifted to a higher temperature, from 155.9°C in uncompatibilised nanocomposite, to 160.4°C in PP/NCST2 with 2 *wt%* of MAPP. The T_m values remained essentially unchanged (160.2°C) on further addition of 5 *wt%* and 8 *wt%* of MAPP. The ΔH_m of nanocomposites also increased by about 19.0 J g^{-1} from 88.3 J g^{-1} for uncompatibilised PP/NCST2 to 107.3 J g^{-1} with incorporation of 2 wt% of MAPP in the system. On the other hand, further addition of both 5 *wt%* and 8 *wt%* of MAPP resulted in lowering the magnitude of the increment in ΔH_m to 102.5 J g^{-1} and 105.9 J g^{-1}, respectively.

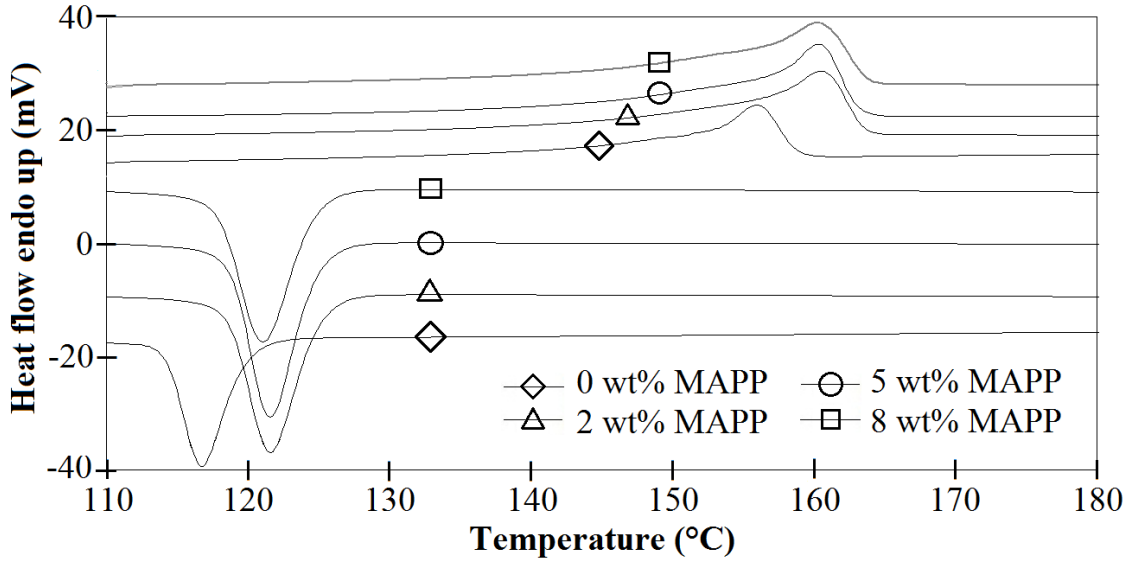

Figure 4.31: The DSC thermograms of injection-moulded PP/NCST2 nanocomposite with different MAPP content

From Table 4.5, it can be seen that the X_c values were enhanced up to 9% by the addition of 2 *wt%* of MAPP into the nanocomposites. This behaviour can be explained as the nucleating effect of the dispersed treated clay platelets in the PP matrix. MAPP improved exfoliation by promoting the separation of clay layers, thus increasing the number of the potential nucleating sites.

This idea is supported by the increment observed in T_c. The T_c of nanocomposite increased by about 5°C with the incorporation of 2 *wt%* of MAPP into the system. Higher T_c values indicated ease of crystallisation, which accelerated a faster nucleation process of PP. The same trend was observed for the ΔH_c. This value increased from 89.5 J g^{-1} for PP/NCST2 to 101.0 J g^{-1}, 101.6 J g^{-1} and 97.1 J g^{-1} with the presence in the nanocomposites material of 2 *wt%*, 5 *wt%* and 8 *wt%* of MAPP, respectively. From these results, the addition of MAPP to the nanocomposites gave significant effect on the thermal behaviour of the nanocomposites, relative to the uncompatibilised nanocomposites. However, for the compatibilised nanocomposites, irrespective the amount of MAPP present, the thermal behaviour of these materials remained the same for low and high MAPP contents.

4.5.2.2 Glass fibre composites

The melting and crystallisation behaviours of neat PP and glass fibre composites are shown in Figure 4.32. The melting temperature slightly reduced from 163.7°C for PP to 161.6°C for composite with 15 w*t%* of GF. However, as the GF content increased to 30 *wt%* and 45 *wt%*, no significant trend in the T_m value was observed. Similar behaviour was also reported by Samal *et al.* [88] and Nayak and Mohanty [147]. A slight increment in ΔH_m value from 86.5 J g^{-1} for PP to 87.7 J g^{-1} for PP/G15 composite was recorded. Meanwhile, a reduction in this value to 85.4 J g^{-1} was obtained as 30 *wt%*

of GF was added to the system. Further addition of 45 *wt%* of GF to the system resulted in an increment in this value to 87.5 J g^{-1}.

The X_c values depicted in Table 4.5 revealed that the degree of crystallinity slightly increased from 41.4% for PP matrix to 42.0% with the incorporation of 15 *wt%* of GF. This indicates the formation of nucleation sites of PP with the presence of GF in the composite system [147]. However, as previously observed for ΔH_m, further addition of 30 *wt%* of GF in the system resulted in a slight decrement in this value, to 40.9%, and again, the X_c increased to 41.9% with 45 *wt%* of GF loading (Table 4.5). There was no significant change observed for T_c value with the addition of 15 *wt%* to 45 *wt%* of GF. On the other hand, the incorporation of GF in the system showed some improvement in ΔH_c values. The ΔH_c of PP matrix is 91.9 J g^{-1}; increased to 94.1 J g^{-1}, 94.8 J g^{-1} and 95.4 J g^{-1} for composites with 15 *wt%*, 30 *wt%* and 45 *wt%* of GF loading, respectively. The enhancement in this value is in agreement with the behaviour previously observed for X_c.

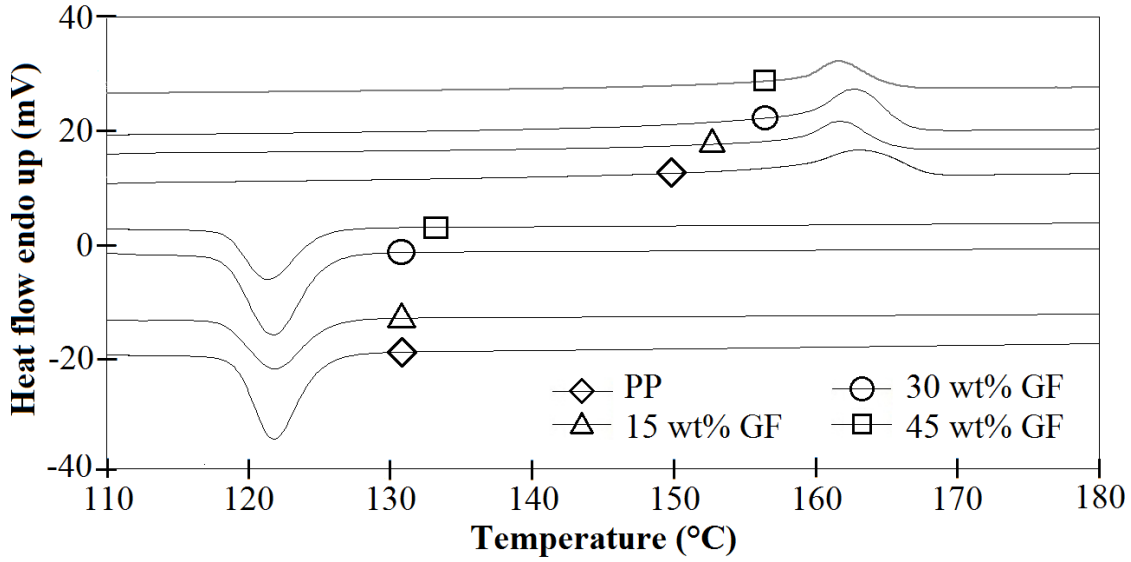

Figure 4.32: The DSC thermograms of injection-moulded PP/GF composites

The effect of processing screw speed on the thermal properties of (PP:C8)/G15 composites is shown in Appendix 4.8. Data from Table 4.5 show that the difference in

the processing screw speed (50 rpm – 150 rpm) had no significant effect on the thermal properties of the glass fibre composites.

DSC thermograms of PP/G15 with various contents of MAPP are shown in Figure 4.33. The addition of compatibiliser to glass fibre composites showed some influence on the thermal behaviour of the corresponding composites. Data from Table 4.5 shows that the T_m value for the uncompatibilised PP/G15 shifted to lower temperature from 161.6°C to 158.3°C with the presence of 2 wt% of MAPP. As the compatibiliser content increased, only a slight reduction in this value, to 157.8°C and 157.3°C was observed for 5 *wt%* and 8 *wt%* of MAPP, respectively. It is possible that the incorporation of MAPP in the system increased the mobility of the polymer chain, resulting in a lower T_m value.

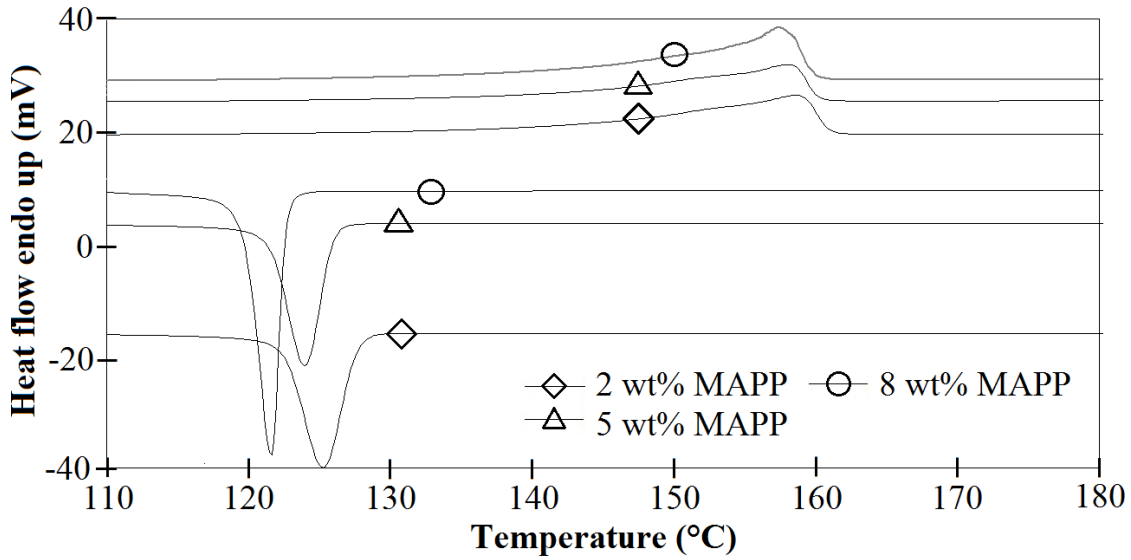

Figure 4.33: The DSC thermograms of injection-moulded PP/G15 composite with different MAPP contents

The ΔH_m value of the uncompatibilised PP/G15 is 87.7 J g^{-1} and increased to 98 6 J g^{-1} with 2 *wt%* of MAPP (Table 4.5). However, further addition of 5 *wt%* and 8 *wt%* of MAPP resulted in lower magnitudes increments in ΔH_m to 97.2 J g^{-1} and 92.6 J g^{-1}, respectively. The same trend was observed for X_c. This value increased by about

5.2%, from 42.0% for the uncompatibilised PP/G15 to 47.2% as 2 *wt%* of MAPP was added, which indicated an enhancement in the crystallisation process of PP in presence of compatibiliser [147]. It can also be seen that the T_c value of composite shifted to a comparatively higher temperature, from 121.7°C for PP/G15 to 125.0°C for composites with 2 *wt%* of MAPP due to the nucleation effect of fibres and MAPP. By contrast, further addition of 5 *wt%* and 8 *wt%* of MAPP reduced the T_c value to 123.7°C and 121.4°C. Composite with the highest MAPP content (8 *wt%*) gave the lowest T_c value when compared with the others, as self entanglement of excess MAPP (among themselves) might be responsible for the observed trend.

4.5.2.3 Glass fibre/nanoclay hybrid composites

Figure 4.34 shows the DSC thermograms for PP/G15 composites containing various amounts of untreated nanoclay (0–9 phr). This provides information on the thermal stability of PP/GF/NC composites when compared to the corresponding PP/GF composites. Table 4.5 shows that the presence of NC in the hybrid composites increased the melting temperature by about 2.2°C to 3.9°C, from 161.6°C for PP/G15 to 163.8°C, 165.5°C and 164.9°C for hybrid composites containing of 3 phr, 6 phr and 9 phr of NC, respectively. For this particular system, hybrid of 15 *wt%* GF with 6 phr NC ((PP/G15)/NCUT6) had the highest T_m value of 165.5°C. Incorporation of GF and NC in PP restricted the mobility of the polymer chain, resulting in higher T_m [15]. The ΔH_m of PP/G15 composite was 87.7 J g^{-1} (Table 4.5). For the hybrid system, it was observed that the ΔH_m value of composites increased from 87.7 J g^{-1} for PP/G15 to 91.4 J g^{-1}, 105.3 J g^{-1} and 104.4 J g^{-1} with the addition of 3 phr, 6 phr and 9 phr of NC loading, respectively.

Meanwhile, X_c values showed the same trend as observed for ΔH_m. The X_c of PP/G15 composite was 42.0% The addition of clay in the 15 *wt%* GF composite showed

some increment in the degree of crystallinity. PP/G15/NCUT6 had the highest X_c value (50.4%) for the PP/G15/NC hybrid composites system (Table 4.5). It has been suggested that the presence of NC platelets dispersed in GF composites promotes the heterogeneous nucleation of the PP molecular chains, thus increasing the degree of crystallinity [15, 144]. It acts as a nucleating agent for the PP and changes the crystalline behaviour of this polymer matrix [148]. As the clay content in the hybrid composite increased to 9 phr (PP/G15/NC9), the X_c value remained essentially unchanged when compared to PP/G15 containing 6 phr of NC loading hybrid composites. This is probably because the degree of crystallinity is very close to the maximum that the PP can achieve, considering its stereoregularity [144]. Also, the presence of a high concentration of dispersed NC would prevent the formation of large crystalline domains due to the limited space and restrictions imposed on the polymer chain by a high number of silicate platelets [149].

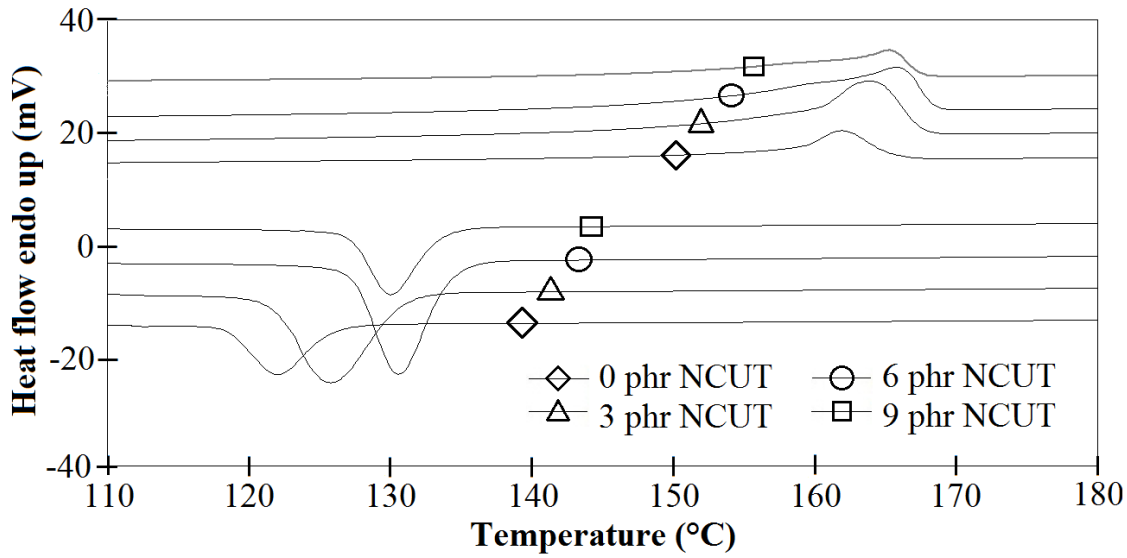

Figure 4.34: The DSC thermograms of injection-moulded PP/G15/NC hybrid composites with 0 phr to 9 phr of NCUT

The crystalline peak temperature (T_c) of the hybrid composites were enhanced to higher temperatures when compared with PP/G15 glass fibre composite. The T_c of the

hybrids increased by about 3.8°C, 8.6°C and 8.0°C, respectively, for the (PP/G15)/NC3, (PP/G15)/NC6 and (PP/G15)/NC9, relative to that of PP/G15 (121.7°C). These increments indicate the nucleating effect of the NC in the crystallisation of PP [150]. Incorporation of GF and NC may accelerate the crystallisation of PP, thereby making it to crystallise at higher temperature, hence shortening the moulding cycle in practical production [14]. The same trend was observed for the enthalpy heat of crystallisation, ΔH_c. The same behaviour was observed for the (PP/G30)/NC and (PP/G45)/NC hybrid composites (Table 4.5 and Appendices 4.9 and 4.10).

The effect of clay surface treatment on the thermal properties of hybrid composites is shown in Appendix 4.11. Data from Table 4.5 show that the clay surface treatment did not give any significant effect on the thermal properties of the nanocomposites. The T_m value was recorded at 160.4°C for the untreated (PP/GF/NCUT) and treated clay hybrid composites (PP/GF/NCST). The X_c, T_c and ΔH_c values also remained essentially the same for PP/GF/NCUT and PP/GF/NCST hybrid composites.

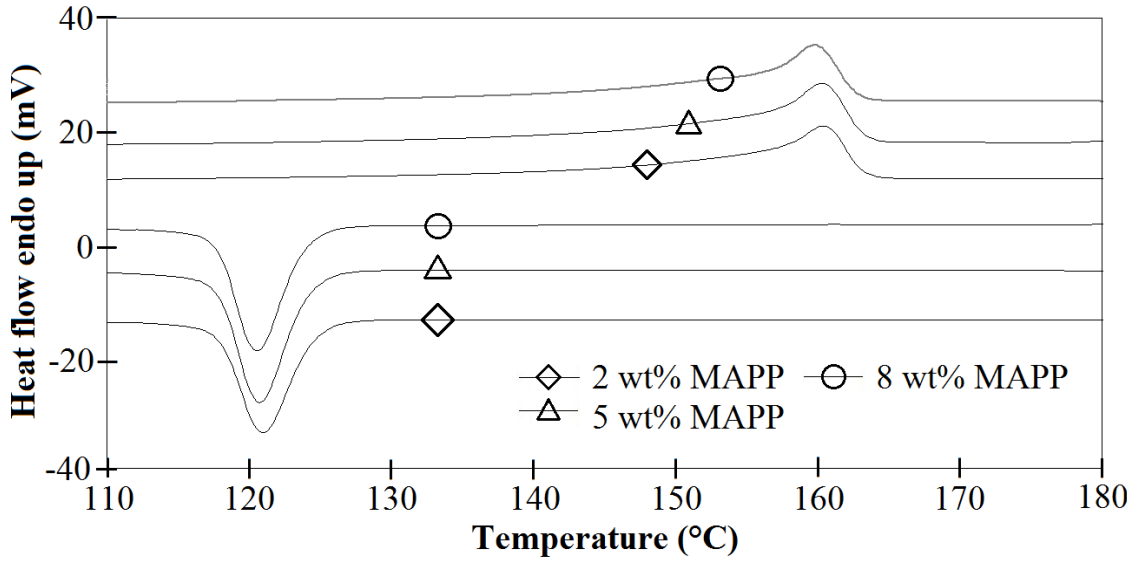

Figure 4.35: The DSC thermograms of injection-moulded PP/G15/NCUT6 hybrid composites with different MAPP contents

DSC thermograms of PP/G15/NCUT6 hybrid composite with various contents of MAPP are shown in Figure 4.35. Data from Table 4.5 shows that the T_m value significantly reduced, from 165.5°C for the uncompatibilised PP/G15/NCUT6 to 160.4°C with the addition of 2 *wt%* of MAPP. Further incorporation of 5 *wt%* and 8 *wt%* of MAPP into the system further reduced this value, however with a very minimal decrement, to 160.2°C and 159.7°C, respectively. It is interesting to mention here that the compatibiliser in hybrid composites showed similar effect in the melting temperature in the composites system as previously observed for both PP/NC (Figure 4.30) and PP/GF (Figure 4.33).

The ΔH_m value of PP/G15/NCUT6 was 105.3 J g^{-1} and reduced to 104.5 J g^{-1} and 103.1 J g^{-1} with the addition of 2 *wt%* and 5 *wt%* of MAPP, respectively. However, further addition of 8 *wt%* of MAPP to the system slightly increased this value to 106.6 J g^{-1}. The same trend was observed for X_c. A sharp decrement of T_c value by about 9°C from 130.3°C for PP/G15/NCUT6 to 121.0°C was observed with the presence of 2 *wt%* of MAPP. This value remained essentially unchanged with further addition of MAPP loading.

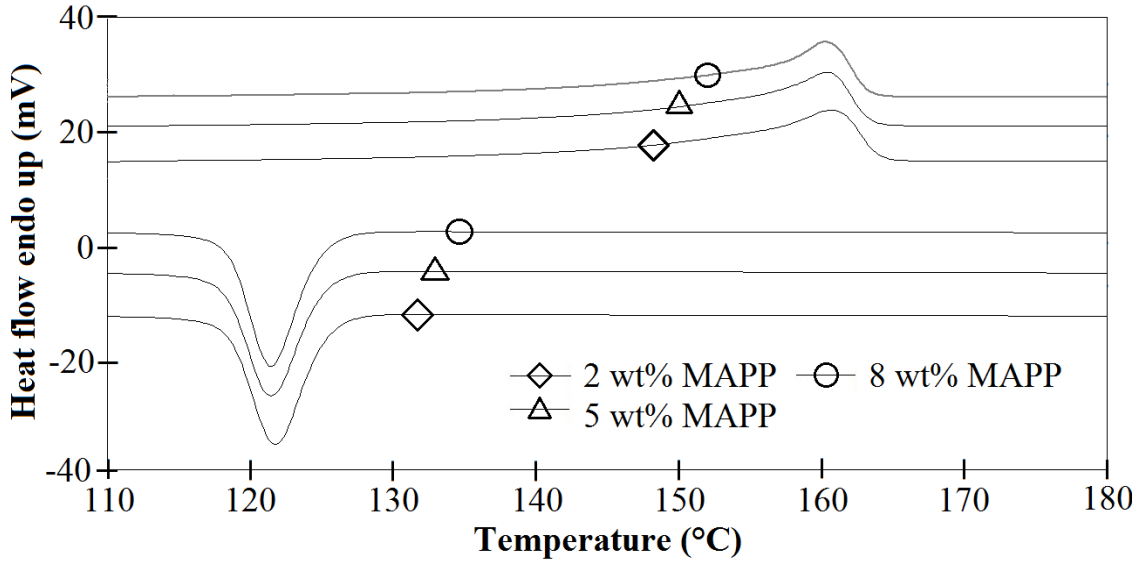

Figure 4.36: The DSC thermograms of injection-moulded PP/G15/NCST2 hybrid composites with different MAPP contents

DSC thermograms of PP/G15/NCST2 hybrid composite with various contents of MAPP are shown in Figure 4.36. In the previous section, it was reported that the additions of compatibiliser into treated clay nanocomposites (PP/NCST) showed greater influences in the thermal behaviour of the corresponding nanocomposites (Figure 4.31). However, a different trend was observed in this hybrid composite. Most of the thermal characteristics determined from DSC measurement showed insignificant changes, as MAPP was added to the system.

4.6 Dynamic mechanical analysis (DMA)

Results from the dynamic mechanical analyses (DMA) of composite specimens are shown in Figures 4.37 – 4.64. The thermomechanical data extracted from these curves are tabulated in Table 4.6.

Table 4.6: DMA thermomechanical data of PP, PP/GF, PP/NC and PP/GF/NC composites

Sample	Storage modulus (E')			Loss modulus (E'')			Tan delta		
	T_α (°C)	$E'_{-100°C}$ (GPa)	$E'_{25°C}$ (GPa)	$T_\alpha^{E''}$ (°C)	E''_{max} (MPa)	$E''_{25°C}$ (MPa)	T_g (°C)	$tan\ \delta_{max}$ (x10^{-2})	$tan\ \delta_{25°C}$ (x10^{-2})
PP	-16.3	4.06	1.28	-2.3	140.2	74.9	2.9	6.7	5.9
PP100/NCUT3	-15.9	3.88	1.22	-2.6	123.2	66.9	2.9	6.2	5.5
PP100/NCUT6	-16.1	4.10	1.33	-3.5	126.9	66.9	1.7	5.9	5.0
PP100/NCUT9	-12.1	4.51	1.43	-1.5	133.0	73.7	3.2	5.9	5.2
(PP100:C0)/NCST2$_{800}$	-8.7	4.88	1.70	1.5	153.6	91.6	6.7	6.0	5.4
(PP92:C8)/NCST2$_{100}$	-9.2	5.01	1.79	2.9	148.6	96.7	8.4	5.6	5.4
(PP92:C8)/NCST2$_{300}$	-9.2	4.88	1.74	2.9	152.1	96.2	8.4	5.9	5.5
(PP92:C8)/NCST2$_{500}$	-10.4	5.10	1.70	2.3	169.7	98.7	7.8	6.5	5.8
(PP92:C8)/NCST2$_{800}$	-10.2	5.33	1.90	1.7	163.4	99.5	7.0	5.7	5.2
(PP95:C5)/NCUT3	-11.4	5.31	1.87	1.7	168.0	94.5	6.6	5.9	5.1
(PP98:C2)/NCUT6	-12.2	5.38	1.91	1.7	169.0	94.4	6.6	5.9	5.0
(PP95:C5)/NCUT6	-11.0	5.15	1.80	1.7	165.2	91.7	6.5	6.0	5.1
(PP92:C8)/NCUT6	-11.2	5.06	1.77	1.7	167.9	92.7	6.7	6.3	5.2
(PP95:C5)/NCUT9	-13.7	5.19	1.91	1.2	156.9	88.7	6.0	5.6	4.7
(PP98:C2)/NCST2	-8.8	5.65	2.02	2.9	173.3	107.4	7.8	5.8	5.3
(PP95:C5)/NCST2	-9.0	5.36	1.91	2.4	170.9	106.4	7.8	6.0	5.6
(PP92:C8)/NCST2	-10.0	5.66	1.82	1.5	201.7	119.0	7.5	7.1	6.5
PP85/G15	-16.4	6.36	2.39	-2.9	226.1	125.6	1.7	6.1	5.3
PP70/G30	-16.9	8.72	3.85	-2.6	287.5	196.4	2.6	5.3	5.1
PP55/G45	-17.4	11.89	5.97	-2.3	376.9	289.2	2.3	4.7	4.9

Table 4.6, continued

Sample	Storage modulus (E')			Loss modulus (E'')			Tan delta		
	T_α (°C)	$E'_{-100°C}$ (GPa)	$E'_{25°C}$ (GPa)	$T_\alpha^{E''}$ (°C)	E''_{max} (MPa)	$E''_{25°C}$ (MPa)	T_g (°C)	$tan\ \delta_{max}$ (x10^{-2})	$tan\ \delta_{25°C}$ (x10^{-2})
(PP77:C8)/G15$_{50}$	-14.9	6.49	2.81	2.7	190.4	124.9	7.2	4.9	4.4
(PP77:C8)/G15$_{100}$	-14.2	6.73	2.54	1.9	241.6	141.7	7.2	6.4	5.6
(PP77:C8)/G15$_{150}$	-9.6	6.70	2.89	2.6	199.6	130.9	7.2	5.0	4.5
(PP83:C2)/G15	-13.5	6.90	3.20	1.2	192.1	126.6	5.5	4.5	4.0
(PP80:C5)/G15	-10.8	6.88	3.42	1.1	179.2	120.4	4.8	4.0	3.5
(PP77:C8)/G15	-10.8	6.86	3.34	1.1	181.4	119.7	4.8	4.1	3.6
(PP65:C5)/G30	-12.6	8.70	4.78	1.2	218.1	151.2	4.4	3.6	3.2
(PP50:C5)/G45	-14.1	10.75	6.12	1.0	272.6	191.9	3.9	3.6	3.1
(PP85)/G15/NCUT3	-15.8	6.08	2.32	-3.2	201.5	117.2	1.4	5.7	5.0
(PP85)/G15/NCUT6	-17.1	6.65	2.94	-3.3	185.2	125.3	1.1	4.5	4.3
(PP85)/G15/NCUT9	-16.0	7.04	2.96	-4.1	199.3	114.3	0.2	4.6	3.8
(PP70)/G30/NCUT3	-16.9	8.31	3.66	-2.9	276.9	179.3	1.4	5.3	4.9
(PP70)/G30/NCUT6	-17.1	8.52	4.22	-3.5	228.2	167.6	1.1	4.0	4.0
(PP70)/G30/NCUT9	-17.9	8.71	4.22	-3.8	228.6	148.3	-0.2	4.0	3.5
(PP55)/G45/NCUT3	-16.3	11.18	5.67	-2.3	337.8	263.6	1.4	4.5	4.6
(PP55)/G45/NCUT6	-18.6	11.37	6.15	-2.7	309.6	264.3	1.4	3.9	4.3
(PP55)/G45/NCUT9	-18.0	11.79	6.31	-3.5	299.7	222.6	0.2	3.7	3.5
(PP83:C2)/G15/NCUT6	-10.9	7.42	3.29	1.1	210.0	132.0	5.6	4.7	4.0
(PP80:C5)/G15/NCUT6	-10.9	7.21	2.91	2.0	225.5	138.3	6.6	5.5	4.7
(PP77:C8)/G15/NCUT6	-10.6	6.98	3.17	2.3	199.7	129.0	6.3	4.7	4.0
(PP82:C2)/G15/NCST2	-8.6	7.36	3.39	3.4	201.5	135.9	7.0	4.4	4.0
(PP80:C5)/G15/NCST2	-8.2	7.52	3.31	3.1	227.2	152.2	7.0	5.1	4.6
(PP77:C8)/G15/NCST2	-6.1	7.45	3.36	3.9	218.4	146.3	7.8	4.8	4.3

4.6.1 Storage modulus (E')

The dynamic storage modulus (E') is closely related to the load bearing capacity of a material and is analogous to the flexural modulus, measured as per ASTM D-790 standard [10]. It is very well known that the dynamic storage modulus in many structural applications is very important. A clear understanding of the storage modulus-temperature curve, obtained during a dynamic mechanical test, provides valuable insights into the stiffness of a material as a function of temperature. This is useful in assessing the molecular basis of the mechanical properties of materials since it is very sensitive to structural changes, such as: molecular weight, degree of cross-linking and fibre-matrix interfacial bonding [151]. The storage modulus value at –100°C and 25°C, are referred to as $E'_{-100°C}$ and $E'_{25°C}$, respectively. Variation of E' as a function of temperature for virgin PP, PP/NC, PP/GF and PP/GF/NC composites is graphically illustrated in Figures 4.37 – 4.47.

Generally, from these figures, a decreasing trend in the storage modulus throughout the temperature range was observed. Two apparent changes in E' with temperature can be observed for all composites tested. A sharp rate of decrease in E' from –25°C to about 25°C is believed to be associated with the relaxation of the amorphous phase (α-relaxation). In this case, the glassy state of the amorphous phase in the polymer matrix goes through its glass transition, followed by a sharp drop in E'. At about 15°C, the E' continued to fall and the slope was flatter than what was obtained in the first drop in E'. From 70°C and above, the reduction in E' was less severe.

4.6.1.1 Clay nanocomposites

Figure 4.37 illustrates the fact that the storage modulus of clay nanocomposites showed a dependence on the extent of NC loading below the glass transition temperature (T_g) in the region 0°C – 9°C, while insignificant variation of E' between the

nanocomposites is seen above the T_g. The nanocomposites with 6 phr and 9 phr of NC loading displayed higher modulus than the pure PP throughout the temperature range. It is evident from Table 4.6 and Figure 4.37 that there was a notable increase of about 6% in the $E'_{-100°C}$, from 4.06 GPa for PP matrix, to 4.51 GPa for PP/NCUT9 nanocomposite. This is probably due to the increase in the stiffness of the matrix, resulting from the restriction of molecular motions imparted by the nanoclay [87, 140]. It is also possible that the increment in the degree of crystallinity in the system with the presence of nanoclay, as previously discussed in DSC section (Table 4.5), makes the material to become more rigid, hence results in the improvement in the storage modulus value. In contrast, the addition of 3 phr of clay to the system, resulted in a slight decrement of about 4% (3.88 GPa) in the $E'_{-100°C}$, relative to PP matrix. Thus, it seems that at lower content, instead of strengthening the material, the clay, as a filler to the composite system, only manifested a negative effect.

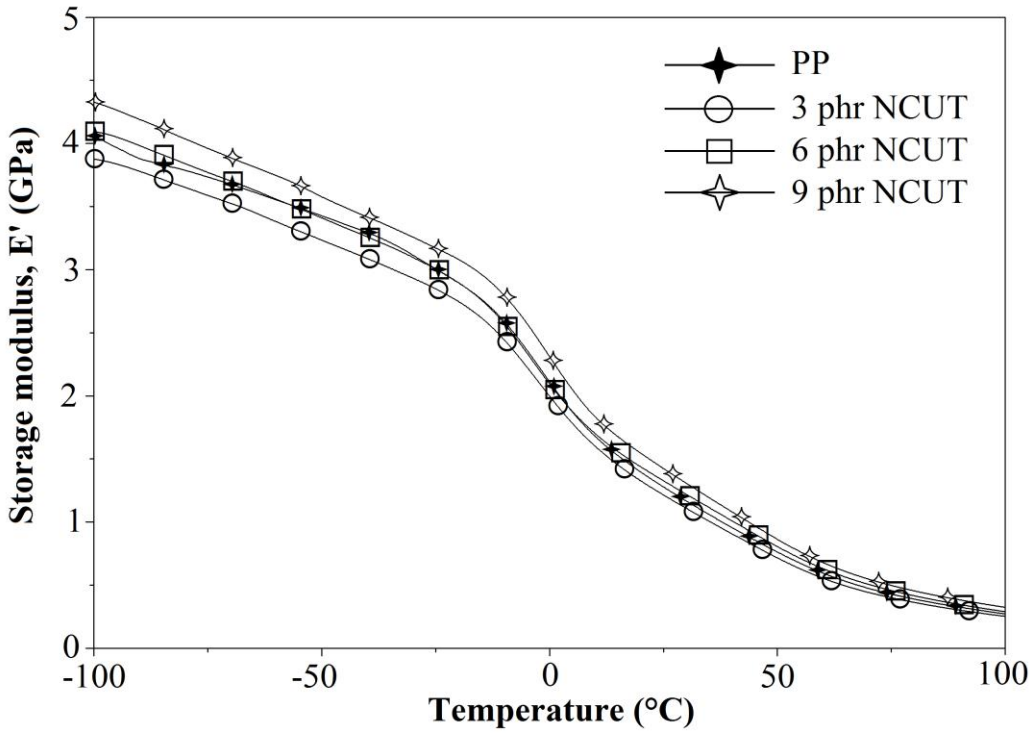

Figure 4.37: The storage modulus curves of clay nanocomposites

The storage modulus curves of PP nanocomposites, with untreated and treated clay are presented in Figure 4.38. On the addition of 6 phr untreated clay, the *E'* increased from 4.06 GPa for PP matrix, to 4.10 GPa for PP/NCUT6 nanocomposites, due to the partial reinforcement, restricting the flexibility and the mobility of the polymer chain segment. Meanwhile, with the addition of 2 phr of treated clay in the PP matrix, a remarkable increment in the *E'* value to 4.88 GPa was observed. It should be noted that the stiffness and storage modulus values are directly proportional to the reinforcement effect [142]. Thus, the obvious improvement in the *E'* with the addition of treated clay indicated the formation of exfoliated nanocomposites. This could be due to the presence of surfactant in the treated clay. The surfactant is able to swell/delaminate the stacked layer of nanoclay and hence, the polymer matrix can diffuse easily, into the silicate layer.

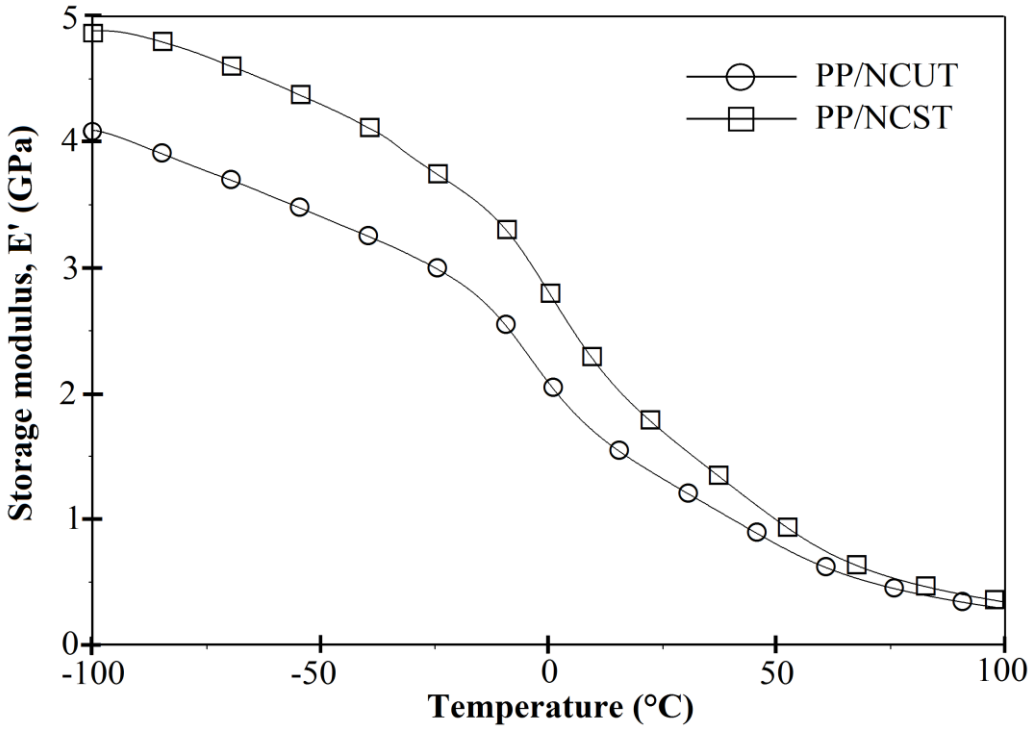

Figure 4.38: The storage modulus curves of nanocomposites with untreated and treated nanoclays

Analysing the storage modulus (*E′*) curves of PP/NCST2 nanocomposites obtained with different processing screw speeds from 100 rpm to 800 rpm (Figure 4.39), it is evident that the *E′* were influenced by the screw speed. Despite the fact that the same amount of clay was used in this nanocomposite, less improvement in the $E'_{-100^{o}C}$ value was observed at low processing screw speed. This scenario is plausible because at low screw speed, clay structures remain as microtactoids contributing to the deterioration of the storage modulus [121]. The highest *E′* value (5.33 GPa) was observed using the highest screw speed (800 rpm). The extrusion of polymer nanocomposite with high screw rate transmits higher shear stress to the molten polymer, thus bringing a higher degree of nanoclay platelets dispersion, which is responsible for the remarkable enhancements in the reinforcing effect and of the stiffness [144].

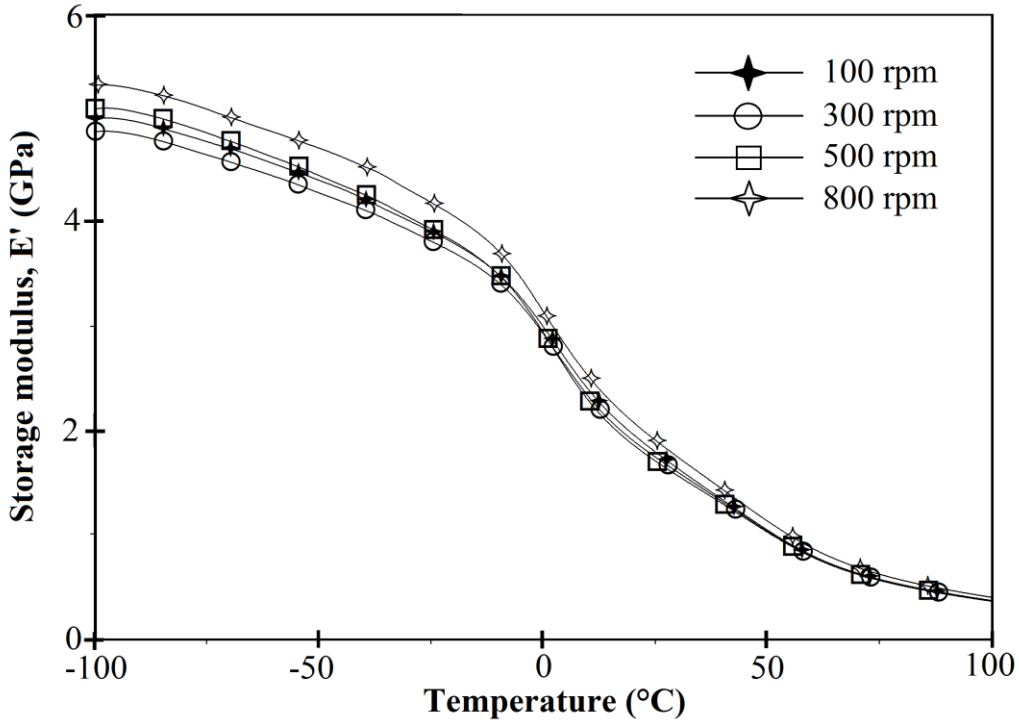

Figure 4.39: The storage modulus curves of PP/NCST2 nanocomposites at different screw speeds

Figure 4.40 shows the storage modulus (*E′*) curves obtained for PP/NCUT6 nanocomposites with variation in MAPP loading, from 0 *wt%* to 8 *wt%*. Apparently, the

compatibilised nanocomposites displayed improved E' values throughout the experimental temperature range when compared with the uncompatibilised system, indicating that more reinforcing effect was induced by the compatibiliser [146]. This scenario is considered to be due to the real reinforcement effect of clays [152]. It is also suggested by Modesti *et al.* [144] and Lai *et al.* [153] that obvious increment in storage modulus values probably results from the better dispersion of the clay in the presence of the compatibiliser. From Table 4.6, the addition of 2 *wt%* of MAPP increased the $E'_{-100°C}$ values of the nanocomposites by about 31% from 4.10 GPa for uncompatibilised PP/NCUT6 to 5.38 GPa. However, further addition of 5 *wt%* and 8 *wt%* of MAPP resulted in a lower magnitude of increment in $E'_{-100°C}$, i.e. to 5.15 GPa and 5.06 GPa, respectively. The $E'_{25°C}$ values showed a similar trend as observed for $E'_{-100°C}$. The improvement of about 44% in the $E'_{25°C}$ was calculated from 1.33 GPa for uncompatibilised PP/NCUT6 to 1.91 GPa, with the incorporation of 2 *wt%* of MAPP.

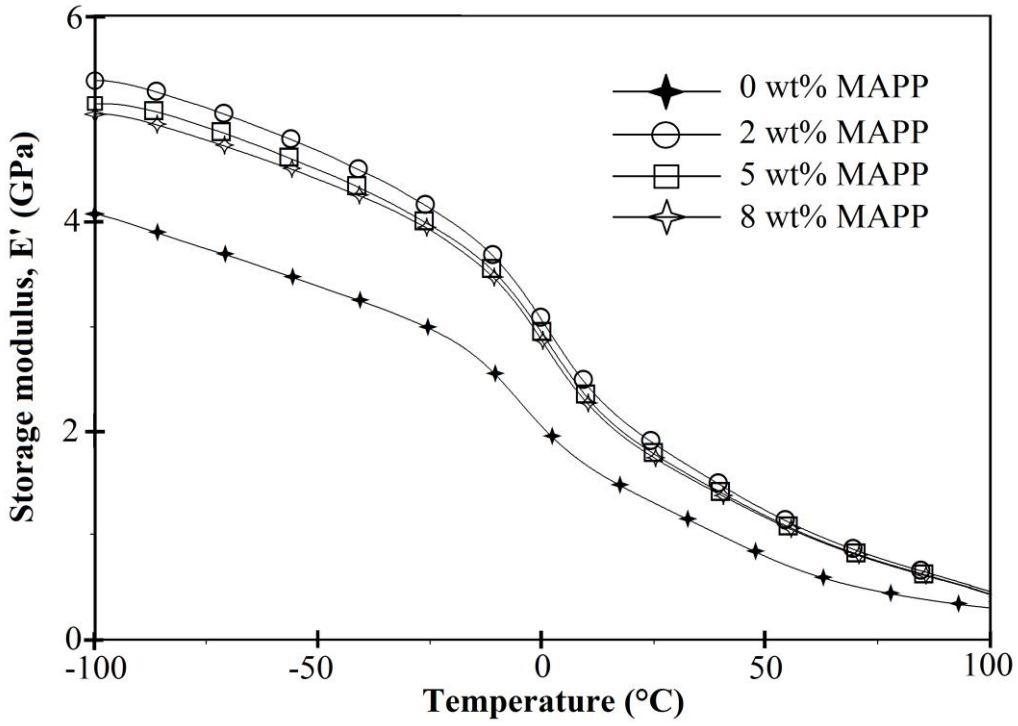

Figure 4.40: The storage modulus curves of PP/NCUT6 nanocomposites with different MAPP contents

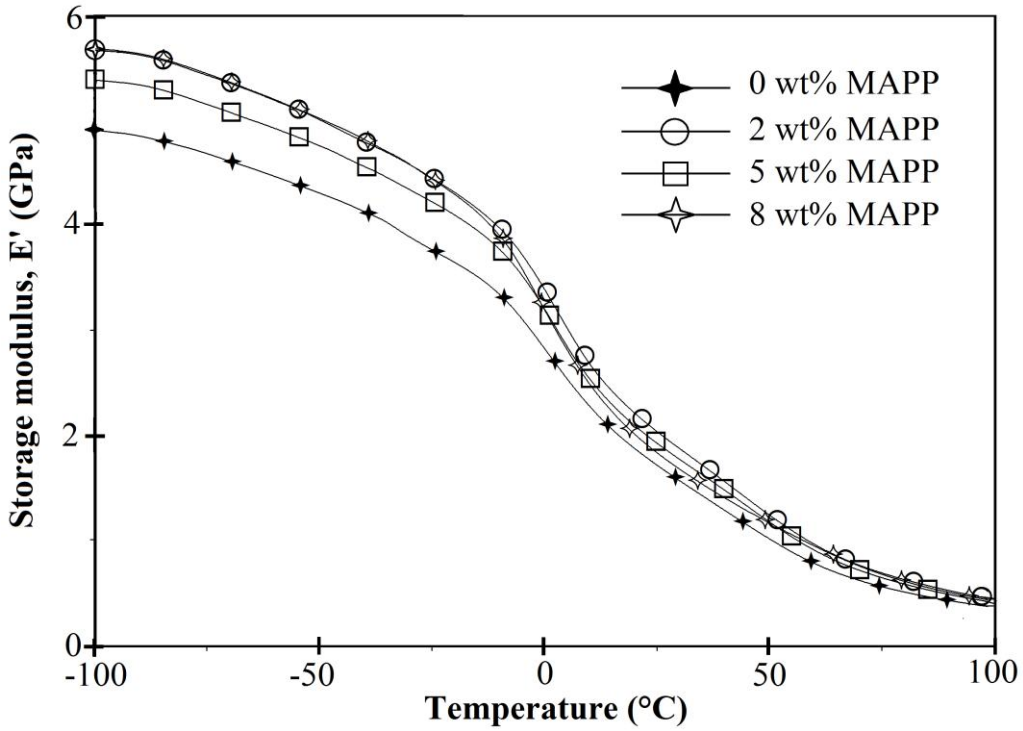

Figure 4.41: The storage modulus curves of PP/NCST2 nanocomposites with different MAPP contents

Figure 4.41 shows the storage modulus (*E'*) curves obtained for PP/NCST2 nanocomposites with variation in MAPP loading, from 0 *wt%* to 8 *wt%*. From Table 4.6, the $E'_{-100°C}$ of nanocomposites increased from 4.88 GPa for uncompatibilised PP/NCST2 to 5.65 GPa with the addition of 2 *wt%* of MAPP. Further addition of 5 *wt%* of MAPP resulted in a lower magnitude of increment in $E'_{-100°C}$ to 5.36 GPa, while the addition of 8 *wt%* of MAPP increased this value to 5.66 GPa. Generally, the presence of MAPP in the treated PP/NCST2 nanocomposite showed a similar effect towards the $E'_{-100°C}$ and $E'_{25°C}$ values, as observed in PP/NCUT6 nanocomposites. However, with the addition of compatibiliser, a more obvious increment was obtained in the treated clay when compared with untreated clay composites. As mentioned in the previous section, the penetration of polymer into the nanoclay layers was presumably easier in the presence of surfactant in the treated nanoclay. It has been suggested that favourable bonding created between surfactant of clay, MAPP and PP matrix itself, was responsible for the improvement observed [142].

4.6.1.2 Glass fibre composites

Variation of storage modulus (*E'*) as a function of temperature for virgin PP and composites with 15 *wt%* to 45 *wt%* of glass fibre loading is graphically represented in Figure 4.42. It is evident from this figure that there was a notable increase in the modulus of PP matrix with incorporation of glass fibres. This is probably due to the increase in the stiffness of the matrix, from the reinforcing effect imparted by the fibres, which allows greater degree of stress transfer at the interface [154]. The $E'_{-100°C}$ value of the composite increased from 4.06 GPa for PP to 6.36 GPa, 8.72 GPa and 11.89 GPa, for composites with 15 *wt%*, 30 *wt%* and 45 *wt%* of glass fibre, respectively (Table 4.6). The same trend was observed for the $E'_{25°C}$ value of the composites at 25°C.

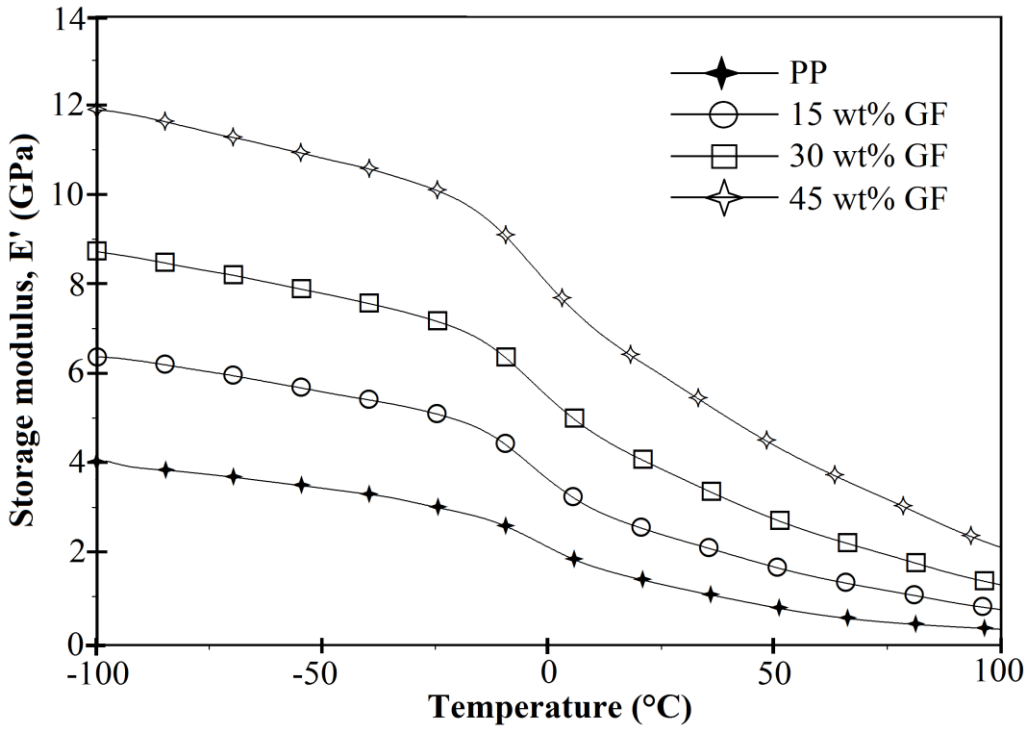

Figure 4.42: The storage modulus curves of glass fibre composites

Figure 4.43 shows the effect of extrusion screw speeds from 50 rpm to 150 rpm on the storage modulus of PP/G15 composite. From Table 4.6, it is evident that the *E'* values were influenced by the screw speed. Composite processed with 50 rpm screw

speed exhibited $E'_{-100^{o}C}$ value of 6.49 GPa. By using 100 rpm processing screw speed, the $E'_{-100^{o}C}$ of the composite was enhanced to 6.73 GPa. It can be suggested that higher screw speed provided higher shear stress to the polymer melts, hence resulted in better dispersion of the glass fibre in the PP matrix. Even though it has been proved from previous section (Figures 4.3 – 4.6, Table 4.2) that composites processed with higher screw speed will have the tendency for lower average fibre length, which can affect the properties of the material, this negative effect may be compensated for, by the improvement in the composite homogeneity [155]. By contrast, the composite processed with a high screw speed at 150 rpm showed a lower magnitude of increment in $E'_{-100^{o}C}$ value to 6.70 GPa. As discussed earlier in FLD section (Table 4.1), the composite processed with 150 rpm showed the least value in the fibre length measurement, when compared with composites compounded with 50 rpm and 100 rpm screw speeds. At this stage, it is possible that the effect of fibre length becomes a prominent factor, rather than materials dispersion.

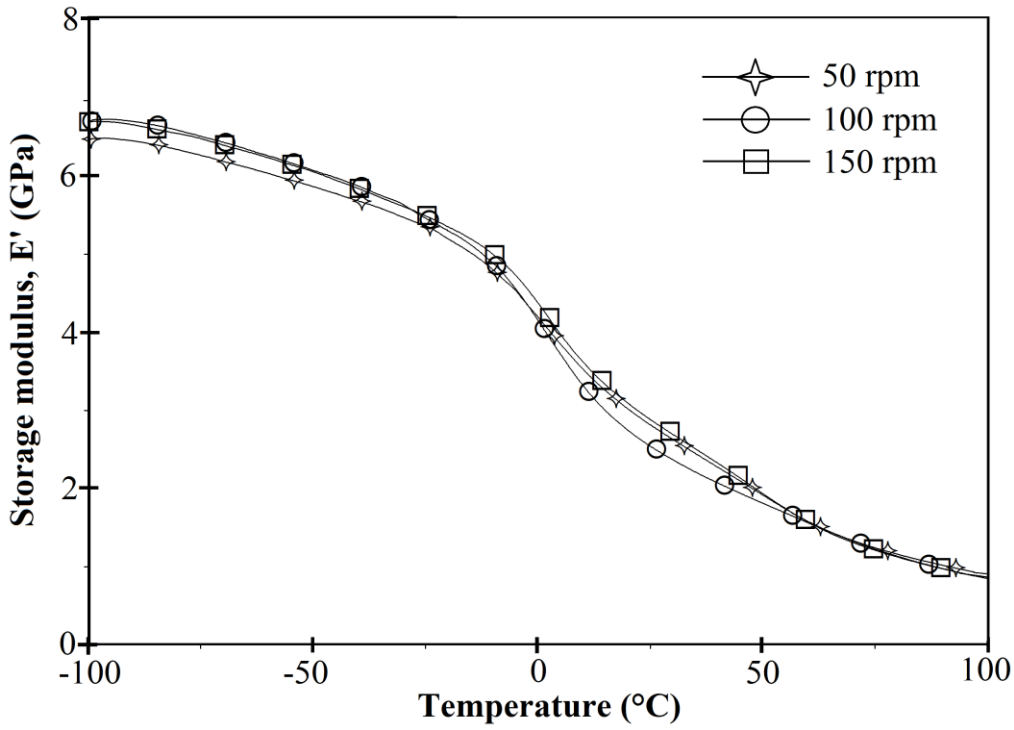

Figure 4.43: The storage modulus curves of glass fibre composites at different screw speeds

The incorporation of 15 *wt%* glass fibre into PP matrix greatly increased the value of $E'_{-100^{o}C}$ to 6.36 GPa. The addition of 2 *wt%*, 5 *wt%* and 8 *wt%* of MAPP to the composite further increased the *E′* value of hybrid composite to 6.90 GPa, 6.88 GPa and 6.86 GPa, respectively (Table 4.6 and Figure 4.44). It is suggested that the interfacial adhesion between the glass fibre and the PP matrix is enhanced by the presence of compatibiliser in the composite system [10]. The strong bonding created between the surface of the glass fibre and PP matrix resulted in a more rigid material and consequently reduced the flexibility of the composites and thus improved the storage modulus value. The $E'_{25^{o}C}$ also follow of the same trend, as observed for $E'_{-100^{o}C}$.

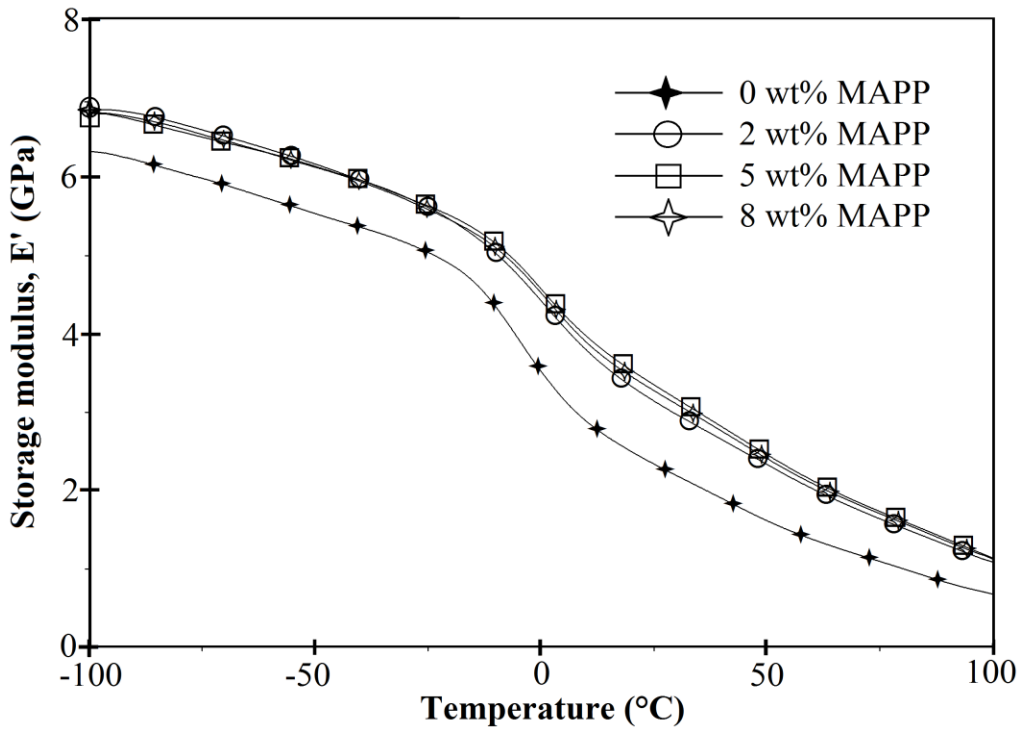

Figure 4.44: The storage modulus curves of PP/GF15 composites with different MAPP contents

4.6.1.3 Glass fibre/nanoclay hybrid composites

As mentioned in the earlier section, the PP/G15 composite has its $E'_{-100^{o}C}$ value of 6.36 GPa, which is significantly higher than the PP matrix (4.06 GPa) (Table 4.6).

The incorporation of NC into PP/GF system further enhanced this property. The $E'_{-100^{o}C}$ values of hybrid composites increased to 6.65 GPa and 7.04 GPa respectively, as 6 phr and 9 phr of untreated clay were added to the PP/G15 composite system. This improvement may be attributed mainly, to the enhancement of the matrix modulus resulting from the particulate filler dispersion. Thus, a synergistic effect did take place by incorporating particulate filler in the polymer matrix, leading to higher stiffness than would otherwise be expected, due solely to the change of the matrix modulus. In addition, this behaviour can be attributed to the constraining effect of clay layers on the molecular motion of the polymer chain, which is also dependent on the clay aspect ratio and the clay dispersion [156]. In contrast, as similarly observed in the PP/NC composites (Figure 4.37), the addition of 3 phr of clay to the composite registered a slight decrement of about 4% (6.08 GPa) in the $E'_{-100^{o}C}$, relative to PP/G15 composite over the whole temperature range. Thus, at low content, the clay only gave a negative effect, as filler for the hybrid system.

Appendices 4.12 and 4.13 show the effect of NC content on the PP/G30/NCUT and PP/G45/NCUT hybrid composite systems. The $E'_{-100^{o}C}$ was significantly reduced from 8.72 GPa for PP/G30 to 8.31 GPa with the addition of 3 phr of NC to the system. Incorporation of 6 phr and 9 phr of NC increased this value to 8.52 GPa and 8.71 GPa, respectively (Table 4.6). A similar trend was obtained for the PP/G45 hybrid composites system. Meanwhile, the presence of NC in the PP/G30 and PP/G45 composites further increased the $E'_{25^{o}C}$ values, except for 3 phr of NC content. At low clay loading (3 phr), the $E'_{25^{o}C}$ values for the PP/G30 and PP/G45 composites reduced from 3.85 GPa to 3.66 GPa and from 5.97 GPa to 5.67 GPa, respectively, when compared with composite without clay content. By contrast, as the clay loading increased to 6 phr and 9 phr, a noticeable increment in this value was obtained, for both

systems. From Appendices 4.12 and 4.13, it is obvious that the synergistic effect of the addition of NC can only be observed at a high temperature range.

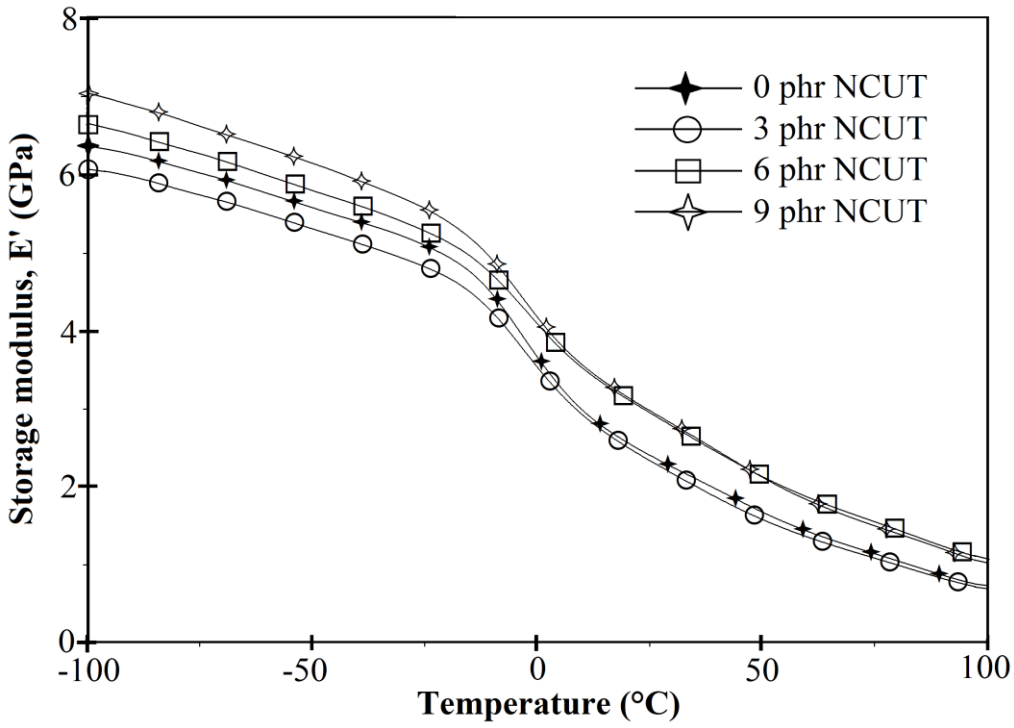

Figure 4.45: The storage modulus curves of PP/G15 hybrid composites with different NCUT contents

The storage modulus curves of PP/G15 hybrid composites, with untreated and treated clay, compatibilised with 5 *wt%* of MAPP are presented in Figure 4.46. On the addition of 6 phr untreated clay, an increment in the $E'_{-100^{o}C}$ of about 5% from 6.88 GPa for (PP:C5)/G15 composite to 7.21 GPa for (PP:C5)/G15/NCUT6 hybrid composite was observed (Table 4.6). Meanwhile, the addition of 2 phr of treated clay in the PP/G15 composite resulted in a high increment (9%) in this value, to 7.52 GPa. This improvement was due to the stiffer matrix (in this case, (PP:C5)/NCST2 nanocomposite) used to prepare the hybrid composites, (PP:C5)/G15/NCST2, when compared with (PP:C5)/NCUT6 nanocomposites, which was the matrix used to prepare (PP:C5)/G15/NCUT6 hybrid composite. As previously discussed, the $E'_{-100^{o}C}$ value for (PP:C5)/NCUT6 nanocomposites was 5.15 GPa, where as for (PP:C5)/NCST2, the

value was 5.36 GPa. The large increment in the $E'_{-100^{o}C}$ value in the hybrid system containing treated clay implies that a combination of glass fibre and treated nanoclay gave a better synergistic effect on the dynamic mechanical properties of the hybrid nanocomposite. This is due to the reduction in the material flexibility which resulted from the enhancement of the interfacial bonding between the matrix and fillers that the treated hybrid composites experienced. The $E'_{25^{o}C}$ values showed a similar trend, as observed for $E'_{-100^{o}C}$.

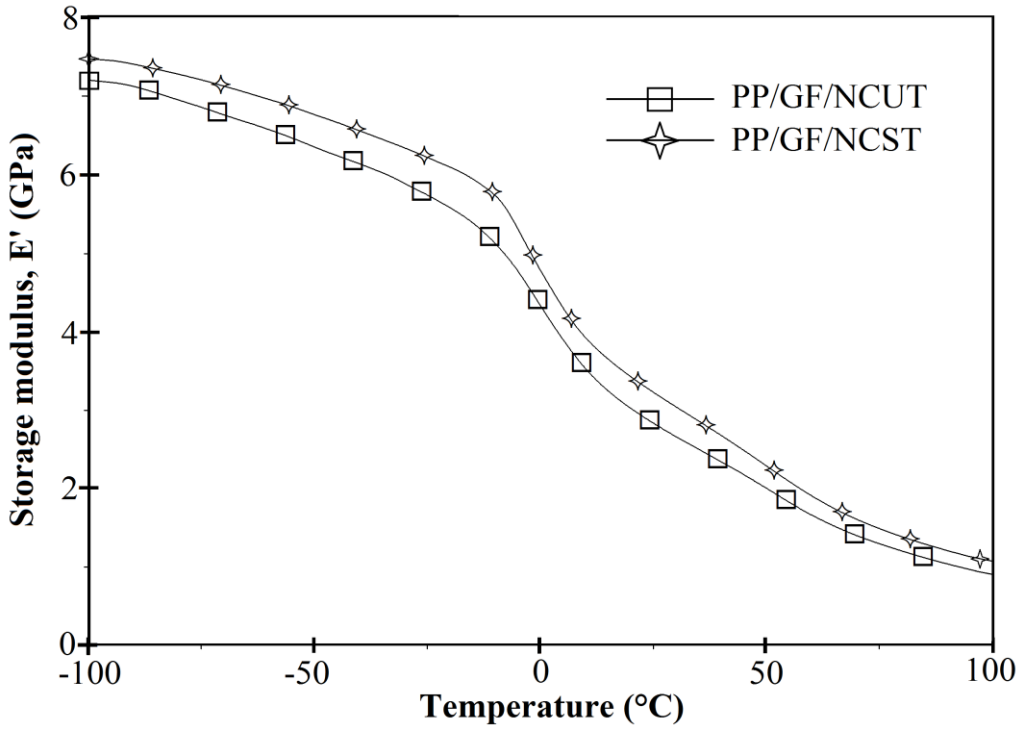

Figure 4.46: The storage modulus curves of (PP:C5)/G15 hybrid composites with treated and untreated nanoclays

Figure 4.47 shows the storage modulus (*E'*) curves obtained for PP/G15/NCUT6 hybrid composites with variation in MAPP loading, from 0 *wt%* to 8 *wt%*. Generally, the compatibilised hybrid composites displayed improved *E'* values throughout the experimental temperature range, following the same trend as previously observed for PP/NC and PP/GF composites. The $E'_{-100^{o}C}$ of PP/G15/NCUT6 hybrid composite

increased by about 12% from 6.65 GPa for uncompatibilised system to 7.42 GPa with the addition of 2 *wt%* of MAPP. On the other hand, the addition of 5 *wt%* and 8 *wt%* of MAPP resulted in a low magnitudes of increments in $E'_{-100^{o}C}$ to 7.21 GPa and 6.98 GPa, respectively (Table 4.6). The $E'_{25^{o}C}$ values showed a similar trend, as observed for $E'_{-100^{o}C}$.

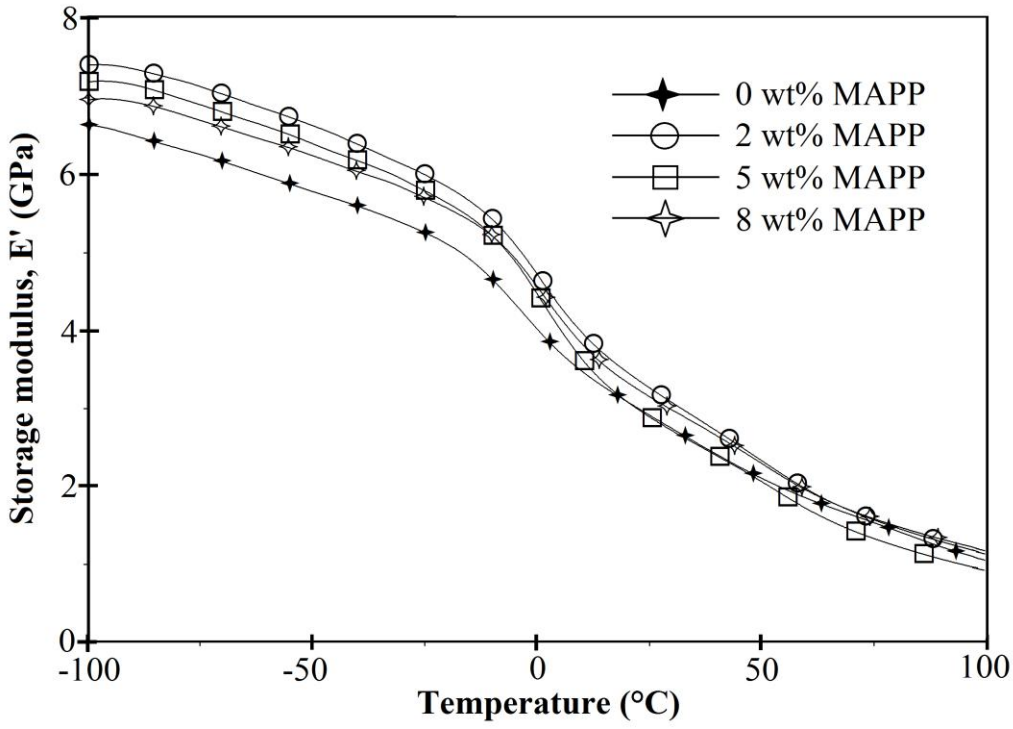

Figure 4.47: The storage modulus curves of PP/G15/NCUT6 hybrid composites with different MAPP contents

By analyzing the storage modulus (*E'*) curves for PP/G15/NCST2 hybrid composites in Appendix 4.14, a significant improvement in *E'* values can be observed, which indicated that the *E'* was significantly affected by the presence of compatibiliser. The $E'_{-100^{o}C}$ of PP/G15/NCST2 hybrid composite increased to 7.36 GPa and 7.52 GPa, with the addition of 2 *wt%* and 5 *wt%* of MAPP, respectively. However, the addition of 8 *wt%* of MAPP resulted in a lower magnitude of increment in this value to 7.45 GPa (Table 4.6). Meanwhile, the $E'_{25^{o}C}$ values of hybrid composites showed a different trend

with the addition of MAPP to the system. The presence of 2 *wt%* of MAPP gives the highest $E'_{25°C}$ value, meanwhile further addition of 5 *wt%* and 8 *wt%* of MAPP result in a slight decrement in this value to 3.31 GPa and 3.36 GPa, respectively.

4.6.2 Loss modulus (*E″*)

The loss modulus (*E″*) is defined as the amount of energy dissipated or lost as heat per cycle of sinusoidal deformation, when different systems are compared at the same strain amplitude. It is the viscous response of the material. The loss modulus is most sensitive to the molecular motions [151]. The variation of *E″* as a function of temperature for virgin PP, PP/NC, PP/GF and PP/GF/NC composites is graphically illustrated in Figures 4.48 – 4.56. Samal *et al.* [88] reported that PP exhibits three transition peaks (*α, β* and *γ*) at different temperatures within the investigated temperature range (–150°C to 150°C). The *γ*-transition at around –100°C is related to the relaxation of the amorphous propylene segments of the PP chain. However, within the temperature range studied, the *β*– and *γ*–transition peaks of the matrix polymer are not detected. The *α*–transition is due to the glass transition temperature (T_g) in the range of –10°C to 10°C and is associated with the motion of the long chain segments in the amorphous region of the PP. In this study, the *α*–transition peak of the matrix was observed at around –3°C (Table 4.6). In this work, $T_\alpha^{E"}$ is referred to as the temperature at the maximum value of loss modulus in the *α*–transition region, while the E''_{max} and $E''_{25°C}$ are the maximum magnitude of loss modulus at $T_\alpha^{E"}$ and at 25°C, respectively.

4.6.2.1 Clay nanocomposites

The $T_\alpha^{E"}$ for PP matrix appeared at –2.3°C. As observed in Figure 4.48 and Table 4.6, the addition of 3 phr and 6 phr of clay in the PP matrix reduced the $T_\alpha^{E"}$

values to –2.6°C and –3.5°C, respectively (Table 4.6). The addition of 9 phr clay results in an increment of this value to –1.5°C. Generally, the E''_{max} values for the all PP/NC nanocomposites are lower than that of the PP matrix. The incorporation of 3 phr of untreated clay reduced the E''_{max} from 140.2 MPa for PP matrix to 123.2 MPa for the PP/NCUT3. On the other hand, an increment in these values to 126.9 MPa and 133.0 MPa were obtained on the addition of 6 phr and 9 phr of clay, respectively, indicating a reduction in material flexibility. A similar trend was observed for $E''_{25°C}$.

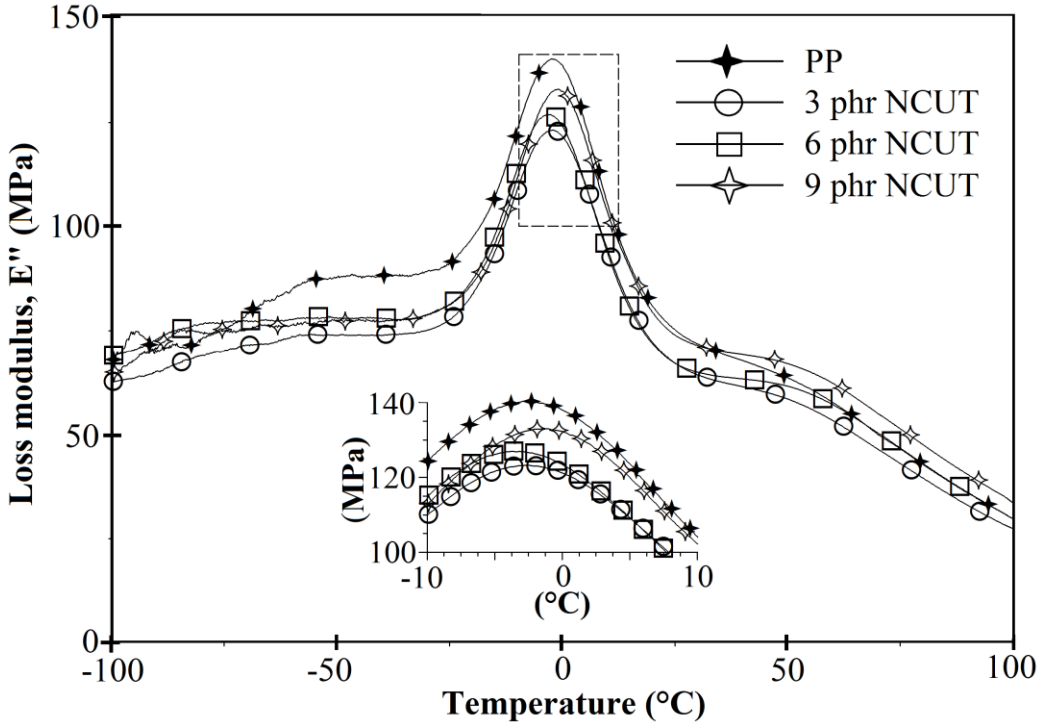

Figure 4.48: The loss modulus curves of clay nanocomposites

The loss modulus, *E''* curves of PP nanocomposites, with untreated and treated clay are presented in Figure 4.49. The addition of 6 phr untreated clay in the PP matrix slightly shifted the $T_\alpha^{E''}$ to a lower temperature, from –2.3°C for PP to –3.5°C. By contrast, with the addition of 2 phr of treated clay, the $T_\alpha^{E''}$ shifted to higher temperature (1.5°C) indicating a more rigid material was obtained. Meanwhile, E''_{max} values

observed for the PP/NCST2 nanocomposites was 153.6 MPa, which is 21% higher compared with PP/NCUT6 nanocomposites (126.9 MPa). It should be noted that the increment in the E''_{max} value indicated an enhancement in the stiffness of the material. It has already been discussed in the storage modulus section that the presence of surfactant in treated nanoclay improved the nanoclay dispersion in the PP matrix and at the same time reduced the flexibility of the composite, hence it resulted in a stiffer material relative to the untreated clay nanocomposite. A similar trend was observed for $E''_{25°C}$. From Table 4.6, an increment of about 37% from 66.9 MPa for PP/NCUT6 nanocomposite to 91.6 MPa for PP/NCST2 nanocomposite was observed.

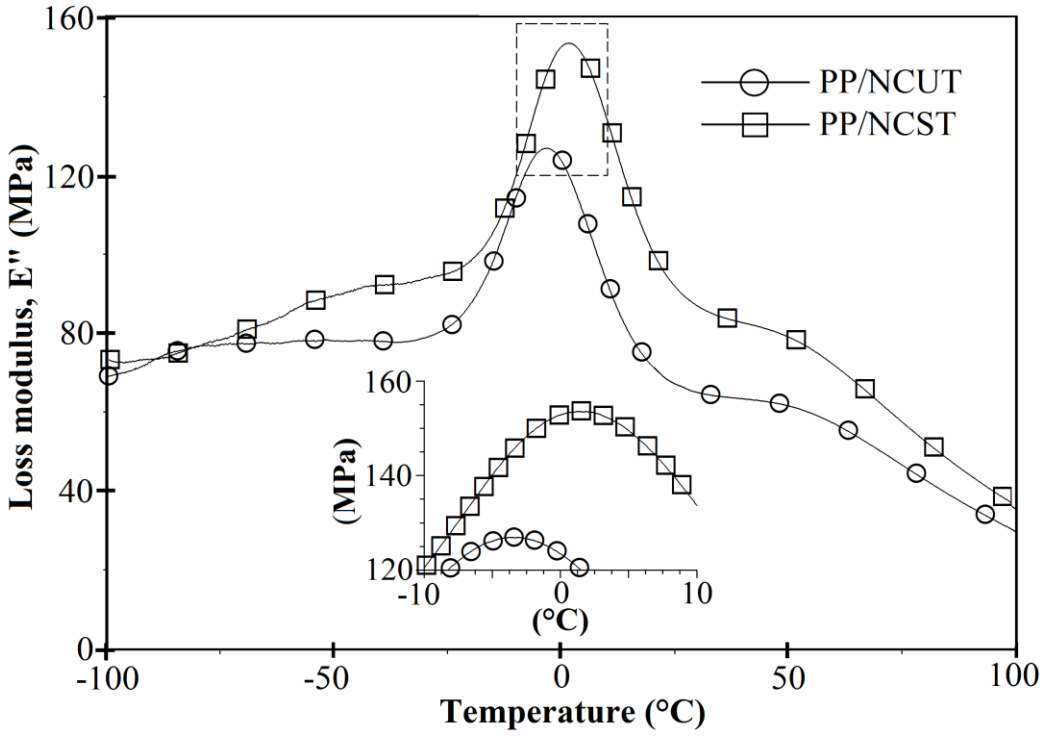

Figure 4.49: The loss modulus curves of nanocomposites with untreated and treated nanoclays

The loss modulus (E'') curves of PP/NCST2 nanocomposites obtained with different processing screw speeds varying from 100 rpm to 800 rpm are shown in Appendix 4.15. A slight reduction in the $T_{\alpha}^{E''}$ value is observed with the increment in

the processing screw speed. This value reduced from 2.9°C to 1.7°C as the screw speed increased from 100 rpm to 800 rpm. On the other hand, the E''_{max} values generally increased proportionately with increase in the processing screw speed from 148.6 MPa for the material compounded with 100 rpm to 169.7 MPa for material compounded with 500 rpm (Table 4.6). It can be deduced that higher processing screw speed was required to create higher shear stress in the polymer melts, in order to provide a favourable medium for better clay dispersion. However, as the screw speed increased to 800 rpm, this value reduced to 163.4 MPa.

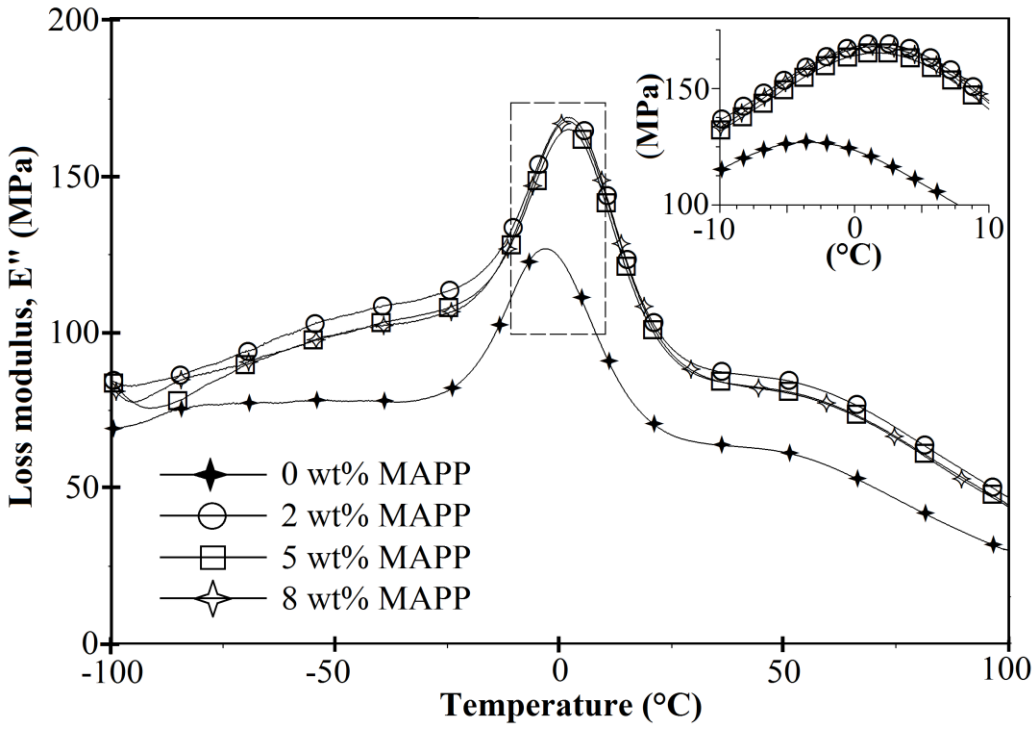

Figure 4.50: The loss modulus curves of PP/NCUT6 nanocomposites with different MAPP contents

Figure 4.50 shows the loss modulus (*E″*) curves obtained for PP/NCUT6 nanocomposites with variation in MAPP loading, from 0 *wt%* to 8 *wt%*. It is evident from this figure, that there was a significant increase in the $T_{\alpha}^{E''}$ values, from –3.5°C for uncompatibilised PP/NCUT6 to 1.7°C with the addition of 2 *wt%* of MAPP (Table 4.6). No significant change was observed with the addition of 5 *wt%* and 8 *wt%* of MAPP.

The increment in $T_{\alpha}^{E"}$ indicated a more rigid material was produced. This may be attributed to the presence of MAPP which improved the interfacial adhesion between PP and nanoclay, thus resulted in a reduction in the crystal's mobility in the amorphous phase of the PP matrix. Contrary to expectations, the E''_{max} value obtained for composite compatibilised with 2 *wt%* of MAPP increased by about 33% from 126.9 MPa to 169 MPa. However, a slight reduction in this value to 165.2 MPa was observed as the MAPP content increased to 5 wt%. This drop seems to indicate an improvement in the fibre/matrix interphase.

The loss modulus (E'') curves obtained for PP/NCST2 nanocomposites with variation in MAPP loading, from 0 *wt%* to 8 *wt%* is shown in Appendix 4.16. The addition of 2 *wt%* of MAPP in the nanocomposites increased the $T_{\alpha}^{E"}$ value from 1.5°C for uncompatibilised PP/NCST2 to 2.9°C (Table 4.6). However, as the MAPP content increased to 5 *wt%* and 8 *wt%*, the increment in this value was less obvious. A noticeable increment was observed in the E''_{max} values with the addition of MAPP. The maximum value of E''_{max} was obtained for PP/NCST2 compatibilised with 8 *wt%* of MAPP. This behaviour is attributed to the migration of excess MAPP around the clay particles, resulting in self entanglement among themselves, rather than the matrix [157]. The same trend was observed for $E''_{25°C}$.

4.6.2.2 Glass fibre composites

The loss modulus, E'' curves for PP matrix and composites at different glass fibre loading are shown in Figure 4.51. The addition of glass fibres in the PP matrix showed insignificant changes in the $T_{\alpha}^{E"}$ value, relative to the neat PP. By contrast, the E''_{max} values for the PP/GF composites are higher when compared to PP matrix. The E''_{max} value recorded for PP matrix was 140.2 MPa and increased to 226.2 MPa (61%),

287.5 MPa (105%) and 376.9 MPa (168%) with the addition of 15 *wt%*, 30 *wt%* and 45 *wt%* of glass fibre, respectively (Table 4.6). The higher E''_{max} value was due to the presence of glass fibres which reduced the flexibility of the material by introducing constraints on the segmental mobility of the polymer chains at the relaxation temperature. Moreover, broadening of the transition region is observed in all PP/GF composites system, indicating a segmental immobilization of matrix chain [147]. A similar trend was observed for $E''_{25°C}$ with a more profound increment. Increments of about 68%, 162% and 286% relative to PP matrix (74.9 MPa) were obtained with the incorporation of 15 *wt%*, 30 *wt%* and 45 *wt%* of glass fibre, respectively (Table 4.6).

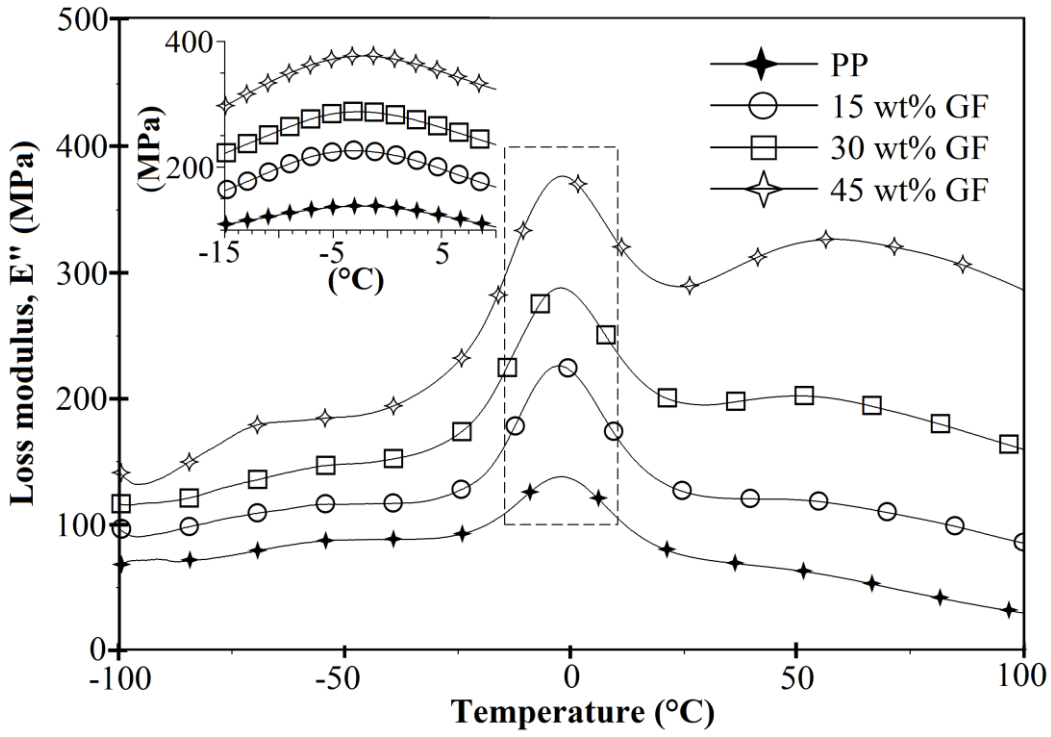

Figure 4.51: The loss modulus curves of glass fibre composites

Figure 4.52 shows the effect of the different processing screw speeds from 50 rpm to 150 rpm on the loss modulus of PP/G15 composites. No significant change was observed in the $T_{\alpha}^{E''}$. Composite processed with 50 rpm screw speed showed an E''_{max} value of 190.4 MPa. Meanwhile, by using 100 rpm processing screw speed, the E''_{max} of

the composite was enhanced to 241.6 MPa. It is possible that higher screw speed resulted in a better dispersion of the glass fibre in the PP matrix, hence increasing the stiffness of the material. On the other hand, composite processed with higher screw speed of 150 rpm, showed a slight decrement in E''_{max} value (199.6 MPa). It has been mentioned earlier in the FLD section (Table 4.1), that composites compounded with the highest screw speed (800 rpm) experienced fibre breakage more than composites compounded with lower screw speed. The reduction in the fibre length might have affected the function of glass fibre as a strengthening agent for the PP matrix. It is clear that for this particular composition, the use of 100 rpm screw speed was apparently the optimum parameter for material processing, in order to produce composites with good dynamic mechanical properties.

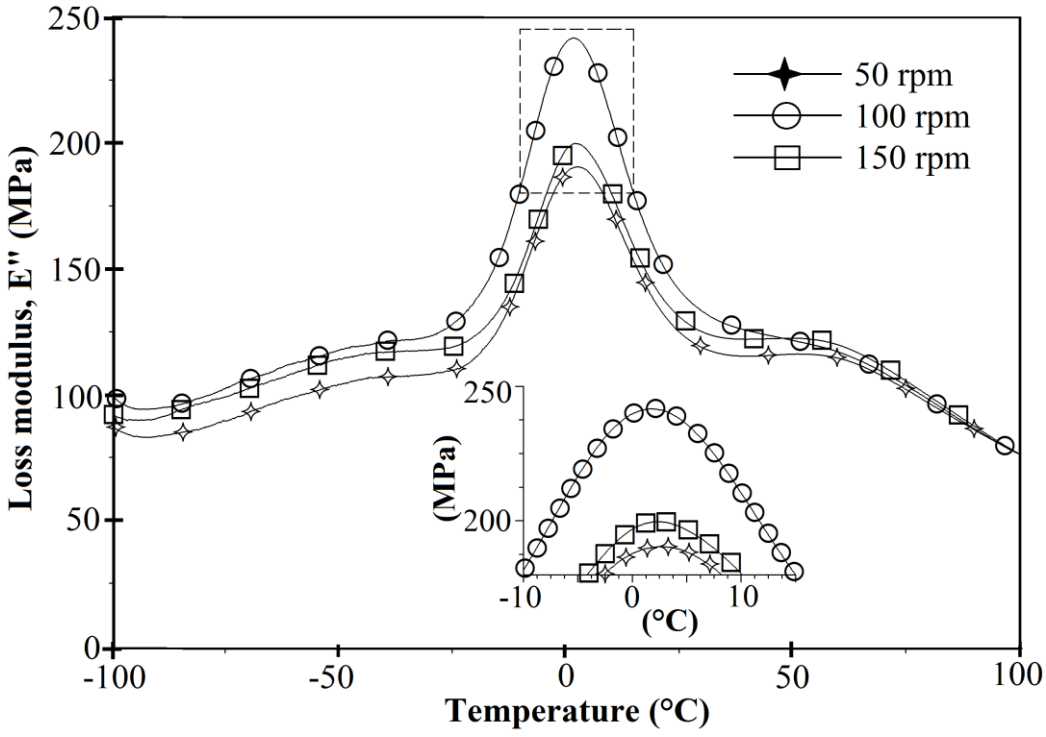

Figure 4.52: The loss modulus curves of glass fibre composites at different screw speeds

Figure 4.53 shows the effect of MAPP content on the loss modulus of glass fibre composites. The $T_{\alpha}^{E''}$ values of the compatibilised composites shifted to higher

temperature from -2.3°C for PP matrix and -2.9°C for uncompatibilised PP/G15 to 1.2°C with the presence of 2 *wt%* of MAPP and 1.1°C for 5 *wt%* and 8 *wt%* of MAPP. This is probably due to the restricted segmental motion of the amorphous PP chains at the fibre–matrix interface resulting in a more rigid material [147]. Meanwhile, the value of $E''_{25°C}$ for composite compatibilised with 2 wt% of MAPP showed only a slight increment (126.6 MPa) when compared with uncompatibilised composite (125.6 MPa). However, as the MAPP content increased to *5 wt%* and 8 *wt%*, this value reduced to 120.4 MPa and 119.7 MPa, respectively, indicating an improvement in the material compatibility. The same trend was observed by Nayak and Mohanty [147].

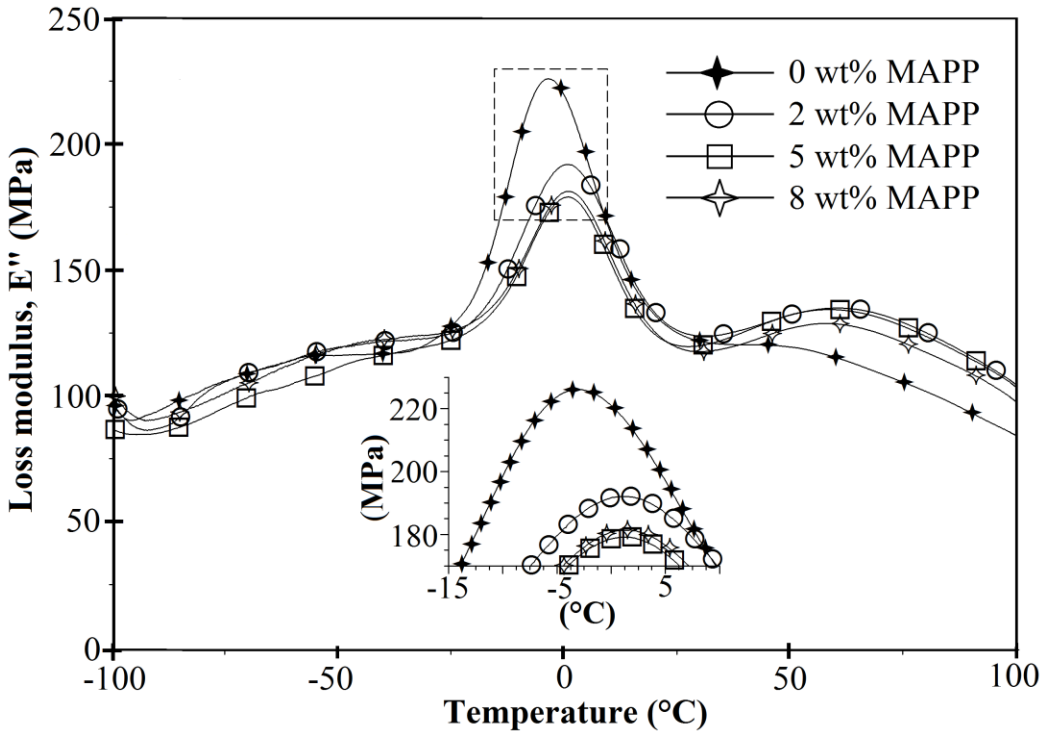

Figure 4.53: The loss modulus curves of PP/GF15 composites with different MAPP contents

4.6.2.3 Glass fibre/nanoclay hybrid composites

Figure 4.54 shows the effect of nanoclay hybridisation on the loss modulus of PP/GF composites. The $T_{\alpha}^{E''}$ value shifted to a lower temperature as the amount of clay in the hybrid composites increased. This value reduced from -2.9°C for PP/G15 to -

3.2°C, -3.3°C and -4.1°C with the presence of 3 phr, 6 phr and 9 phr of nanoclay, respectively (Table 4.6). This phenomenon indicates increased mobility of the amorphous part in the hybrid composites at lower temperature, relative to glass fibre composite system [15].

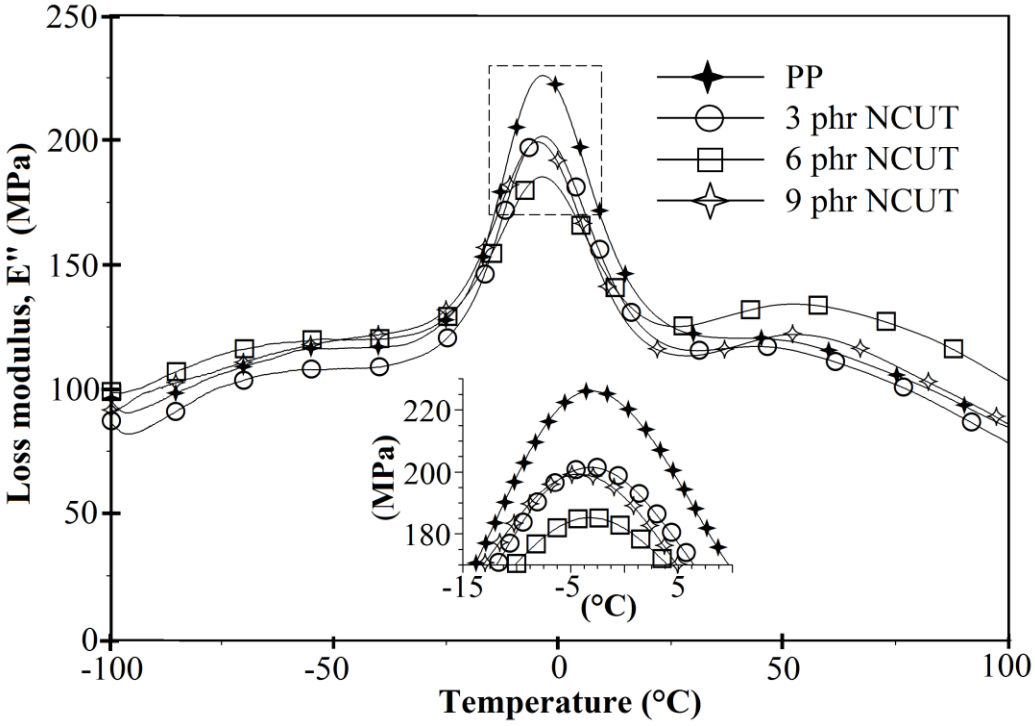

Figure 4.54: The loss modulus curves of PP/G15 hybrid composites with different NCUT contents

The E''_{max} value decreased, generally, with nanoclay loading, which is an indication of improvement of filler–matrix interface. The addition of 6 phr of clay to PP/G15 hybrid composite showed the highest reduction of about 18% in this value, from 226.1 MPa for PP/G15 composite to 185.2 MPa. For PP/G30/NCUT and PP/G45/NCUT hybrid composites system, the effect of clay hybridization was more pronounced (See Appendices 4.17 and 4.18). Higher reductions of E''_{max} values (up to 21%) were obtained as 9 phr of clay was added into the PP/G30 and PP/G45 hybrid composites system.

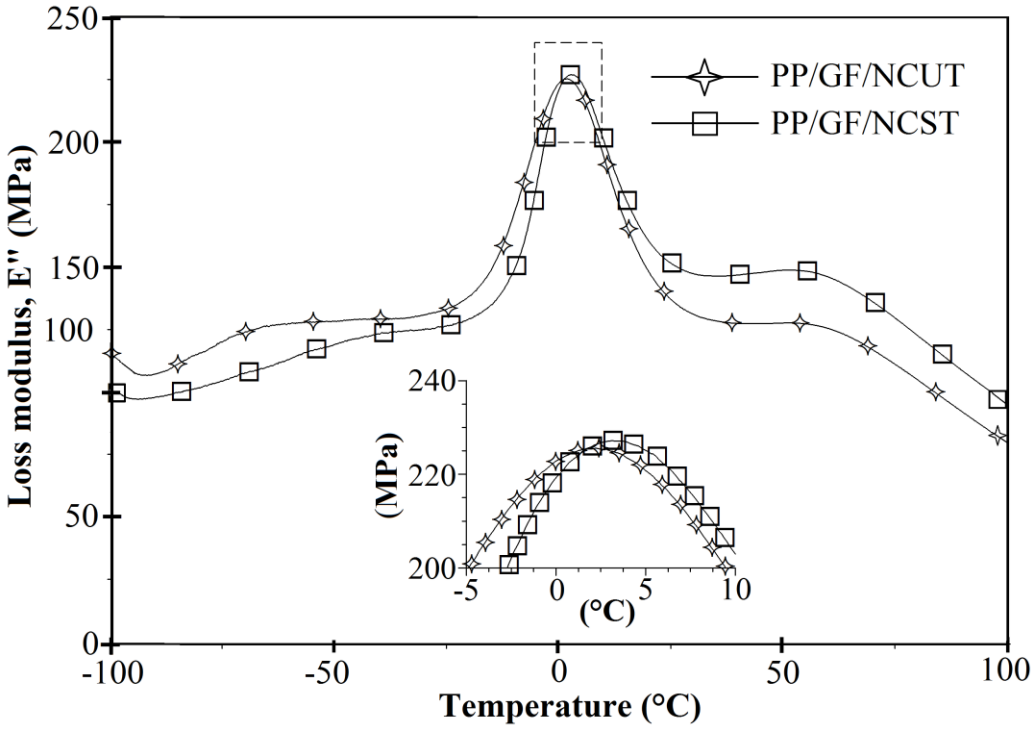

Figure 4.55: The loss modulus curves of (PP:C5)/G15 hybrid composites with treated and untreated nanoclays

The loss modulus curves of (PP:C5)/G15 hybrid composites, with untreated and treated clay are presented in Figure 4.55. The addition of 6 phr untreated clay in the composite slightly shifted the $T_{\alpha}^{E"}$ to a higher temperature, from 1.1°C for (PP:C5)/G15 to 2.0°C. As 2 phr of treated clay was added, the $T_{\alpha}^{E"}$ value further increased to 3.1°C (Table 4.6). The E''_{max} of hybrid composites showed identical value, irrespective the type of clay used. On the other hand, the $E''_{25°C}$ value in the hybrid system was significantly affected at room temperature. An increment of about 15% and 26% were observed for (PP:C5)/G15/NCUT6 and (PP:C5)/G15/NCST2, respectively, relative to (PP:C5)/G15 composite (120.4 MPa), indicating a reduction in the flexibility of the material. This result implies that a stiffer hybrid system was produced with the addition of treated clay when compared with untreated clay.

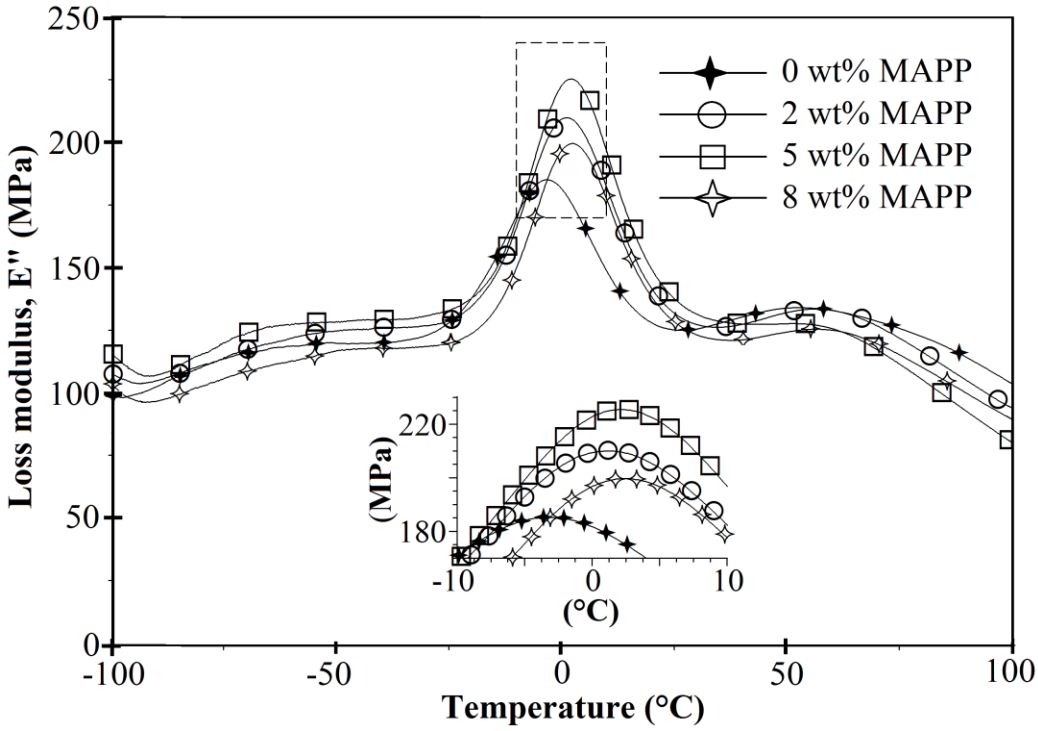

Figure 4.56: The loss modulus curves of PP/G15/NCUT6 hybrid composites with different MAPP contents

Figure 4.56 shows the loss modulus (E'') curves obtained for PP/G15/NCUT6 hybrid composites with variation in MAPP loading, from 0 *wt%* to 8 *wt%*. Generally, the compatibilised hybrid composites displayed improved E'' values throughout the experimental temperature range. The addition of MAPP shifted the $T_{\alpha}^{E''}$ value of hybrid composites to higher temperature from –3.3°C for uncompatibilised PP/G15/NCUT6 to 1.1°C, 2.0°C and 2.3°C with the presence of 2 *wt%*, 5 *wt%* and 8 *wt%*, respectively (Table 4.6). The increment in $T_{\alpha}^{E''}$ is attributed to the presence of MAPP which restricted the mobility of polymer chains in the hybrid system. This is also in line with the trend previously observed for PP/NC and PP/GF composites. Contrary to expectations, the E''_{max} value increased generally with MAPP loading. The maximum value was obtained with the addition of 5 *wt%* of MAPP (225.5 MPa). However, further addition of 8 *wt%* of MAPP resulted in a decrement in this value to 199.7 MPa, indicating an improvement in the filler/matrix interphase.

From Appendix 4.19, PP/G15/NCST2 hybrid composites with the addition of 8 *wt%* of MAPP was observed to have the highest $T_{\alpha}^{E''}$ value (3.9°C) relative to the hybrid nanocomposites compatibilised with 2 *wt%* and 5 *wt%* of MAPP. Meanwhile, as similarly observed for the untreated hybrid nanocomposites, the maximum E''_{max} value was obtained with the addition of 5 *wt%* of MAPP (227.2MPa) (Table 4.6). Again, further addition of 8 *wt%* of MAPP also results in a decrement in this value to 218.4 MPa. The same trend was observed for $E''_{25°C}$.

4.6.3 Tan delta

The ratio of the loss modulus to the storage modulus (*tan δ*) is a measure of the mechanical loss or damping factor. The damping properties of the material give the balance between the elastic phase and viscous phase in a polymeric structure [10]. Since the damping peak occurs in the region of the glass transition where the material changes from a rigid to a more elastic state, it is associated with the movement of small groups and chains of molecules within the polymer structure [151]. In a composite system, damping is affected by the incorporation of fibres. This is due mainly, to stress concentration at the fibre ends in association with the additional viscoelastic energy dissipation in the matrix material. Chen *et al.* [158] reported that the *tan δ* curve of pure PP is generally related to three relaxations localised in the neighbourhood of –50°C, 10°C and 100°C. In other word, the dominant peak appearing at about 10°C is the glass rubber transition temperature of the amorphous PP molecular chains. This transition region as indicated by a damping maxima, is usually known as the *α*-transition. The weak transition appearing as a shoulder at about 100°C is associated with the crystalline regions of PP chains.

The variations of *tan δ* as a function of temperature are represented in Figures 4.57 to 4.64. The peak, which is the maximum value of *tan δ* is the *α*-transition, T_{α} is

generally known as the glass transition temperature, T_g. It is well known that the T_g of a polymer depends on the mobility of the chain segment of the macromolecules in the polymer matrix. If the molecular chain is restricted, motion or relaxation of the chain segment becomes difficult at the original glass transition temperature, but becomes easy at higher temperatures [145]. In this work, T_g is referred to as the temperature at the maximum value of *tan* δ in the α-transition region, while the *tan* δ_{max} and *tan* $\delta_{25°C}$ are the magnitudes of *tan* δ at T_g and at 25°C, respectively.

4.6.3.1 Clay nanocomposites

From Table 4.6, the T_g value recorded for PP matrix is 2.9°C. By analyzing the *tan* δ curves for clay nanocomposites (Figure 4.57), no significant difference in T_g value was observed with the addition of 3 phr of clay (2.9°C), relative to PP matrix, which indicates that T_g was not significantly affected by the presence of lower nanoclay content. The same trend has been reported by Modesti *et al.* [144]. Meanwhile, this value reduced to 1.7°C as 6 phr of clay was added to the system. By contrast, the addition of 9 phr resulted in an increment in the T_g to 3.2°C, as similarly observed by Zhang *et al.* [145]. It is suggested that when the PP molecules are intercalated in the silicate gallery and silicate layer is partially exfoliated in the PP matrix, the chain conformation of the PP molecules was not readily changed because of the geometric constraints and the interactions between the polymers chains and the surface of the silicate layers becomes stronger. Therefore, their dynamic behaviour is different from that pure PP.

On the other hand, the presence of the nanoclay reduced the *tan* δ_{max} value, from 0.067 for PP matrix to 0.062 for PP/NCUT3 nanocomposite. Further decrement in this value to 0.059 was observed as the nanoclay content increased to 6 phr and 9 phr. As mentioned earlier in DSC section (Table 4.5), the addition of nanoclay in the PP matrix

increased the degree of crystallinity, indicating a more ordered structure of the nanocomposite material. This behaviour led to the reduction of the material's flexibility, thus resulting in a decrement in the *tan* δ_{max} value, as experienced in this particular system. The *tan* $\delta_{25°C}$ values also show a similar trend.

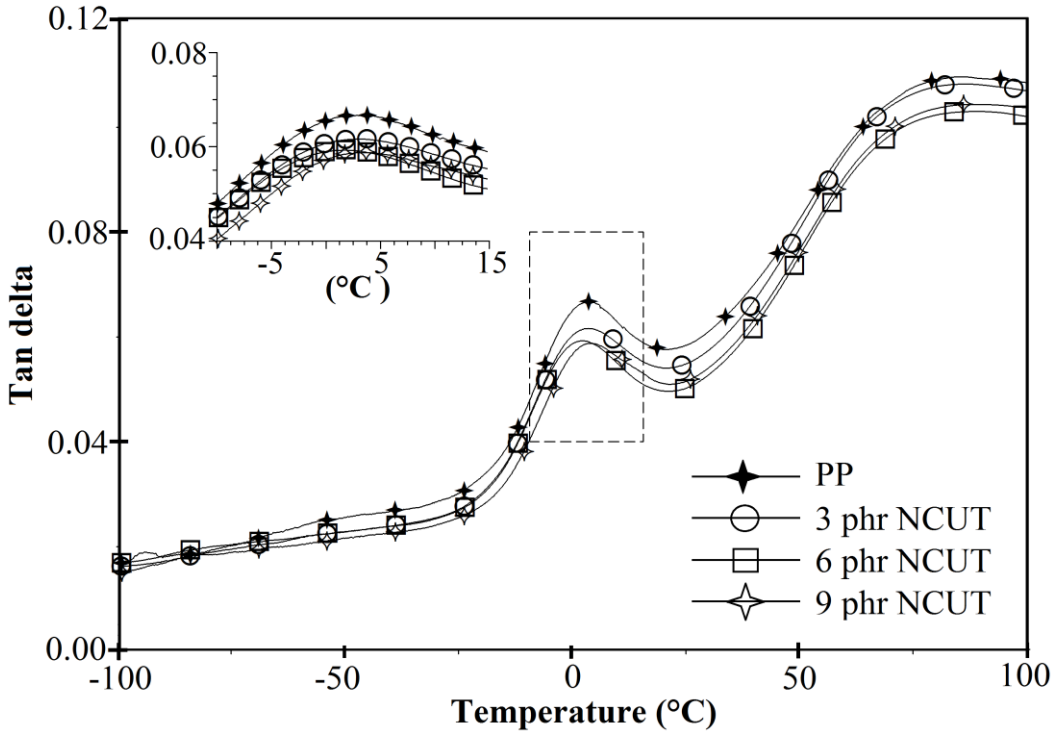

Figure 4.57: The *tan δ* curves of clay nanocomposites

The *tan* δ curves of PP nanocomposites, with untreated and treated clay are presented in Figure 4.58. The T_g value recorded for PP matrix was 2.9°C. A slight decrement in T_g value to 1.7°C was observed with the addition of 6 phr untreated clay. However, the incorporation of 2 phr of treated clay in the PP matrix resulted in a remarkable increment in this value, to 6.7°C (Table 4.6). It should be noted that the increase in the T_g value in the composites with treated clay indicated that higher energy was required for the glass transition to take place, implying a restriction in the polymer chain mobility has occurred in the PP/NCST2 nanocomposite system which resulted in reduction of material's flexibility. This is due to the better interaction or dispersion of

treated nanoclay in the polymer matrix. As discussed in the XRD section, the treated clay had a higher d-spacing value, relative to untreated clay. Therefore, it is suggested that the ability of the polymer matrix to diffuse into the nanoclay layers was increased, consequently leading to the formation of exfoliated nanocomposites. Meanwhile, the *tan* δ_{max} value remained essentially unchanged, regardless the type of clay used in the system. On the other hand, a slight increment in the *tan* $\delta_{25°C}$ from 0.050 for PP/NCUT6 to 0.054 was observed for PP/NCST2 nanocomposite (Table 4.6).

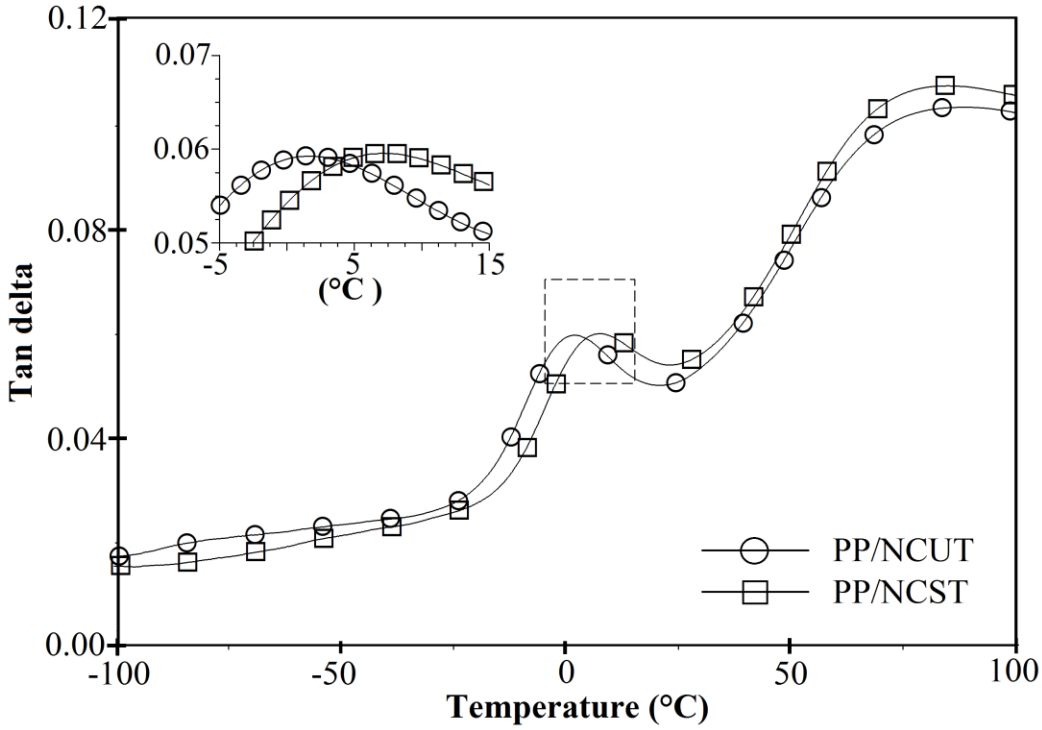

Figure 4.58: The *tan δ* curves of nanocomposites with untreated and treated nanoclays

By analysing the *tan* δ curves for PP/NCST2 with different processing screw speeds (Appendix 4.20), the T_g value slightly reduced from 8.4°C for 100 rpm to 7.0°C for 800 rpm as the compounding screw speed increased. Contrary to expectations, the *tan* δ_{max} value obtained in this system increased from 0.056 for 100 rpm to 0.059 and 0.065 for 300 rpm and 500 rpm, respectively. However, as the processing screw speed increased to 800 rpm, this value slightly reduced to 0.057 (Table 4.6). The reduction in

the *tan* δ_{max} value indicates an improvement in the material stiffness which may be due to better dispersion of nanoclay in the system, as is expected for nanocomposite with the higher processing screw speed. A similar behaviour was also observed for the *tan* $\delta_{25°C}$ value at room temperature.

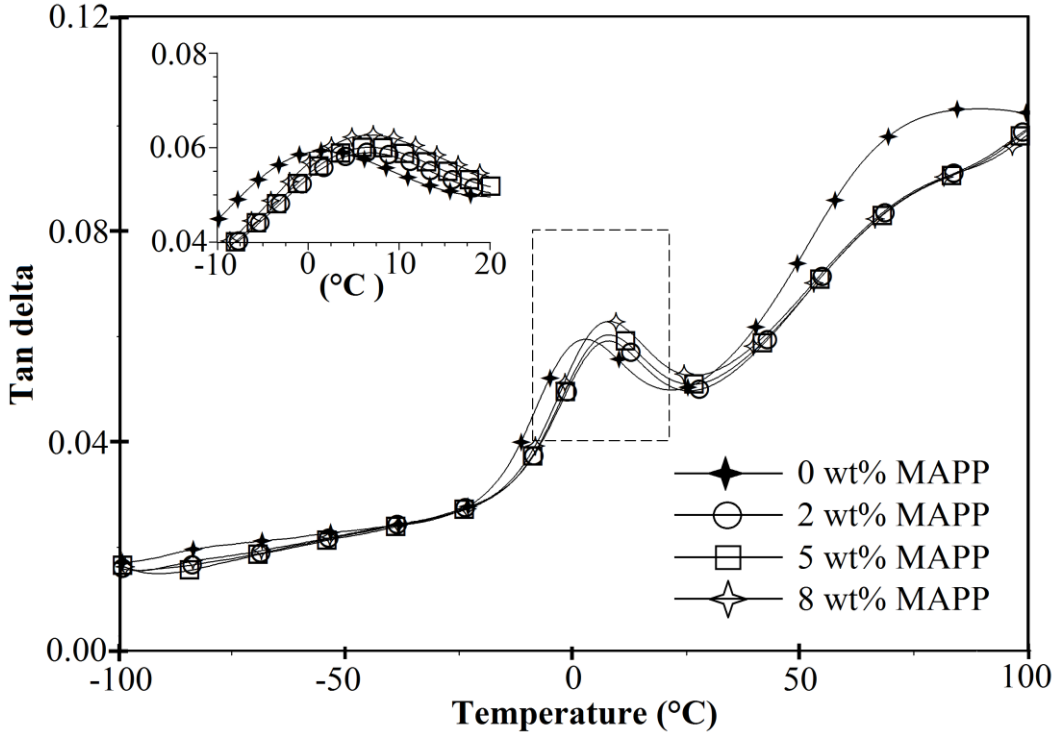

Figure 4.59: The *tan δ* curves of PP/NCUT6 nanocomposites with different MAPP contents

Figure 4.59 displays the effects of the compatibiliser loadings on the *tan* δ curves for PP/NCUT6 nanocomposites. A remarkable shift of T_g to a higher temperature recorded with the presence of MAPP. The T_g shifted from 1.7°C for the uncompatibilised nanocomposite to 6.6°C with the addition of 2 *wt%* of MAPP to the system, indicating a restriction in the polymer chain mobility due to the improvement in the interfacial bonding between the nanoclay and PP matrix. The addition of 5 *wt%* and 8 *wt%* MAPP only resulted in a slight change in the T_g value (Table 4.6). The $tan\,\delta_{max}$ value increased with the MAPP content. As previously observed for $tan\,\delta_{max}$, the addition of 6 phr clay to the PP matrix resulted in a decrement in this value to 0.059,

relative to PP (0.067), which indicates that a strengthening effect has been experienced. From Table 4.6, no changes in *tan* δ_{max} was observed with the presence of low MAPP loading (2 *wt%*). However, the addition of MAPP to 5 *wt%* and 8 *wt%* led to a further increase in *tan* δ_{max}. Although the presence of compatibiliser was expected to improve the material stiffness by increasing the interfacial bonding between PP matrix and nanoclay and Lee *et al.* [146] suggested that higher content of MAPP (more than 5 *wt%*) will act as a lubricating modifier in the glass transition temperature region, thus increasing the *tan* δ_{max} value.

The *tan* δ curves obtained for PP/NCST2 nanocomposites with variation in MAPP loading, from 2 *wt%* to 8 *wt%* is shown in Appendix 4.21. The addition of 2 *wt%* and 5 *wt%* of MAPP increased the T_g value from 6.7°C for uncompatibilised PP/NCST2 to 7.8°C implying a reduction in material's flexibility, as a result of the improvement in the PP matrix-nanoclay interfacial adhesion. In agreement with the observation in the T_g behaviour, slight reduction in the *tan* δ_{max} and *tan* $\delta_{25°C}$ were recorded in nanocomposites with 2 *wt%* of MAPP. Conversely, the addition of 5 *wt%* and 8 *wt%* of MAPP resulted in a slight increment in this value. As discussed earlier, plasticisation effect due to self-entanglement of the excess MAPP among themselves, which led to increased damping of the nanocomposites may be responsible for the observed trend [159].

4.6.3.2 Glass fibre composites

From Table 4.6, the incorporation of glass fibres slightly reduced the T_g value of PP matrix, from 2.9°C, to 1.7°C, 2.6°C and 2.3°C with the presence of 15 *wt%*, 30 *wt%* and 45 *wt%* of GF loadings, respectively. On the other hand, the presence of the glass fibre significantly reduced the magnitude of *tan* δ_{max} value. Higher reduction of *tan* δ_{max} for composites with higher fibre loadings is thought to be the result of the strengthening

effect by the glass fibres. As shown in Figure 4.60, the *tan* δ_{max} of PP/G45 composites show a maximum decrease of about 30% when compared with the pure matrix (0.067 to 0.047). In this instance, the fibres incorporated acted as barriers to the mobility of polymer chain, leading to a lower degree of molecular motion and hence lower damping characteristics [160]. Another possible reason is that there was less weight fraction of PP matrix to dissipate the vibration energy [112]. The *tan* $\delta_{25°C}$ value also showed a decreasing pattern as glass fibre was added to the composite system.

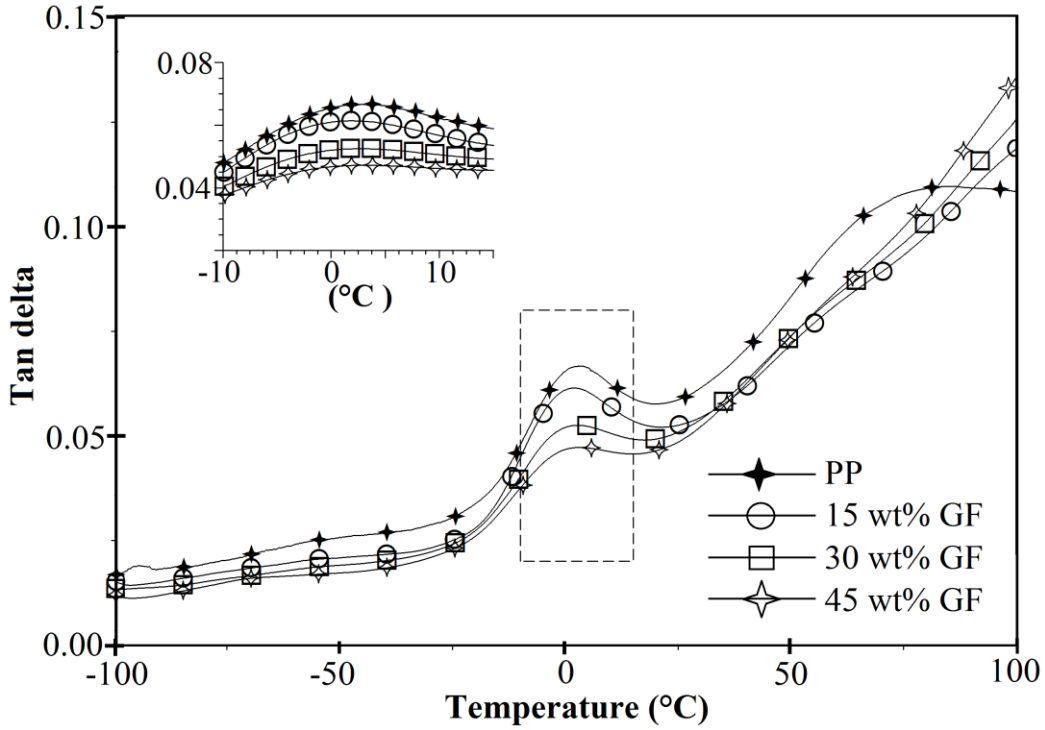

Figure 4.60: The *tan δ* curves of glass fibre composites

The effect of the different processing screw speeds from 50 rpm to 150 rpm on the *tan* δ of PP/G15 composite is shown in Appendix 4.22. No significant change in the T_g was observed. Composite processed with 50 rpm screw speed showed a *tan* δ_{max} value of 0.049. Meanwhile, by using 100 rpm processing screw speed, the *tan* δ_{max} of the composite increased to 0.064, indicating an increase in the damping property from 50 rpm to 100 rpm. As the screw speed further increased to 150 rpm, this value reduced

to 0.050 (Table 4.6). This result is in agreement with the observation mentioned earlier in the DSC section. From Table 4.5, composite processed with 100 rpm manifested the lowest degree of crystallinity (X_c) value. The reduction in this value is responsible for the increment in the *tan* δ_{max} value of composite compounded at 100 rpm, indicating the reduction of the material's rigidity. The *tan* $\delta_{25°C}$ values also showed a similar trend at room temperature.

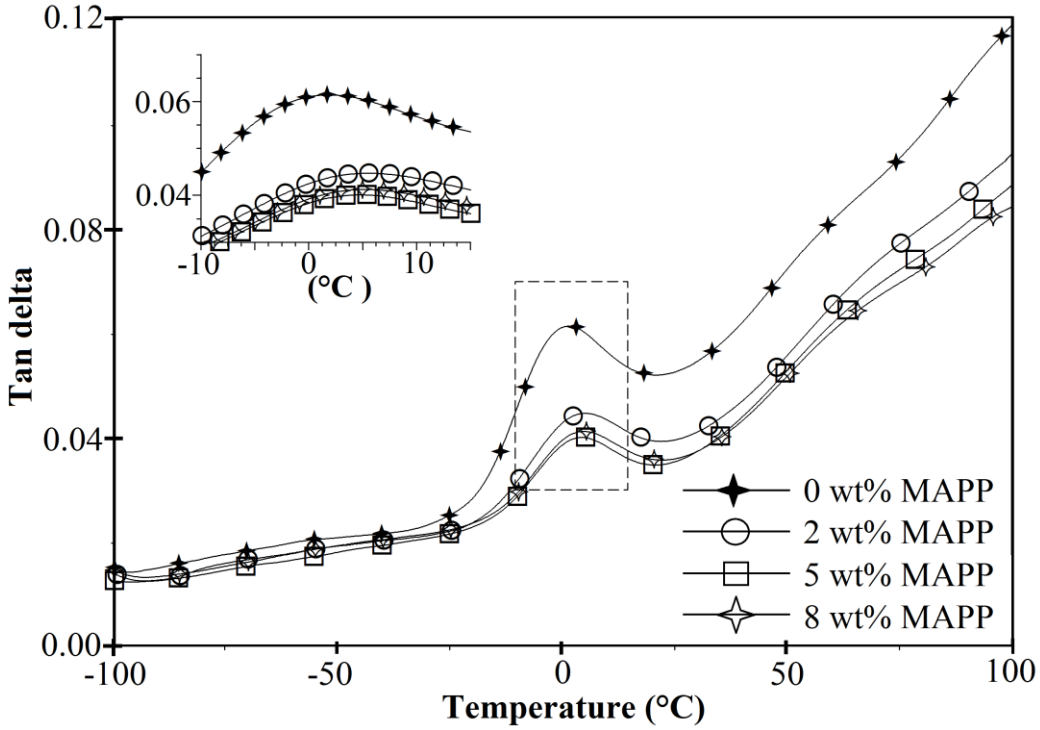

Figure 4.61: The *tan δ* curves of PP/GF15 composites with different MAPP contents

From Table 4.6, the incorporation of MAPP increased the T_g value of PP/G15 composite, from 1.7°C to 5.5°C for 2 *wt%* and to 4.8°C for 5 *wt%* and 8 *wt%* of MAPP. As discussed previously, the presence of glass fibre in the composite system lowered the value of *tan* δ_{max}, relative to PP matrix. Even though the glass fibre loading was suggested to be the major factor in determining the *tan* δ_{max}, the interaction between glass fibre and PP matrix is also expected to affect the damping properties of composites. The incorporation of 2 *wt%* to 8 *wt%* compatibiliser in PP/G15 composites

resulted in a further reduction in this value (Figure 4.61). The *tan* δ_{max} for PP/G15 recorded at 0.061 and this value dropped to 0.041 as 8 *wt%* of MAPP was added. A decline in *tan* δ_{max} with the addition of MAPP indicated an improvement in the interfacial adhesion in the composites, which reduced the material's flexibility. Nayak and Mohanty [147] have also suggested that a good interfacial adhesion in the composites will result in a lower damping property.

4.6.3.3 Glass fibre/nanoclay hybrid composites

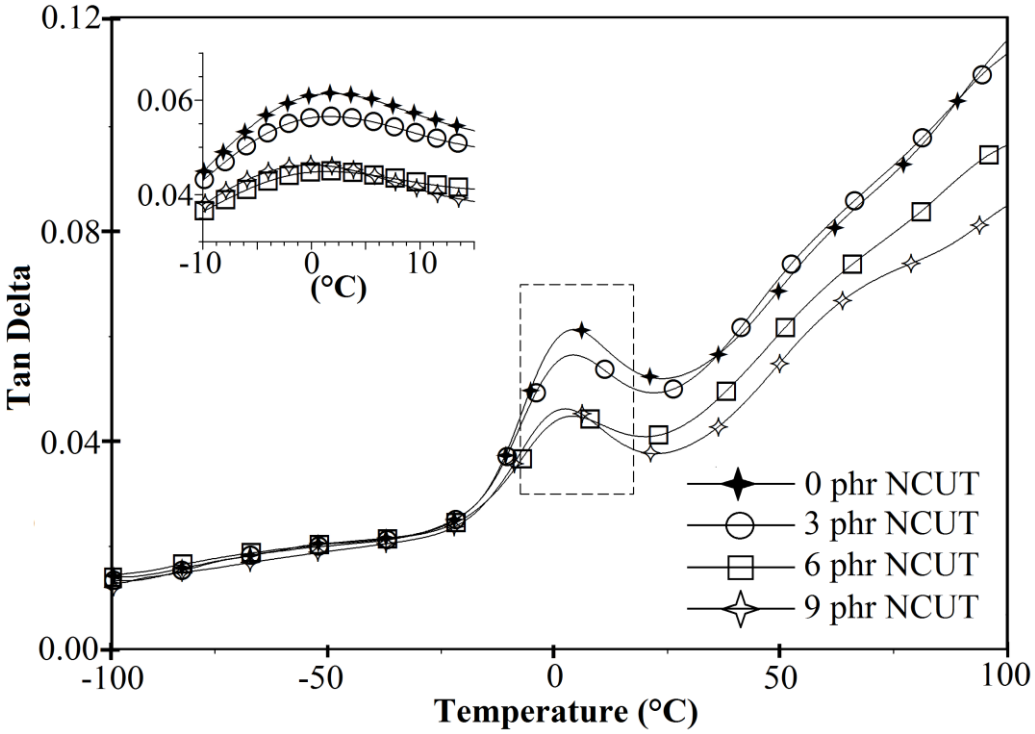

Figure 4.62: The tan δ curves of PP/G15 hybrid composites with different NCUT contents

By analyzing the *tan* δ curves for PP/GF/NC composites in Figure 4.62, the T_g value slightly reduced as the nanoclay content increased from 3 phr to 9 phr in the hybrid systems. On the other hand, the presence of the GF and NC generally reduced the magnitude of *tan* δ_{max} values. Higher reduction of *tan* δ_{max} for composite with higher filler loading is believed to be due to the strengthening effect of the GF and NC, which

may result from the increment in fillers compatibility, thus limiting the mobility of the polymer matrix and consequently lowering damping values [161]. The *tan* δ_{max} for (PP/G15)/NC6 showed a maximum decrease of about 26% (from 0.061 to 0.045) when compared with the PP/G15 composite (Table 4.6). A slight increase on the addition of 9 phr clay is related to the agglomerated structure of untreated silicate layers at higher clay concentration, as similarly observed by Bozkurt *et al.* [87]. It is also suggested that the increment in the damping properties at high concentration of clay (9 phr) may be due to the reduction in organised crystalline phase [143], which was discussed in the DSC section (Figure 4.34, Table 4.5). A similar trend was observed for PP/G30/NCUT and PP/G45/NCUT hybrid composites (Appendices 4.23 and 4.24).

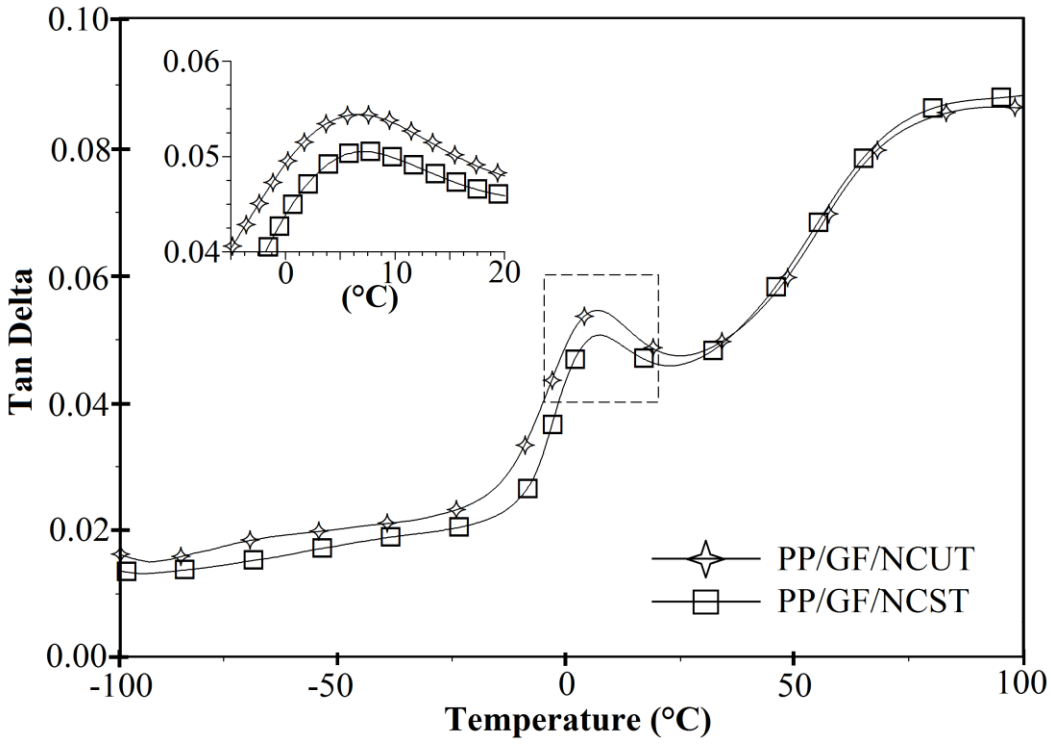

Figure 4.63: The *tan δ* curves of (PP:C5)/G15 hybrid composites with treated and untreated nanoclays

The *tan δ* curves of (PP:C5)/G15 hybrid composites, with untreated and treated clays are presented in Figure 4.63. A slight increment in the T_g value from 6.6°C for untreated clay hybrid composite to 7.0°C for treated clay hybrid composite was

observed, indicating that the surface treatment slightly modifies the glass transition property in the hybrid systems. On the other hand, the *tan* δ_{max} of the hybrid nanocomposites with treated clay showed a slightly lower value (0.051), when compared with untreated clay hybrid composite (0.055). This observation is attributed to the improvement in the interfacial adhesion between the fillers and PP matrix, induced by the clay surfactant which restricted the polymer chain mobility and consequently reduced the damping properties. The *tan* $\delta_{25°C}$ values showed a similar trend as observed for *tan* δ_{max}.

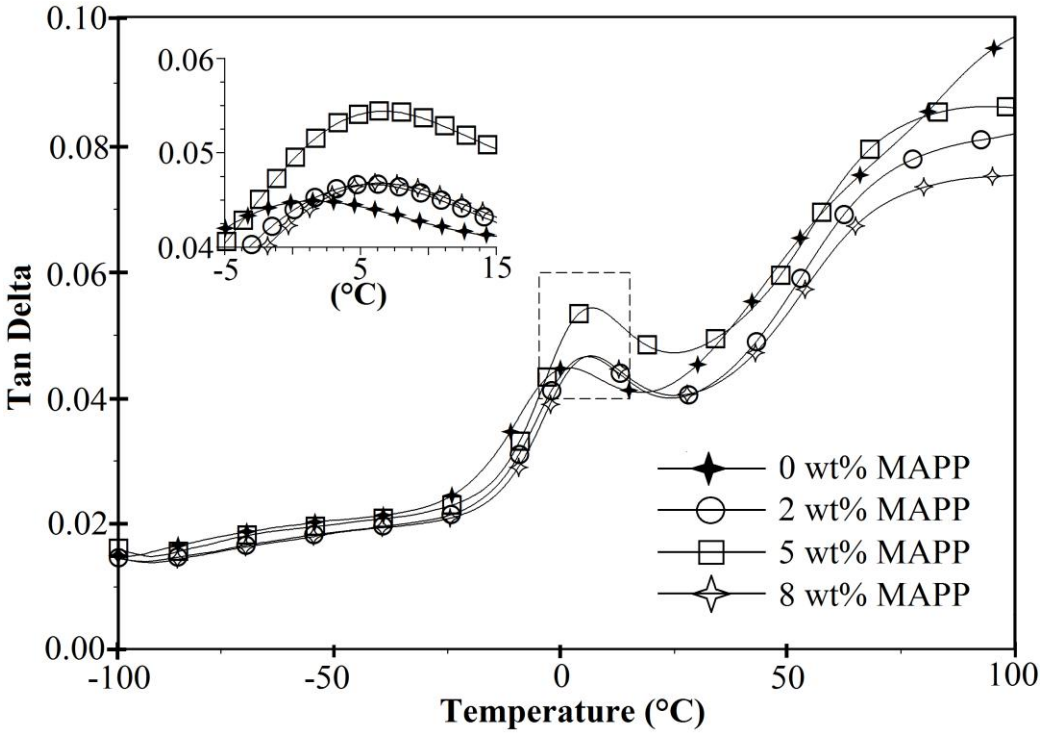

Figure 4.64: The *tan δ* curves of PP/G15/NCUT6 hybrid composites with different MAPP contents

Figure 4.64 shows the *tan* δ curves obtained for PP/G15/NCUT6 hybrid composites with variation in MAPP loading, from 0 *wt%* to 8 *wt%*. A remarkable increment in the T_g value was recorded with the presence of MAPP. From Table 4.6, the T_g value shifted from 1.1°C in the uncompatibilised hybrid composite to 5.6°C, 6.6°C and 6.3°C with the addition of 2 *wt%*, 5 *wt%* and 8 *wt%* of MAPP to the system,

respectively. This appreciable change implied that an improvement in the interfacial adhesion between the glass fibre, nanoclay and the matrix itself has been achieved, resulting in a restriction in the polymer chain mobility, consequently shifting the T_g value to a higher temperature. However, the presence of the MAPP slightly increased the magnitude of *tan* δ_{max} values. This phenomenon may be related to the lubricating effect of the compatibiliser at high MAPP content. PP/G15/NCUT6 hybrid composite with the addition of 5 *wt%* of MAPP showed the highest value of *tan* δ_{max} (0.055) when compared with other compositions. The *tan* $\delta_{25°C}$ values also showed a similar trend.

Tan δ curves obtained for PP/G15/NCST2 hybrid composites with variation in MAPP loading, from 2 *wt%* to 8 *wt%* are shown in Appendix 4.25. Similar results, as previously discussed for untreated clay hybrid composites (Figure 4.64), were obtained for treated clay hybrid composites.

4.7 Mechanical properties

4.7.1 Tensile properties

Results for the tensile properties of composite specimens together with the supporting images from SEM and TEM characterisations are shown in Figures 4.65 – 4.85. The data extracted from these figures are tabulated in Table 4.7.

Table 4.7: Tensile properties data of PP, PP/GF, PP/NC and PP/GF/NC composites

Sample	Tensile strength, σ (MPa)	Tensile modulus, E (GPa)	Tensile strain, ε (%)
PP	31.24	2.02	9.77
PP100/NCUT3	29.83	2.87	8.59
PP100/NCUT6	29.51	3.02	7.57
PP100/NCUT9	27.87	3.11	6.96
(PP100:C0)/$NCST2_{800}$	31.60	2.52	7.98
(PP92:C8)/$NCST2_{100}$	30.08	2.48	8.91
(PP92:C8)/$NCST2_{300}$	30.80	2.96	8.59
(PP92:C8)/$NCST2_{500}$	30.88	2.67	8.52
(PP92:C8)/$NCST2_{800}$	32.37	3.04	7.85

Table 4.7, continued

Sample	Tensile strength, σ (MPa)	Tensile modulus, E (GPa)	Tensile strain, ε (%)
(PP95:C5)/NCUT3	32.71	3.02	6.69
(PP98:C2)/NCUT6	31.39	3.25	5.81
(PP95:C5)/NCUT6	31.19	3.19	6.01
(PP92:C8)/NCUT6	30.99	3.12	6.13
(PP95:C5)/NCUT9	31.98	3.03	5.49
(PP98:C2)/NCST2	33.73	2.38	8.18
(PP95:C5)/NCST2	32.82	2.46	8.17
(PP92:C8)/NCST2	32.89	2.59	8.06
PP85/G15	28.20	3.43	7.42
PP70/G30	27.13	4.16	5.31
PP55/G45	25.80	4.80	2.82
(PP77:C8)/$G15_{50}$	33.40	3.02	6.33
(PP77:C8)/$G15_{100}$	32.41	3.82	5.97
(PP77:C8)/$G15_{150}$	32.22	2.86	6.65
(PP83:C2)/G15	35.88	4.46	3.46
(PP80:C5)/G15	37.40	4.71	2.95
(PP77:C8)/G15	36.87	4.81	3.09
(PP65:C5)/G30	38.24	5.67	1.71
(PP50:C5)/G45	36.15	6.11	1.26
(PP85)/G15/NCUT3	27.94	3.42	6.58
(PP85)/G15/NCUT6	30.89	4.05	4.15
(PP85)/G15/NCUT9	29.73	4.19	3.86
(PP70)/G30/NCUT3	26.21	3.96	4.96
(PP70)/G30/NCUT6	28.82	4.29	2.94
(PP70)/G30/NCUT9	28.26	4.55	2.79
(PP55)/G45/NCUT3	25.24	4.84	2.09
(PP55)/G45/NCUT6	26.70	4.95	1.37
(PP55)/G45/NCUT9	25.64	4.99	1.27
(PP83:C2)/G15/NCUT6	41.20	4.13	3.19
(PP80:C5)/G15/NCUT6	38.64	4.32	3.90
(PP77:C8)/G15/NCUT6	45.07	4.53	3.29
(PP82:C2)/G15/NCST2	34.08	4.31	4.91
(PP80:C5)/G15/NCST2	33.49	4.43	4.87
(PP77:C8)/G15/NCST2	33.01	4.96	4.80

4.7.1.1 Clay nanocomposites

Tensile strength and tensile modulus

The strength of a material is defined as the maximum stress that the material can sustain under uniaxial tensile loading. For micro- and nano-particulate composites, this relies on the effectiveness of the stress transfer between the matrix and fillers. Factors

like particle size, particle/matrix interfacial strength and particle loading, significantly affect the tensile strength of the composite [162].

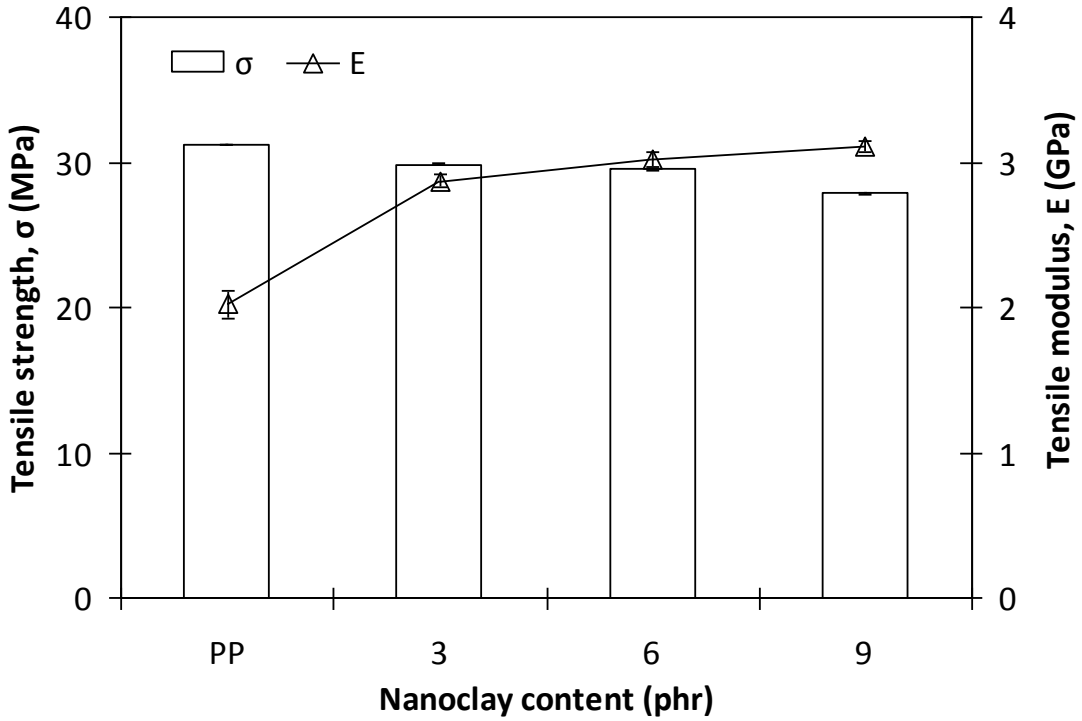

Figure 4.65: Tensile strength and tensile modulus of untreated clay nanocomposites

The tensile properties of PP/NC nanocomposites are summarised in Table 4.7. Figure 4.65 shows the effect of untreated nanoclay loadings on the tensile properties of nanocomposites. The tensile strength for PP matrix was 31.24 MPa. The addition of nanoclay from 3 phr, 6 phr and 9 phr resulted in a decrement in the tensile strength values to 29.83 MPa, 29.51 MPa and 27.87 MPa, respectively. The tensile strength continuously reduced with the addition of nanoclay, indicating poor dispersion of untreated nanoclay in the nanocomposites system, which led to the formation of agglomerated particles in the PP matrix. This agglomerated site acted as a stress concentration area during tensile testing and could have resulted in premature failure under loading conditions. The SEM images from the fractured surfaces from tensile

specimen of clay nanocomposites as previously discussed in the XRD section, are shown in Figure 4.12.

Despite some reductions in tensile strength with the addition of untreated nanoclay, the tensile modulus of clay nanocomposites increased with increase in the nanoclay loadings (Figure 4.65). The presence of nanoclay improved the tensile modulus by about 42% to 2.87 GPa with 3 phr of nanoclay loading, relative to pure PP (2.02 GPa). The adhesion between the particles and the PP matrix restricted the mobility of polymer chains under loading at lower strain and allowed the shear deformation and stress to transfer from the matrix to the nanoclay particles. Similar phenomena have been reported by Shi *et al.* [163]. It is suggested that the enhancement in the tensile modulus can be attributed to the increment in stiffness and brittleness of PP matrix by the addition of nanoclay [86, 164]. Further addition of clay only resulted in a slight improvement in the tensile modulus. Rather, there was a very nominal increment in the tensile modulus by 50% and 54%, with the presence of 6 and 9 phr of clay, respectively, when compared with PP matrix. This may be attributed to the presence of aggregate, which can be seen in the SEM images in the XRD section (Figure 4.12).

The effect of clay surface treatment on the tensile properties is shown in Figure 4.66. On the addition of 6 phr untreated nanoclay, the tensile strength value of 29.51 MPa was observed. On the other hand, the presence of 2 phr treated nanoclay resulted in a higher tensile strength value of 31.60 MPa (Table 4.7). This improvement may be due to the better dispersion of treated clay in the nanocomposite system. As discussed in the XRD section, treated clay resulted in higher interlayer d-spacing when compared with untreated clay (Figure 4.9, Table 4.3), thus there is a high possibility for the polymer matrix to diffuse into the treated silicate layers in order to form an exfoliated nanocomposite. Moreover, the particle/matrix interfacial adhesion can also can affect, significantly the tensile strength of particulate composites, as discussed by Fu *et al.*

[162]. A strong interfacial bonding between the particles and the polymer matrix is critical for effective stress transfer leading to a higher tensile strength. Conversely, a weak particle/matrix interfacial bonding will only result in a low tensile strength, as observed for untreated clay nanocomposite.

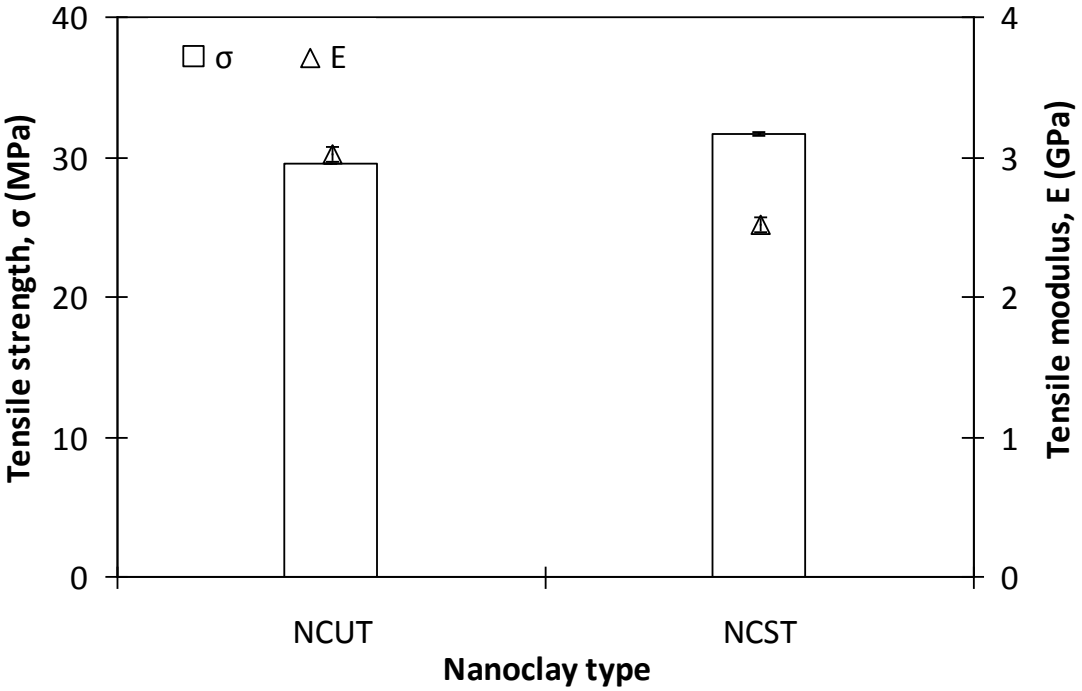

Figure 4.66: Tensile strength and tensile modulus of nanocomposites with untreated and treated nanoclays

Contrary to expectations, the tensile modulus of treated clay nanocomposite in Figure 4.66 exhibited a low value (2.52 GPa) when compared with untreated clay nanocomposite (3.02 GPa). In this case, the surface treatment of nanoclay seemed to have yielded a negative effect on the stiffness of the material. Fu *et al.* [162] suggested that the tensile modulus is independent of the better interfacial adhesion provided by surface treatment, but increases almost linearly with filler loading. Since tensile modulus is measured at relatively low deformation (at 0.5% tensile strain), there is insufficient dilation to cause a separation of the interface, implying that the adhesion

strength does not, noticeably, affect the elastic modulus, thus resulted in the observed trend.

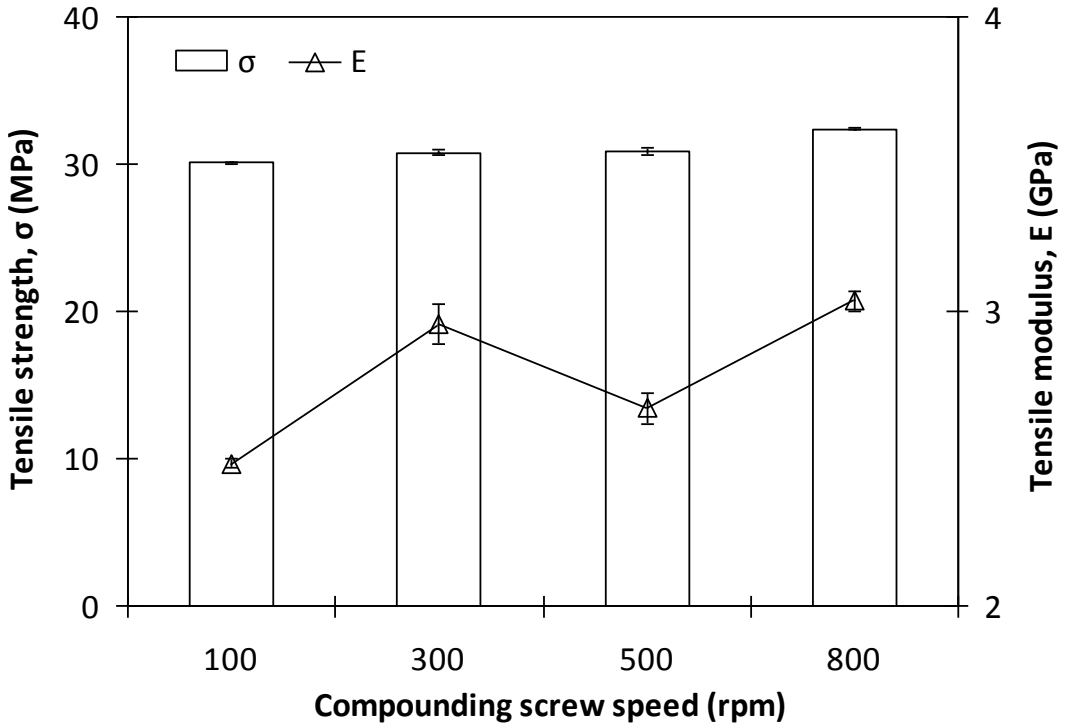

Figure 4.67: Tensile strength and tensile modulus of PP/NCST2 nanocomposites at different screw speeds

Figure 4.67 shows the effect of processing screw speed on the tensile properties of PP/NCST2 nanocomposites. Generally, the tensile strength of PP/NCST2 nanocomposites increased with increasing screw speed. At low screw speed (100 rpm), the least tensile strength was recorded (30.08 MPa) (Table 4.7). It is possible that at low screw speed, the possibility for nanoclay to agglomerate in matrix was high due to the low shear forces during melt mixing which resulted in poor clay dispersion. The highest tensile strength value was observed for nanocomposite compounded with 800 rpm. It is suggested that the higher shear forces provided by increasing the processing screw speed played a dominant role in the dispersion of treated clay particles in the matrix, hence it enhanced the tensile strength [97]. Figure 4.14 (in XRD section) shows the TEM images of PP/NCST2 nanocomposites series processed with 100 rpm and 800 rpm

screw speed. From this figure, it can be observed that the distribution of nanoclays was relatively better in nanocomposite processed with 800 rpm screw speed, which resulted in improved tensile properties, due to the better dispersions of particles.

The tensile modulus of PP/NCST2 nanocomposites compounded with different processing screw speeds in Figure 4.67 also shows similar behaviour, as observed in the tensile strength. Tensile modulus for the nanocomposite compounded with 800 rpm of screw speed resulted in an increment of about 23% from 2.48 GPa to 3.04 GPa, relative to nanocomposite compounded with 100 rpm screw speed (Table 4.7). Wahit *et al.* [140] suggested that the tensile properties of nanocomposite are governed by the delamination of nanoclay, which is strongly dependent on the processing method. In a nanocomposites system, due to the limitation in processing period, it is possible for the polymer to have not enough time to diffuse between the nanoclay layers. However, at high levels of shear force-induced processing, the induced high stress can lead to the breaking of the agglomerated clay particles into finer particulates and this can result in a better dispersion, hence improve the mechanical properties [97].

Figure 4.68 shows the influence of compatibiliser on the tensile properties of PP/NCUT6 nanocomposite. A slight increment was observed with the addition of MAPP. The tensile strength of the nanocomposites increased from 29.51 MPa for uncompatibilised PP/NCUT6 to 31.39 MPa, 31.19 MPa and 30.99 MPa for 2 *wt%*, 5 *wt%* and 8 *wt%* of MAPP, respectively (Table 4.7). The improvement in the tensile strength may be due to the intercalation phenomenon of clay layers by the MAPP [86]. Moreover, as in nanocomposites system, the quality of adhesion at the interface is of crucial importance for the behaviour of particulate composite [162]. Adhesion strength was observed to be enhanced with the presence of MAPP in the nanocomposite system, resulting in the increment of tensile strength values.

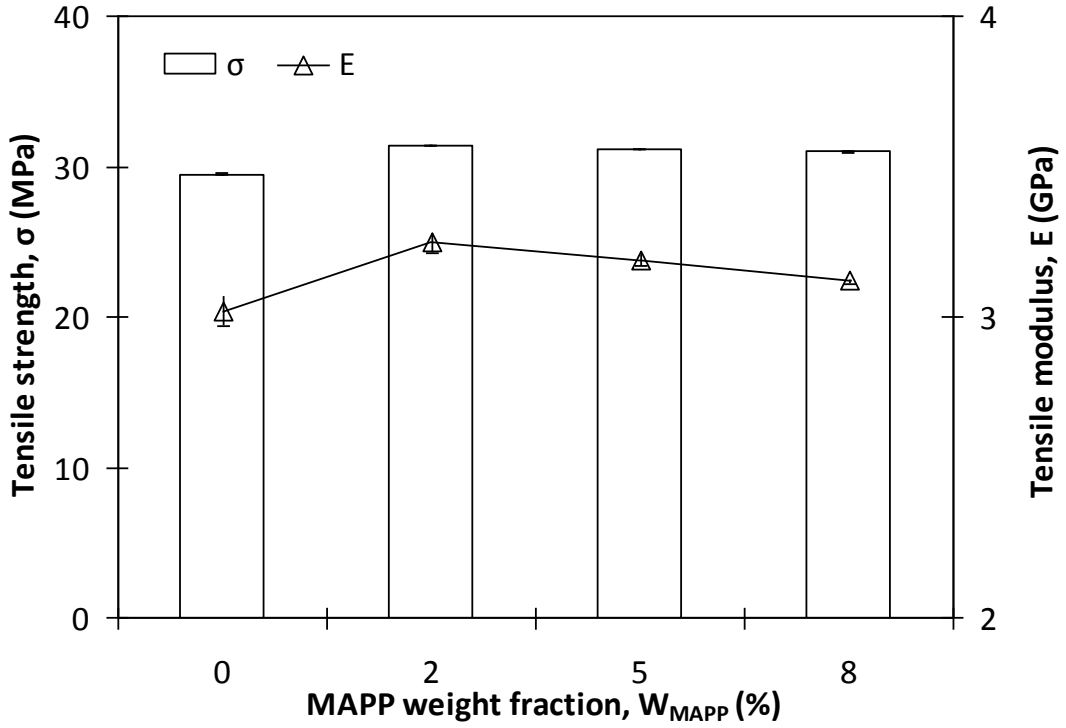

Figure 4.68: Tensile strength and tensile modulus of injection-moulded PP/NCUT6 nanocomposites with different MAPP contents

The variation of the tensile modulus of PP/NCUT6 with MAPP loadings is also shown in Figure 4.68. The tensile modulus for the compatibilised nanocomposites showed a relatively high value than the uncompatibilised materials. This is due to the improved compatibility between the matrix and the nanoclay. An increment of about 8% in the tensile modulus was obtained with the addition of 2 *wt%* of MAPP (3.25 GPa) relative to the uncompatibilised PP/NCUT6 (3.02 GPa). The addition of 5 *wt%* and 8*wt%* of MAPP only resulted in a marginal increment of about 6% and 3%, respectively. It seems that the addition of higher MAPP loading has no significant effect on the mechanical properties of the nanocomposites. As previously mentioned by Dong and Bhattacharyya [159], there is an optimum amount of MAPP that should be added in achieving the greatest compatibility effect. Beyond this threshold, the entanglement of MAPP among themselves rather than between MAPP and the filler results in slippage during the tensile testing. Moreover, excessive amount of MAPP also could lead to plasticisation effect which softens the nanocomposite materials. As a result, their

mechanical properties do not show a consistent increasing trend with increasing MAPP content, but more or less posses an insignificant enhancement above certain level of MAPP content.

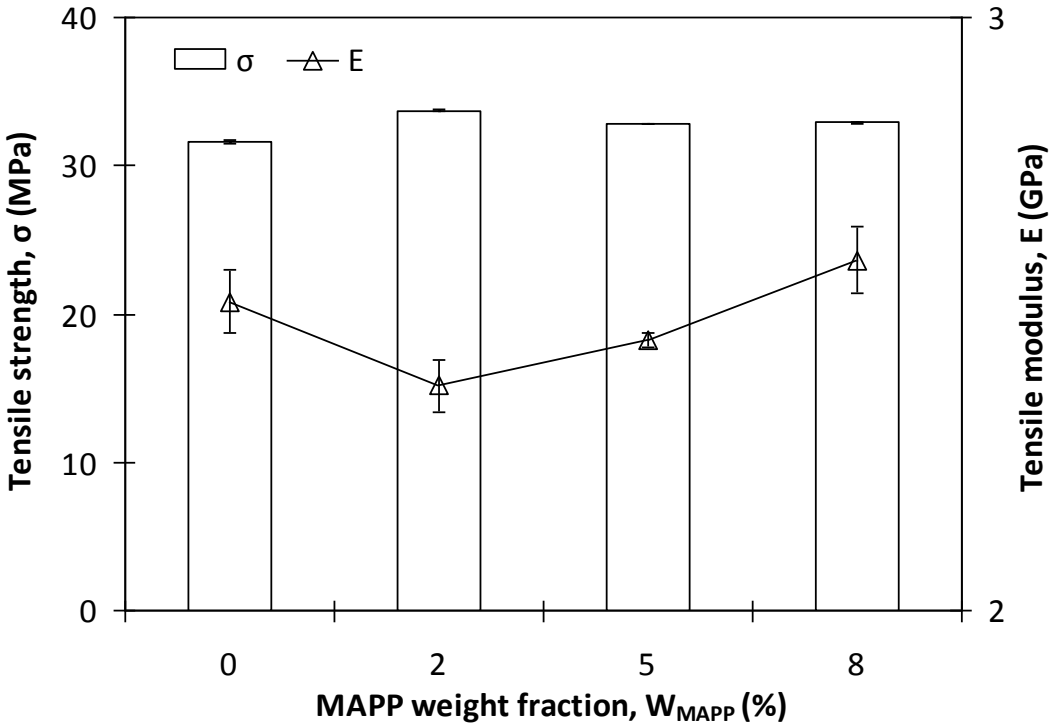

Figure 4.69: Tensile strength and tensile modulus of injection-moulded PP/NCST2 nanocomposites with different MAPP contents

Figure 4.69 shows the tensile properties values obtained for PP/NCST2 nanocomposites with variation in the MAPP loadings, from 0 *wt%* to 8 *wt%*. The addition of 2 *wt%* of MAPP increased the tensile strength of uncompatibilised PP/NCST2 nanocomposites from 31.60 MPa to 33.73 MPa. However, further addition of 5 wt% and 8 wt% of MAPP resulted in low magnitudes of increment in the tensile strength to 32.82 MPa and 32.89 MPa, respectively. Generally, the presence of MAPP in the treated PP/NCST2 nanocomposite showed similar effect for the tensile strength values, as observed earlier in the PP/NCUT6 nanocomposites. However, with the addition of compatibiliser, a more obvious increment was obtained in the treated clay when compared with untreated clay composites. The diffusion of polymer into nanoclay

layers can be easier in the presence of surfactant in the treated nanoclay. This is due to favourable bonding created between surfactant of clay, MAPP and PP matrix. The presence of MAPP facilitated the expansion of the interlayer d-spacing by the inclusion of some polar groups (maleic anhydride) to intercalate between the silicate layers through hydrogen bonding to the amine terminal group of the organic modifier within treated nanoclay. This enhanced the interlayer d-spacing of stacked nanolayers which in turn resulted in exfoliated structure [156]. The miscibility of MAPP with polar group of the treated nanoclay and PP matrix mediated between the surface chemistry of polymer and nanoclay at the interphase and contributed to the enhancement in the tensile strength [165].

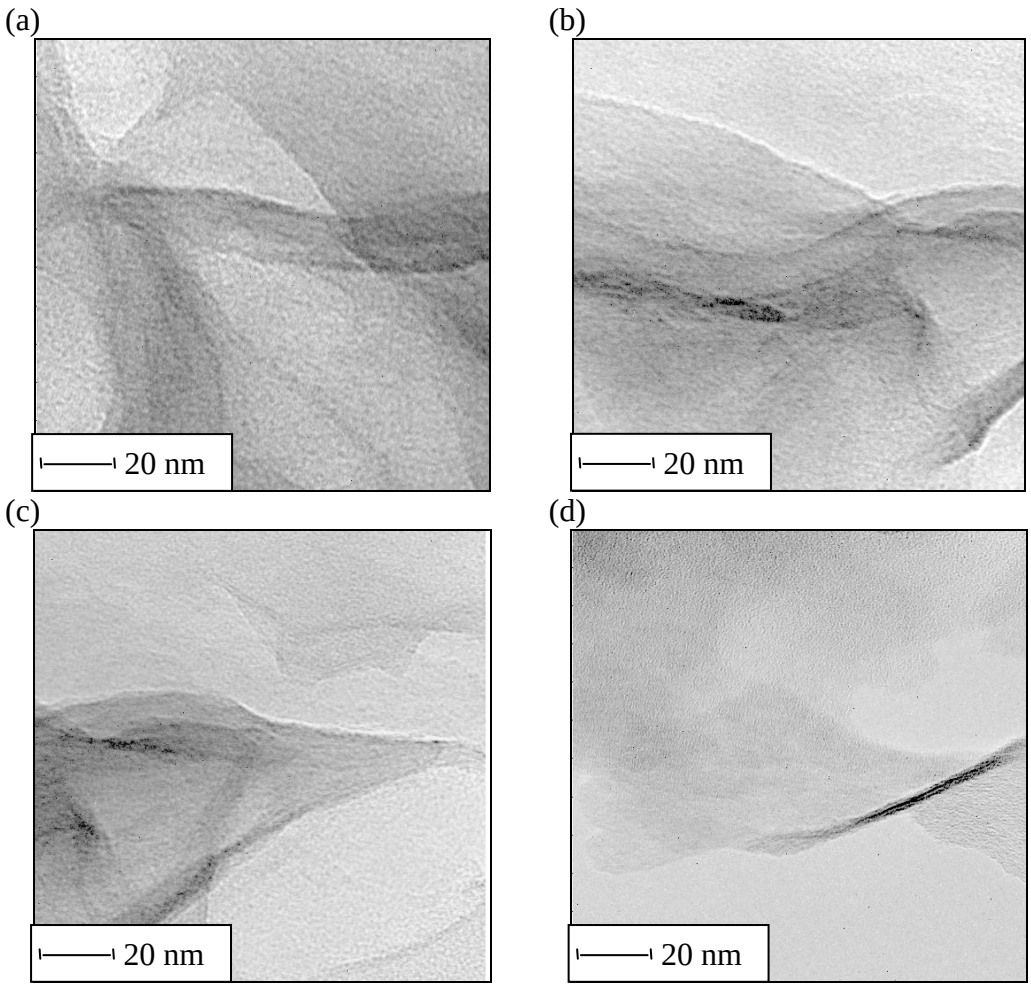

Figure 4.70: TEM images of PP/NCST2 nanocomposites with different MAPP contents: (a) 0 *wt%*, (b) 2 *wt%*, (c) 5 *wt%* and (d) 8 *wt%* of MAPP

On the other hand, the addition of low MAPP loading lowered the tensile modulus value from 2.52 GPa for PP/NCST2 nanocomposite, to 2.38 GPa with the presence of 2 *wt%* of MAPP. Meanwhile, the tensile modulus increased continuously with the addition of 5 *wt%* and 8 *wt%* of MAPP to 2.46 GPa and 2.59 GPa respectively. The level of reinforcement, in this case, is defined by the morphology of the nanocomposite (filler aspect ratio, filler orientation, *etc.*) and the interaction between the nanoclay and the matrix [166]. As shown in the morphological analysis (Figure 4.70), the addition of MAPP provided better dispersion of the clay, reducing the particle thickness and increasing the aspect ratio. A higher nucleation effect was observed when the MAPP was used, indicating high interaction between filler and matrix. These interpretations are in agreement with the results of tensile modulus obtained for treated clay nanocomposite.

Tensile strain

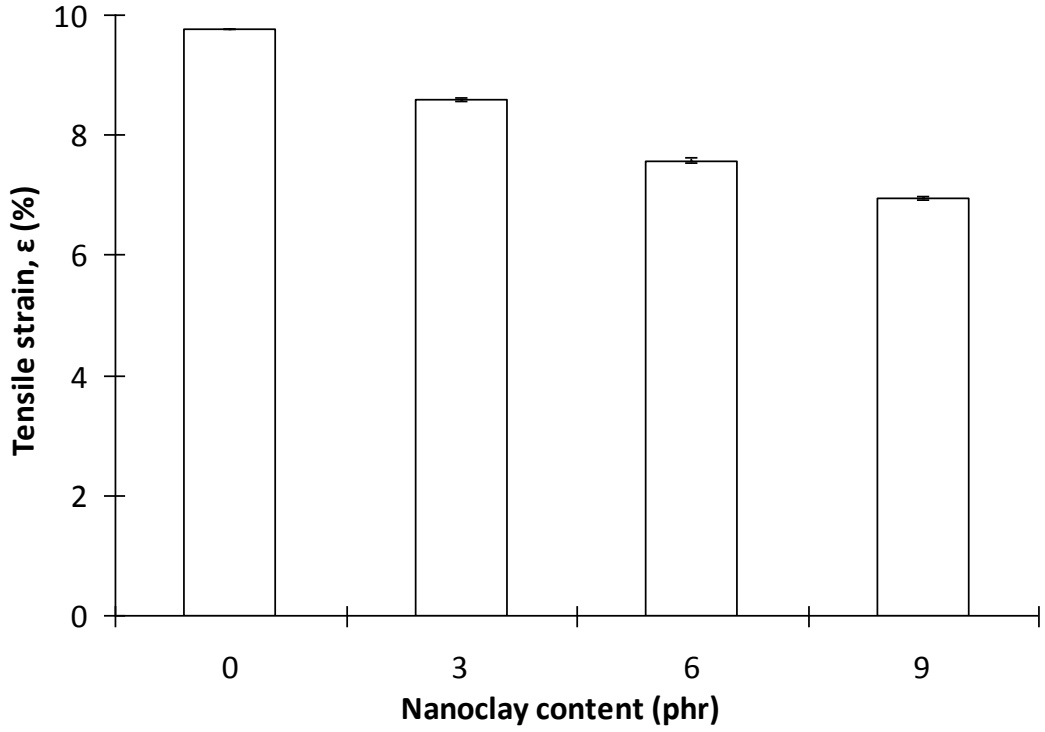

Figure 4.71: Tensile strain of untreated clay nanocomposites

From Figure 4.71, it can be seen that the tensile strain of the nanocomposites are greatly affected by the presence of nanoclay. As expected, the tensile strain decreased gradually with the addition of clay loadings from 3 phr to 9 phr. The tensile strain for PP was 9.77% and reduced to 8.59%, 7.57% and 6.96%, as 3 phr, 6 phr and 9 phr of nanoclay addition to the system, respectively. It is suggested that with the addition of silicate layers, the nanocomposites behaved in a brittle manner and the material tended to break in the elastic part of the stress-strain curve. Apparently, the silicate layers constrained the matrix, so that plastic deformations were prevented in the nanocomposites [167].

The effect of clay surface treatment on the tensile strain of nanocomposites is shown in Appendix 4.26. Tensile strain for PP/NCUT6 was recorded at 7.57%, whereas, with treated clay, PP/NCST2 nanocomposite, this value increased to 7.98%. The increment in tensile strain value could be due to the reduction in degree of crystallinity of treated clay nanocomposite when compared with untreated clay nanocomposite (see Table 4.5), which is believed to be responsible for the increment in the ductility [156]. This result is in agreement with the highly exfoliated nature and nanomeric size of the clay particles, which minimises any stress concentration that may lead to premature failure. In addition, this high tensile strain is also an indication of the presence of some organic substituent of the treated nanoclay in the matrix [168].

As previously discussed in earlier sections, high processing screw speed improved the tensile strength and tensile modulus of PP/NCST2 nanocomposite. This enhancement is due to the higher shear force experienced by the material in the melt processing phase, resulting from the use of high processing screw speed, thus the better dispersion of silicate layers in the matrix. With that, as expected, the lowest tensile strain value was observed for PP/NCST2 nanocomposite that was processed with 800

rpm screw speed, as an indication of the restriction in the matrix deformation with the presence of exfoliated nanoclay in the system (Appendix 4.27).

In agreement with the tensile strength and tensile modulus trends (Figure 4.68), the tensile strain of PP/NCUT6 nanocomposite decreased with the addition of 2 *wt%* of MAPP in the system (Appendix 4.28). Sharma and Nayak [142] suggested that the elongation behaviour reduced with increase in the dispersed phase and reinforcement by nanoclay. A slight increment was detected with the addition of higher MAPP loading. This phenomenon could be due to the presence of excess low molecular weight of MAPP, which imparted a plasticisation effect at the interface, causing an increase in the tensile strain [159].

As for PP/NCST2 nanocomposite, the addition of MAPP resulted in a slight increment in the tensile strain values (Appendix 4.29). By contrast, the tensile strength for this particular nanocomposite was enhanced, which means, traditionally, the tensile strain should reduce. Kim *et al.* [169] also reported an increment in the elongation at break of the composites when compatibiliser was added. This trend can be seen to result from the increased compatibility due to the reaction of PP, treated clay surface and the compatibiliser. The increase in the interfacial adhesive forces caused a delay of debonding of the matrix and nanoclay at the interface, which extensively inhibited the initiation and propagation of voids that caused cracks. Thus, plastic deformation can occur at a greater strain.

4.7.1.2 Glass fibre composites

The tensile properties of glass fibre reinforced PP composites together with the supporting images from SEM characterisation, are shown in Figures 4.72 to 4.78. It is well known that the properties of short-fibre composites are determined by the nature of

the fibre, the fibre volume fraction, the fibre orientation factor, the aspect ratio of the reinforcement and by the quality of the fibre/matrix interface [170].

Tensile strength and tensile modulus

The PP matrix has a tensile strength of 31.24 MPa and a tensile modulus of 2.02 GPa. From Table 4.7, a reduction in the tensile strength was observed when glass fibre was incorporated into the polymer matrix. Figure 4.72 shows a continuous decrement in the reinforcement efficiency as the glass fibre content increased. The tensile strength reduced from 31.24 MPa for pure PP to 28.20 MPa for 15 *wt%* of glass fibre composites. Further addition of 30 *wt%* and 45 *wt%* of glass fibres, resulted in a further reduction in the tensile strength values. The addition of fibres shows no improvement in the tensile strength value, which is an indication of poor fibre–matrix adhesion and lack of stress transfer capability of the fibre [171, 172].

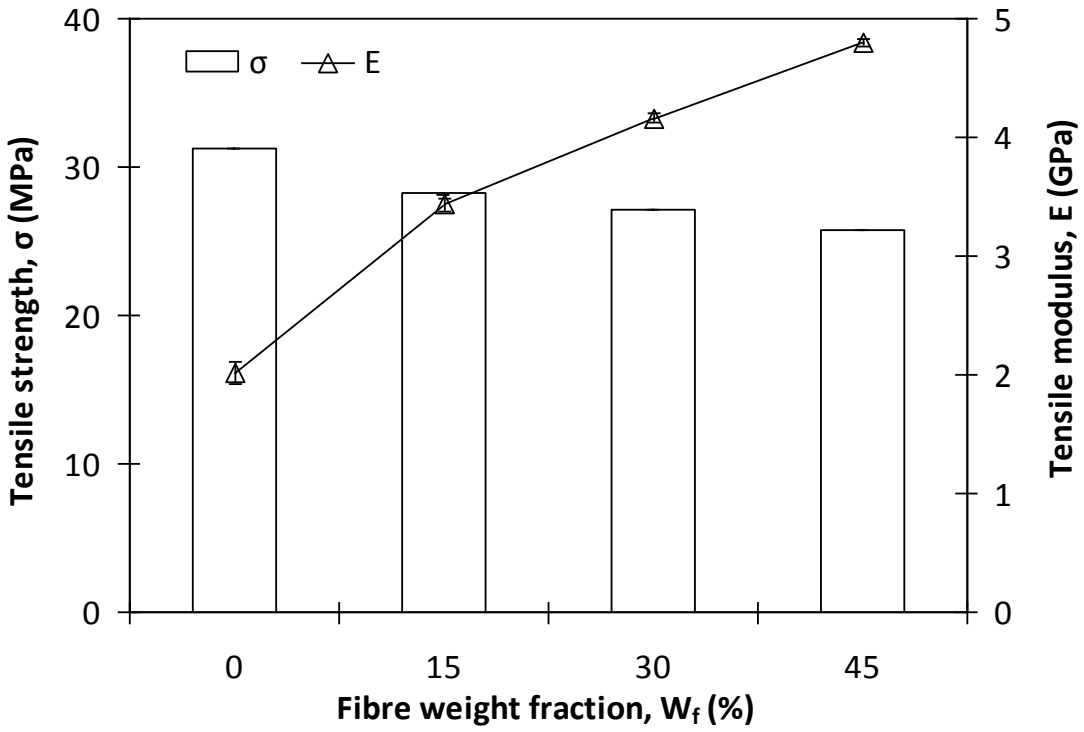

Figure 4.72: Tensile strength and tensile modulus of glass fibre composites

It is assumed that when there is poor adhesion at the interface, at high deformations, as it happens in the tensile test, the presence of fillers or fibres in a polymer matrix gives rise to defect at the interface, which is responsible for the strength reduction [173]. From microscopic studies, it can clearly be seen that the fibre surface is smooth without the existence of resin particles at the glass fibre surfaces which indicates a poor fibre-matrix bonding (Figure 4.73). Composite failure could be due mainly, to fibre/matrix interfacial debonding, rather than fibre fracture. Furthermore, as mentioned in earlier section, the FLD result showed that the glass fibre length decreased almost linearly with increase in the glass fibre content (Figures 4.1 – 4.3, Table 4.2). The reduction in the fibre length is also suggested to be responsible for the decrement of the tensile strength as the fibre loading increased.

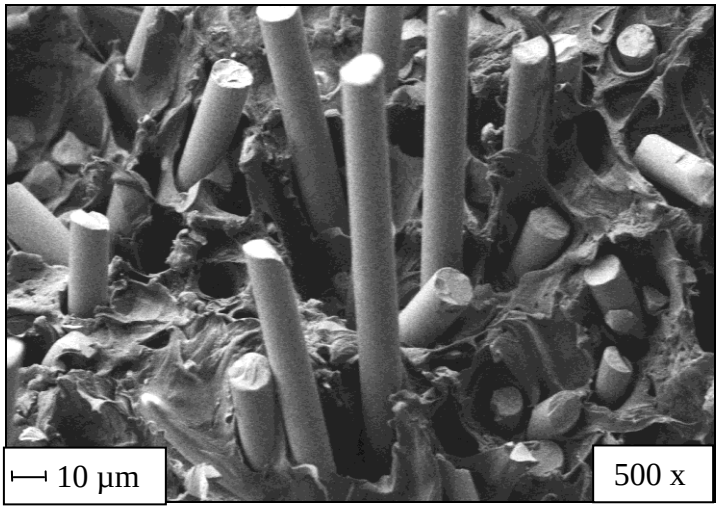

Figure 4.73: SEM image of tensile fracture surfaces of PP/G45 glass fibre composite

Despite the reduction in the tensile strength (uncompatibilised system), the tensile modulus increased with increase in glass fibre content. The modulus increased from 2.02 GPa for pure PP to 4.80 GPa for composites with 45 *wt%* of GF (Figure 4.72). The same behaviour has also been reported by previous researchers [170, 174]. Haneefa *et al.* [175] suggested that the addition of glass fibre increased the effective

mechanical interlocking, which in turn increased the frictional force between the fibre and matrix. Increasing the amount of glass fibre led to higher stiffness of composite thus more energy was required to break the specimens.

The converse effect of the increase in modulus was believed to be due to this property being measured at low strain of 0.5% when compared at fracture for the tensile strength. At low strain, the stress applied caused the specimen to deform in a total elastic manner where fibre matrix adhesion may not really be in a stretchable condition, whereas at the fracture point, all possible mechanisms of fracture, such as fibre pull out, fibre breakage *etc.* may exist. Any poor fibre matrix interface may lead to premature failure causing a reduction in the tensile strength. In addition, from the fibre length points of view, at low strain, most of the fibres are super-critical or longer than the critical fibre length ($L>L_c$) and fibre failure can be due mainly, to breakage mechanism. On the other hand, at higher strain, most fibres turn sub-critical ($L<L_c$) leading to fibre failure by pull-out [116].

Figure 4.74 shows the effect of the different processing screw speeds (from 50 rpm to 150 rpm) on the tensile properties of (PP:C8)/G15 composite. There is no significant difference in the tensile strength for the composites processed with different screw speeds. It can be suggested that in the composites, fibre content was the predominant factor in the tensile strength determination, rather than fibre dispersion and fibre length.

From Figure 4.74, it is evident that the tensile modulus was influenced by the processing screw speeds. Composite processed with 50 rpm screw speed resulted in a tensile modulus value of 3.02 GPa. This value increased to 3.82 GPa by using 100 rpm processing screw speed. It can be deduced that this particular screw rate provided high shear forces to the polymer melts during processing and hence resulted in a better dispersion of the glass fibre in the PP matrix. Meanwhile, the tensile modulus showed a

substantial reduction to 2.86 GPa, as the processing screw speed was increased to 150 rpm. This may be due to the high possibility of fibre breakage resulting from the high processing screw speed, as can be observed in Figures 4.4 – 4.6 and Table 4.2.

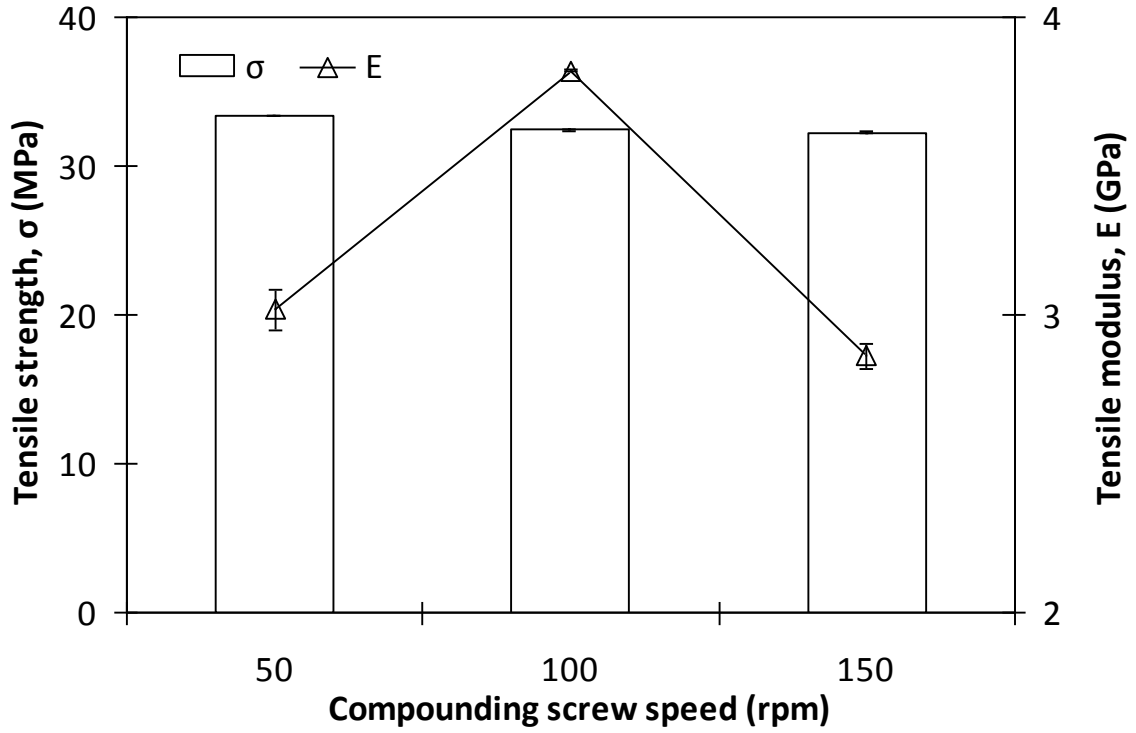

Figure 4.74: Tensile strength and tensile modulus of PP/GF composites at different screw speeds

Several studies have already shown the important effect of MAPP to the mechanical properties of fibre-reinforced composites [170, 171, 176]. The effect of different amounts of MAPP on the tensile properties of PP/G15 composites is presented in Figure 4.75. From Table 4.7, the effectiveness of MAPP as compatibiliser is clearly seen. The addition of MAPP coupling agent improved the tensile strength from 28.20 MPa for PP/G15 to a maximum of 37.40 MPa with the addition of 5 *wt%* of MAPP. The enhancement of tensile properties of composites has been attributed to the improved interfacial adhesion between fibre and matrix [177]. A slight decrement in this value was obtained with the addition of 8 *wt%* of MAPP. This may be due to the plasticising effect caused by coagulation, with the excess of MAPP loading [159].

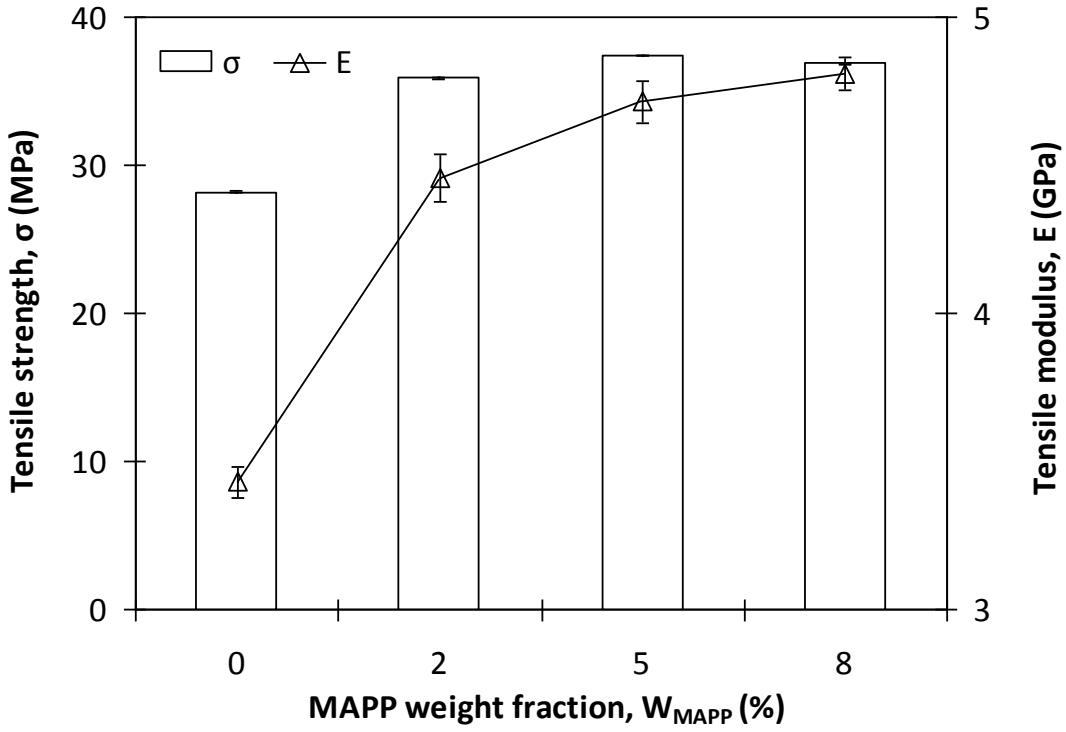

Figure 4.75: Tensile strength and tensile modulus of PP/GF15 composites with different MAPP contents

It can also be observed that the use of MAPP as a coupling agent further improved the stiffness of the composites (Figure 4.75). The presence of 2 *wt%* of MAPP in PP/G15 composite resulted in an increment of about 30% in the tensile modulus, from 3.43 GPa to 4.46 GPa. The tensile modulus was further improved with the addition of 5 *wt%* and 8 *wt%* of MAPP to 4.71 GPa and 4.81 GPa, respectively (Table 4.7). The enhancement in the tensile properties of the composites is attributed to the improved interfacial adhesion between the fibre and matrix [177] resulting in greater applied load being transferred to the strong and stiff fibres through the fibre-matrix interface [173]. From microscopic studies, it can clearly be seen that some polymer matrix adhered to the fibre surface, indicating a good fibre-matrix bonding (Figure 4.76 (a)). However, if the fibre-matrix adhesion was weak, cracks tended to form at the interface and link up quickly through highly stressed sections of the matrix, resulting in premature failure of the composite (Figure 4.76 (b)).

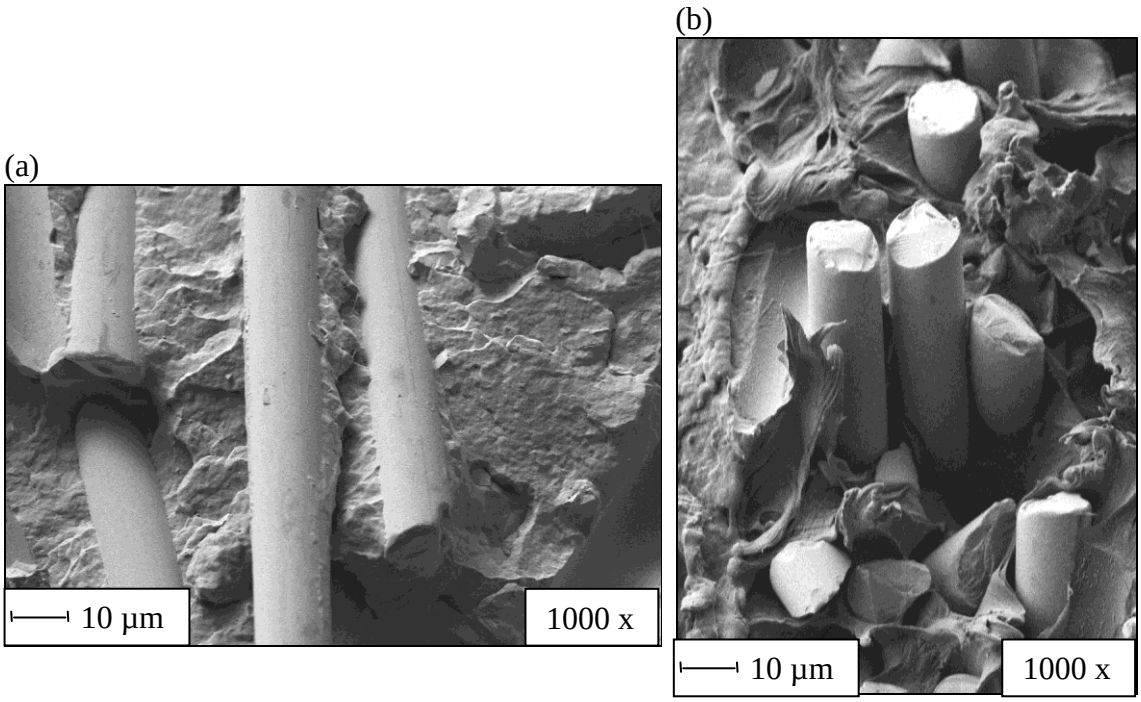

Figure 4.76: SEM images of tensile fracture surfaces of PP/G15 glass fibre composite with different MAPP loading: (a) 5 *wt%* MAPP and (b) 0 *wt%* MAPP

The mechanical properties of the composites containing 5 *wt%* of MAPP content are illustrated in Figure 4.77. As mentioned earlier, for uncompatibilised composites, the tensile strength of the composite reduced with the addition of glass fibre in the system (Figure 4.72). By contrast, with the addition of 5 *wt%* of MAPP, the tensile strength of the composites increased by between 32% – 41% when compared with the same composite formulations without the compatibiliser. Obviously, with addition of 5 *wt%* of MAPP into the system, composite with 30 *wt%* showed a 2% increment in tensile strength when compared to composite with 15 *wt%*. Further increase in fibre content up to 45 *wt%*, only resulted in a reduction of tensile strength to about 3%. The inclusion of 5 *wt%* of MAPP is probably not enough to compatibilise the system with 45 *wt%* of glass fibre composites.

With the addition of 5 *wt%* of MAPP, the tensile modulus of the composites also increased to between 27% – 37% when compared to the uncompatibilised systems (Figure 4.72). These results confirm that with incorporation of compatibiliser in the

system, the fibres acted as an effective reinforcing agent for PP, giving rise to a more rigid material [160]. It can be seen that with the presence of compatibiliser in the system, the tensile strength and modulus of composites increased with increase in the fibre loading.

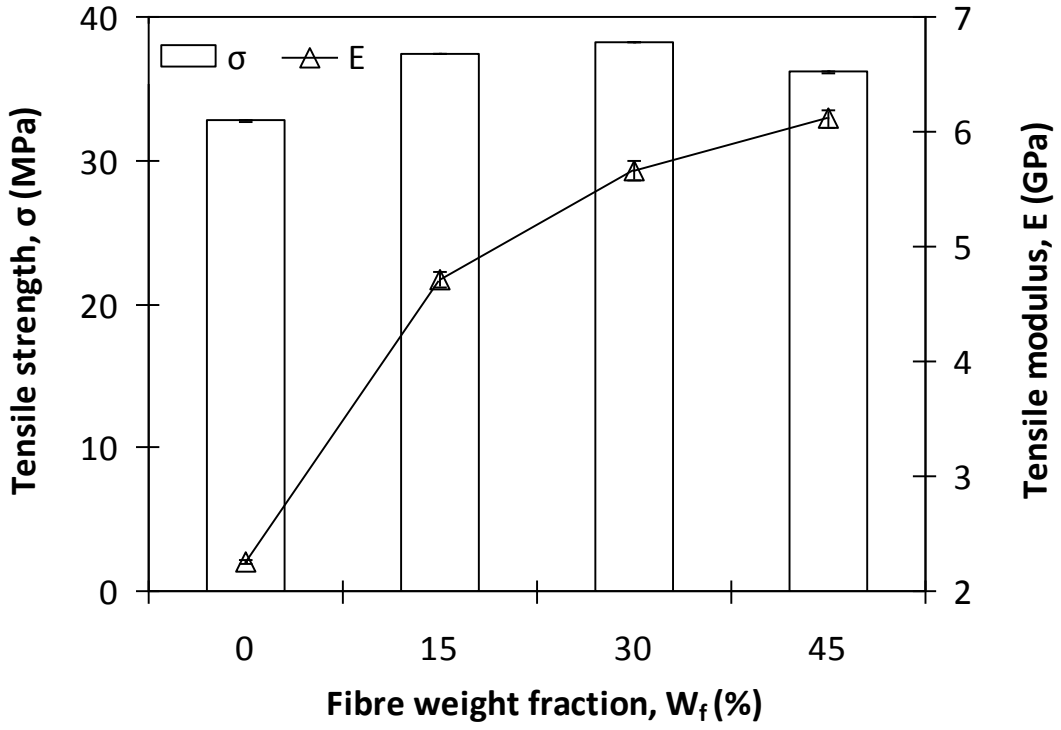

Figure 4.77: Tensile strength and tensile modulus of glass fibre composites with 5 *wt%* MAPP

Tensile strain

All specimens of fibre-filled materials failed at strains below the normal yield strain of the matrix. The tensile strain as a function of W_f, is shown in Figure 4.78. The tensile strain reduced from 9.77% for pure PP to 2.82% for composites with 45 *wt%* of glass fibre content. This trend was also reported by previous researchers [172, 178], who explained that the stress concentrations at the fibre ends led to matrix cracking, which ultimately caused failure when the surrounding matrix and fibres could no longer support the increased load caused by the local failure. Mouhmid *et al.* [179] have also reported the decrement in tensile strain with increase in the glass fibre content. Due to

the introduction of fibres, the composites became less ductile as the molecular rearrangement did not have time to take place. The notching effect of the fibres in which considerable stress concentration is induced in the matrix at the fibre end and matrix flow is constrained by adjacent fibres, is also important. Takahashi and Choi [180] who studied the failure mechanisms in such composites have shown that under tensile stress loading, the cracks start at the fibre ends and propagate along the fibre-matrix interface or cross through the matrix and finally, failure takes place.

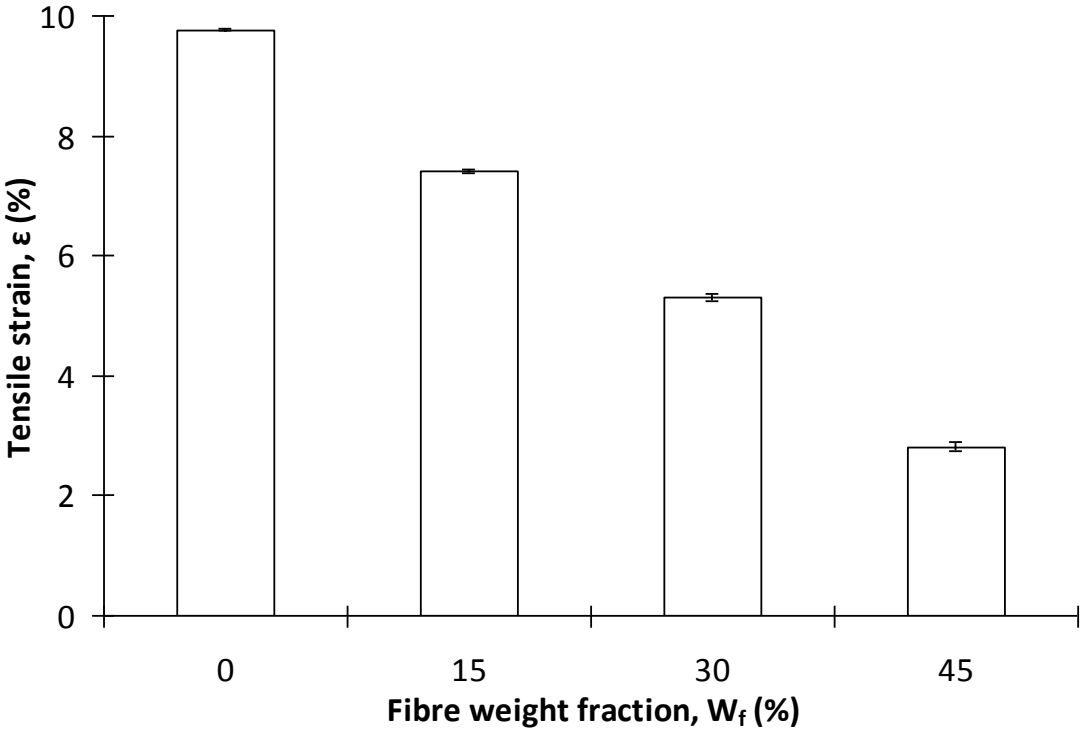

Figure 4.78: Tensile strain of glass fibre composites

From Appendix 4.30, it is evident that the tensile strain was influenced by the processing screw speeds. Composite processed with 50 rpm screw speed showed a tensile strain value of 6.33%. This value decreased to 5.97% when using a 100 rpm processing screw speed. As discussed previously, it can be suggested that at this particular screw speed, a better dispersion of the glass fibre in the PP matrix was obtained, which resulted in a reduction of the material ductility. Meanwhile, an

increment in the tensile strain value to 6.65% was observed as the processing screw speed was increased to 150 rpm.

From Appendix 4.31, it can also be seen that the tensile strain of the composites was greatly affected by the presence of MAPP. The tensile strain of PP/G15 composite was 7.42%. Obviously, with the addition of 2 *wt%* and 5 *wt%* of MAPP, a sharp reduction to 3.46% and 2.95% were observed. It can be suggested that the elongation behaviour is reduced on increased compatibility between PP matrix and glass fibre, with the addition of MAPP. On the other hand, further incorporation of 8 *wt%* of MAPP resulted in a slight increment in this value to 3.09%. The plasticisation effect at higher compatibiliser contents which can soften the nanocomposites system may be responsible for this trend. Such saturation mechanism [159] has been well understood in the general polymer blending process when the part of compatibiliser loses its functionality and becomes more or less like a plasticiser.

4.7.1.3 Glass fibre/ nanoclay hybrid composites

Tensile strength and tensile modulus

Figure 4.79 shows tensile properties of 15 *wt%* of GF composite as a function of NC contents. It was observed that the tensile strength of the composites generally increased with increasing clay contents. An insignificant change (1% reduction) in the tensile strength was observed with the addition of 3 phr of clay into PP/GF15 composite (27.94 MPa) relative to PP/G15 composite (28.20 MPa). Further addition of 6 phr of clay in the system, (PP/G15)/NC6 increased the tensile strength by 10% (Table 4.7). It is possible that the presence of clay increased the interfacial adhesion between GF and PP, hence improving the tensile strength of the PP/GF/NC composite. In addition, the silane treatment of the GF could also have intensified the synergy between PP, GF and NC as enhanced coupling between fillers was achieved, as expected.

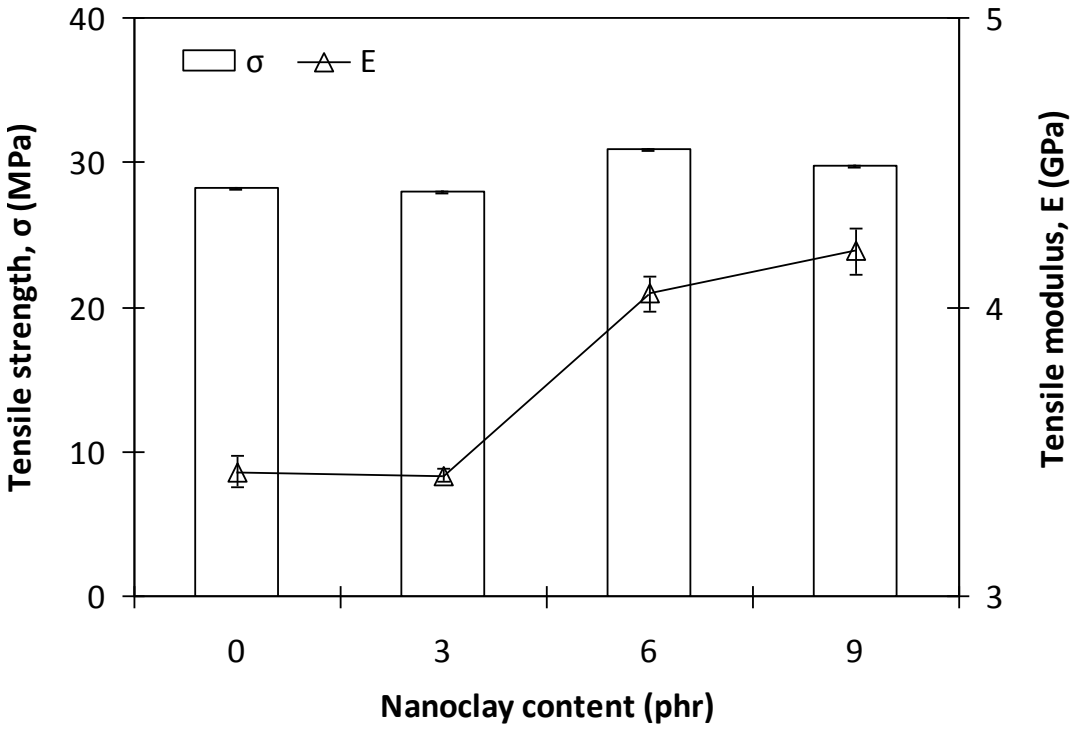

Figure 4.79: Tensile strength and tensile modulus of PP/G15 hybrid composites with different NCUT contents

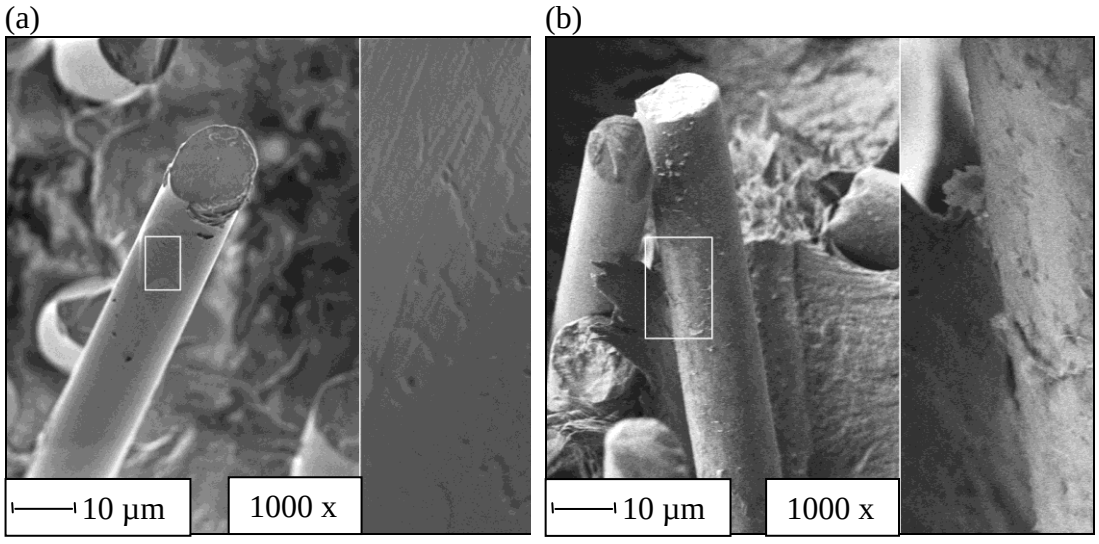

Figure 4.80: SEM images of: (a) PP/G15 composite and (b) PP/G15/NCUT6 hybrid composite

Figure 4.80 illustrates the SEM fracture surface images of glass fibre composites and glass fibre/clay hybrid composite obtained from tensile test specimens. As seen in Figure 4.80 (a), fracture occurred along the interface and smooth fracture surfaces were formed due to weak interfacial debonding in glass fibre composite without clay

addition. In contrast, in the case of hybrid composite, it is evident that the fracture mechanism was altered because of the presence of clay. It can be seen clearly that the matrix adhered to the glass fibre surface, indicating that a stronger fibre-matrix interface was formed in this composite (Figure 4.80 (b)).

However, composite with 9 phr of clay, (PP/G15)/NC9 showed a slight decrease in tensile strength. For optimum mechanical properties, there has to be good dispersion of clay within the composite. The existence of agglomeration or unexfoliated aggregates at higher clay concentrations could have resulted in a low tensile strength value. At higher clay content, the melt viscosity during the processing of PP matrix–glass fibre–nanoclay was high. This phenomenon could possibly hinder the complete dispersion of nanoclays during melt mixing and thus, resulted in the improper distribution of nanoclays within the matrix polymer [97].

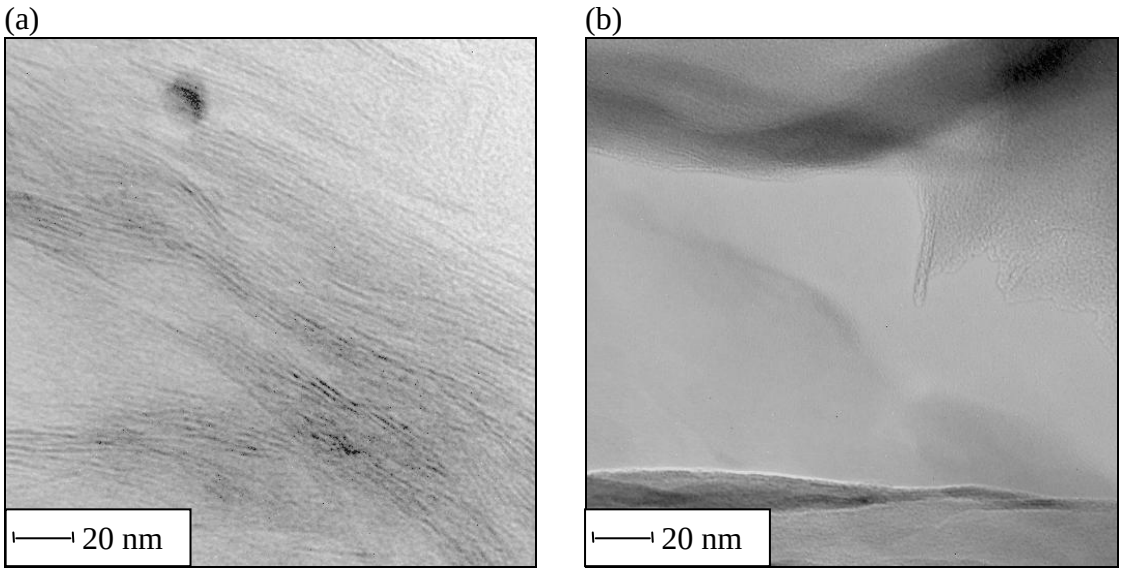

Figure 4.81: TEM images of: (a) PP/G15/NCUT6 and (b) PP/G15/NCUT9 hybrid composites

To examine this effect, TEM images of these composites were taken at relatively lower magnification and shown in Figure 4.81. In the PP/G15/NCUT6 hybrid composite (Figure 4.81 (a)), the distribution of particles in the matrix was good and uniform

whereas in PP/G15/NCUT9 hybrid composite, there was the formation of agglomerated particle in the matrix (Figure 4.81 (b)). This agglomerated site will initiate stress concentration areas, especially in tension, thus resulting in premature failure. Other researchers [164, 181] have also reported that the presence of agglomeration in epoxy-GF composites, which led to the deterioration of the mechanical properties of the material.

From the XRD results (Figure 4.16, Table 4.3), PP/G15/NC9 had a lower d-spacing, relative to PP/G15/NC6. The lower interlayer d-spacing implied the presence of agglomerations of the NC in the composite system. On the other hand, higher interlayer d-spacing may mean a better dispersion of the NC within the matrix and consequently, enhanced the properties. This is reflected in the enhancement as well as the reduction of the tensile strength in (PP/G15)/NC6 and (PP/G15)/NC9 hybrid composites, respectively (Table 4.7).

Meanwhile, it was observed that the tensile modulus of hybrid composites increased with increasing clay content (Figure 4.79). An insignificant change in the tensile modulus was observed with the addition of 3 phr of clay (3.42 GPa) into PP/G15 composite (3.43 GPa). Further addition of 6 phr clay increased the tensile modulus by about 18% to 4.05 GPa, which is in accordance with the trend reported elsewhere [12]. The improvement of modulus could be due to the exfoliation of clay nanoparticles in the matrix, which restricts the mobility of polymer chains under loading. The orientation of clay platelets and polymer chains with respect to loading direction can also contribute to the reinforcement effect [97]. It has been reported by other researchers [164] that the improvement in modulus in the hybrid composites (PP/GF/NC) is mainly attributed to the improvement of the matrix modulus from particulate filler dispersion. Thus, it seems that a synergistic effect has take place by incorporating particulate filler in the matrix, leading to higher stiffness than would otherwise be expected, solely on

the basis of the change in the matrix modulus. However, with the addition of 9 phr of clay to the system, the tensile modulus increased by about 22%, which was only 4% higher than composite with 6 phr of clay. The marginal rate of increment in the tensile modulus could be due to the presence of excessive agglomeration in the hybrid system [97]. Agglomeration of nanoclay leads to a reduction of the aspect ratio of the clay and thus reduces the contact surface between nanoclay and glass fibre composite [140]. Similar trends have been observed for PP/G30/NC and PP/G45/NC hybrid composites (Appendices 4.32 and 4.33).

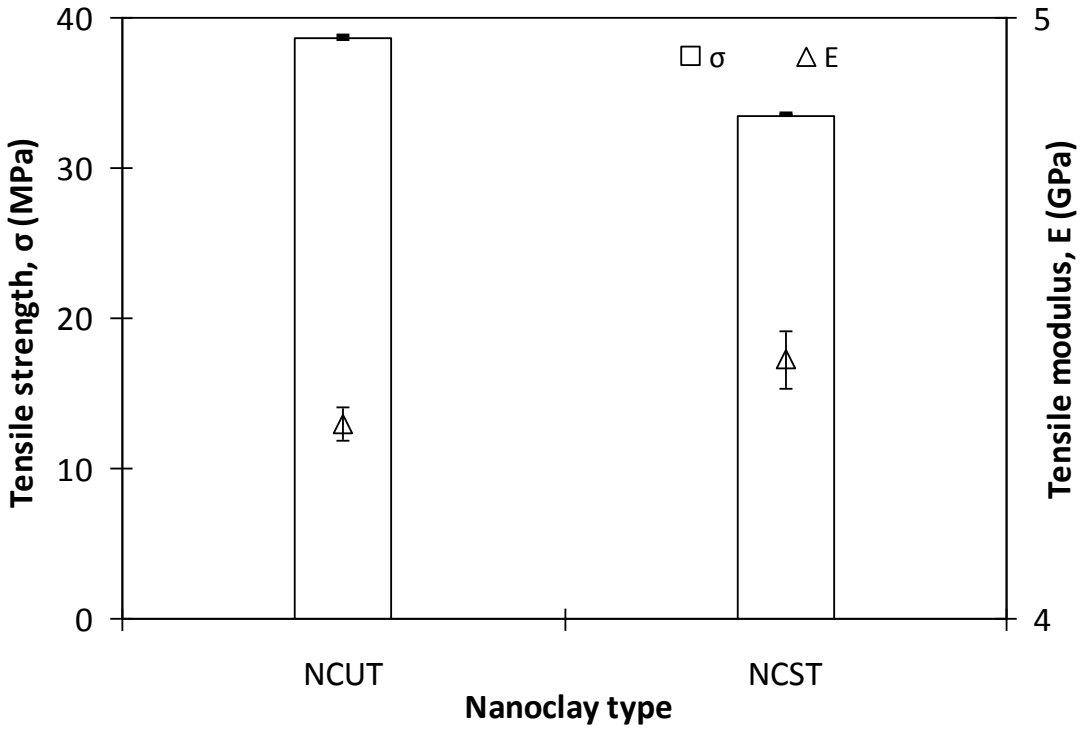

Figure 4.82: Tensile strength and tensile modulus of (PP:C5)/G15 hybrid composites with treated and untreated nanoclays

Figure 4.82 shows the effect of treated and untreated clay additions on the tensile behaviour of the (PP:C5)/G15 composite hybrid composite. It can be seen that the hybrid composite with untreated clay exhibited slightly higher tensile strength values, 38.64 MPa, as compared to those with treated clay, 33.49 MPa. This result indicates that modifying the clay surface had no significant influence on the tensile

strength of the hybrid composite due to the dominating effect of fibre reinforcement. The same trend has been obtained by Bozkurt *et al.* [87].

Interestingly, there was a synergistic effect on the tensile modulus when the untreated and treated nanocomposites were used as the matrix for glass fibre reinforced composite. As shown in Table 4.7, the tensile modulus of the PP/G15/NCUT6 hybrid composite improved by about 35% to 4.32 GPa relative to (PP:C5)/NCUT6 nanocomposite (3.19 GPa), whereas, the tensile modulus of the PP/G15/NCST2 hybrid composite resulted in better improvement of about 80% to 4.43 GPa relative to (PP:C5)/NCST2 nanocomposite (2.46 GPa). The increment in tensile modulus observed for treated clay hybrid composite than untreated clay hybrid composite could be attributed to the improvement in the interfacial adhesion between the fillers and the matrix.

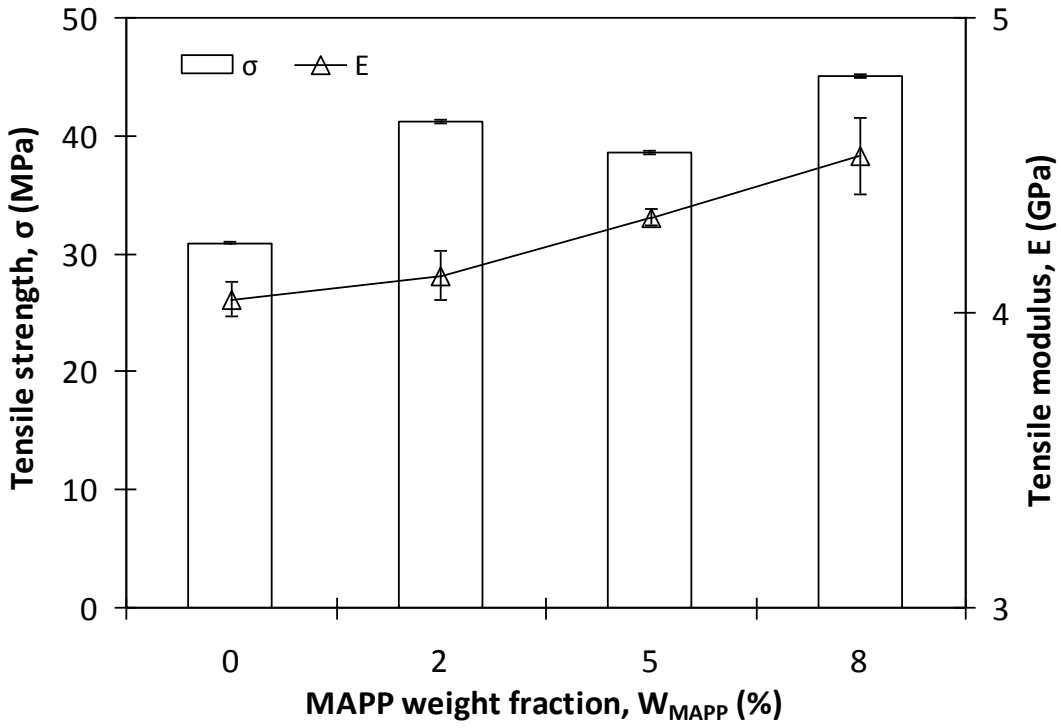

Figure 4.83: Tensile strength and tensile modulus of PP/G15/NCUT6 hybrid composites with different MAPP contents

Figure 4.83 shows the tensile properties of PP/G15/NCUT6 hybrid composite as a function of MAPP loadings. Generally, it can be observed that the tensile strength of the composites increased with increasing MAPP content. An increment of about 33% was recorded for hybrid composite with the presence of 2 *wt%* of MAPP (41.20 MPa) when compared with uncompatibilised PP/G15/NCUT6 hybrid composite (30.89 MPa). On the other hand, a slight reduction in this value was observed with the addition of 5 *wt%* of MAPP (38.64 MPa). Meanwhile, further addition of 8 *wt%* of MAPP resulted in an improvement of about 45% in the tensile strength of the hybrid composite (Table 4.7). Hybrid composite containing of compatibiliser showed higher mechanical properties than the uncompatibilised materials, since MAPP provides bonding between clay and glass fibre, resulting in the improved interfacial adhesion between matrix and both fillers [98].

The tensile modulus for compatibilised nanocomposites showed continuous increment with the addition of MAPP relative to uncompatibilised materials (Table 4.7). This appears to be due to the improved compatibility between the matrix and the fillers. The highest tensile modulus was obtained for hybrid composites compatibilised with 8 *wt%* of MAPP (4.53 GPa).

As shown in Figure 4.84, the addition of MAPP in PP/NCST2 nanocomposite resulted in no significant change in the tensile strength value. The addition of 2 *wt%* to 8 *wt%* of MAPP only maintained this value between 33 – 34 MPa (Table 4.7). On the other hand, the tensile modulus increased monotonously, with increase in MAPP contents from 2 *wt%* to 8 *wt%*. The improvement in tensile modulus is an indicator of an enhancement in the material stiffness, resulting from good dispersion and improved interfacial adhesion between treated nanoclay, glass fibre and the PP matrix. Moreover, it is believed that the interlayer expansion resulted mainly from the penetration of

MAPP molecules between clay platelets, leading to a higher possibility for the matrix to diffuse within nanoclay layers.

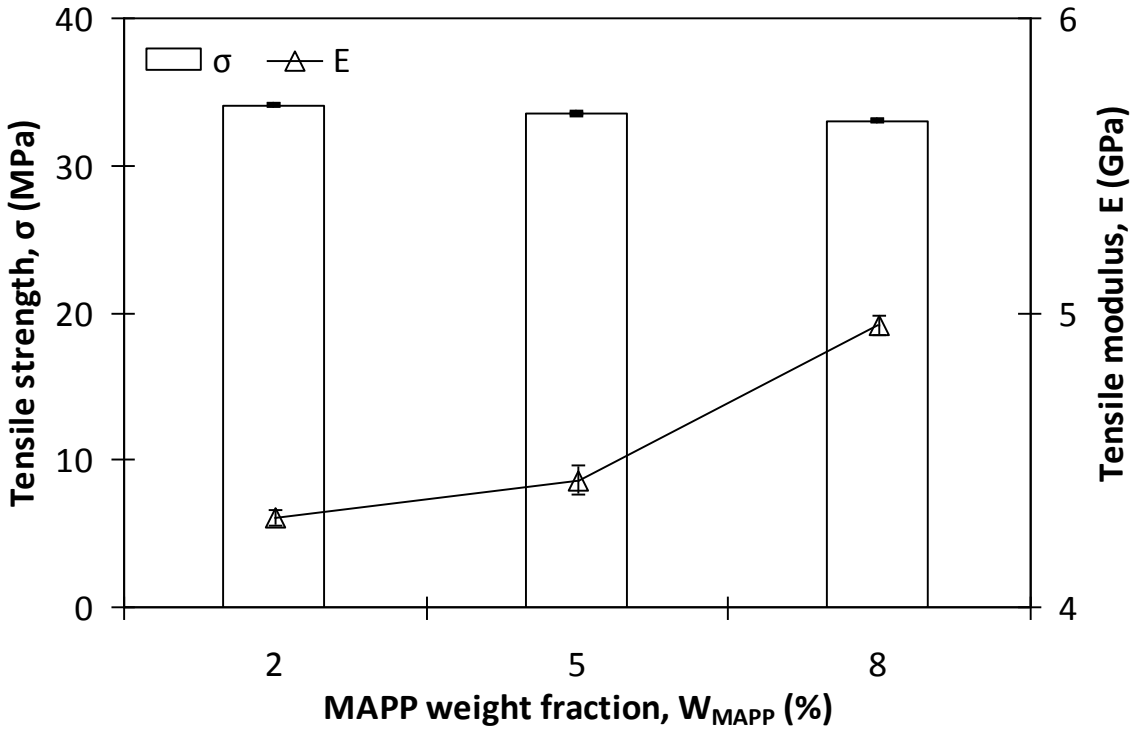

Figure 4.84: Tensile strength and tensile modulus of PP/G15/NCST2 hybrid composites with different MAPP contents

Tensile strain

Tensile strain was simultaneously reduced with increase in clay particle content (Figure 4.85). The tensile strain reduced from 7.42% for PP/G15 to 6.58%, 4.15% and 3.86% with the addition of 3 phr, 6 phr and 9 phr of clay, respectively. These results can be attributed to the fact that reinforcing fibres strongly restrains the deformation of the matrix polymer, as demonstrated in several previous studies [182, 183]. The trend remained essentially unchanged for PP/G30/NC and PP/G45/NC hybrid composites (Appendices 4.34 and 4.35).

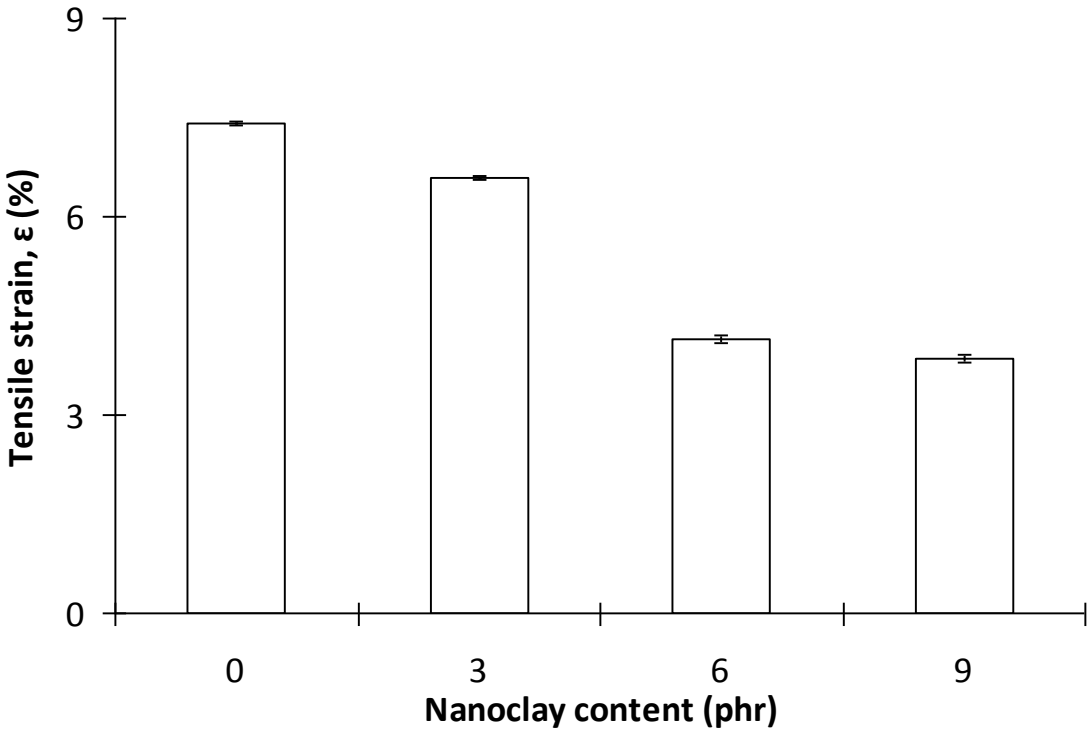

Figure 4.85: Tensile strain of injection-moulded PP/G15 hybrid composites with different NCUT contents

Appendix 4.36 shows the tensile strain of hybrid composites as a function of clay surface treatment. The tensile strain for untreated clay hybrid composite was found to be 3.90%. Meanwhile, a slight increment in this value, to 4.87%, was obtained for treated clay hybrid composite, which indicated an improvement in material ductility due to the presence of organic clay surfactant. There was no significant change in tensile strain with the addition of MAPP in the untreated clay (Appendix 4.37) and treated clay hybrid composites (Appendix 4.38).

4.7.2 Flexural properties

Results for flexural properties of composite specimens, together with the supporting images from SEM are shown in Figures 4.86 – 4.99. The data extracted from these figures are tabulated in Table 4.8.

Table 4.8: Flexural properties data of PP, PP/GF, PP/NC and PP/GF/NC composites

Sample	Flexural strength (MPa)	Flexural modulus (GPa)	Flexural displacement (mm/mm)
PP	37.26	1.02	0.073
PP100/NCUT3	38.60	1.04	0.078
PP100/NCUT6	40.81	1.13	0.073
PP100/NCUT9	41.75	1.23	0.069
(PP100:C0)/$NCST2_{800}$	41.22	1.31	0.072
(PP92:C8)/$NCST2_{100}$	41.33	1.28	0.073
(PP92:C8)/$NCST2_{300}$	41.82	1.30	0.072
(PP92:C8)/$NCST2_{500}$	41.03	1.29	0.072
(PP92:C8)/$NCST2_{800}$	42.16	1.35	0.071
(PP95:C5)/NCUT3	42.77	1.37	0.072
(PP98:C2)/NCUT6	44.23	1.47	0.071
(PP95:C5)/NCUT6	45.97	1.51	0.070
(PP92:C8)/NCUT6	45.53	1.51	0.068
(PP95:C5)/NCUT9	46.28	1.56	0.067
(PP98:C2)/NCST2	48.23	1.58	0.069
(PP95:C5)/NCST2	49.66	1.65	0.066
(PP92:C8)/NCST2	48.01	1.57	0.072
PP85/G15	42.29	1.91	0.069
PP70/G30	46.94	3.09	0.053
PP55/G45	51.23	5.20	0.036
(PP77:C8)/$G15_{50}$	50.07	2.20	0.060
(PP77:C8)/$G15_{100}$	51.14	2.33	0.060
(PP77:C8)/$G15_{150}$	49.99	2.21	0.060
(PP83:C2)/G15	56.34	2.54	0.055
(PP80:C5)/G15	56.21	2.55	0.053
(PP77:C8)/G15	55.86	2.57	0.053
(PP65:C5)/G30	61.96	3.90	0.032
(PP50:C5)/G45	61.12	5.20	0.022
(PP85)/G15/NCUT3	43.27	1.89	0.066
(PP85)/G15/NCUT6	52.10	2.44	0.059
(PP85)/G15/NCUT9	51.16	2.46	0.056
(PP70)/G30/NCUT3	47.11	3.12	0.052
(PP70)/G30/NCUT6	50.37	3.31	0.049
(PP70)/G30/NCUT9	52.39	3.56	0.045
(PP55)/G45/NCUT3	47.98	5.26	0.027
(PP55)/G45/NCUT6	51.47	5.24	0.031
(PP55)/G45/NCUT9	50.52	5.00	0.034
(PP83:C2)/G15/NCUT6	62.29	2.67	0.046
(PP80:C5)/G15/NCUT6	62.55	2.59	0.053
(PP77:C8)/G15/NCUT6	69.36	2.91	0.043
(PP82:C2)/G15/NCST2	55.47	2.70	0.057
(PP80:C5)/G15/NCST2	53.70	2.54	0.059
(PP77:C8)/G15/NCST2	54.83	2.66	0.059

4.7.2.1 Clay nanocomposites

Flexural strength and flexural modulus

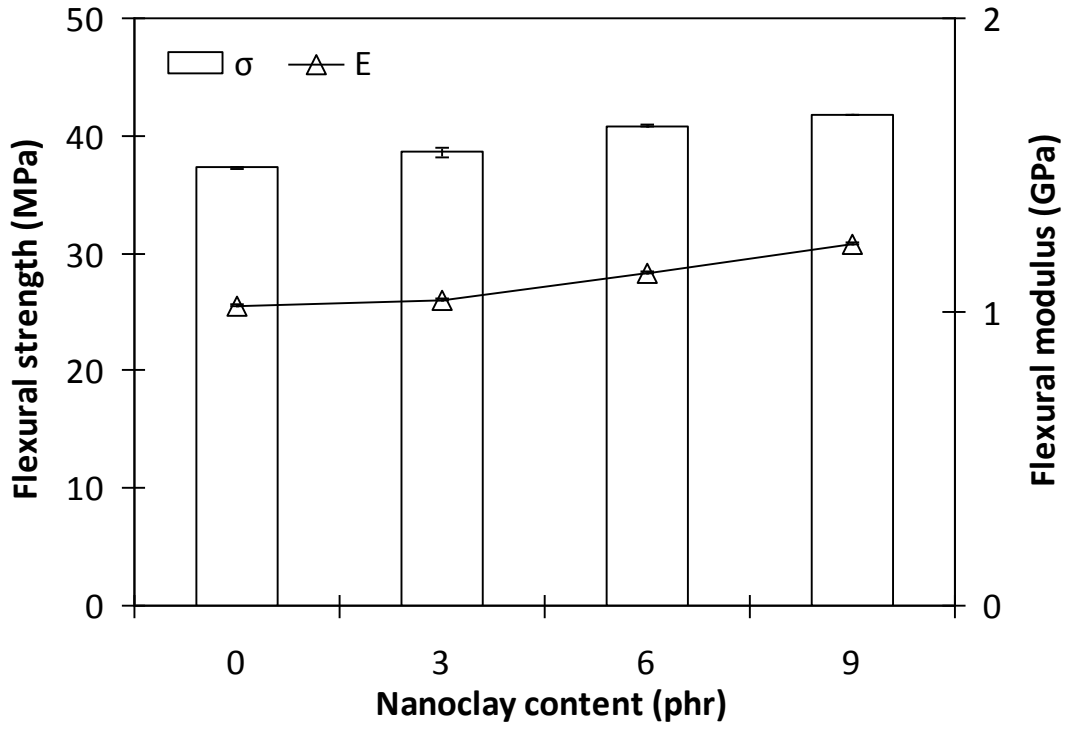

Figure 4.86: Flexural strength and flexural modulus of untreated clay nanocomposites

Figure 4.86 shows the effect of untreated nanoclay loading on the flexural strength and flexural modulus of PP/NC nanocomposites. From Table 4.8, the addition nanoclay significantly led to a continuous improvement in the flexural strength from 37.26 MPa for PP matrix to 38.60 MPa, 40.81 MPa and 41.75 MPa for nanocomposites with the incorporation of 3 phr, 6 phr and 9 phr of NC, respectively. Meanwhile, only a slight increment in the flexural modulus was observed with the addition of 3 phr nanoclay in the system (1.04 GPa), relative to PP matrix (1.02 GPa). However, further increase in the nanoclay content to 6 phr and 9 phr resulted in substantial enhancement in this value to 1.13 GPa and 1.23 GPa, respectively. The silicate layer orientation may also contribute to the reinforcement effects observed. Kusmono *et al.* [156] and Ding *et*

al. [184] suggested that the improvement in these properties could be attributed to higher stiffness and aspect ratio of silicate layers in the composites system.

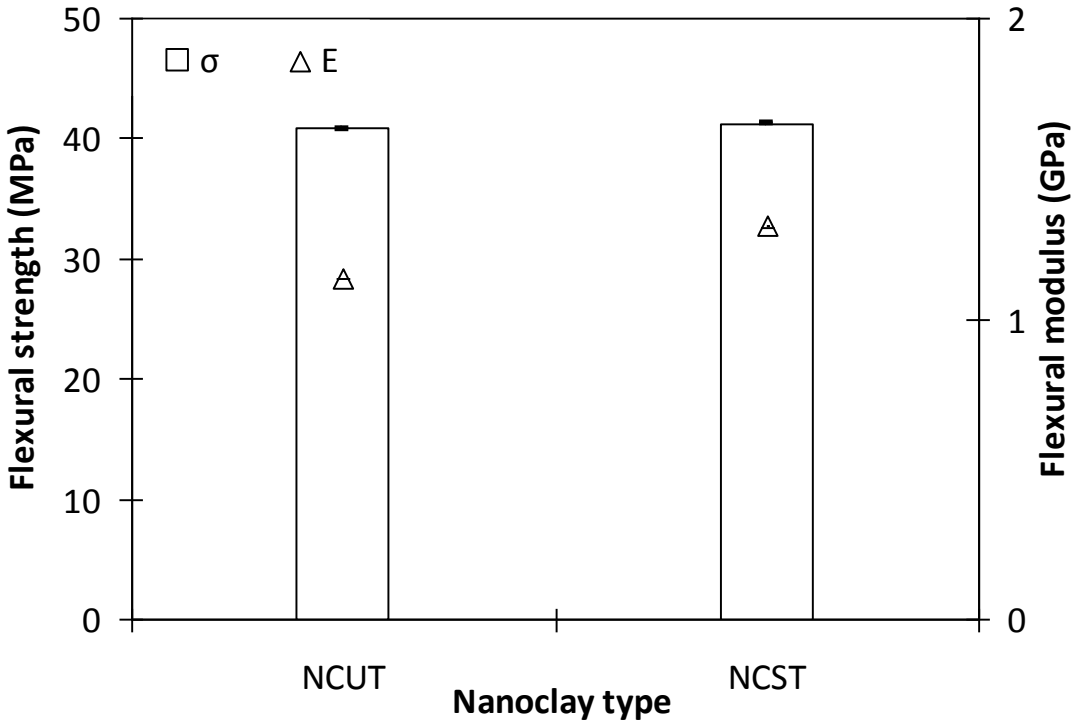

Figure 4.87: Flexural strength and flexural modulus of nanocomposites with untreated and treated nanoclays

Figure 4.87 presents the flexural strength and flexural modulus for untreated and treated nanocomposites. As expected, from Table 4.8, the addition of treated clay nanoclay, PP/NCST2 significantly improved the flexural strength (41.22 MPa) and flexural modulus (1.31 GPa), when compared with untreated clay nanocomposite, PP/NCUT6. This behaviour can be explained by the finer and more uniform dispersion of clay in the system, due to the presence of surface treatment in the treated nanoclay, which improved the interfacial adhesion between clay and PP matrix. In the untreated clay nanocomposite system, because of the incompatibility between the polar clay and the non-polar PP matrix, the possibility for the clay to form agglomeration is higher, hence deterioration in the flexural properties [185]. A similar trend was also observed by Bozkurt *et al.* [87].

Figure 4.88 shows the effect of processing screw speed on the flexural properties of PP/NCST2 nanocomposites. Similarly, as observed for tensile properties, these values increased consistently with increase in screw speeds. The highest flexural strength (42.16 MPa) and flexural modulus values (1.35 GPa) were observed for nanocomposite compounded with 800 rpm (Table 4.8). Ahmad *et al.* [186] suggested that the reinforcement effect depends on four factors, with respect to the nanoclay; which are rigidity, aspect ratio, degree of exfoliation and the affinity with the matrix polymer. It should be noted that, the shear forces created during the melt processing is one of the main factors in determining the dispersion of nanoclay in the nanocomposites system. By using a high screw speed during extrusion, high shear force is induced, thus resulting in nanocomposite with higher degree of exfoliation.

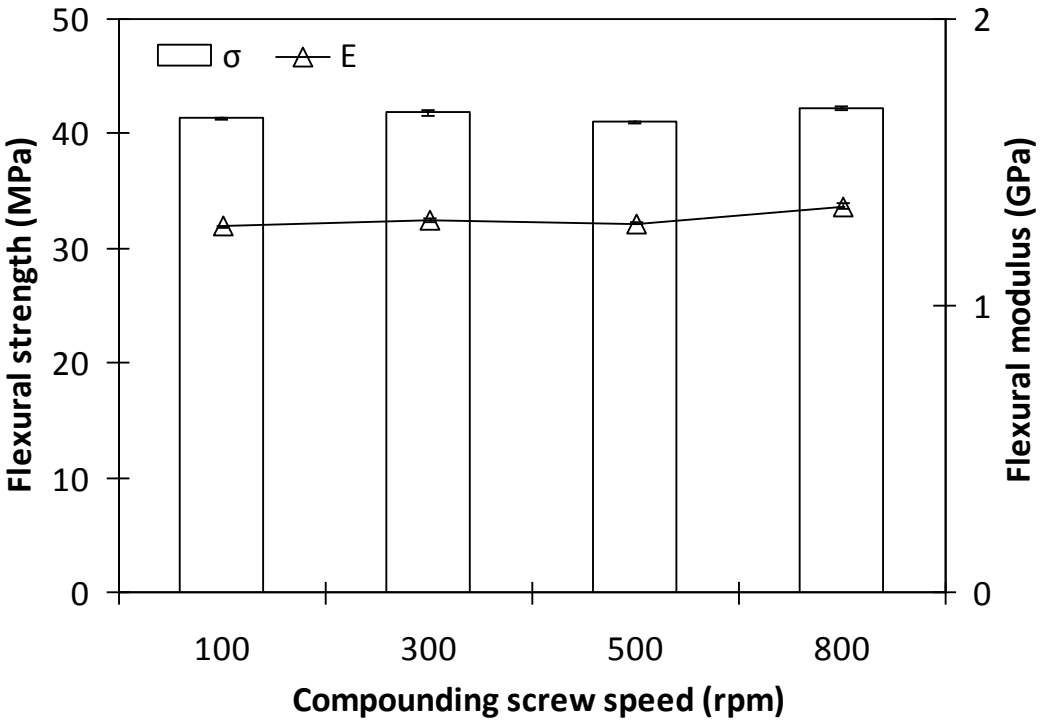

Figure 4.88: Flexural strength and flexural modulus of PP/NCST2 nanocomposites at different screw speeds

From Table 4.8, the addition of compatibiliser increased the flexural strength and flexural modulus of the nanocomposites. As seen from Figure 4.89, a sharp

increment of both properties were noticed when 2 *wt%* of MAPP was incorporated into the system. Further addition of 5 *wt%* and 8*wt%* MAPP only resulted in a slight increment in these values. It is possible that the presence of compatibiliser improved the clay-matrix compatibility, irrespective of the MAPP amount.

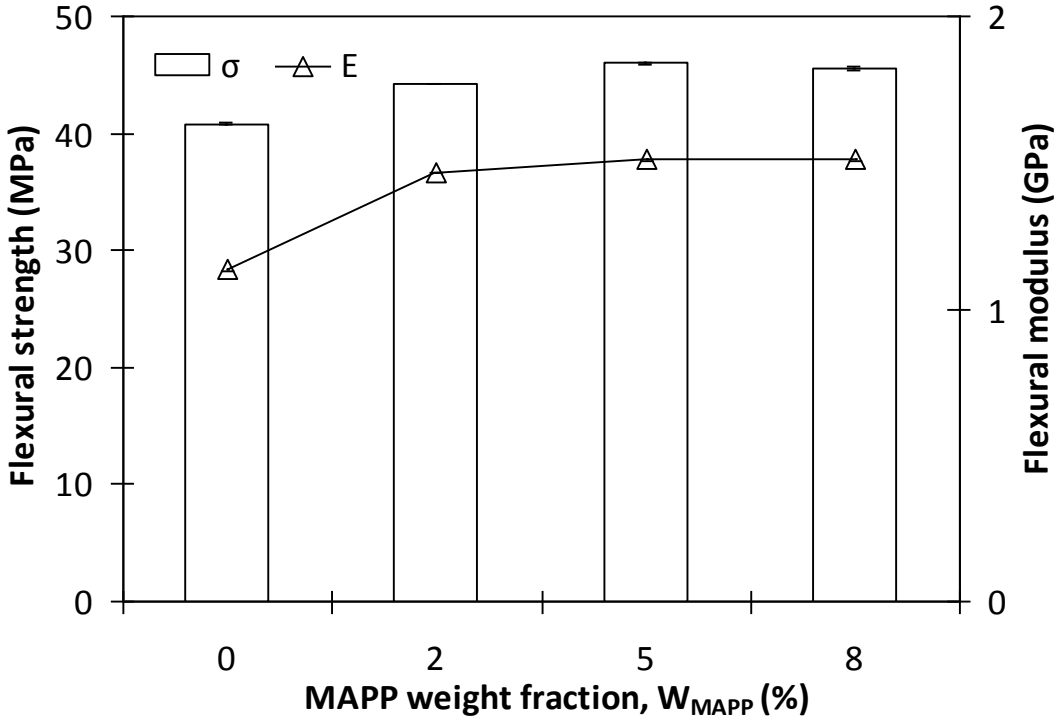

Figure 4.89: Flexural strength and flexural modulus of PP/NCUT6 nanocomposites with different MAPP contents

The variations in the flexural strength and flexural modulus of PP/NCST2 with different MAPP loadings are shown in Figure 4.90. From Table 4.8, a substantial increment in flexural strength and flexural modulus to 49.66 MPa (20%) and 1.65 GPa (26%), respectively were observed with the addition of 5 *wt%* of MAPP, relative to the uncompatibilised PP/NCST2. Meanwhile, further addition of 8 *wt%* of MAPP resulted in a slight decrement in both values. As previously discussed in tensile properties section, beyond an optimum concentration of MAPP, plasticisation effect might occur, which can lead to a decrement in the target properties.

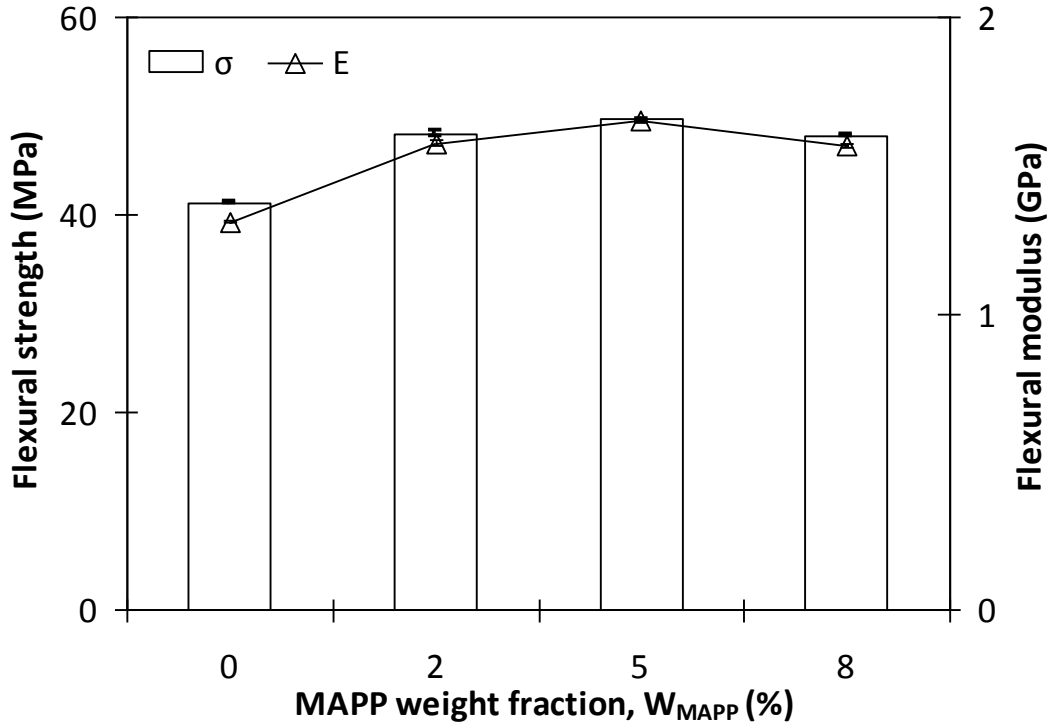

Figure 4.90: Flexural strength and flexural modulus of PP/NCST2 nanocomposites with different MAPP contents

Flexural displacement

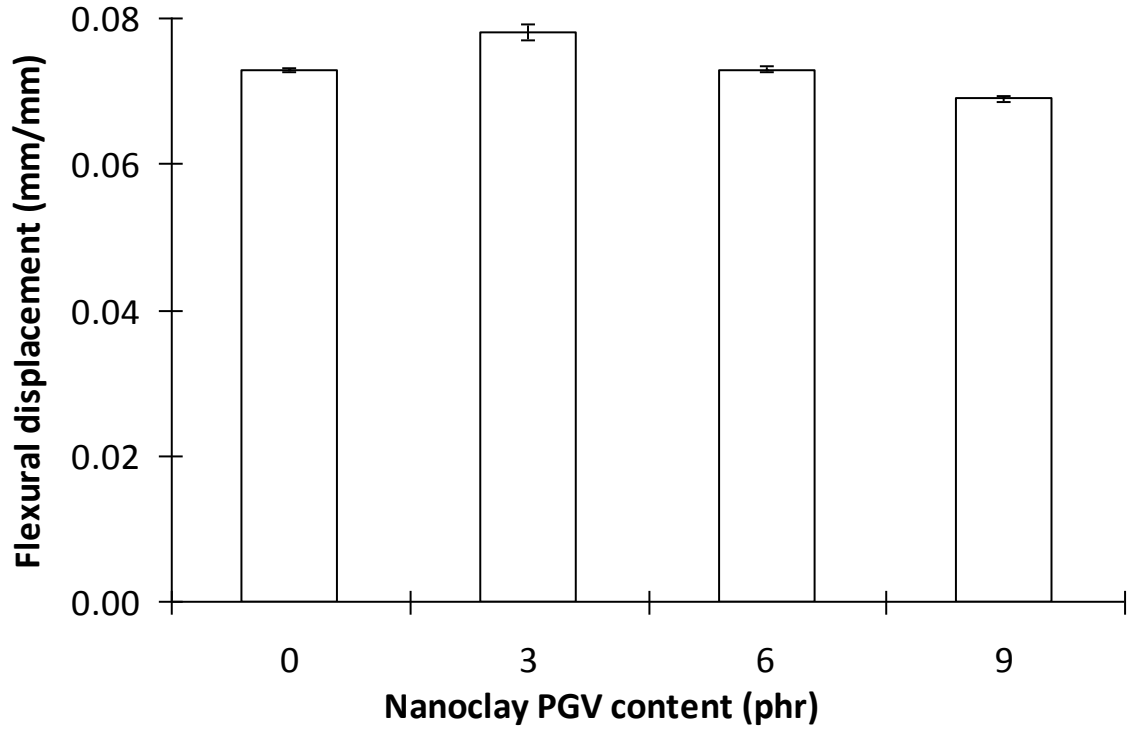

Figure 4.91: Flexural displacement of clay nanocomposites

From Figure 4.91, it can be seen that the flexural displacement of the nanocomposites were greatly affected by the addition of high nanoclay loading. Flexural displacement for PP was recorded at 0.073 mm/mm, increased to 0.078 mm/mm as 3 phr of nanoclay was added into the system. By contrast, the incorporation of 6 phr and 9 phr of clay resulted in the reduction of this value to 0.073 mm/mm and 0.069 mm/mm, respectively. It is suggested that with the addition of nanoclay, the nanocomposites behaved in a brittle manner due to rigid and stiff behaviours of the nanoclay itself.

Meanwhile, the effect of clay surface treatment on the flexural displacement of the nanocomposites is shown in Appendix 4.39. A slight decrement in the flexural displacement value was noticed with the addition of treated, relative to the untreated clay nanocomposite. Similar trend was observed for PP/NCST2 nanocomposites with respect to the extrusion screw speed. The flexural displacement value also slightly reduced as the screw speed increased during extrusion processing (Appendix 4.40). Moreover, the flexural displacement of PP/NCUT6 and PP/NCST2 nanocomposites also slightly decreased with the addition of MAPP in the system (Appendices 4.41 and 4.42).

4.7.2.2 Glass fibre composites

Flexural strength and flexural modulus

Figure 4.92 shows that increase in fibre contents led to increases in the flexural strength and the flexural modulus. The flexural strength increased from 37.26 MPa for PP matrix to 42.29 MPa, 46.94 MPa and 51.23 MPa for composites with 15 *wt%*, 30 *wt%* and 45 *wt%* of GF contents. This observation was expected and can be explained by the contribution of glass fibre, as a brittle and tough material [10]. The flexural modulus was also enhanced by increasing the glass fibre contents in the composite system.

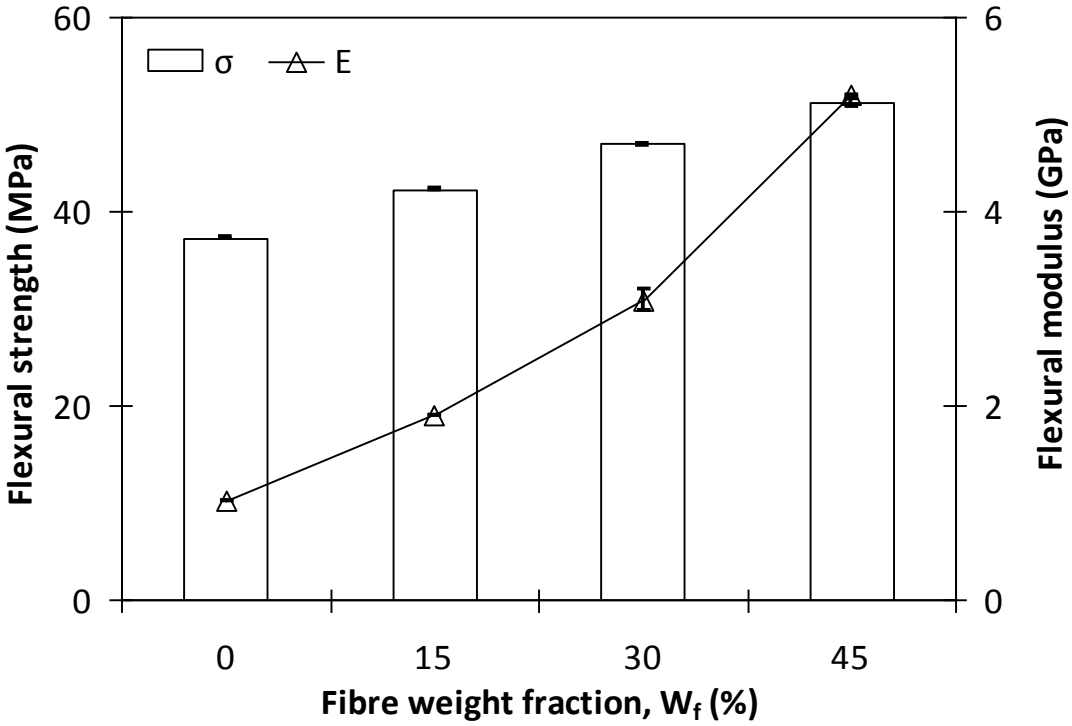

Figure 4.92: Flexural strength and flexural modulus of glass fibre composites

In flexural testing, the maximum stresses in stress-deflection curves occurred not at maximum deflection. Within that region, the effect of even poor interfacial adhesion may not fully affect the flexural properties. In the tensile test however, maximum stress in stress-strain curve occurred when the specimen ruptured. The specimens were most likely to rupture at the poor interfacial area. This could explain the reduction in tensile strength, and an increment in flexural strength with incorporation of glass fibre.

Figure 4.93 shows the effect of the different extrusion screw speeds, from 50 rpm to 150 rpm, on the flexural strength and flexural modulus of PP/G15 composites. Composite processed with 50 rpm screw speed, exhibited flexural strength and flexural modulus values of 50.07 MPa and 2.20 GPa, respectively. Meanwhile, when 100 rpm processing screw speed was used, both properties were enhanced to 51.14 MPa and 2.33 GPa. A possible reasoning is that at higher screw speed, the possibility of a better glass fibre dispersion in the PP matrix was high. On the other hand, composite processed with the highest screw speed, which is 150 rpm, showed a slight decrement in the flexural

strength and flexural modulus values. This may be due to the reduction in the fibre length as a result of the fibre breakage. This result is in agreement with the FLD measurement (Figures 4.4 – 4.6, Table 4.2). This behaviour indicated that for this particular composition, the 100 rpm screw speed is apparently the optimum parameter for material processing in order to obtain composites with acceptable degree of homogeneity in terms of wettability and fibre bundle dispersion.

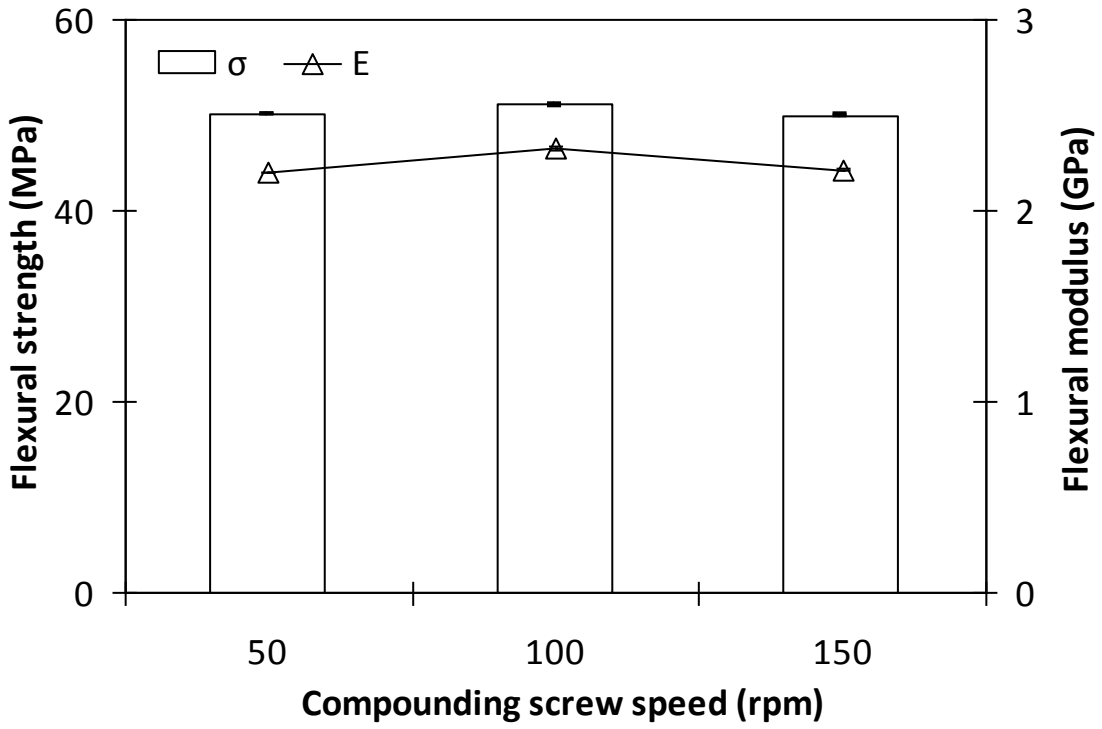

Figure 4.93: Flexural strength and flexural modulus of PP/G15 composites at different screw speeds

Figure 4.94 also clearly demonstrates that the incorporation of MAPP significantly improved the flexural strength of PP/G15 composite. With 2 *wt%* inclusion of MAPP, the flexural strength of the composite increased by about 33% (56.34 MPa) when compared with uncompatibilised composite systems (42.29 MPa). Further addition (5 *wt%* and 8 *wt%*) of MAPP resulted in a lower magnitude of increment, to 56.21 MPa and 55.86 MPa, respectively (Table 4.8). The flexural modulus of the compatibilised composites also showed a continuous improvement with the addition of

MAPP. It increased from 1.91 GPa for PP/G15 composite, to 2.54 GPa, 2.55 GPa and 2.57 GPa, with the incorporation of 2 *wt%*, 5 *wt%* and 8 *wt%* of MAPP, respectively.

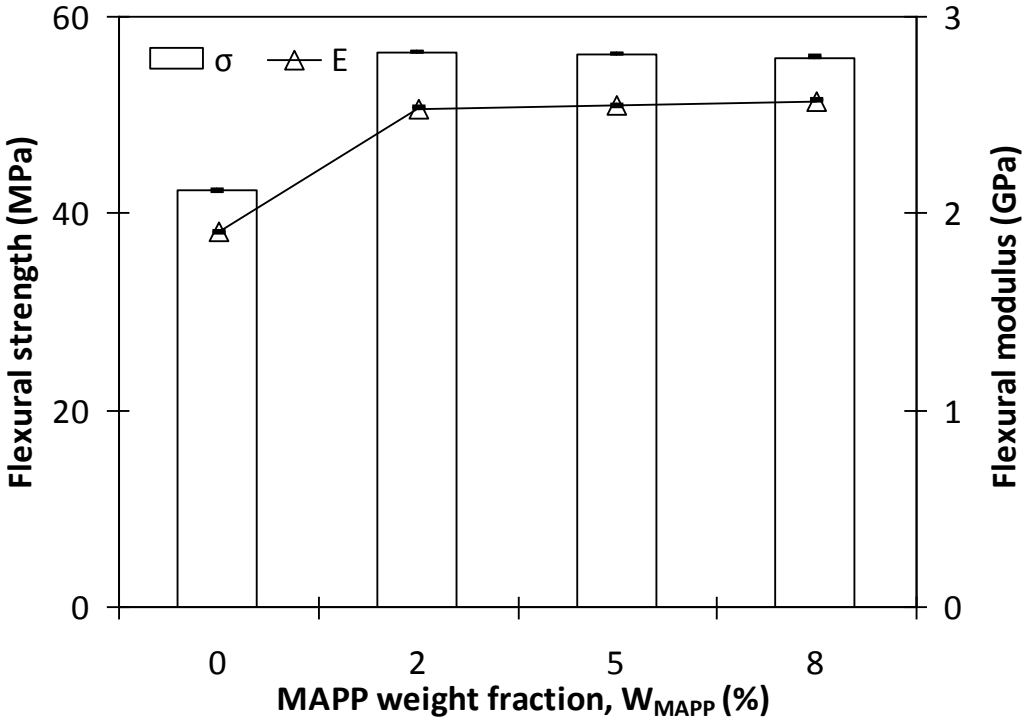

Figure 4.94: Flexural strength and flexural modulus of PP/GF15 composites with different MAPP contents

Flexural displacement

Flexural displacement decreased consistently with increase in glass fibre contents (Figure 4.95). This means that the material became tougher with the increase in fibre content. The flexural displacement obtained for PP matrix was 0.073 mm/mm. From Table 4.8, the maximum reduction of about 51% to 0.036 mm/mm was recorded for composite containing the highest glass fibre content, PP/G45 composite. This is due to the stiff and rigid behaviour of the glass fibre which reduced the ductility of the composites. Moreover, the stress concentrations at the fibre ends also resulted in the notching effect, which led to failure at low displacement.

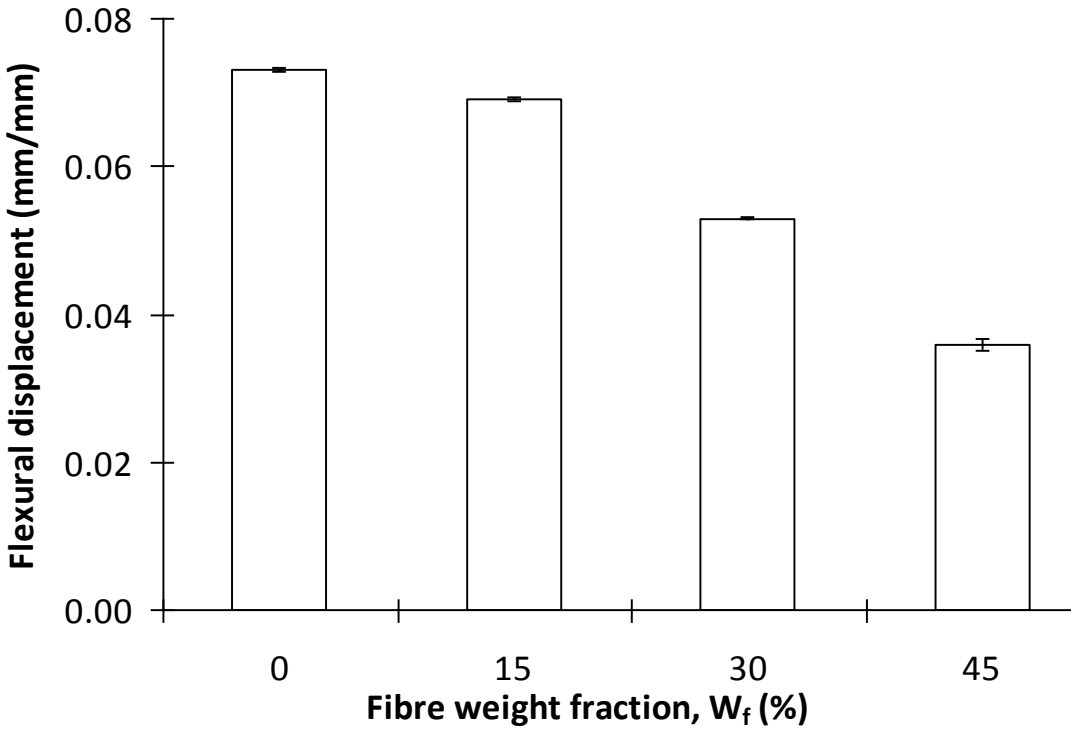

Figure 4.95: Flexural displacement of glass fibre composites

Meanwhile, there is no significant change in the flexural displacement of the (PP:C8)/G15 composites compounded with different screw speeds (Appendix 4.43). On the other hand, the flexural displacement recorded for PP/G15 composite is 0.069 mm/mm, which is lower than that observed for PP matrix (0.073 mm/mm). The incorporation of MAPP into the composites further reduced the flexural displacement of the composites, indicating an enhancement of the material's stiffness (Appendix 4.44).

4.7.2.3 Glass fibre/ nanoclay hybrid composites

Flexural strength and flexural modulus

Figure 4.96 shows the effect of clay loading on the flexural properties (strength and modulus) of 15 *wt%* of glass fibre composites. From this figure, it can be seen that the flexural strength and flexural modulus of the hybrid composites, successively increased with increasing in clay loading. Although the flexural failure strength of the composite is a fibre dependent property, the matrix also has an influence on the overall

properties of the composite. Haque *et al.* [123] demonstrated that the enhancement in flexural properties of fibre/nanocomposite is achieved due to the improvement in the properties of the matrix-clay phase composites portion and also the unique interfacial fibre-matrix bonding characteristics. A slight increment in the flexural strength by about 2% (to 43.27 MPa) is observed with the addition of 3 phr of untreated nanoclay in the hybrid composite system, relative to PP/G15 composite (42.29 MPa). Further incorporation of 6 phr and 9 phr of nanoclay significantly enhanced this value by about 23% and 21%, respectively (Table 4.8).

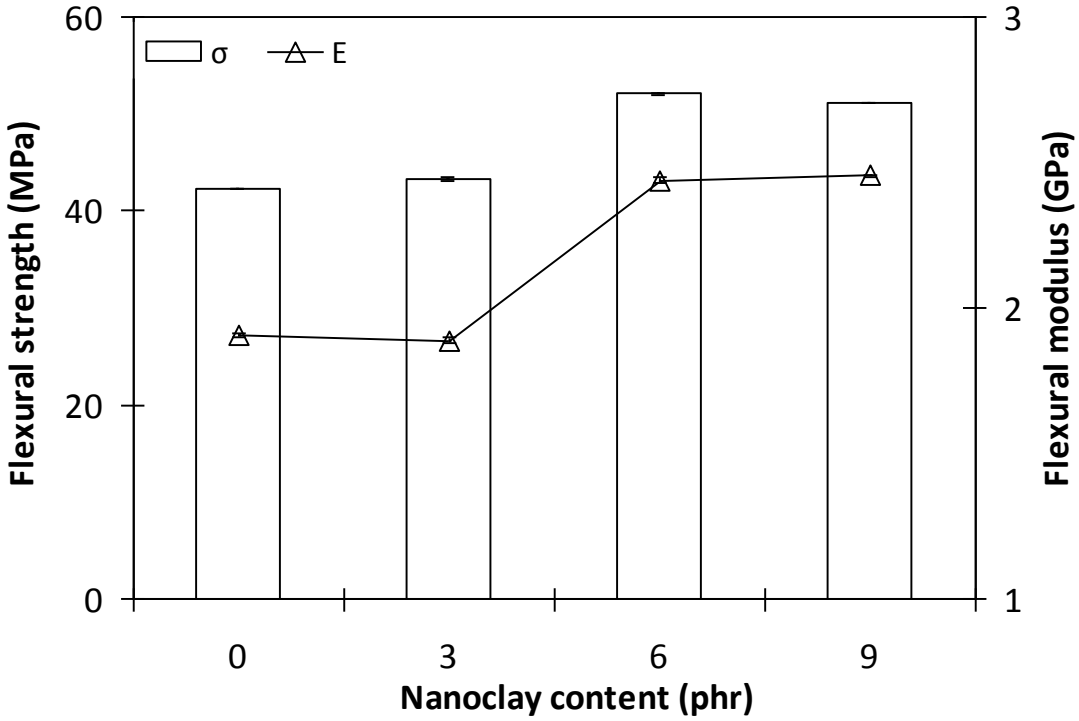

Figure 4.96: Flexural strength and flexural modulus of PP/G15 hybrid composites with different NCUT contents

Kornmann *et al.* [167] reported that the strength of the matrix is improved by the presence of nanoclay. The addition of GF and NC appeared to have provided a good combination of reinforcements to carry the load during the flexural deformation of the composite. This unique combination of nano- and micro-scale reinforcements offer the opportunity to design new PP composites with reduced overall filler levels, offering the

advantages of high specific modulus and strength, lighter weight parts with improved surface gloss, reduced mould and tool wear *etc.* [187]. However, it is also observed that the optimum flexural strength was achieved at 6 phr of clay (52.10 MPa). At 9 phr of NC loading, the flexural strength decreased to 51.16 MPa. The distribution of particles in the matrix is an important factor to be considered in this case. The possibility for a formation of agglomerates is greater at higher clay content, consequently this can lead to a stress concentration effect. The same behaviour has been reported by other researchers [167, 188, 189].

The incorporation of clay yields a significant improvement in the flexural modulus of the PP/G15 composites, which is attributed to the stiffness and rigidity of the clay nanoparticle itself. There is an insignificant change in the flexural modulus with the addition of 3 phr of nanoclay. Meanwhile, as for the composite with higher clay loading, a 28% and 29% increment in the flexural modulus values were observed with the incorporation of 6 phr and 9 phr of nanoclay, respectively (Table 4.8). Nanoclay can adhere on the GF surface as well as to the PP matrix which affect the interfacial properties, such as: the adhesive strength and interfacial stiffness of the composite medium [190, 191]. These factors play a crucial role in the stress transfer efficiency from the matrix to the reinforcement agents and the elastic deformation. The high surface area of clay increased the contact area with the matrix, thereby increasing the interface. The enhanced interfacial property and the effective stress transfer increased the modulus of the fibre composites, based on the nanocomposite matrix.

Figure 4.97 shows the SEM micrographs of the fractured surface for PP/G15 composite and PP/G15/NCUT6 hybrid composite. The fibre surface morphology of the conventional PP/GF composite (Figure 4.97 (a)), is observed to be very clean at the interface region. In the other case (Figure 4.97 (b)), the hybrid nanocomposite shows a significant resin cracking at the interface and the surface morphology is seen to be

comparatively coarse, indicating enhancement in the interfacial bond strength. The same trend is observed for PP/G30/NC and PP/G45/NC hybrid composites (Appendices 4.45 and 4.46). On the other hand, the reduction in the flexural strength and flexural modulus values are observed for treated clay hybrid composites, relative to the untreated clay hybrid composite (Appendix 4.47).

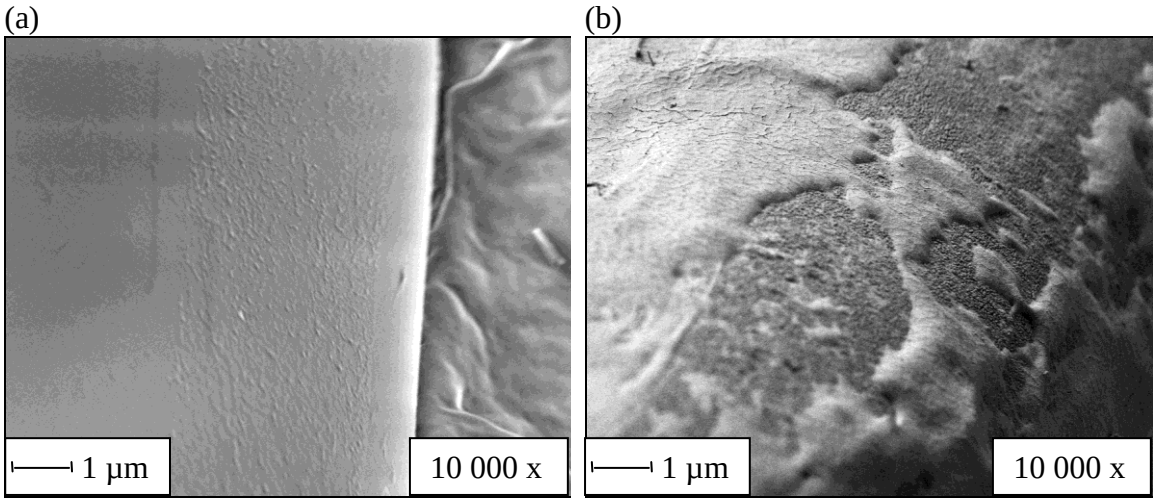

Figure 4.97: SEM images of glass fibre surface of: (a) PP/G15 composite and (b) PP/G15/NCUT6 hybrid composite

Figure 4.98 shows the variation of flexural strength and flexural modulus of PP/G15/NCUT6 hybrid composite at different levels of MAPP contents. The flexural strength and flexural modulus of hybrid composites increased with increase of MAPP (Table 4.8). It is well established that the presence of MAPP, as a coupling agent enhances the interfacial adhesion between the filler and the PP matrix, which resulted in the improvement of the flexural properties. It seems that there are two functions for MAPP in the PP/GF/NC hybrid composites. In addition to the enhancement of the interfacial between PP and glass fibre, MAPP can also be a coupling agent between PP and the nanosilicate layers [96]. By contrast, there is no significant difference in the flexural properties in respect of MAPP loadings for PP/G15/NCST2 hybrid composites (Appendix 4.48).

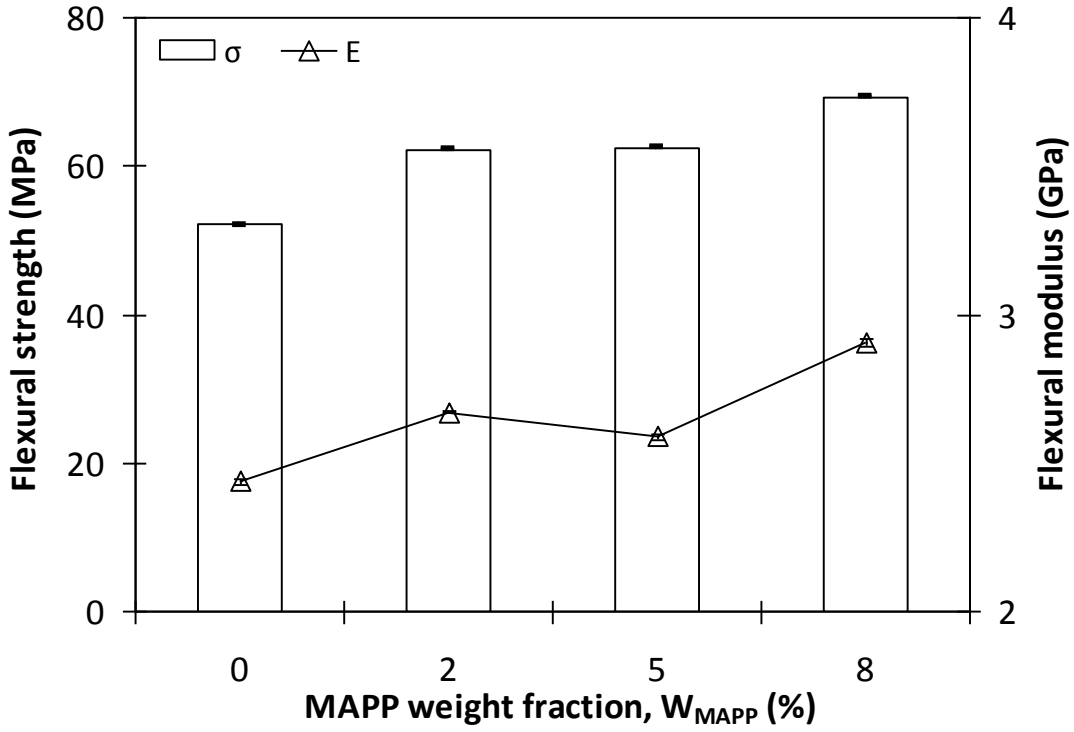

Figure 4.98: Flexural strength and flexural modulus of PP/G15/NCUT6 hybrid composites with different MAPP contents

Flexural displacement

The flexural displacement reduced with increase in clay contents in the hybrid composite (Figure 4.99). From Table 4.8, the flexural displacement reduces from 0.069 mm/mm for PP/G15 to 0.066 mm/mm, 0.059 mm/mm and 0.056 mm/mm with the addition of 3 phr, 6 phr and 9 phr of clay, respectively. These results can be attributed to the polymer chains restriction by the reinforcing fibre and nanoclay. The same trend is observed for PP/G30/NC and PP/G45/NC hybrid composites (Appendices 4.49 and 4.50).

On the other hand, the effect of clay surface treatment on the flexural displacement of nanocomposites is shown in Appendix 4.51. The flexural displacement for PP/NCUT6 was recorded at 0.053 mm/mm, whereas, with treated clay, PP/NCST2 nanocomposite, this value increased to 0.059 mm/mm. The increment in this value indicates an improvement in the material's ductility. By contrast, the addition of MAPP in PP/G15/NCUT6 hybrid composite resulted in no significant trend (Appendix 4.52).

Meanwhile, a slight increment in this value is noticed when MAPP is incorporated into PP/G15/NCST2 hybrid composites (Appendix 4.53).

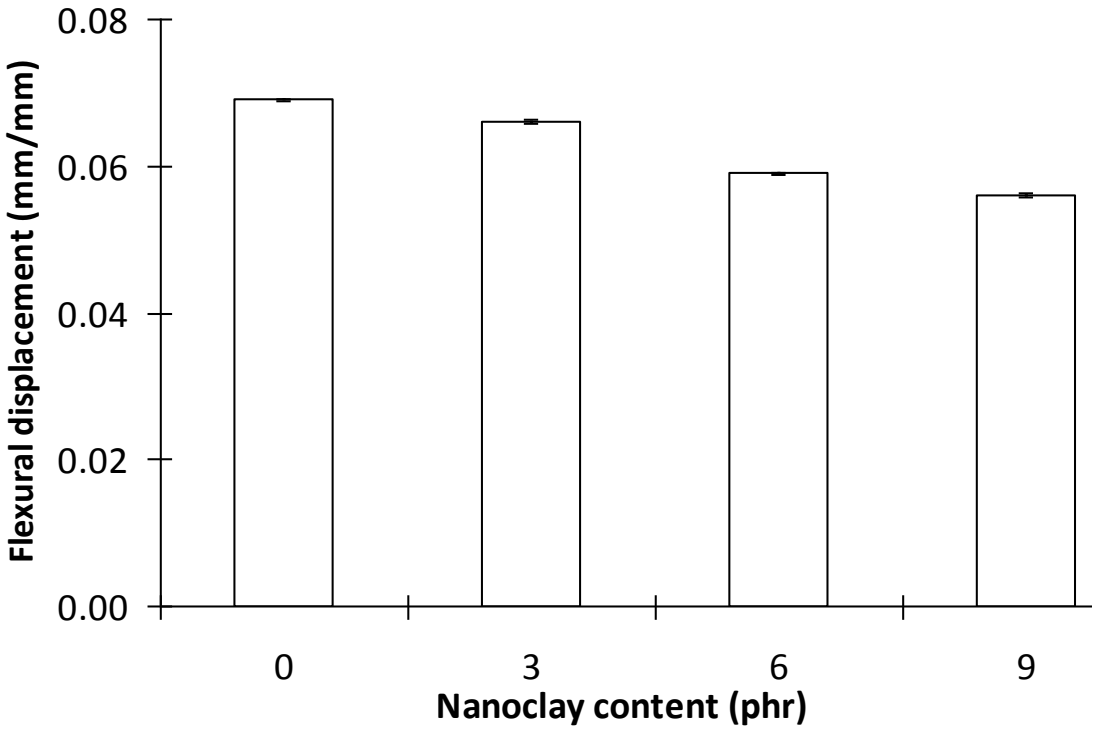

Figure 4.99: Flexural displacement of PP/G15 hybrid composites with different NCUT contents

4.7.3 Impact properties

Results from the impact measurement of composite specimens are shown in Figures 4.100 – 4.112. The data extracted from these plots are tabulated in Table 4.9. Generally, the resistance to crack propagation or fracture toughness of the PP/NC and PP/GF/NC composites is characterised by measuring the *P* (peak load), *W* (fracture energy), G_c (critical strain energy release rate) and K_c (critical stress intensity factor), using single edge notched (SEN) specimens in a three point bending (3-PB) set-up, according to ASTM E-23 standard [99]. G_c and K_c can be taken as measures of the interfacial strength. Linear elastic fracture mechanics (LEFM) methodologies have been used to characterise the toughness of composites and plastics in terms of G_c or K_c of

polymeric materials. They have been found to be effective in the characterisation of brittle polymers.

The relationship [192] between W, G_c and specimen geometry parameter ($BD\Phi$) is given by:

$$W = G_c BD\Phi \tag{4.4}$$

where B and D are the thickness and depth of the specimen, respectively. A correction factor, Φ is given by:

$$\phi = \frac{1}{2}\left(\frac{a}{D}\right) + \frac{1}{18\pi}\left(\frac{S}{D}\right)\left(\frac{a}{D}\right)^{-1} \tag{4.5}$$

where a and S are the notch depth (or crack length) and span of the specimens, respectively.

On a plot of W against $BD\Phi$ (Appendix 4.54), a straight line is obtained through the origin and its slope is taken as the G_c of the materials. The relationship between the K_c with nominal fracture stress (σ), geometry correction factor (Y) and notch or crack length (a) is given by:

$$\sigma Y = K_c / \sqrt{a} \tag{4.6}$$

In a three-point bend test, σ is given by the simple bending theory as:

$$\sigma = 6PS/\left(4BD^2\right) \tag{4.7}$$

For the three-point bend test specimen, where S/D is equal to 4, Y is given by:

$$Y = 1.93 - 3.07\left(\frac{a}{D}\right) + 14.53\left(\frac{a}{D}\right)^2 - 25.11\left(\frac{a}{D}\right)^3 + 25.80\left(\frac{a}{D}\right)^4 \tag{4.8}$$

On a plot of σY against $a^{-0.5}$ (Appendix 4.55), a straight line is obtained through the origin and its slope is taken as the K_c of the material. Details of this method have been explained by Karger-Kocsis [193] and Hassan *et al.* [194].

Table 4.9: Impact properties data of PP, PP/GF, PP/NC and PP/GF/NC composites

Sample	*P* (N)				*W* (mJ)				G_c (kJ m^{-2})	K_c (MPa $m^{0.5}$)
	a/D				a/D					
	0.1	0.2	0.3	0.4	0.1	0.2	0.3	0.4		
PP	543.41	379.25	313.92	283.70	157.79	102.22	78.82	56.20	2.77	2.77
PP100/NCUT3	513.88	440.02	292.28	253.54	185.31	106.31	74.00	52.50	3.02	2.71
PP100/NCUT6	514.42	410.49	304.50	265.46	172.02	100.34	76.28	52.92	2.86	2.70
PP100/NCUT9	518.52	402.21	312.04	266.88	178.01	103.48	72.62	54.88	2.88	2.69
(PP100:C0)/$NCST2_{800}$	505.56	375.43	274.30	211.21	211.21	127.62	77.61	55.59	3.60	2.64
(PP92:C8)/$NCST2_{100}$	447.71	336.20	245.28	204.29	168.53	100.86	58.50	48.78	2.80	2.38
(PP92:C8)/$NCST2_{300}$	444.39	338.78	241.69	195.01	159.67	99.04	57.05	38.87	2.69	2.36
(PP92:C8)/$NCST2_{500}$	451.96	342.53	244.77	192.53	166.68	100.93	58.57	39.20	2.80	2.40
(PP92:C8)/$NCST2_{800}$	473.17	370.66	281.45	206.69	184.10	121.27	75.53	44.82	3.17	2.56
(PP95:C5)/NCUT3	439.17	339.34	254.06	195.50	162.61	106.07	65.45	44.47	2.89	2.42
(PP98:C2)/NCUT6	482.22	344.63	261.87	207.89	182.28	96.70	64.52	43.40	2.90	2.51
(PP95:C5)/NCUT6	473.33	347.19	253.49	198.86	170.33	97.42	61.59	42.77	2.78	2.46
(PP92:C8)/NCUT6	466.09	334.49	251.39	193.11	170.86	91.17	61.58	40.39	2.77	2.43
(PP95:C5)/NCUT9	458.30	330.98	253.23	197.93	162.00	92.83	62.75	46.16	2.66	2.38
(PP98:C2)/NCST2	549.70	383.93	273.83	224.48	251.24	119.67	65.80	45.05	3.66	2.75
(PP95:C5)/NCST2	522.05	365.86	250.30	226.24	223.22	109.10	53.07	32.71	3.16	2.59
(PP92:C8)/NCST2	500.57	356.24	259.92	188.32	198.24	98.53	41.16	28.55	2.80	2.49
PP85/G15	580.18	418.10	342.96	292.86	159.68	100.73	75.30	59.24	2.76	2.96
PP70/G30	556.69	488.02	390.74	329.80	152.79	99.52	75.54	59.72	2.70	3.16
PP55/G45	606.99	545.91	439.94	371.64	161.05	115.87	90.24	76.44	3.01	3.50

Table 4.9, continued

Sample	*P* (N) a/D				*W* (mJ) a/D				G_c (kJ m^{-2})	K_c (MPa m$^{0.5}$)
	0.1	0.2	0.3	0.4	0.1	0.2	0.3	0.4		
(PP77:C8)/G15$_{50}$	496.27	369.13	297.12	235.40	181.06	94.23	74.26	49.39	2.89	2.62
(PP77:C8)/G15$_{100}$	534.37	406.32	302.51	238.74	181.08	110.00	71.77	47.34	2.98	2.79
(PP77:C8)/G15$_{150}$	377.89	291.65	276.50	216.40	109.61	78.80	63.50	55.20	2.05	2.13
(PP83:C2)/G15	513.00	380.15	290.28	217.65	142.92	85.01	59.30	41.99	2.42	2.71
(PP80:C5)/G15	516.22	364.28	284.27	227.26	150.81	83.99	58.86	41.44	2.49	2.69
(PP77:C8)/G15	502.99	368.41	273.87	231.55	145.10	81.14	55.17	46.46	2.38	2.63
(PP65:C5)/G30	558.90	407.70	316.62	243.22	147.53	90.18	66.47	47.85	2.55	2.94
(PP50:C5)/G45	572.75	426.86	315.32	257.75	131.33	81.91	58.10	47.25	2.32	3.05
(PP85)/G15/NCUT3	543.41	379.25	313.92	283.70	157.79	102.22	78.82	56.20	2.77	2.77
(PP85)/G15/NCUT6	589.40	392.12	351.80	286.36	154.98	95.79	66.90	48.60	2.56	2.95
(PP85)/G15/NCUT9	586.68	394.65	361.95	304.40	149.09	90.85	68.20	48.56	2.47	2.99
(PP70)/G30/NCUT3	558.26	454.57	377.78	322.62	154.03	100.68	72.52	62.06	2.79	3.12
(PP70)/G30/NCUT6	537.71	449.51	384.48	333.80	151.24	101.37	75.66	60.83	2.65	3.03
(PP70)/G30/NCUT9	533.88	461.07	400.94	337.56	145.03	96.37	72.14	59.42	2.55	3.07
(PP55)/G45/NCUT3	595.50	499.69	426.82	351.04	159.61	131.34	104.52	94.52	3.34	3.39
(PP55)/G45/NCUT6	564.07	504.52	421.34	366.38	146.70	112.63	87.28	70.64	2.84	3.32
(PP55)/G45/NCUT9	593.71	505.32	424.54	349.14	145.07	107.76	88.44	68.20	2.78	3.36
(PP83:C2)/G15/NCUT6	598.27	428.03	321.75	258.42	207.87	113.30	71.53	46.43	3.15	3.01
(PP80:C5)/G15/NCUT6	587.70	444.51	321.10	247.57	220.25	120.59	74.63	49.10	3.31	2.98
(PP77:C8)/G15/NCUT6	700.49	463.66	370.24	274.25	295.17	141.93	100.60	73.14	4.33	3.39
(PP82:C2)/G15/NCST2	551.61	391.07	313.39	256.80	175.24	94.99	58.55	44.61	2.71	2.84
(PP80:C5)/G15/NCST2	544.91	394.86	290.22	243.13	169.60	90.69	50.28	40.70	2.60	2.81
(PP77:C8)/G15/NCST2	535.56	394.15	285.90	256.02	169.00	92.62	49.43	39.08	2.55	2.79

4.7.3.1 Clay nanocomposites

Peak load (P) and fracture energy (W)

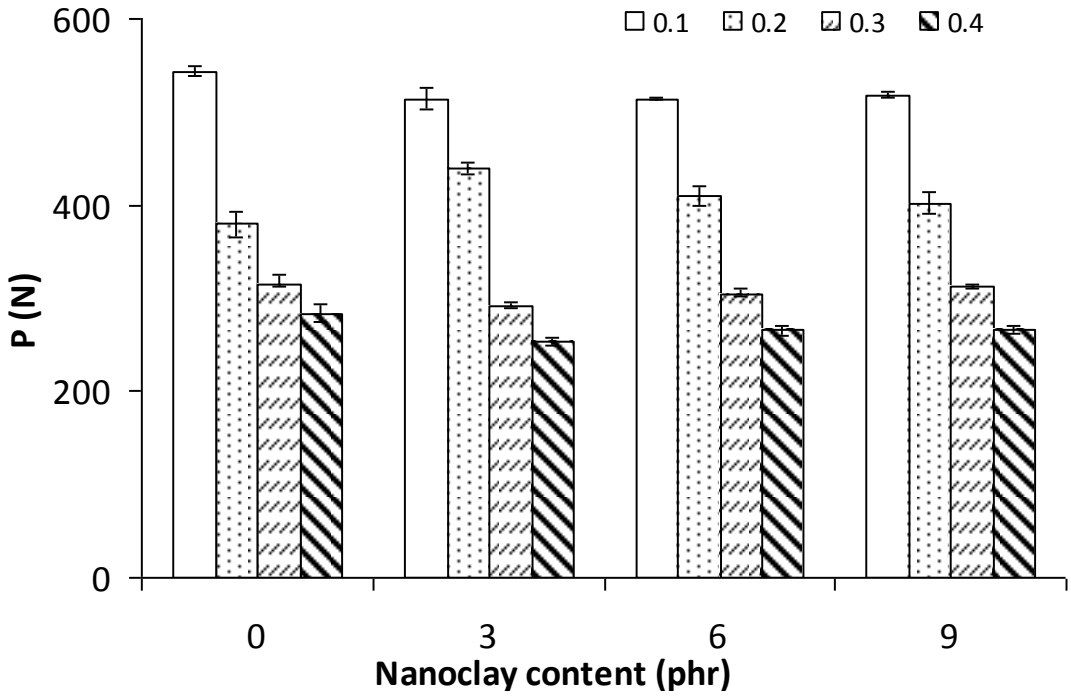

Figure 4.100: Peak load (*P*) of clay nanocomposites

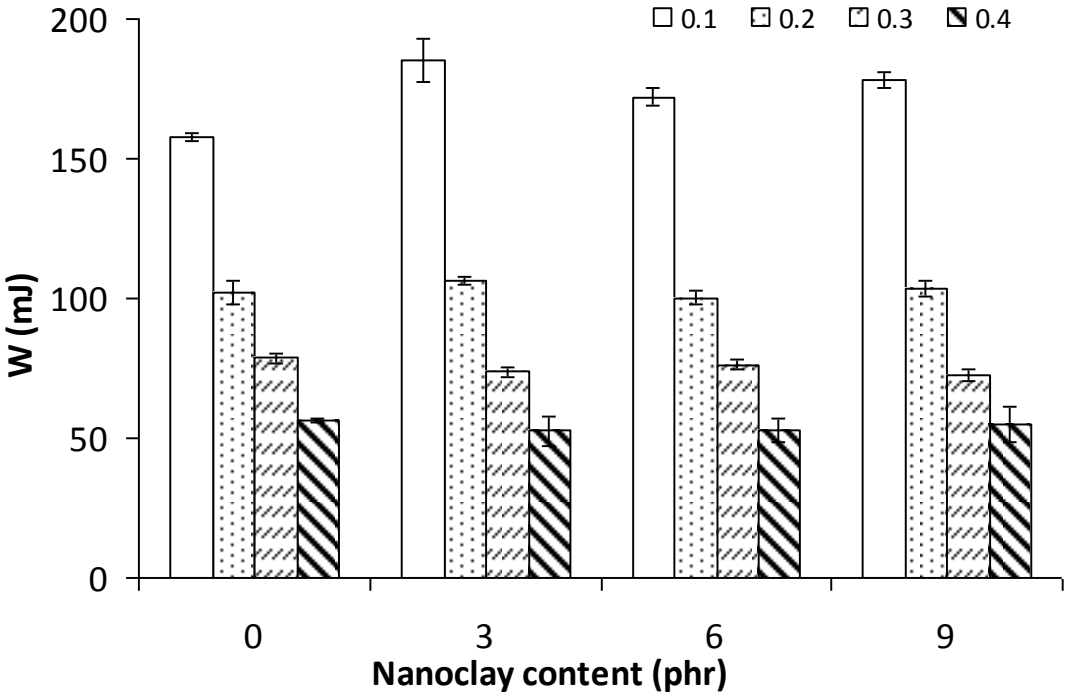

Figure 4.101: Fracture energy (*W*) of clay nanocomposites

Peak load (*P*) and fracture energy (*W*) of untreated clay nanocomposites are shown in Figures 4.100 and 4.101, respectively. It can be seen that both values increased up to 3 phr of clay loading and further addition of untreated clay to 6 phr and 9 phr reduce these values. A decrement in the *P* and *W* values at higher clay content may be due to the existence of agglomerations of nanoclay within the PP matrix.

Meanwhile, the incorporation of treated clay in the PP matrix resulted in a slight decrement in *P* values, when compared with untreated clay (Appendix 4.56). By contrast, a reverse trend is observed for *W* value (Appendix 4.57). On the other hand, *P* and *W* were increased as the processing screw speeds were increase from 100 rpm to 800 rpm (Appendices 4.58 and 4.59). A continuous reduction in *P* and *W* were observed with the addition of 2 *wt%* to 8 *wt%* of compatibiliser to PP/NCUT6 nanocomposite systems (Appendices 4.60 and 4.61).

G_c and K_c

The G_c and K_c values for PP/NC composites, as extracted from the plots of *W* against $BD\Phi$ and the plot of σY against $a^{-0.5}$, are shown in Figure 4.102. The PP matrix has a G_c value of 2.77 kJ m^{-2}. From Table 4.9, there is a substantial increase in the G_c (9%) with the initial incorporation of 3 phr of NC loading to 3.02 kJ m^{-2}, when compared with the PP matrix. It is interesting to note that further addition of NC to 6 and 9 phr resulted in a slight reduction of this value to 2.86 kJ m^{-2} and 2.88 kJ m^{-2}, respectively. Wahit *et al.* [140] suggested that the reduction in the G_c of nanocomposite with higher clay content implies that the composite became more brittle when compared to the composite with lower clay loading. Hemmasi *et al.* [96] suggested that this observation is probably due to the formation of clay agglomerations and the presence of unexfoliated aggregates and voids. Meanwhile, the presence 3 phr, 6 phr and 9 phr of

clay resulted in a slight continuous reduction in the K_c value from 2.77 MPa $m^{0.5}$ for PP matrix to 2.71 MPa $m^{0.5}$, 2.70 MPa $m^{0.5}$ and 2.69 MPa $m^{0.5}$, respectively.

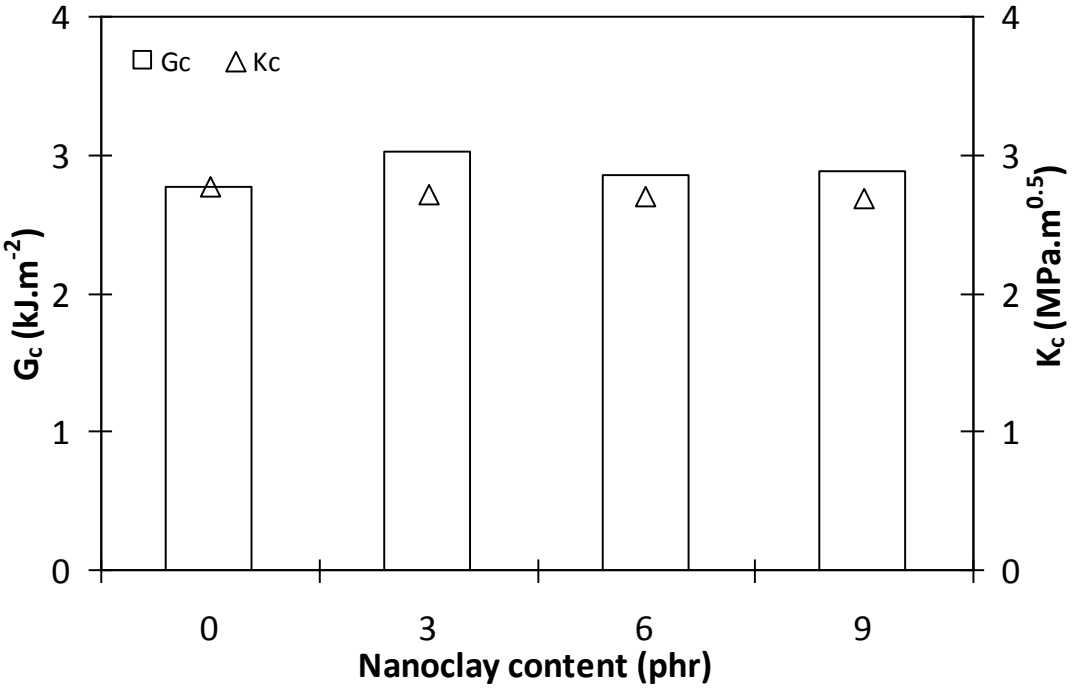

Figure 4.102: G_c and K_c of clay nanocomposites

To show the effect of clay surface treatment on the impact properties of the nanocomposite, G_c and K_c of the treated clay nanocomposite is compared with untreated clay nanocomposite. As shown in Figure 4.103, the G_c value of nanocomposite using treated clay was 26% higher (3.60 kJ m^{-2}) than that of the untreated clay nanocomposite (2.86 kJ m^{-2}). During the impact testing, the stress in the sample might have been distributed with a significantly higher strength/modulus by the intercalated clay layers than the matrix. The silicate layer orientation may also contribute to the reinforcement effects observed. With higher content of nanoclay incorporated in the PP matrix, the aggregation of clay may take place. These two aspects are competitive and they determine the toughness of the nanocomposites [184]. With a favourable compatibility of treated clay, the stress distribution is dominant in the system, resulting in the enhancement of the impact strength value. In addition, the improved impact strength

could also be caused by the reduction in the degree of crystallinity [187] that might be responsible for the increase in the material's ductility. It has been observed in the DSC section (Table 4.5) that treated clay nanocomposite exhibited lower X_c (42.2%) when compared with untreated clay nanocomposite (44.5%). On the other hand, from Table 4.9, the K_c of the treated nanocomposite, PP/NCST2 was slightly reduced to 2.64 MPa $m^{0.5}$ when compared with the untreated nanocomposite, PP/NCUT6 (2.70 MPa $m^{0.5}$).

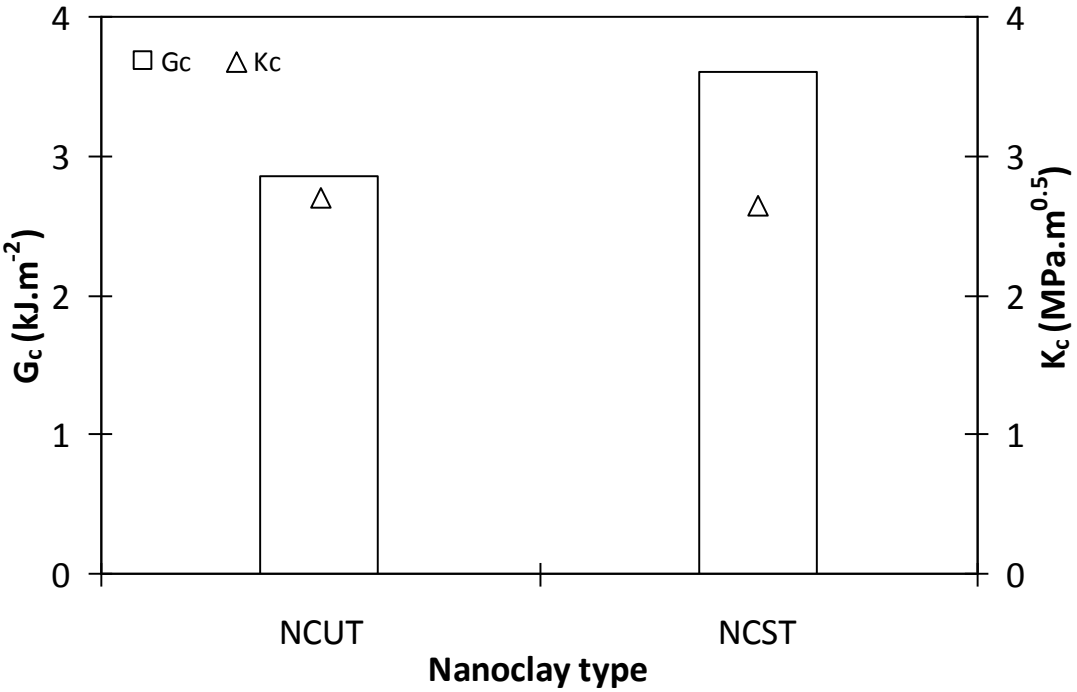

Figure 4.103: G_c and K_c of nanocomposites with untreated and treated nanoclays

Figure 4.104 shows the variation of the impact properties of (PP:C8)/NCST2 nanocomposite with different processing screw speeds. It can be seen that the impact strength (G_c) of the nanocomposites increased with increase in the screw speeds. As the screw speed increased from 100 rpm to 800 rpm, the G_c value improved from 2.80 $kJ\,m^{-2}$ to 3.17 kJ m^{-2} (Table 4.9). The enhancement in the impact strength could be attributed to the better homogeneous dispersion of the clay, resulting from the increment in the shear force during melt compounding, as the screw speed increased. This may

lead to a more uniform distribution of the applied stress. A similar trend is observed for fracture toughness, K_c.

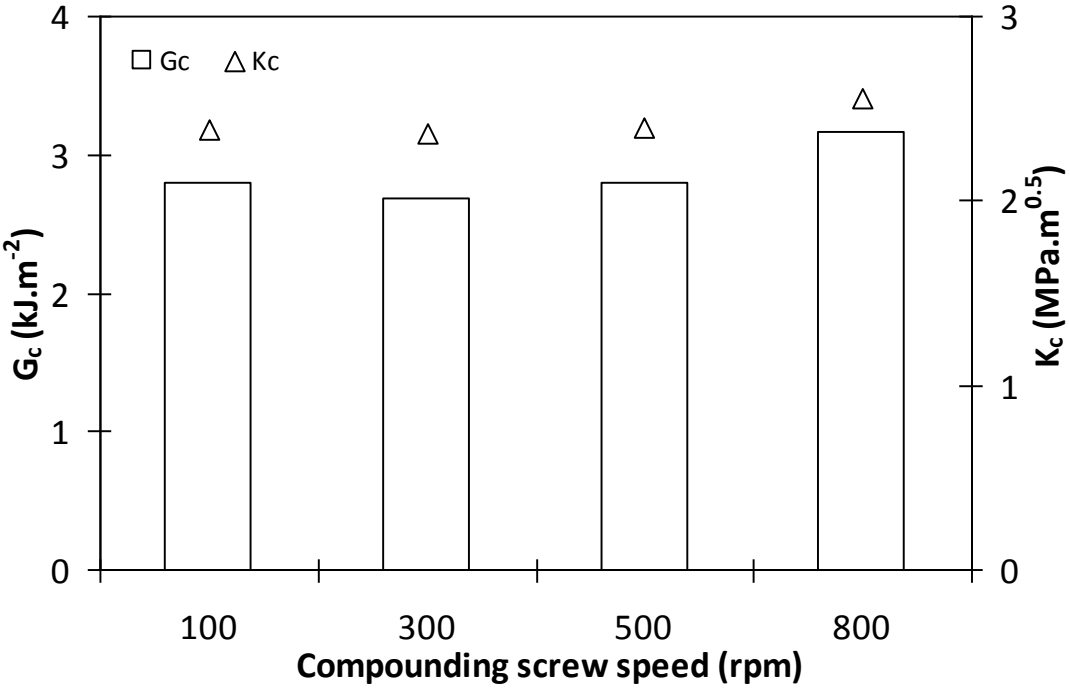

Figure 4.104: G_c and K_c of (PP:C8)/NCST2 nanocomposites at different screw speeds

Figure 4.105 shows the effect of compatibiliser on the impact strength and fracture toughness of the PP/NCUT nanocomposite. The nanocomposites with 2 *wt%* of MAPP showed the highest impact strength (2.90 kJ m^{-2}) among other systems. The enhancement of G_c value could be due to the fact that exfoliated or intercalated clay layers in the compatibilised nanocomposite played a role in hindering the crack path caused by impact [195]. The presence of higher compatibiliser loading gave a negative effect on the G_c of the nanocomposites. The G_c value was reduced as the MAPP content increased to 5 *wt%* and 8 *wt%*. Higher MAPP content may lead to immiscibility with the PP matrix and can lower the impact strength of the nanocomposite [195]. Meanwhile, a continuous decrement in fracture toughness, K_c was observed with the addition of MAPP from 2 *wt%* to 8 *wt%* in the PP/NC6 nanocomposite (Table 4.9).

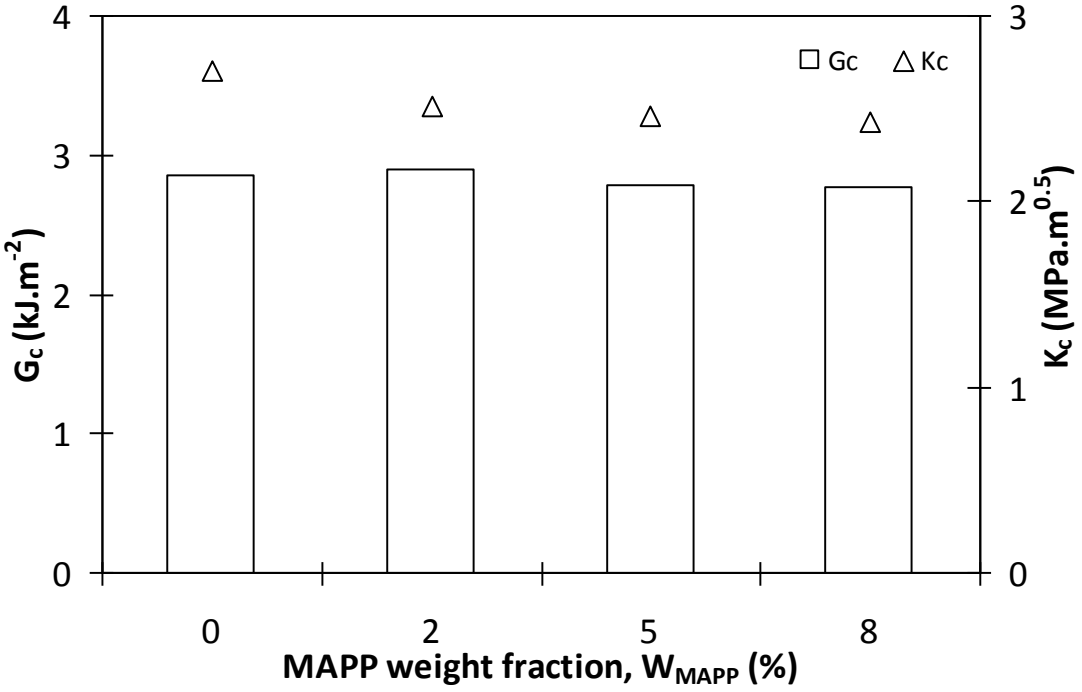

Figure 4.105: G_c and K_c of PP/NCUT6 nanocomposites with different MAPP contents

4.7.3.2Glass fibre composites

Peak load (P) and fracture energy (W)

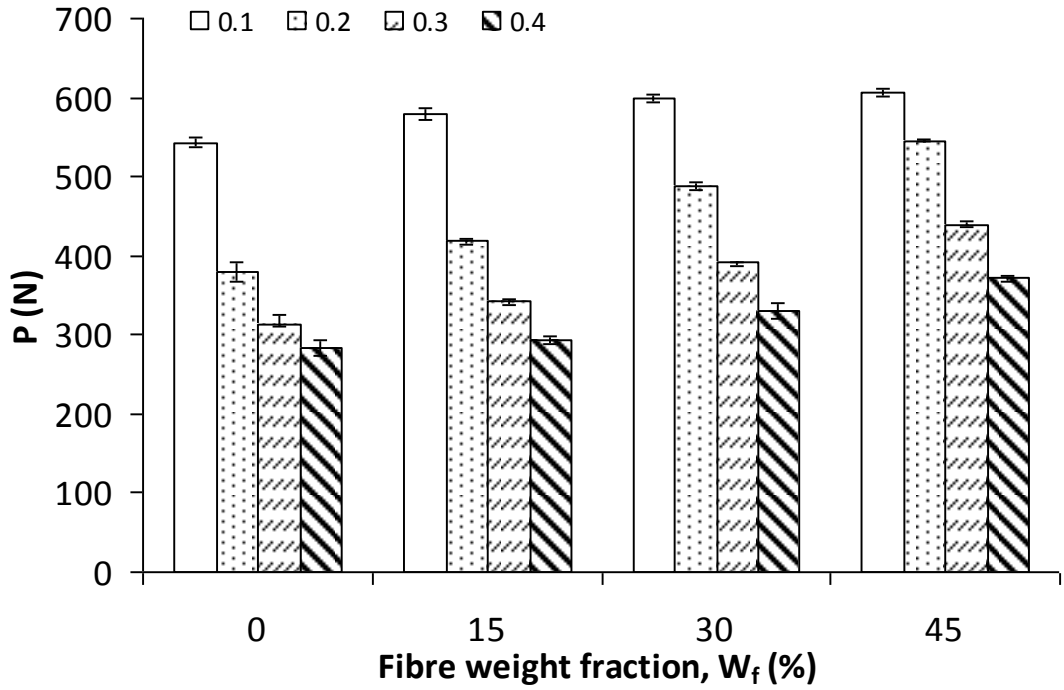

Figure 4.106: Peak load (*P*) of glass fibre composites

Histogram of peak load (*P*) and fracture energy (*W*) as a function of fibre weight fraction (W_f) are depicted in Figures 4.106 and 4.107, respectively. From the histogram, it can be observed that, generally, the *P* and *W* values increased with increasing fibre contents. This trend is expected as the presence of fibres tends to reduce the resistance to crack initiation, therefore increasing the material brittleness, while at the same time reducing crack propagation through the matrix by forcing crack lines around the fibre ends [196]. Also, with regard to the effect of increase in notch to depth ratio (*a/D*), fracture energy and peak load are decreased. A similar trend has been reported by Hassan *et al.* [116].

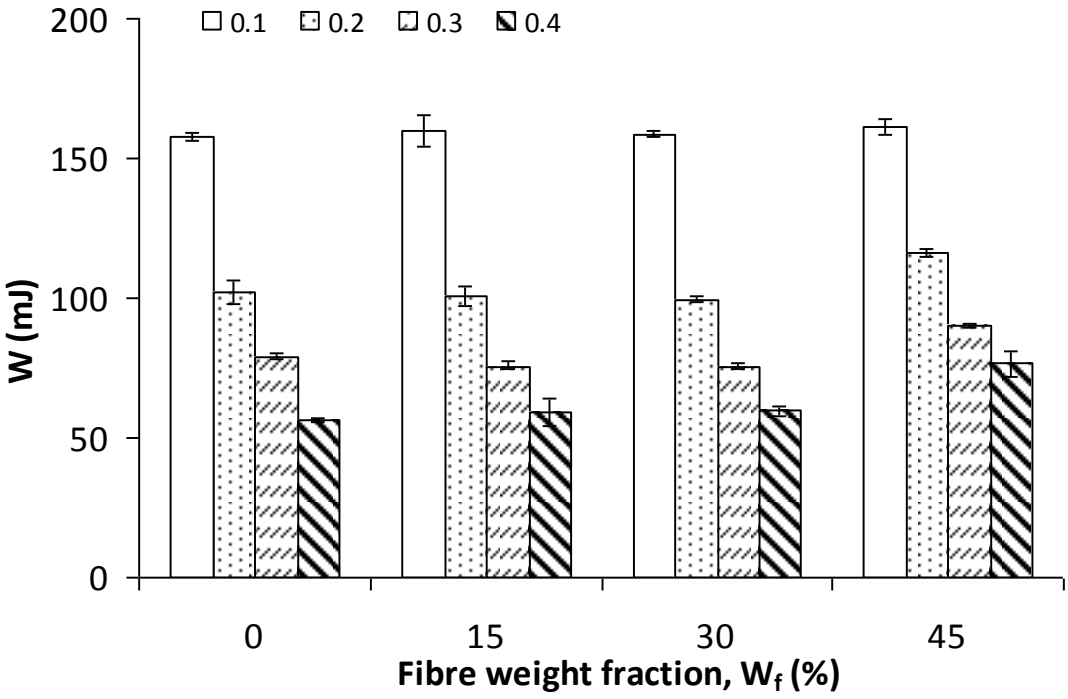

Figure 4.107: Fracture energy (*W*) of glass fibre composites

On the other hand, it is also observed that at the same fibre content, *W* and *P* values increased with extrusion screw speed, from 50 rpm to 100 rpm (Appendices 4.62 and 4.63). By contrast, composite compounded at 150 rpm processing screw speed exhibited sharp decrements in *P* and *W* values. From Appendices 4.64 and 4.65, a noticeable reduction in *P* and *W* values are observed with the presence of 2 *wt%* of

MAPP in the PP/G15 composite system. However, insignificant changes in *P* and *W* were recorded with further additions of MAPP of 5 *wt%* and 8 *wt%* in the system.

G_c and K_c

The variations of G_c and K_c as functions of glass fibre loading are presented in Figure 4.108. From Table 4.9, a slight decrement in the G_c values to 2.76 kJ m^{-2} and 2.70 kJ m^{-2} were observed with the addition of 15 *wt%* and 30 *wt%* of glass fibre, respectively when compared with the PP matrix (2.77 kJ m^{-2}). The poor compatibility between the fibre and the matrix (which could result in a poor interfacial adhesion between these two phases) may be responsible for this trend. By contrast, the G_c value improved as 45 *wt%* of GF was loaded into the system. The fact that the incompatibility issue between the fibre and the matrix has been compensated, by the contribution of the high stiffness of the glass fibre at that particular composition, may be accountable for this observation.

Thomason and Vlug [197] reported that the impact strength obtained in their charpy test increased almost linearly with fibre concentrations. This result indicated that as glass fibre was included in the composite, impact energy dissipation originating from the fibre inclusion was high [198]. The main mechanisms suggested were the debonding between glass fibre and PP matrix and fibre pull-out [199]. The plastic deformation of the PP matrix also contributed to the impact energy absorption. In PP/GF system, the fracture energy absorption was shown to have dominated, resulting from the contribution of the matrix plasticity [200]. The matrix deformation occurs, either through homogeneous deformation of the matrix or from the localised deformation around fibre ends. In the case of K_c, generally, it increased with increasing fibre content. It is evident that the fracture toughness of the glass fibre composites increased progressively with further incorporation of glass fibre. The K_c values increased from

2.77 MPa $m^{0.5}$ for PP matrix to 2.96 MPa $m^{0.5}$, 3.16 MPa $m^{0.5}$ and 3.50 MPa $m^{0.5}$ for composites containing 15 *wt%*, 30 *wt%* and 45 *wt%* of GF, respectively.

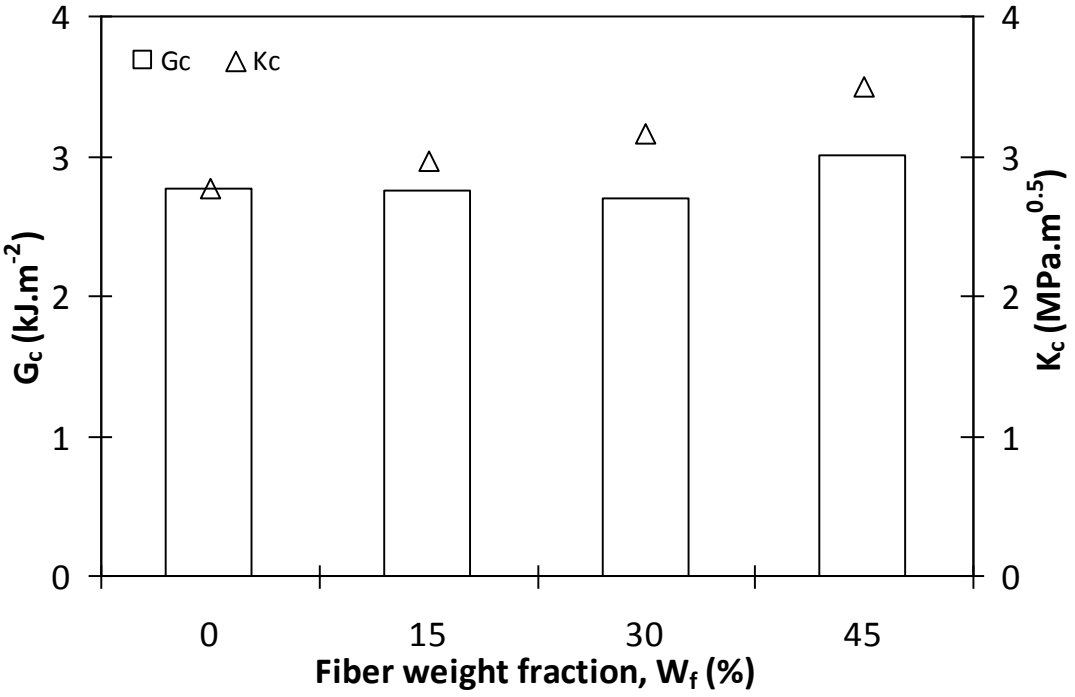

Figure 4.108: G_c and K_c of glass fibre composites

The effect of processing screw speed on the G_c and K_c of glass fibre composite is shown in Appendix 4.66. The highest G_c and K_c values were obtained for composite processed with 100 rpm screw speed. On the other hand, the incorporation of compatibiliser in the glass fibre composite, drastically reduced the G_c and K_c values (Appendix 4.67).

4.7.3.3Glass fibre/nanoclay hybrid composites

Peak load (P) and fracture energy (W)

Figure 4.109 shows the peak load value versus untreated clay contents at different *a/D* values. In these histograms, at the same *a/D*, the highest peak load was recorded for hybrid composite with the highest clay loading. A slight decrement in this value was obtained for the 3 phr of clay presence in the system. On the other hand, the

fracture energy (*W*) value showed a continuous reduction as the untreated clay was added from 3 to 9 phr into the hybrid composites system (Figure 4.110).

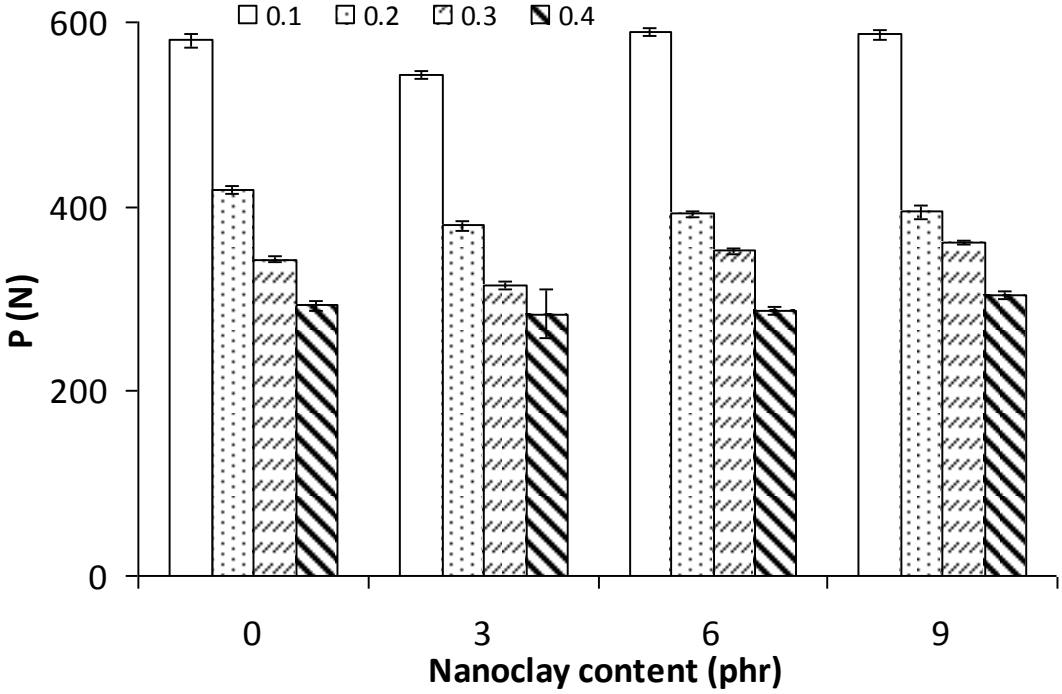

Figure 4.109: Peak load (*P*) of PP/G15 hybrid composites with different NCUT contents

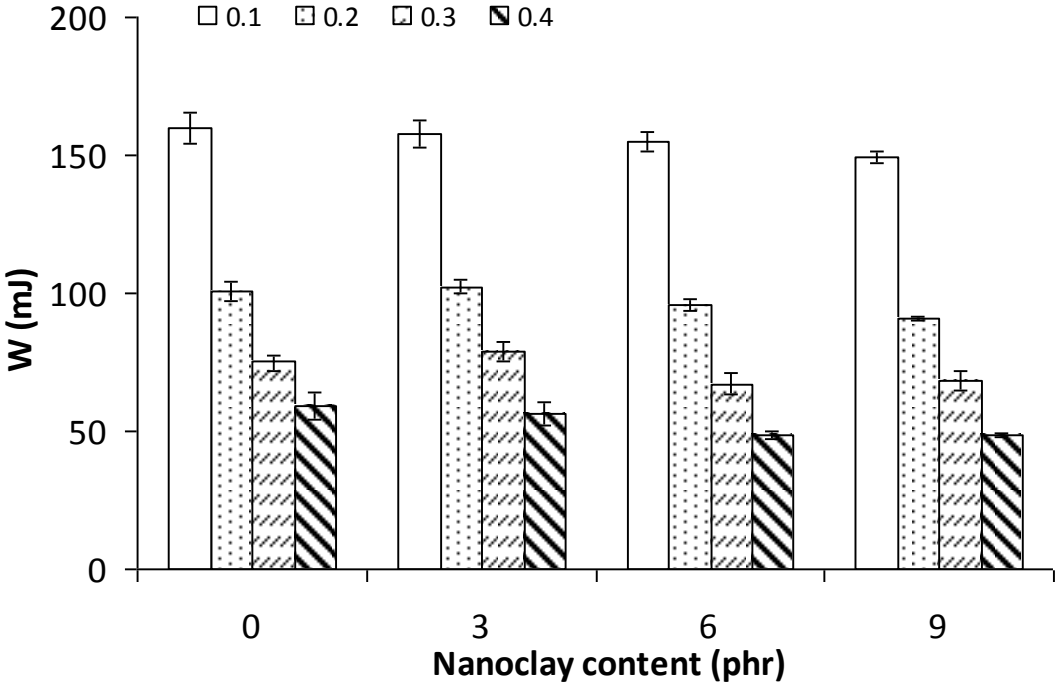

Figure 4.110: Fracture energy (*W*) of PP/G15 hybrid composites with different NCUT contents

Meanwhile, *P* and *W* for treated clay hybrid composite showed a noticeable decrement when compared with untreated clay hybrid composite system (Appendices 4.68 and 4.69). The effect of compatibiliser loadings on the *P* and *W* of hybrid composites are shown in Appendices 4.70 and 4.71. *P* and *W* values constantly increased as the MAPP contents increased.

G_c and K_c

For the hybrid composites, incorporation of 3 phr of untreated nanoclay into the PP/GF15 system, slightly improved the G_c (Figure 4.111). By contrast, as the nanoclay content increased to 6 phr and 9 phr, the G_c values reduced. The highest decrement of about 11% in the G_c value to 2.47 kJ m^{-2} was observed for 9 phr hybrid composite, relative to PP/GF15 composite (2.76 kJ m^{-2}). The reduction in G_c with NC concentration implies that the hybrid composites systems became more brittle when compared with the glass fibre composite. Chow *et al.* [201] suggested that the agglomeration of clay may induce local stress concentration, thus the nanocomposite fails in a more brittle manner. Li *et al.* [202] also reported that any polymer nanocomposites will show an increase in tensile strength and modulus with simultaneous loss in G_c. Lower G_c at high NC content can be attributed to the agglomeration of clay in the nanocomposite system, which is the site of stress concentration and could act as a micro crack initiator [156].

K_c value of 2.96 MPa $m^{-0.5}$ was obtained for the PP/GF15 composite. The addition of 3 phr of clay into PP/GF composite reduced this value to 2.77 MPa $m^{-0.5}$. On the other hand, incorporation of higher clay loading of 6 and 9 phr resulted in no significant changes in the K_c values when compared with PP/G15 composite. Meanwhile, G_c and K_c values reduced with the addition of treated clay in glass fibre hybrid composites, when compared with untreated clay hybrid composite. It is suggested that in treated clay hybrid composite, fracture tends to occur in a brittle

manner, due to the improvement in the filler-matrix adhesion, which resulted in the reduction of both G_c and K_c values (Appendix 4.72).

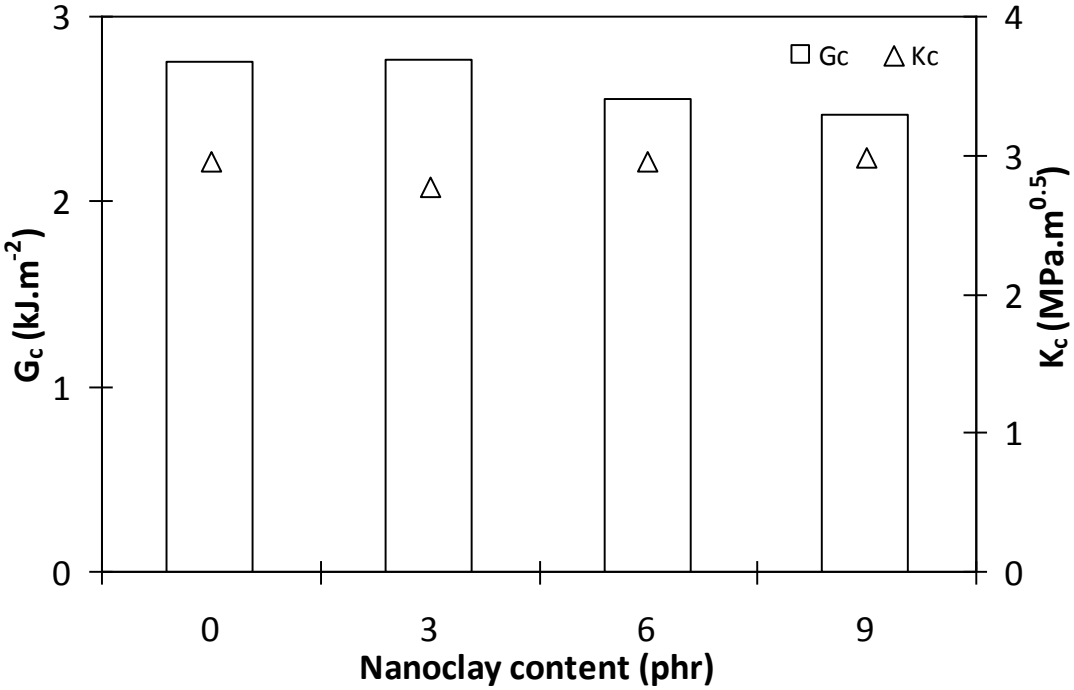

Figure 4.111: G_c and K_c of PP/G15 hybrid composites with different NCUT contents

Figure 4.112 demonstrates the effect of MAPP loading on the impact properties of hybrid composites. It can be seen that the addition of compatibiliser drastically increased the impact strength, G_c of the composites. This observation could be due to the improvement in the nanoclay and fibre dispersion caused by better compatibility between the fillers and the matrix. The presence of intercalated and exfoliated structure in the hybrid composites acts as load-bearing agents and also as crack stopping agents. The intercalated dispersion of the clay platelets prevents the ease of propagation of cracks, by allowing the crack to propagate through torturous pathway, resulting in increased impact strength [121]. On the other hand, a noticeable improvement in K_c was observed at 8 *wt%* of MAPP loading. No significant changes were obtained at lower compatibiliser contents.

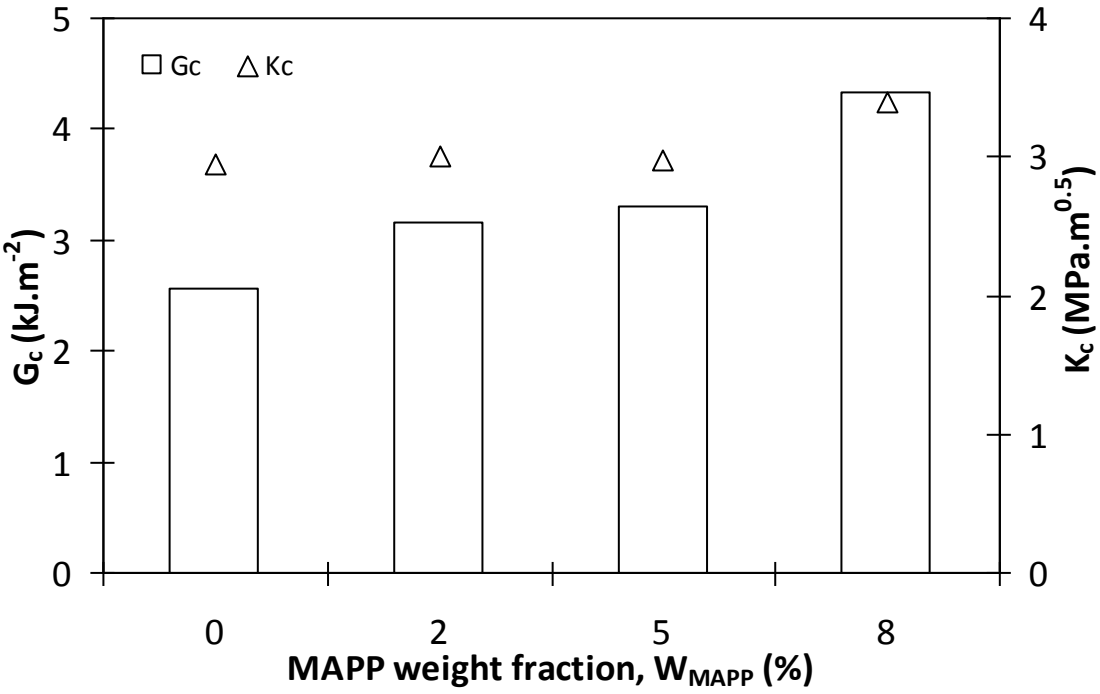

Figure 4.112: G_c and K_c of PP/G15/NCUT6 hybrid composites with different MAPP contents

CHAPTER FIVE

5 Conclusion and recommendations for further work

5.1 Conclusion

In this work, investigations into the structure and properties of hybrid composites of glass fibre/nanoclay/polypropylene were carried out. For the material preparation, a melt compounding procedure, in a twin-screw extruder, was chosen as a production route.

From this research, it can be concluded that surface treatment of nanoclay did not only improve its compatibility with the non polar polymer, but also increased the clay interlayer distance, resulting in better interfacial adhesion between the clay particles and the matrix, leading to enhancement in the thermal and mechanical properties.

The fibre length distribution analysis revealed that composites with high glass fibre loading exhibited lower L_n and L_w values than those containing low glass fibre content, due to the fibre-fibre, fibre-matrix and fibre-machinery interactions during the material processing. Furthermore, lower L_n and L_w values were also observed in the composites compounded with high screw speed, relative to the composites compounded with low screw speed.

Fourier-transform infra-red spectroscopic investigations confirmed that maleic anhydride was present in the compatibilised composites. A difference in the FTIR spectrum was detected due to the presence of added functional groups in the treated nanoclay, relative to the untreated nanoclay.

The XRD patterns revealed that the surface treatment increased the interlayer d-spacing of the treated clay, relative to the untreated clay. Meanwhile, it was shown that the melt compounding technique increased the interlayer d-spacing of clay in the nanocomposite, when compared with the raw powder clay. On the other hand, as the

concentration of the clay in the nanocomposites increased (from 3 phr to 9 phr), reduction in the interlayer d-spacing was observed, as more ordered structures were obtained, indicating a relatively high fraction of clay agglomeration. It was also revealed that the characteristic diffraction peak of nanocomposites shifted towards low diffraction angle as the compounding screw speed and the content of compatibiliser increased, indicating a better dispersion of clay in the system.

Thermogravimetric investigations revealed that the incorporation of clay and glass fibre in PP matrix led to a significant improvement in the thermal stability of the hybrid material. Moreover, treated clay hybrid composite showed better thermal stability when compared with hybrid composites using untreated clay. Also, the thermal stability of the compatibilised composites was enhanced, relative to the uncompatibilised composites system.

Differential scanning calorimetric study showed that incorporating untreated clay and glass fibre into PP had no significant effect on the melting behaviour of the composites. In contrast, the addition of treated clay showed marginal effect on the melting temperature of the composite when compared with the untreated clay. Moreover, the incorporation of untreated clay into the hybrid composite shifted the melting and crystallisation temperatures to higher values. On the other hand, the degree of crystallinity of the nanocomposites increased with the presence of untreated clay and compatibiliser because of the nucleating ability of the clay. Nevertheless, this value was not affected with the incorporation of glass fibre in the composite system. Meanwhile, a remarkable improvement in the degree of crystallinity was observed for hybrid composites.

The dynamic mechanical analysis revealed that the composites made from treated clay exhibited higher storage modulus and loss modulus than those containing untreated clay. Moreover, both values were further improved in the hybrid composites.

On the other hand, low tan delta magnitudes were observed in glass fibre composites system, relative to the neat PP matrix. This is the result of the restriction in the polymer molecular motion with the presence of fillers, hence the low damping characteristics. Nevertheless, no appreciable shifts in the T_g value could be observed with the addition of untreated clay and glass fibre in the hybrid system. However, a remarkable increment in this value was recorded with the incorporation of treated clay and compatibiliser in the nanocomposite systems.

The compatibilised composite showed a notable improvement in the tensile strength than the uncompatibilised material as a result of the improved interfacial adhesion between the fillers and matrix. Meanwhile, the incorporation of nanoclay and glass fibre in the composites increased the tensile modulus values in all the compositions studied. This value was further improved with the presence of compatibiliser in the systems. On the other hand, a decrement in the tensile strain was observed as the filler loading in the composites increased. In addition, the flexural properties (strength and modulus) were found to increase with filler loading in the composites, relative to PP matrix. At the same time, a decreasing trend in the flexural displacement was observed, as the filler content increased.

Peak load and critical stress intensity factor values in the glass fibre composites and hybrid composites were found to increase relative to the neat PP matrix, while in the compatibilised composites system, significant reductions in these values were observed. Nevertheless, the energy to failure and the critical strain energy release rate decreased with clay loading in the clay nanocomposites. The same trend was observed in the hybrid system, as further addition of nanoclay resulted in a further reduction in both values. On the other hand, a remarkable improvement in these values was observed for composite with 45 *wt%* glass fibre content.

5.2 Recommendations for further work

Characterisation of the composites prepared using PP in the powder form will enhance the understanding of the physical properties effect on the overall materials performance.

Preparation and characterisation of composites prepared using different types of nanoclay and compatibiliser in order to further understand the effects of clay surface treatment and grafting level, respectively, on the properties of composites.

Optical microscopy (OM) analysis will shed more information in microstructural properties such as the presence of void/bubble or aggregation of clay in the composites system.

Comprehensive characterisation of the surface of untreated and treated nanoclay by X-ray photoelectron spectroscopy (XPS) and wettability by contact angle measurement will enhance the understanding of the degree of modification by surface treatment.

Environmental tests will allow better understanding of the material's response to different environmental conditions.

REFERENCES

1. Hull D. and Clyne T. W. *An Introduction to Composite Materials*. Cambridge University Press, 2nd Edition, 1996.
2. Matthews F. L. and Rawlings R. D. *Composites Materials: Engineering and Science*. Chapman and Hall, 1999.
3. Spencer B. E. Designing and manufacturing filament wound composites: The basics. In: Proceedings of the Seventh Annual ASM / ESD Advanced Composites Conference. Detroit, Michigan; USA, 1991. 433-442.
4. Gill R. M. *Carbon Fibres in Composite Materials*. London: Iliffe Books for the Plastics Institute, 1972.
5. Karger-Kocsis J. *Polypropylene: Structure, Blends and Composites*. London: Chapman & Hall, 1. 1995.
6. Vandenberg E. J. and Salamone J. C. *Catalysis in Polymer Synthesis*. Oxford University Press, 1992.
7. Natta G., Pino P., Corradini P., Danusso F., Mantica E., Mazzanti G. and Moraglio G. Crystalline high polymers of α-olefins. *Journal of the American Chemical Society* 1955;77(6):1708-1710.
8. Maier C. and Calafut T. *Polypropylene. The Definitive User's Guide and Databook*. New York: Plastics Design Library, 1998.
9. Kaempfer D., Thomann R. and Mulhaupt R. Melt compounding of syndiotactic polypropylene nanocomposites containing organophilic silicates and in situ formed core/shell nanoparticles. *Polymer* 2002;43:2909-2916.
10. Hassan A., Normasmira A. R. and Yahya R. Extrusion and injection-molding of glass fiber/MAPP/polypropylene: Effect of coupling agent on DSC, DMA and mechanical properties. *Journal of Reinforced Plastics and Composites* 2011;30(14):1223-1232.

11. Normasmira A. R., Hassan A., Yahya R., Lafia-Araga R. A. and Hornsby P. R. Micro-structural, thermal and mechanical properties of injection-molded glass-fiber/nanoclay/polypropylene composites. *Journal of Reinforced Plastics and Composites* 2012;31(4):269-281.

12. Hartikainen J., Hine P., Szabó J. S., Lindner M., Harmia T., Duckett R. A. and Friedrich K. Polypropylene hybrid composites reinforced with long glass fibres and particulate filler. *Composites Science and Technology* 2005;65(2):257-267.

13. Vlasveld D. P. N., Bersee H. E. N. and Picken S. J. Nanocomposite matrix for increased fibre composite strength. *Polymer* 2005;46(23):10269-10278.

14. Cui Y. H., Wang X. X., Li Z. Q. and Tao J. Fabrication and properties of nano ZnO/glass fiber reinforced polypropylene composites. *Journal of Vinyl and Additive Technology* 2010;16(3):189-194.

15. Normasmira A. R., Hassan A., Yahya R., Lafia-Araga R. A. and Hornsby P. R. Polypropylene/glass fiber/nanoclay hybrid composites: Morphological, thermal, dynamic mechanical and impact behaviors. *Journal of Reinforced Plastics and Composites* 2012;31(18):1247-1257.

16. Kingery W. D., Bowen H. K. and Uhlmann D. R. *Introduction To Ceramics*. New York: John Wiley & Sons, 2nd edition, 1976. 77.

17. Kato M. and Usuki A., In: Pinnavaia T. J. and Beall G. W., editor. Polymer-Clay Nanocomposites. New York: John Wiley & Sons, 2000. 98.

18. Hay J. N. and Shaw S. J. A review of nanocomposites. 2000:1-15.

19. Strawhecker K. E. and Manias E. Structure and properties of poly (vinyl alcohol)/Na^+ montmorillonite nanocomposites. *Chemistry of Materials* 2000;12(10):2943-2949.

20. Xu R., Manias E., Snyder A. J. and Runt J. New biomedical poly (urethane urea)-layered silicate nanocomposites. *Macromolecules* 2001;34(2):337-339.

21. Vaia R. A., Vasudevan S., Krawiec W., Scanlon L. G. and Giannelis E. P. New polymer electrolyte nanocomposites: Melt intercalation of poly (ethylene oxide) in mica-type silicates. *Advanced Materials* 1995;7(2):154-156.

22. Gao F. Polymer/layered inorganic particle nanocomposites: A better solution to make materials stronger. In: Nanocomposite Workshop. Risley Hall, Derby, UK, September 2001.

23. Alexandre M. and Dubois P. Polymer-layered silicate nanocomposites: Preparation, properties and uses of a new class of materials. *Materials Science and Engineering: R: Reports* 2000;28(1-2):1-63.

24. Hasegawa N., Kawasumi M., Kato M., Usuki A. and Okada A. Preparation and mechanical properties of polypropylene-clay hybrids using a maleic anhydride-modified polypropylene oligomer. *Journal of Applied Polymer Science* 1998;67(1):87-92.

25. Liu X. and Wu Q. PP/clay nanocomposites prepared by grafting-melt intercalation. *Polymer* 2001;42(25):10013-10019.

26. Theng B. K. G. *Formation and Properties of Clay-Polymer Complexes*. Amsterdam: Elsevier, 1979.

27. Theng B. K. G. *The Chemistry of Clay-Organic Reactions*. New York: Wiley, 1974.

28. Kojima Y., Usuki A., Kawasumi M., Okada A., Kurauchi T. T. and Kamigaito O. Synthesis of nylon 6–clay hybrid by montmorillonite intercalated with ϵ-caprolactam. *Journal of Polymer Science Part A: Polymer Chemistry* 1993;31(4):983-986.

29. Kojima Y., Usuki A., Kawasumi M., Okada A., Fukushima Y., Kurauchi T. T. and Kamigaito O. Mechanical properties of nylon 6-clay hybrid. *Journal of Materials Research* 1993;8:1185-1189.

30. Giannelis E. P. Polymer layered silicate nanocomposites. *Journal of Advanced Materials* 1996;8(1):29-35.

31. Vaia R. A., Ishii H. and Giannelis E. P. Synthesis and properties of two-dimensional nanostructures by direct intercalation of polymer melts in layered silicates. *Chemistry of Materials* 1993;5(12):1694-1696.

32. Manias E., Touny A., Wu L., Strawhecker K., Lu B. and Chung T. C. Polypropylene/montmorillonite nanocomposites. Review of the synthetic routes and materials properties. *Chemistry of Materials* 2001;13:3516-3523.

33. Oya A., Kurokawa Y. and Yasuda H. Factors controlling mechanical properties of clay mineral/polypropylene nanocomposites. *Journal of Materials Science* 2000;35(5):1045-1050.

34. Pinnavaia T. J. and Beall G. W. *Polymer-Clay Nanocomposites*. John Wiley & Sons Ltd., 2000. 4.

35. Okada A, Fukushima Y, Kawasumi M, Inagaki S, Usuki A, Sugiyama S, Kurauchi TT and Kamigaito O, U.S. Patent. 1988, Toyota Motor Co.

36. Messersmith P. B. and Giannelis E. P. Synthesis and barrier properties of poly(ε-caprolactone)-layered silicate nanocomposites. *Journal of Polymer Science Part A: Polymer Chemistry* 1995;33(7):1047-1057.

37. Akelah A. and Moet A. Polymer-clay nanocomposites: Free-radical grafting of polystyrene on to organophilic montmorillonite interlayers. *Journal of Materials Science* 1996;31(13):3589-3596.

38. Tudor J., Willington L., O'Hare D. and Royan B. Intercalation of catalytically active metal complexes in phyllosilicates and their application as propene polymerisation catalysts. *Chemical Communications* 1996;(17):2031-2032.

39. Von Werne T. and Patten T. E. Preparation of structurally well-defined polymer−nanoparticle hybrids with controlled/living radical polymerizations. *Journal of the American Chemical Society* 1999;121(32):7409-7410.

40. Bergman J. S., Chen H., Giannelis E. P., Thomas M. G. and Coates G. W. Synthesis and characterization of polyolefin–silicate nanocomposites: A catalyst intercalation and in situ polymerization approach. *Chemical Communications* 1999;(21):2179-2180.

41. Jimenez G., Ogata N., Kawai H. and Ogihara T. Structure and thermal/mechanical properties of poly (ϵ-caprolactone)-clay blend. *Journal of Applied Polymer Science* 1997;64(11):2211-2220.

42. Ogata N., Kawakage S. and Ogihara T. Poly(vinyl alcohol)-clay and poly(ethylene oxide)-clay blends prepared using water as solvent. *Journal of Applied Polymer Science* 1997;66(3):573-581.

43. Ogata N., Jimenez G., Kawai H. and Ogihara T. Structure and thermal/mechanical properties of poly(l-lactide)-clay blend. *Journal of Polymer Science Part B: Polymer Physics* 1997;35(2):389-396.

44. Zanetti M., Lomakin S. and Camino G. Polymer layered silicate nanocomposites. *Macromolecular Materials and Engineering* 2000;279(1):1-9.

45. Vaia R. A. and Giannelis E. P. Polymer melt intercalation in organically-modified layered silicates: Model predictions and experiment. *Macromolecules* 1997;30(25):8000-8009.

46. Zhang Q., Fu Q., Jiang L. and Lei Y. Preparation and properties of polypropylene/montmorillonite layered nanocomposites. *Polymer International* 2000;49(12):1561-1564.

47. Burnside S. S. and Giannelis E. P. Synthesis and properties of new poly(dimethylsiloxane) nanocomposites. *Chemistry of Materials* 1995;7(9):1597-1600.

48. Liu L. M., Qi Z. N. and Zhu X. G. Studies on nylon 6/clay nanocomposites by melt-intercalation process. *Journal of Applied Polymer Science* 1999;71(7):1133-1138.

49. Vaia R. A., D. Jandt. K., Kramer E. J. and Giannelis E. P. Microstructural evolution of melt intercalated polymer−organically modified layered silicates nanocomposites. *Chemistry of Materials* 1996;8(11):2628-2635.

50. Kawasumi M., Hasegawa N., Kato M., Usuki A. and Okada A. Preparation and mechanical properties of polypropylene−clay hybrids. *Macromolecules* 1997;30(20):6333-6338.

51. Alexandre M., Dubois P., Sun T., Garces J. M. and Jérôme R. Polyethylene-layered silicate nanocomposites prepared by the polymerization-filling technique: Synthesis and mechanical properties. *Polymer* 2002;43(8):2123-2132.

52. Schwartz M. *Composite Materials Handbook*. New York: McGraw-Hill, 2nd, 1992.

53. Hoskins B. C. and Baker A. A. *Composite Materials for Aircraft Structures*. New York: American Institute of Aeronautics and Astronautics, 1986. 245.

54. Philip F. C., *Glass fiber-reinforced polypropylene*. In: G. Karian Harutun, editor. Handbook of Polypropylene and Polypropylene Composites Second Edition. Basel, New York: Marcel Dekker, Inc., 2003.

55. Yue C. Y. and Quek M. Y. The interfacial properties of fibrous composites. III: Effect of the thickness of the silane coupling agent. *Journal of Materials Science* 1994;29(9):2487-2490.

56. Wouterson E. M., Boey F. Y. C., Hu X. and Wong S. C. Effect of fiber reinforcement on the tensile, fracture and thermal properties of syntactic foam. *Polymer* 2007;48(11):3183-3191.

57. Ahn Y. C. and Paul D. R. Rubber toughening of nylon 6 nanocomposites. *Polymer* 2006;47(8):2830-2838.

58. Kim K. N., Kim H. and Lee J. W. Effect of interlayer structure, matrix viscosity and composition of a functionaiized polymer on the phase structure of polypropylene-montmorillonite nanocomposites. *Polymer Engineering And Science* 2004;41(11):1963-1969.

59. Hasegawa N., Okamoto H., Kato M. and Usuki A. Preparation and mechanical properties of polypropylene–clay hybrids based on modified polypropylene and organophilic clay. *Journal of Applied Polymer Science* 2000;78(11):1918-1922.

60. Qian G., Cho J. W. and Lan T. Preparation and properties of polyolefin nanocomposites. *Nanocor Technical Papers* 2001:http://www.nanocor.com/tech_papers/properties_polyolefin.asp (accessed April 2012)

61. Gilman G. W., Kashiwagi T., Brown J. E. T. and Lomakin S. Flammability studies of plymer layered silicate nanocomposites. In: 43rd International SAMPE Symposium and Exhibition Society for the Advancement of Materials and Process Engineering. Anaheim, June 1998.

62. Schmidt D., Shah D. and Giannelis E. P. New advances in polymer/layered silicate nanocomposites. *Current Opinion in Solid State and Materials Science* 2002;6(3):205-212.

63. Lan T., Cho J., Liang Y., Qian J. and Maul P. Applications of nanomer in nanocomposites: From concept to reality. *Nanocor Technical Papers* 2001:http://www.nanocor.com/tech_papers/nanocomposites2001.pdf (accessed April 2012).

64. O'Neil C. J., Acquarulo L. A. Jr., Jain N. R. and Faucher J. Designing nylon 12 nanocomposites for catherer shafts, 'more clay is not always better'. In: 61st ANTEC, Society of Plastics Engineers. U.S, May, 2003. 2593-2597.

65. Pacchioli D. Clay into plastic. *Research Penn State* 2003;24(1-2).

66. Cypes S. H., Saltzman W. M. and Giannelis E. P. Organosilicate-polymer drug delivery system: Controlled released and enhanced mechanical properties. *Journal of Controlled Release* 2003;90:163-169.

67. Lucciarini J. M., Ratto J. A., Koene B. E. and Powell B. Nanocomposites study of ethylene co-vinyl alcohol and montmorillonite clay. In: ANTEC, Society of Plastics Engineers. U.S, 2002. 760-764.

68. Thellen C. Montmorillonite layered silicate nanocomposites for military packaging applications. In: Executive Conference Management. Michigan, Brussel, March 2004.

69. Chen C. and Curliss D. Processing and morphological development of montmorillonite epoxy nanocomposites. *Nanotechnology* 2003;14:643-648.

70. Paulo D. J., Silva L. R., Festas A. and Abrao A. M. Machinability study on precision turning of PA66 polyamide with and without glass fiber reinforcing. *Materials and Design* 2009;30(2):228-234.

71. Bikales N. M. *Mechanical Properties of Polymers*. New York: Wiley-Interscience, 1971.

72. Mohr J. G. and Rowe W. P., *Chapter 5: Application of continuous-filament fiber glass product*. In: editor. Fiber Glass. New York: Van Nostrand Reinhold Company, 1978.

73. Folkes M. J., *Chapter 4: Compounding*. In: editor. Short Fibre Reinforced Thermoplastic. New York: John Wiley & Sons, Inc., 1982.

74. Sirabian S., Eise K. and Curry J. Multi-screw compounders for reinforced plastics production. In: Composites Institute 39th Annual Conference. New York, USA, 1984.

75. Cho J. W. and Paul D. R. Nylon 6 nanocomposites by melt compounding. *Polymer* 2001;42(3):1083-1094.

76. Dennis H. R., Hunter D. L., Chang D., Kim S., White J. L., Cho J. W. and Paul D. R. Effect of melt processing conditions on the extent of exfoliation in organoclay-based nanocomposites. *Polymer* 2001;42:9513-9522.

77. Gale M. Compounding with single-screw extruders. *Advances in Polymer Technology* 1998;16(4):251-262.

78. Dennis H. R. and Hunter D. L. Nanocomposites: The importance of processing. In: 58th ANTEC, Society of Plastics Engineers. Orlando, USA, May 2000.

79. Folkes M. J., *Chapter 5: Processing-microstructure correlations*. In: editor. Short Fibre Reinforced Thermoplastic. New York: John Wiley & Sons, Inc., 1982.

80. Darlington M. W. and Smith G. R. Voiding in glass fibre reinforced thermoplastics mouldings. *Polymer* 1975;16(6):459-462.

81. Kojima Y., Usuki A., Kawasumi M., Okada A., Kurauchi T., Kamigaito O. and Kaji K. Novel preferred orientation in injection-molded nylon 6-clay hybrid. *Journal of Polymer Science Part B: Polymer Physics* 1995;33(7):1039-1045.

82. Lew C. Y., Murphy W. R., Yanai G. M. and Abe K. Polymer-clay nanocomposites: Tailoring structures with processing conditions. In: ANTEC 2003 Conference Proceedings. 2003. 178-182.

83. Krishnamoorti R. and Yurekli K. Rheology of polymer layered silicate nanocomposites. *Current Opinion in Colloid & Interface Science* 2001;6(5):464-470.

84. Fong H., Liu W., Wang C. S. and Vaia R. A. Generation of electrospun fibers of nylon 6 and nylon 6-montmorillonite nanocomposite. *Polymer* 2002;43(3):775-780.

85. Zanetti M, Camino G, Reichert P and Mülhaupt R. Thermal behaviour of poly(propylene) layered silicate nanocomposites. *Macromol Rapid Commun* 2001;22(3):176-180.

86. Lee S. Y., Kang I. A., Doh G. H., Kim W. J., Kim J. S., Yoon H. G. and Wu Q. Thermal, mechanical and morphological properties of polypropylene/clay/wood flour nanocomposites. *Express Polymer Letters* 2008;2(2):78–87.

87. Bozkurt E., Kaya E. and Tanoglu M. Mechanical and thermal behavior of non-crimp glass fiber reinforced layered clay/epoxy nanocomposites. *Composites Science and Technology* 2007;67(15-16):3394-3403.

88. Samal S. K., Mohanty S. and Nayak S. K. Polypropylene-bamboo/glass fiber hybrid composites: Fabrication and analysis of mechanical, morphological, thermal and dynamic mechanical behavior. *Journal of Reinforced Plastics and Composites* 2009;28(22):2729-2748.

89. Hancock M. , *Chapter 8 Filled Thermoplastics*. In: Rothon R. N., editor. Particulate-filled Polymer Composites. Shrewsbury, UK: Longman Scientific & Technical, 1st edition, 1995. 279-316.

90. Thomason J. L. Structure-property relationships in glass-reinforced polyamide, part 1: The effects of fibre content. *Polymer Composites* 2006;27(5):552-562.

91. Ray S. S. and Okamoto M. Polymer/layered silicate nanocomposites: A review from preparation to processing. *Progress in Polymer Science* 2003;28(11):1539-1641.

92. Brune D. A. and Bicerano J. Micromechanics of nanocomposites: Comparison of tensile and compressive elastic moduli, and prediction of effects of incomplete exfoliation and imperfect alignment on modulus. *Polymer* 2002;43(2):369-387.

93. Luo J. J. and Daniel I. M. Characterization and modeling of mechanical behavior of polymer/clay nanocomposites. *Composites Science and Technology* 2003;63(11):1607-1616.

94. Kim G. M., Lee D. H., Hoffmann B., Kressler J. and Stöppelmann G. Influence of nanofillers on the deformation process in layered silicate/polyamide-12 nanocomposites. *Polymer* 2001;42(3):1095-1100.

95. Gersappe D. Molecular mechanisms of failure in polymer nanocomposites. *Physical Review Letters* 2002;89(5):58301-58304.

96. Hemmasi A. H., Khademi-Eslam H., Talaiepoor M., Kord B. and Ghasemi I. Effect of nanoclay on the mechanical and morphological properties of wood polymer nanocomposite. *Journal of Reinforced Plastics and Composites* 2010;29(7):964-971.

97. Mohan T. P. and Kanny K. Influence of nanoclay on rheological and mechanical properties of short glass fiber-reinforced polypropylene composites. *Journal of Reinforced Plastics and Composites* 2011;30(2):152-160.

98. Arbelaiz A., Fernandez B., Cantero G., Llano-Ponte R., Valea A. and Mondragon I. Mechanical properties of flax fibre/polypropylene composites. Influence of fibre/matrix modification and glass fibre hybridization. *Composites Part A: Applied Science and Manufacturing* 2005;36(12):1637-1644.

99. ASTM E-23-07ae1 Standard. *Standard Test Method for Notched Bar Impact Testing of Metallic Materials, ASTM International, West Coshoshocken, PA, DOI 10.1520/E0023-07AE01, www.astm.org.*

100. Zhang Z. Y. and Richardson M. O. W. Low velocity impact induced damage evaluation and its effect on the residual flexural properties of pultruded GRP composites. *Composite Structures* 2007;81:195-201.

101. Bledzki A. K. and Faruk O. Creep and impact properties of wood fibre–polypropylene composites: Influence of temperature and moisture content. *Composites Science and Technology* 2004;64(5):693-700.

102. Larson G. P. Kaolinite fractions, their effect on physical properties of reinforced plastics. *Modern Plastics* 1958;35(9):157-166.

103. Bramuzzo M., Savadori A. and Bacci D. Polypropylene composites: Fracture mechanics analysis of impact strength. *Polymer Composites* 1985;6(1):1-8.

104. Lange F. F. The interaction of a crack front with a second-phase dispersion. *Philosophical Magazine* 1970;22(179):983-992.

105. Chemtura Corporation. Polybond H022 Technical Data Sheet. http://www.chemtura-organometallics.com, 2009 (accessed on April 2012).

106. ASTM D-1238 Standard. *Standard Test Method for Melt Flow Rates of Thermoplastics by Extrusion Plastometer, ASTM International, West Coshoshocken, PA, DOI 10.1520/D1238-10, www.astm.org.* 2010.

107. ASTM D-1505 Standard. *Standard Test Method for Density of Plastics by the Density-Gradient Technique, ASTM International, West Coshoshocken, PA, DOI 10.1520/D1505-10, www.astm.org.* 2010.

108. ASTM D-638 Standard. *Standard Test Method for Tensile Properties of Plastics, ASTM International, West Coshoshocken, PA, DOI 10.1520/D0638-03, www.astm.org.* 2003.

109. ASTM D-790 Standard. *Standard Test Methods for Flexural Properties of Unreinforced and Reinforced Plastics and Electrical Insulating Materials, ASTM International, West Coshoshocken, PA, 2010, DOI 10.1520/D0790-10, www.astm.org.* 2010.

110. Nanocor USA. Nanoclay PGV Technical Data Sheet. http://www.sigmaaldrich.com/catalog/product/aldrich/682659, 2006 (accessed on April 2012).

111. Nanocor USA. Nanoclay 1.44 PS Technical Data Sheet. http://www.sigmaaldrich.com/catalog/product/aldrich/682624, 2008 (accessed on April 2012).

112. Hassan A., Normasmira A. R. and Yahya R. Moisture absorption effect on thermal, dynamic mechanical and mechanical properties of injection-molded short glass-fiber/polyamide 6,6 composites *Fibers and Polymers* 2012;13(7):899-906.

113. Hassan A., Salleh N. M., Yahya R. and Sheikh M. R. K. Fiber length, thermal, mechanical and dynamic mechanical properties of injection-molded glass-fiber/polyamide 6,6: Plasticization effect. *Journal of Reinforced Plastics and Composites* 2011;30(6):488-498.

114. Miwa M. and Endo I. Critical fibre length and tensile strength for carbon fibre-epoxy composites. *Journal of Materials Science* 1994;29(5):1174-1178.

115. Denault J., Vu-Khanh T. and Foster B. Tensile properties of injection molded long fiber thermoplastic composite. *Polymer Composites* 1989;10:313-321.

116. Hassan A., Yahya R., Yahaya A. H., Tahir A. R. M. and Hornsby P. R. Tensile, impact and fiber length properties of injection-molded short and long glass fiber-reinforced polyamide 6, 6 composites. *Journal of Reinforced Plastics and Composites* 2004;23(9):969-986.

117. Lunt J. M. and Shortall J. B. The effect of extrusion compounding on fiber degradation and strength properties in short glass-fiber-reinforced nylon 6,6. *Plastics Rubber Process* 1979;4(3):108-111.

118. Hong C. K., Kim M. J., Oh S. H., Lee Y. S. and Nah C. Effects of polypropylene-g-(maleic anhydride/styrene) compatibilizer on mechanical and rheological properties of polypropylene/clay nanocomposites. *Journal of Industrial and Engineering Chemistry* 2008;14(2):236-242.

119. Tarameshlou M., Jafari S. H., Khonakdar H. A., Fakhravar A. and Farmahini-Farahani M. PET-based nanocomposites made by reactive and remodified clays. *Iranian Polymer Journal* 2010;19(7):521-529.

120. Patel H. A., Somani R. S., Bajaj H. C. and Jasra R. V. Nanoclays for polymer nanocomposites, paints, inks, greases and cosmetics formulations, drug delivery vehicle and waste water treatment. *Bulletin of Materials Science* 2006;29(2):133-145.

121. Kanny K., Jawahar P. and Moodley V. K. Mechanical and tribological behavior of clay–polypropylene nanocomposites. *Journal of Materials Science* 2008;43(22):7230-7238.

122. Lertwimolnun W. and Vergnes B. Influence of compatibilizer and processing conditions on the dispersion of nanoclay in a polypropylene matrix. *Polymer* 2005;46(10):3462-3471.

123. Haque A., Shamsuzzoha M., Hussain F. and Dean D. S2-glass/epoxy polymer nanocomposites: Manufacturing, structures, thermal and mechanical properties. *Journal of Composite Materials* 2003;37(20):1821-1837.

124. Timmerman J. F., Hayes B. S. and Seferis J. C. Nanoclay reinforcement effects on the cryogenic microcracking of carbon fiber/epoxy composites. *Composites Science and Technology* 2002;62(9):1249-1258.

125. Ren J., Huang Y., Liu Y. and Tang X. Preparation, characterization and properties of poly (vinyl chloride)/compatibilizer/organophilic-montmorillonite nanocomposites by melt intercalation. *Polymer Testing* 2005;24(3):316-323.

126. Hwang T. Y., Lee S. M., Ahn Y. and Lee J. W. Development of polypropylene-clay nanocomposite with supercritical CO_2 assisted twin screw extrusion. *Korea-Australia Rheology Journal* 2008;20(4):235-243.

127. Krump H., Luyt A. S. and Hudec I. Effect of different modified clays on the thermal and physical properties of polypropylene-montmorillonite nanocomposites. *Materials Letters* 2006;60(23):2877-2880.

128. Duquesne S., Jama C., Le Bras M., Delobel R., Recourt P. and Gloaguen J. M. Elaboration of EVA-nanoclay systems-characterization, thermal behaviour and fire performance. *Composites Science and Technology* 2003;63(8):1141-1148.

129. Qin H., Zhang S., Zhao C., Feng M., Yang M., Shu Z. and Yang S. Thermal stability and flammability of polypropylene/montmorillonite composites. *Polymer Degradation and Stability* 2004;85(2):807-813.

130. Chisholm N., Mahfuz H., Rangari V. K., Ashfaq A. and Jeelani S. Fabrication and mechanical characterization of carbon/SiC-epoxy nanocomposites. *Composite Structures* 2005;67(1):115-124.

131. Kumar R. V., Koltypin Y., Palchik O. and Gedanken A. Preparation and characterization of nickel–polystyrene nanocomposite by ultrasound irradiation. *Journal of Applied Polymer Science* 2002;86(1):160-165.

132. Kumar R. V., Koltypin Y., Cohen Y. S, Cohen Y., Aurbach D., Palchik O., Felner I. and Gedanken A. Preparation of amorphous magnetite nanoparticles embedded in polyvinyl alcohol using ultrasound radiation. *Journal of Materials Chemistry* 2000;10(5):1125-1129.

133. Tang Y., Hu Y., Song L., Zong R., Gui Z., Chen Z. and Fan W. Preparation and thermal stability of polypropylene/montmorillonite nanocomposites. *Polymer Degradation and Stability* 2003;82(1):127-131.

134. Gilnian J. W., Kashivagi T. C. L., Giannelis E. P., Manias E., Lomakin S. and Lichtenhan J. D., *Fire Retardancy of Polymers*. In: Le Bras M., Caniino G., Bourbigot S. and Delobel R., editor. Cambridge: The Royal Society of Chemistry. 1998.

135. Ota W. N., Amico S. C. and Satyanarayana K. G. Studies on the combined effect of injection temperature and fiber content on the properties of polypropylene-glass fiber composites. *Composites Science and Technology* 2005;65(6):873-881.

136. Wang W., Tang L. and Qu B. Mechanical properties and morphological structures of short glass fiber reinforced PP/EPDM composite. *European Polymer Journal* 2003;39(11):2129-2134.

137. Rezaei F., Yunus R. and Ibrahim N. A. Effect of fiber length on thermomechanical properties of short carbon fiber reinforced polypropylene composites. *Materials and Design* 2009;30(2):260-263.

138. Bryk M. T. *Degradation of Filled Polymers: High Temperature and Thermaloxidative Process*. New York: Ellis Horwood, 1991. 71-78.

139. Gilman J. W., Jackson C. L., Morgan A. B., Harris Jr. R., Manias E., Giannelis E. P., Wuthenow M., Hilton D. and Phillips S. H. Flammability properties of polymer-layered-silicate nanocomposites. Polypropylene and polystyrene nanocomposites. *Chemistry of Materials* 2000;12(7):1866-1873.

140. Wahit M. U., Hassan A., Ishak Z. A. M., Rahmat A. R. and Bakar A. A. Morphology, thermal, and mechanical behavior of ethylene octene copolymer toughened polyamide 6/polypropylene nanocomposites. *Journal of Thermoplastic Composite Materials* 2006;19(5):545-567.

141. Liu T., Lim K. P., Tjiu W. C, Pramoda K. P. and Chen Z. K. Preparation and characterization of nylon 11/organoclay nanocomposites. *Polymer* 2003;44(12):3529-3535.

142. Sharma S. K. and Nayak S. K. Surface modified clay/polypropylene (PP) nanocomposites: Effect on physico-mechanical, thermal and morphological properties. *Polymer Degradation and Stability* 2009;94(1):132-138.

143. Özdilek C., Kazimierczak K., van der Beek D. and Picken S. J. Preparation and properties of polyamide-6-boehmite nanocomposites. *Polymer* 2004;45(15):5207-5214.

144. Modesti M., Lorenzetti A., Bon D. and Besco S. Thermal behaviour of compatibilised polypropylene nanocomposite: Effect of processing conditions. *Polymer Degradation and Stability* 2006;91(4):672-680.

145. Zhang Y. Q., Lee J. H., Jang H. J. and Nah C. W. Preparing PP/clay nanocomposites using a swelling agent. *Composites Part B: Engineering* 2004;35(2):133-138.

146. Lee S. H., Kim S. Y. and Youn J. R. Effects of maleination and heat treatment on morphology and dynamic mechanical thermal behavior of polypropylene/organoclay nanocomposites. *Composites Part A: Applied Science and Manufacturing* 2009;40(6):968-974.

147. Nayak S. K. and Mohanty S. Sisal glass fiber reinforced PP hybrid composites: Effect of MAPP on the dynamic mechanical and thermal properties. *Journal of Reinforced Plastics and Composites* 2010;29(10):1551-1568.

148. Kulshreshtha A. K., Maiti A. K., Choudhary M. S. and Rao K. V. Nano addition of raw bentonite enhances polypropylene (PP) properties. *Journal of Applied Polymer Science* 2006;99(3):1004-1009.

149. Fornes T. D. and Paul D. R. Crystallization behavior of nylon 6 nanocomposites. *Polymer* 2003;44(14):3945-3961.

150. Lei S. G., Hoa S. V. and Ton-That M. T. Effect of clay types on the processing and properties of polypropylene nanocomposites. *Composites Science and Technology* 2006;66(10):1274-1279.

151. Mandal S. and Alam S. Dynamic mechanical analysis and morphological studies of glass/bamboo fiber reinforced unsaturated polyester resin-based hybrid composites. *Journal of Applied Polymer Science* 2012;125:E382-E387.

152. Wang Y., Chen F. B., Li Y. C. and Wu K. C. Melt processing of polypropylene/clay nanocomposites modified with maleated polypropylene compatibilizers. *Composites Part B: Engineering* 2004;35(2):111-124.

153. Lai S. M., Chen W. C. and Zhu X. S. Melt mixed compatibilized polypropylene/clay nanocomposites: Part 1-the effect of compatibilizers on optical transmittance and mechanical properties. *Composites Part A: Applied Science and Manufacturing* 2009;40(6-7):754-765.

154. George J., Bhagawan S. S. and Thomas S. Thermogravimetric and dynamic mechanical thermal analysis of pineapple fibre reinforced polyethylene composites. *Journal of Thermal Analysis and Calorimetry* 1996;47(4):1121-1140.

155. Yilmazer U. and Cansever M. Effects of processing conditions on the fiber length distribution and mechanical properties of glass fiber reinforced nylon-6. *Polymer Composites* 2002;23(1):61-71.

156. Kusmono, Mohd Ishak Z. A., Chow W. S., Takeichi T. and Rochmadi. Compatibilizing effect of SEBS-g-MA on the mechanical properties of different types of OMMT filled polyamide 6/polypropylene nanocomposites. *Composites Part A: Applied Science and Manufacturing* 2008;39(12):1802-1814.

157. Rana A. K., Mandal A., Mitra B. C., Jacobson R., Rowell R. and Banerjee A. N. Short jute fiber-reinforced polypropylene composites: Effect of compatibilizer. *Journal of Applied Polymer Science* 1998;69(2):329-338.

158. Chen M., Wan C., Shou W., Zhang Y. and Zhang J. Effects of interfacial adhesion on properties of polypropylene/Wollastonite composites. *Journal of Applied Polymer Science* 2008;107(3):1718-1723.

159. Dong Y. and Bhattacharyya D. Effects of clay type, clay/compatibiliser content and matrix viscosity on the mechanical properties of polypropylene/organoclay nanocomposites. *Composites Part A: Applied Science and Manufacturing* 2008;39(7):1177-1191.

160. Lopez-Manchado M. A., Biagiotti J. and Kenny J. M. Comparative study of the effects of different fibres on the processing and properties of polypropylene matrix composites. *Journal of Thermoplastic Composite Materials* 2002;15:337-353.

161. Kumar R., Yakabu M. K. and Anandjiwala R. D. Effect of montmorillonite clay on flax fabric reinforced poly lactic acid composites with amphiphilic additives. *Composites Part A: Applied Science and Manufacturing* 2010;41(11):1620-1627.

162. Fu S. Y., Feng X. Q., Lauke B. and Mai Y. W. Effects of particle size, particle/matrix interface adhesion and particle loading on mechanical properties of particulate–polymer composites. *Composites Part B: Engineering* 2008;39(6):933-961.

163. Shi Y., Kanny K. and Jawahar P. Hybrid nanocomposites: Processing and properties. *Advanced Composite Materials* 2009;18(4):365-379.

164. Hussain M., Nakahira A. and Niihara K. Mechanical property improvement of carbon fiber reinforced epoxy composites by Al_2O_3 filler dispersion. *Materials Letters* 1996;26(3):185-191.

165. Parija S., Nayak S. K., Verma S. K. and Tripathy S. S. Studies on physico-mechanical properties and thermal characteristics of polypropylene/layered silicate nanocomposites. *Polymer Composites* 2004;25(6):646-652.

166. Dal Castel C., Pelegrini T., Barbosa R. V., Liberman S. A. and Mauler R. S. Properties of silane grafted polypropylene/montmorillonite nanocomposites. *Composites Part A: Applied Science and Manufacturing* 2010;41(2):185-191.

167. Kornmann X., Rees M., Thomann Y., Necola A., Barbezat M. and Thomann R. Epoxy-layered silicate nanocomposites as matrix in glass fibre-reinforced composites. *Composites Science and Technology* 2005;65(14):2259-2268.

168. Gonzalez I., Eguiazabal J. I. and Nazabal J. Nanocomposites based on a polyamide 6/maleated styrene–butylene-co-ethylene–styrene blend: Effects of clay loading on morphology and mechanical properties. *European Polymer Journal* 2006;42(11):2905-2913.

169. Kim K. J., Cho H. W. and Yoon K. J. Effect of P(MMA-co-MAA) compatibilizer on the miscibility of nylon 6/PVDF blends. *European Polymer Journal* 2003;39(6):1249-1265.

170. Vilaseca F., Valadez-Gonzalez A., Herrera-Franco P. J., Pelach M. A., López J. P. and Mutjé P. Biocomposites from abaca strands and polypropylene. Part I: Evaluation of the tensile properties. *Bioresource Technology* 2010;101(1):387-395.

171. Oksman K., Mathew A. P., Långström R., Nyström B. and Joseph K. The influence of fibre microstructure on fibre breakage and mechanical properties of natural fibre reinforced polypropylene. *Composites Science and Technology* 2009;69(11-12):1847-1853.

172. Thomason J. L. The influence of fibre length and concentration on the properties of glass fibre reinforced polypropylene: 5. Injection moulded long and short fibre PP. *Composites Part A: Applied Science and Manufacturing* 2002;33(12):1641-1652.

173. Mohd Ishak Z. A., Ariffin A. and Senawi R. Effects of hygrothermal aging and a silane coupling agent on the tensile properties of injection molded short glass fiber reinforced poly (butylene terephthalate) composites. *European Polymer Journal* 2001;37(8):1635-1647.

174. Thomason J. L. The influence of fibre length and concentration on the properties of glass fibre reinforced polypropylene: 7. Interface strength and fibre strain in injection moulded long fibre PP at high fibre content. *Composites Part A: Applied Science and Manufacturing* 2007;38(1):210-216.

175. Haneefa A., Bindu P., Aravind I. and Thomas S. Studies on tensile and flexural properties of short banana/glass hybrid fiber reinforced polystyrene composites. *Journal of Composite Materials* 2008;42(15):1471-1489.

176. Patankar S. N., Das A. and Kranov Y. A. Interface engineering via compatibilization in HDPE composite reinforced with sodium borosilicate hollow glass microspheres. *Composites Part A: Applied Science and Manufacturing* 2009;40(6-7):897-903.

177. Jarukumjorn K. and Suppakarn N. Effect of glass fiber hybridization on properties of sisal fiber-polypropylene composites. *Composites Part B: Engineering* 2009;40(7):623-627.

178. Thomason J. L. and Vlug M. A. Influence of fibre length and concentration on the properties of glass fibre-reinforced polypropylene: 1. Tensile and flexural modulus. *Composites Part A: Applied Science and Manufacturing* 1996;27(6):477-484.

179. Mouhmid B., Imad A., Benseddiq N., Benmedakhene S. and Maazouz A. A study of the mechanical behaviour of a glass fibre reinforced polyamide 6, 6: Experimental investigation. *Polymer Testing* 2006;25(4):544-552.

180. Takahashi K. and Choi N. S. Influence of fibre weight fraction on failure mechanisms of poly (ethylene terephthalate) reinforced by short-glass-fibres. *Journal of Materials Science* 1991;26(17):4648-4656.

181. Wetzel B., Haupert F. and Qiu Zhang M. Epoxy nanocomposites with high mechanical and tribological performance. *Composites Science and Technology* 2003;63(14):2055-2067.

182. Fu S. Y. and Lauke B. Characterization of tensile behaviour of hybrid short glass fibre/calcite particle/ABS composites. *Composites Part A: Applied Science and Manufacturing* 1998;29(5-6):575-583.

183. Thomason J. L., Vlug M. A., Schipper G. and Krikor H. Influence of fibre length and concentration on the properties of glass fibre-reinforced polypropylene: Part 3. Strength and strain at failure. *Composites Part A: Applied Science and Manufacturing* 1996;27(11):1075-1084.

184. Ding C., Jia D., He H., Guo B. and Hong H. How organo-montmorillonite truly affects the structure and properties of polypropylene. *Polymer Testing* 2005;24(1):94-100.

185. Mohanty S. and Nayak S. K. Melt blended polystyrene/layered silicate nanocomposites: Effect of clay modification on the mechanical, thermal, morphological and viscoelastic behavior. *Journal of Thermoplastic Composite Materials* 2007;20(2):175-193.

186. Ahmad S. H., Rasid R., Surip S. N., Anuar H., Czigany T. and Abdul Razak S. B. Mechanical and fracture toughness behavior of TPNR nanocomposites. *Journal of Composite Materials* 2007;41(17):2147-2159.

187. Akkapeddi M. K. Glass fiber reinforced polyamide-6 nanocomposites. *Polymer Composites* 2004;21(4):576-585.

188. Chandradass J., Ramesh Kumar M. and Velmurugan R. Effect of clay dispersion on mechanical, thermal and vibration properties of glass fiber-reinforced vinyl ester composites. *Journal of Reinforced Plastics and Composites* 2008;27(15):1585-1601.

189. Asi O. Mechanical properties of glass-fiber reinforced epoxy composites filled with Al_2O_3 particles. *Journal of Reinforced Plastics and Composites* 2009;28(23):2861-2867.

190. Wetzel B., Haupert F., Friedrich K., Zhang M. Q. and Rong M. Z. Impact and wear resistance of polymer nanocomposites at low filler content. *Polymer Engineering and Science* 2002;42(9):1919-1927.

191. Norkhairunnisa M., Azhar A. B. and Shyang C. W. Effects of organo montmorillonite on the mechanical and morphological properties of epoxy/glass fiber composites. *Polymer International* 2007;56(4):512-517.

192. Hassan A., Hornsby P. R. and Folkes M. J. Structure-property relationship of injection moulded carbon fibre reinforced polyamide 6,6 composites: The effect of compounding routes. *Polymer Testing* 2003;22(2):185-189.

193. Karger-Kocsis J. Instrumented impact fracture and related behavior in short- and long-glass-fiber-reinforced polypropylene. *Composites Science and Technology* 1993;48:273-283.

194. Hassan A., Hassan A. A. and Mohd Rafiq M. I. Impact properties of injection molded glass fiber/polyamide-6 composites: Effect of testing parameters. *Journal of Reinforced Plastics and Composites* 2011;30(10):889-898.

195. Shariatpanahi H., Sarabi F., Mirali M., Hemmati M. and Mahdavi F. Polypropylene-organoclay nanocomposite: Preparation, microstructure, and mechanical properties. *Journal of Applied Polymer Science* 2009;113:922-926.

196. Crosby J. M. and Drye T. R. Fracture studies of discontinuous fiber reinforced thermoplastic composites. *Journal of Reinforced Plastics and Composites* 1987;6(2):162-177.

197. Thomason J. L. and Vlug M. A. Influence of fibre length and concentration on the properties of glass fibre-reinforced polypropylene: 4. Impact properties. *Composites Part A: Applied Science and Manufacturing* 1997;28A:277-288.

198. Lee N. J. and Jang J. The effect of fibre content on the mechanical properties of glass fibre mat/polypropylene composites. *Composites Part A: Applied Science and Manufacturing* 1999;30(6):815-822.

199. Wells J. K. and Beaumont P. W. R. Debonding and pull-out processes in fibrous composites. *Journal of Materials Science* 1985;20(4):1275-1284.

200. Gupta V. B., Mittal R. K. and Goel M. Energy absorbing mechanisms in short-glass-fibre-reinforced polypropylene. *Composites Science and Technology* 1990;37(4):353-369.

201. Chow W. S., Mohd Ishak Z. A., Karger-Kocsis J., Apostolov A. A. and Ishiaku U. S. Compatibilizing effect of maleated polypropylene on the mechanical properties and morphology of injection molded polyamide 6/polypropylene/organoclay nanocomposites. *Polymer* 2003;44(24):7427-7440.

202. Li X., Park H. M., Lee J. O. and Ha C. S. Effect of blending sequence on the microstructure and properties of PBT/EVA g MAH/organoclay ternary nanocomposites. *Polymer Engineering & Science* 2002;42(11):2156-2164.

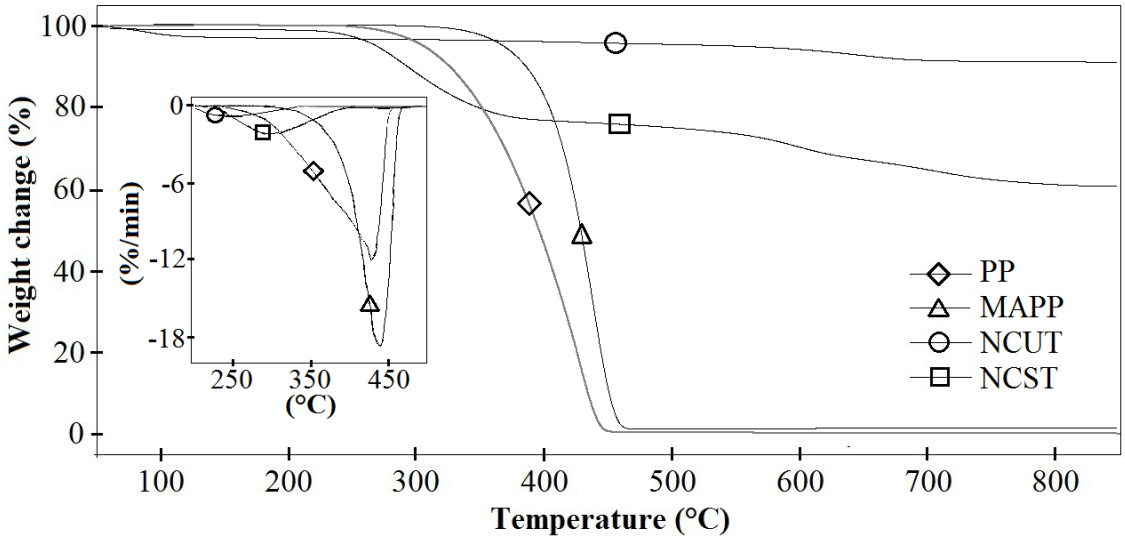

Appendix 4.1: TGA and DTG thermograms of PP, MAPP, untreated (NCUT) and surface treated (NCST) nanoclays

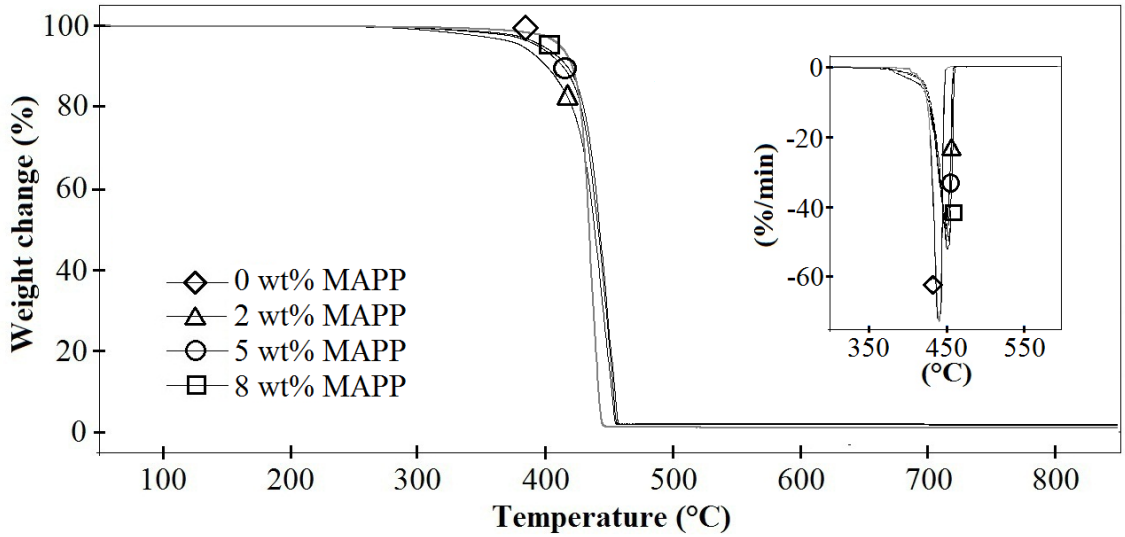

Appendix 4.2: TGA and DTG thermograms of PP/NCST2 nanocomposites with 0 *wt%* to 8 *wt%* of MAPP

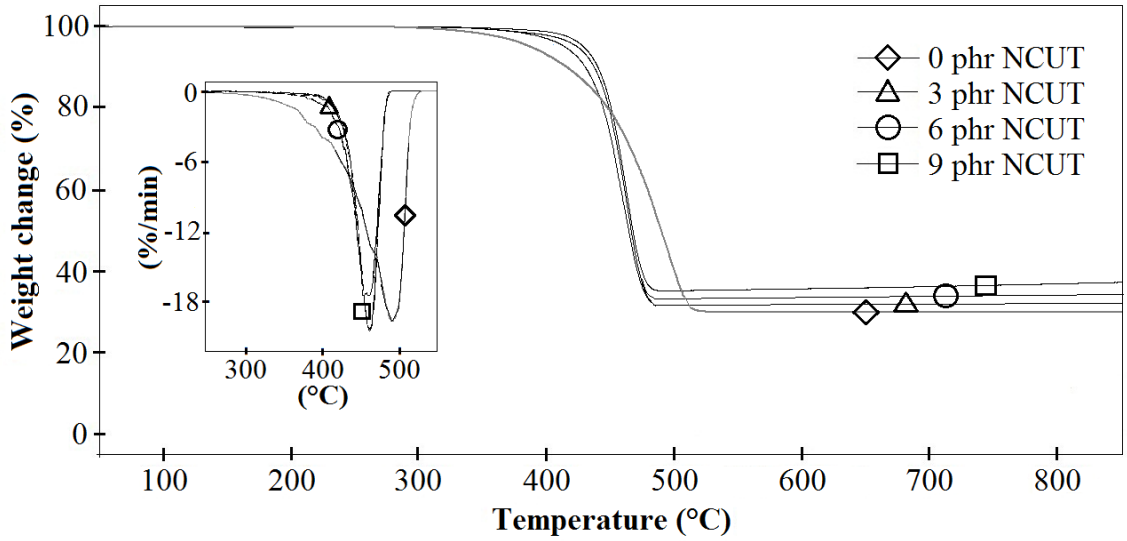

Appendix 4.3: TGA and DTG thermograms of PP/G30/NC nanocomposites with 0 phr to 9 phr of untreated clay

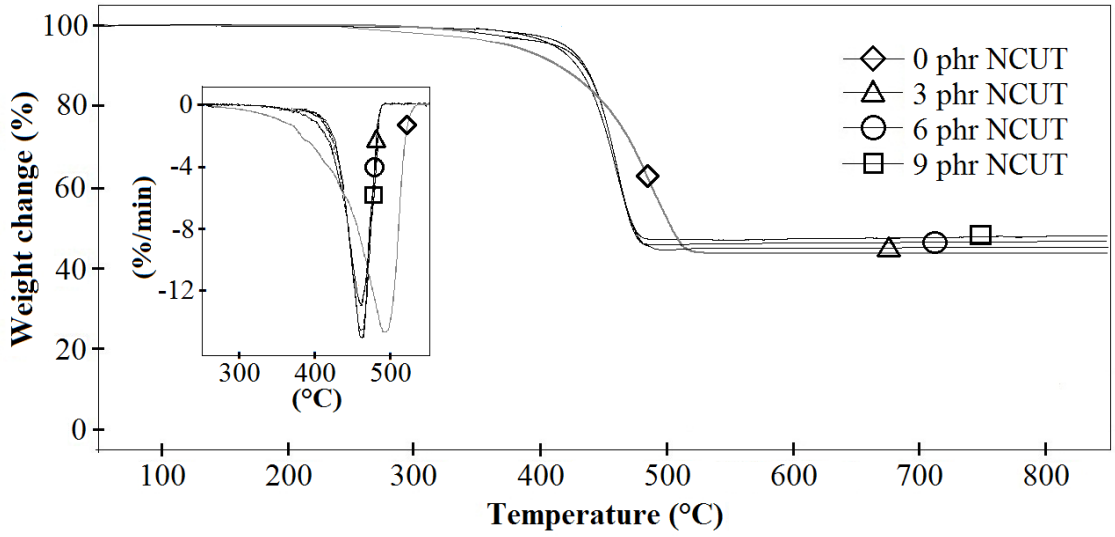

Appendix 4.4: TGA and DTG thermograms of PP/G45/NC nanocomposites with 0 phr to 9 phr of untreated clay

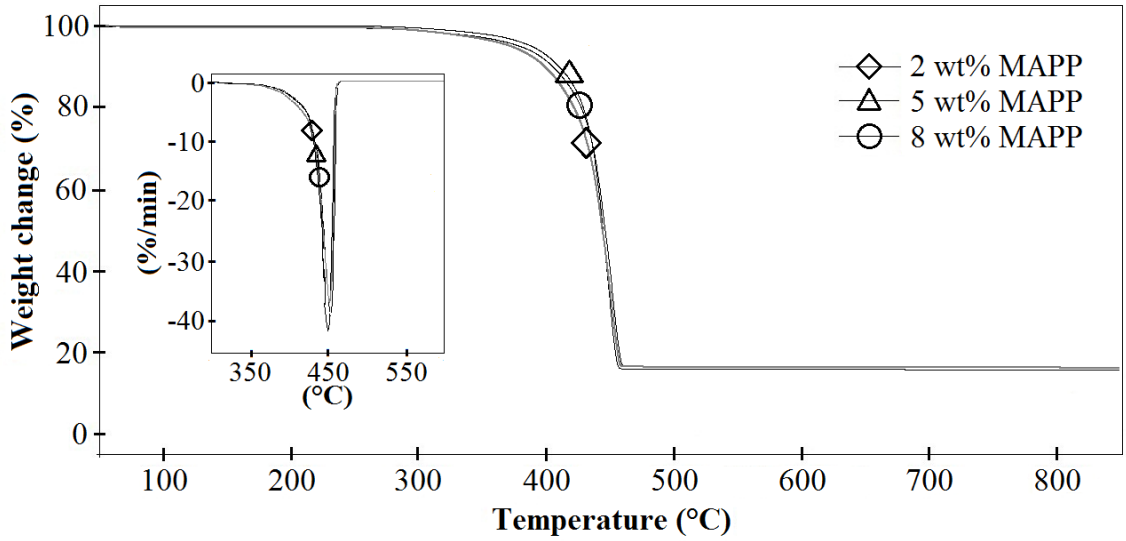

Appendix 4.5: TGA and DTG thermograms of PP/G15/NCST2 hybrid composites with 2 *wt%* to 8 *wt%* of MAPP

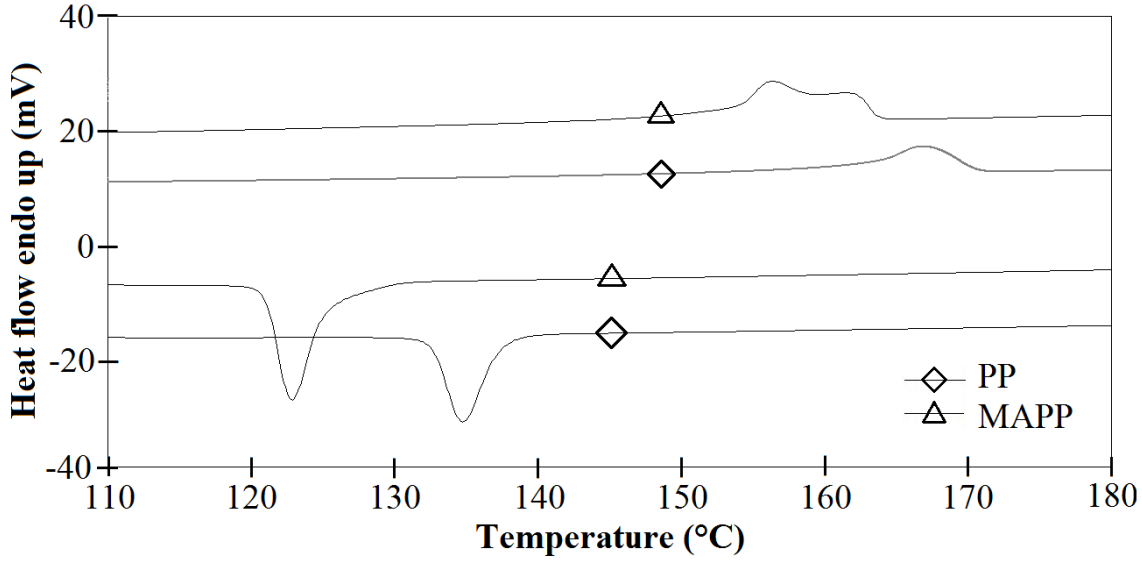

Appendix 4.6: The DSC thermograms of PP and MAPP

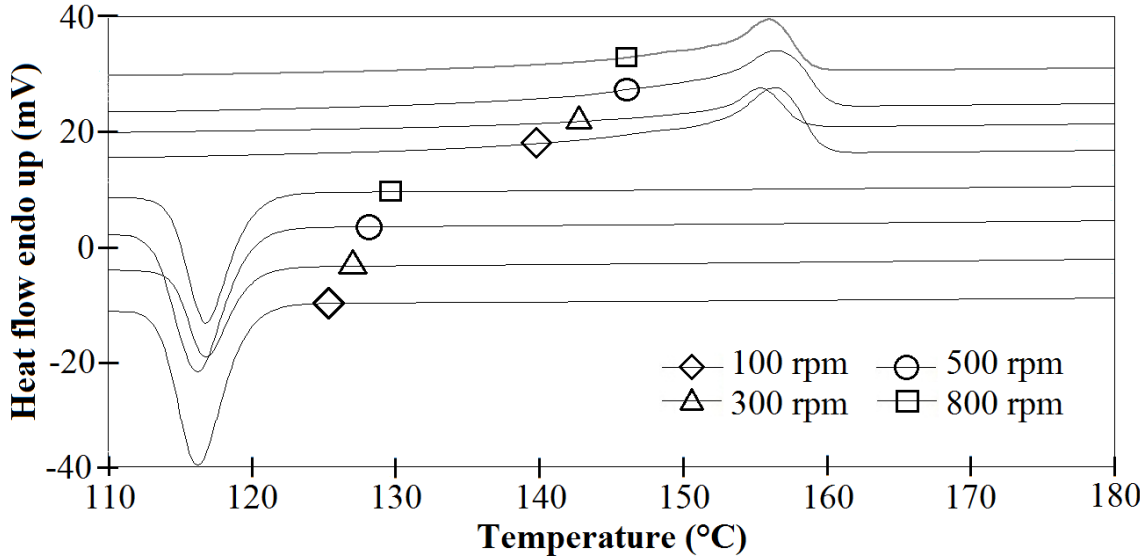

Appendix 4.7: The DSC thermograms of treated clay nanocomposites at different screw speeds

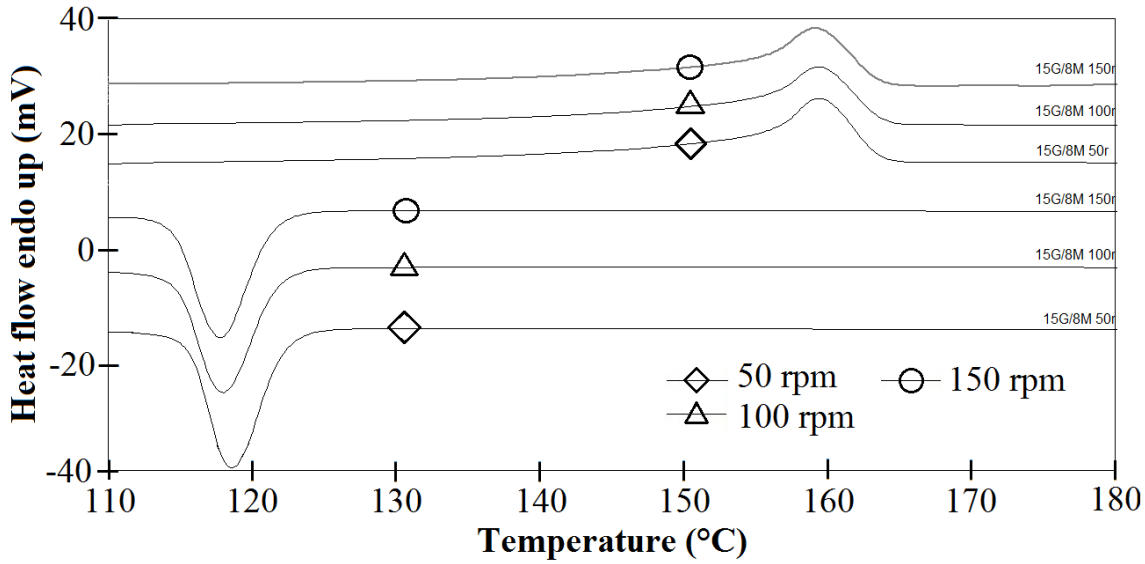

Appendix 4.8: The DSC thermograms of PP/G15 composites at different screw speeds

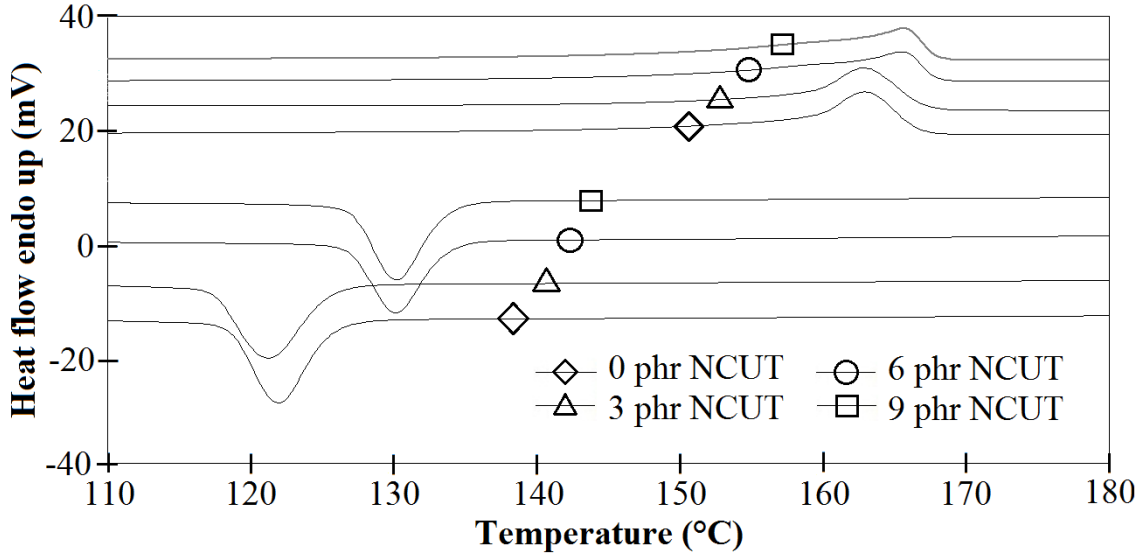

Appendix 4.9: The DSC thermograms of PP/G30/NC hybrid composites

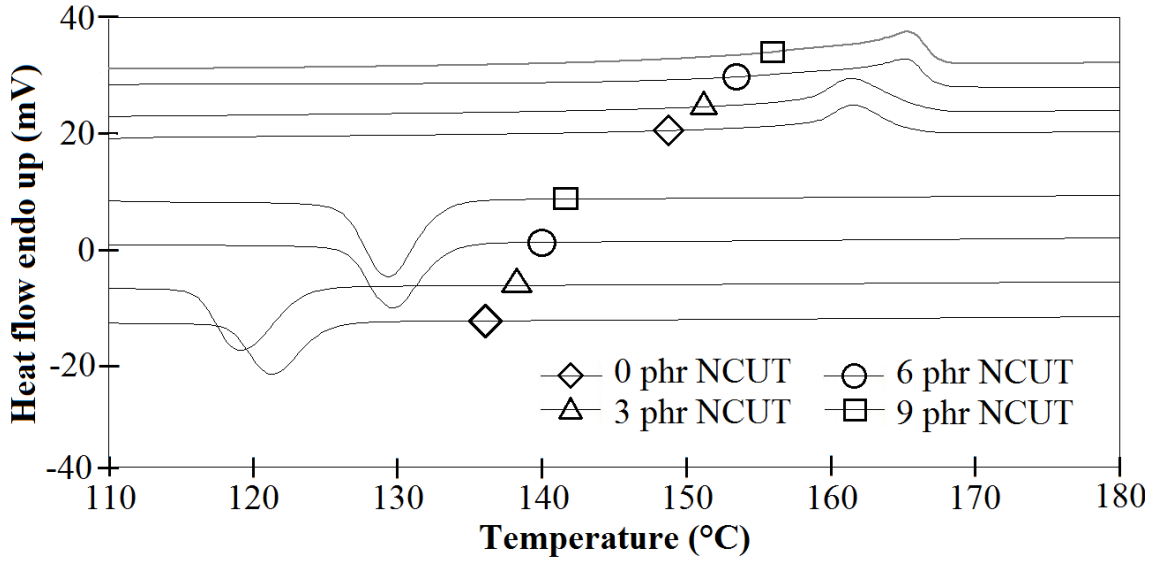

Appendix 4.10: The DSC thermograms of PP/G45/NC hybrid composites

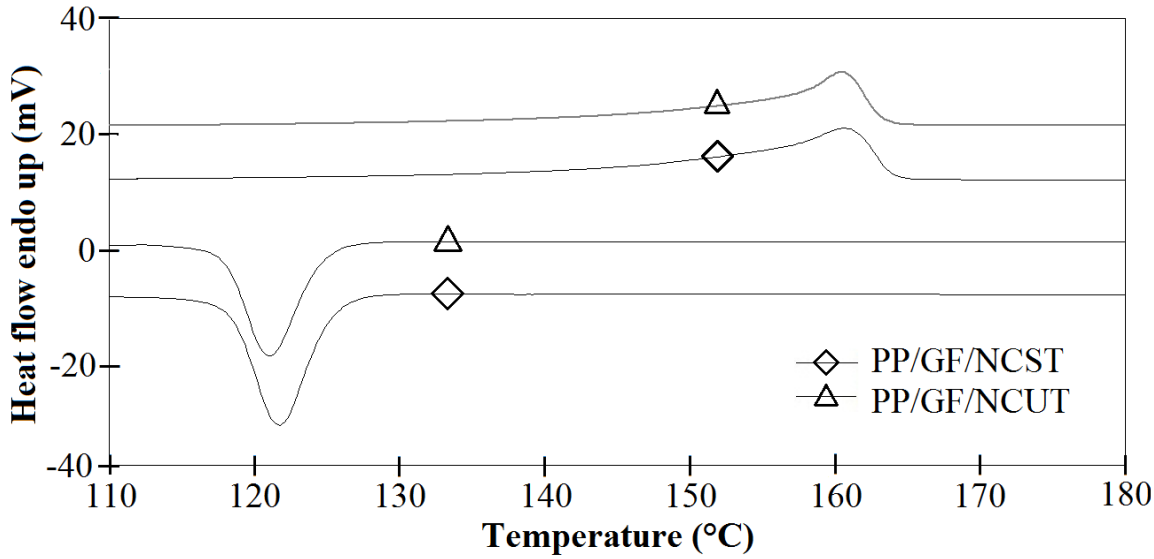

Appendix 4.11: The DSC thermograms of PP/GF/NCUT6 and PP/GF/NCST2 hybrid composites

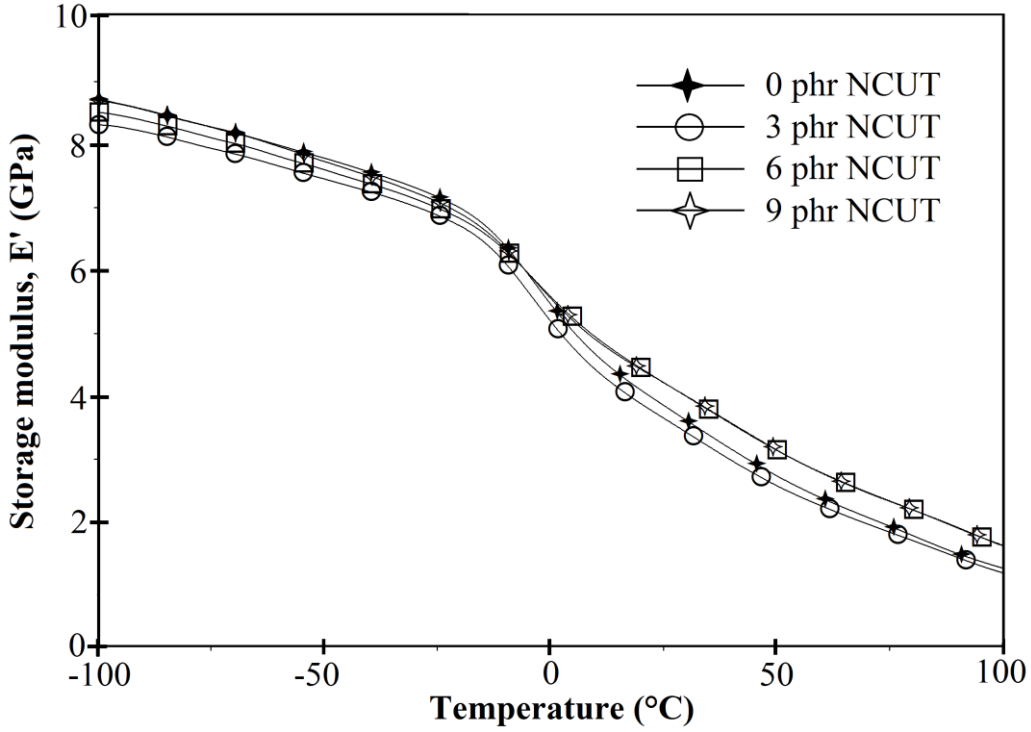

Appendix 4.12: The storage modulus curves of PP/G30 hybrid composites with different NCUT contents

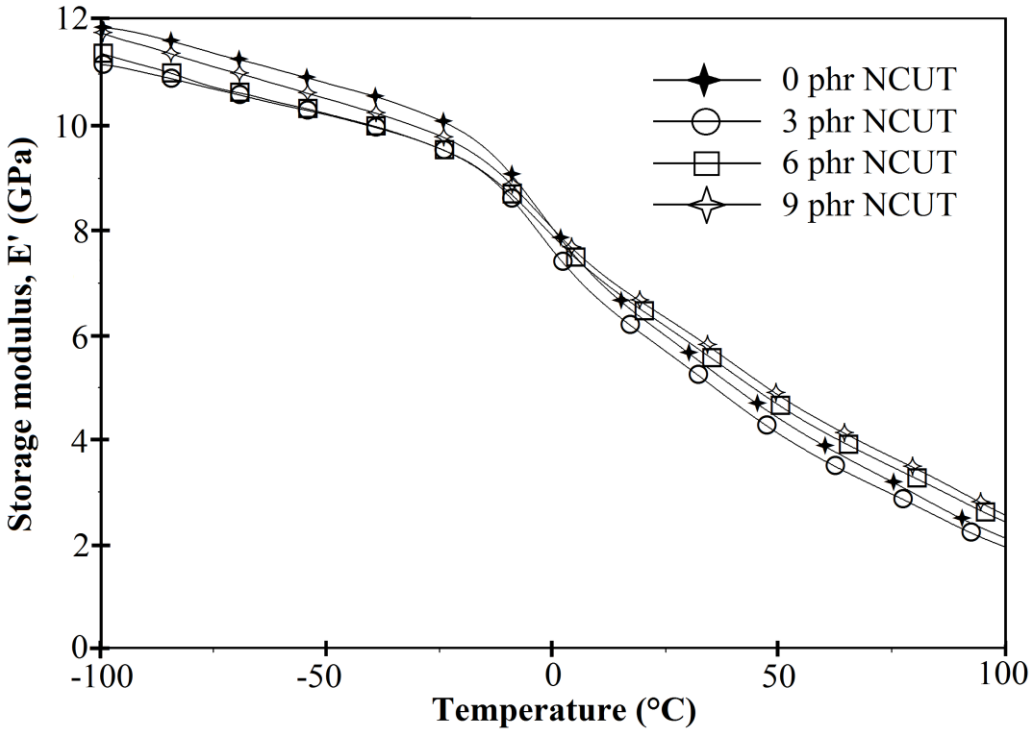

Appendix 4.13: The storage modulus curves of PP/G45 hybrid composites with different NCUT contents

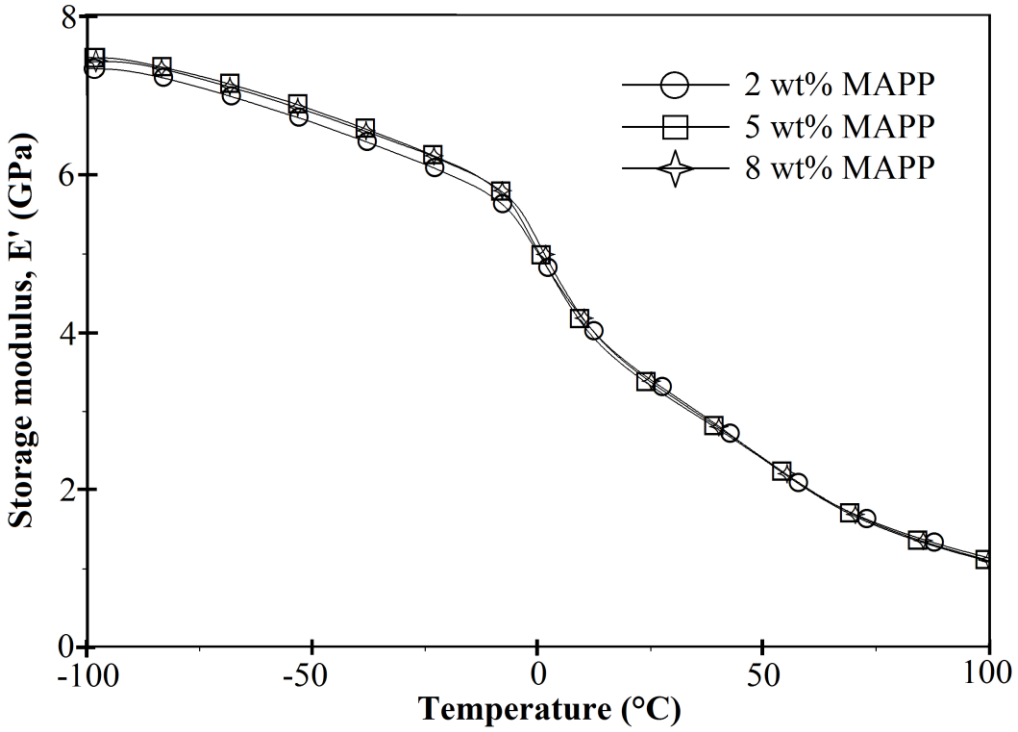

Appendix 4.14: The storage modulus curves of PP/G15/NCST2 hybrid composites with different MAPP contents

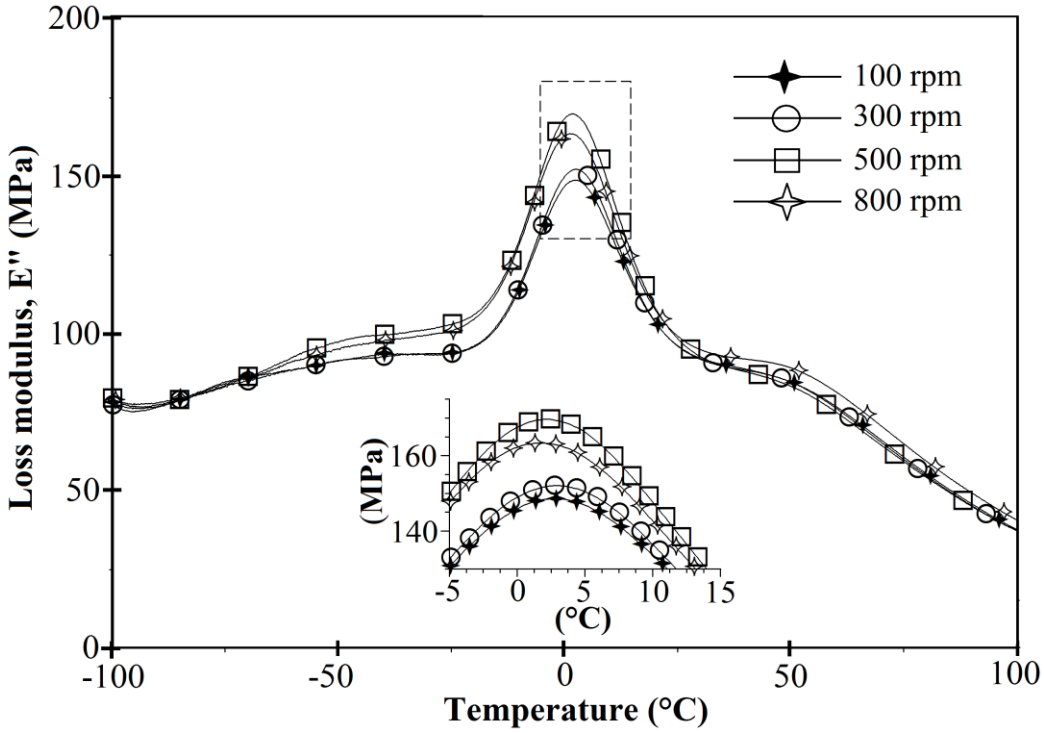

Appendix 4.15: The loss modulus curves of PP/NCST2 nanocomposites at different screw speeds

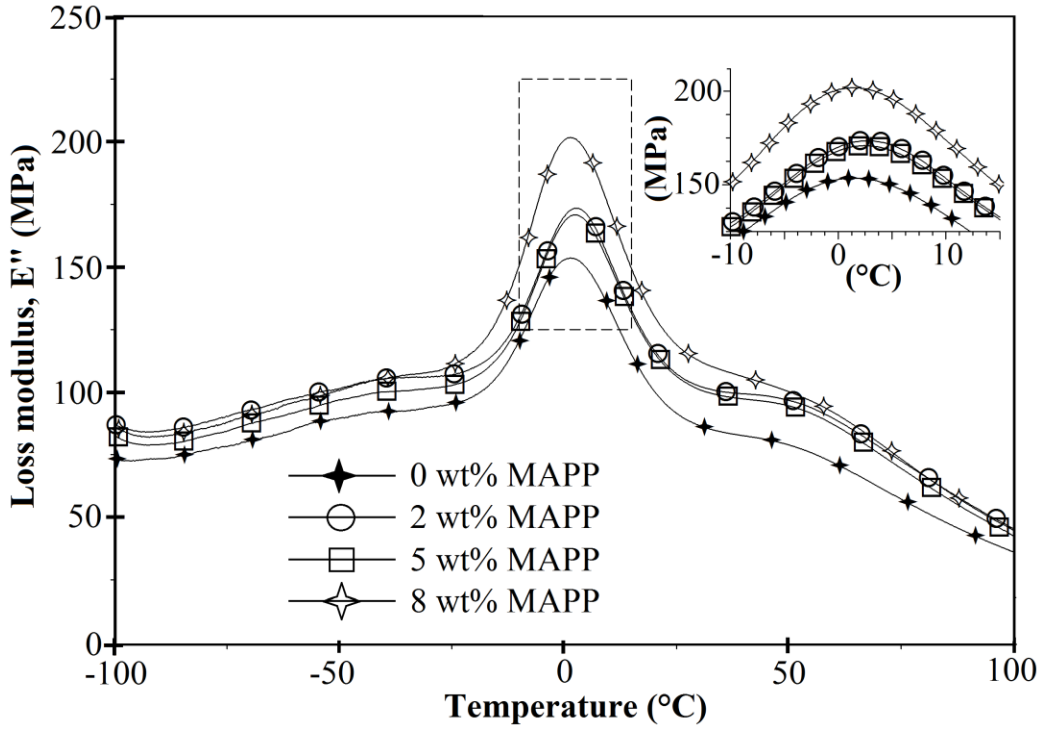

Appendix 4.16: The loss modulus curves of PP/NCST2 nanocomposites with different MAPP contents

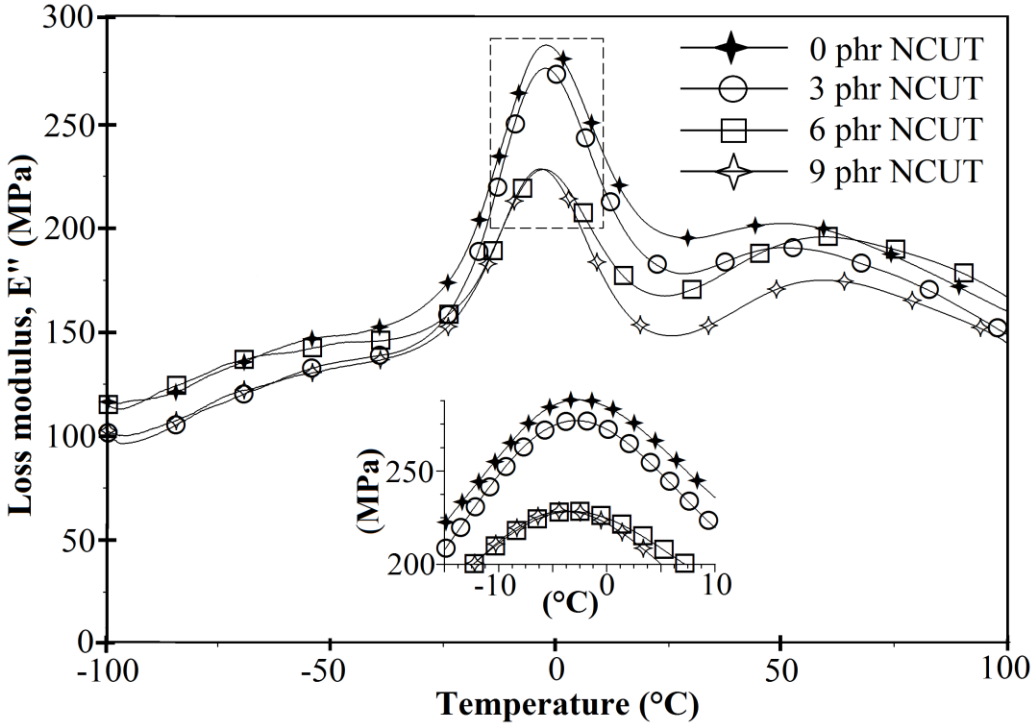

Appendix 4.17: The loss modulus curves of PP/G30 hybrid composites with different NCUT contents

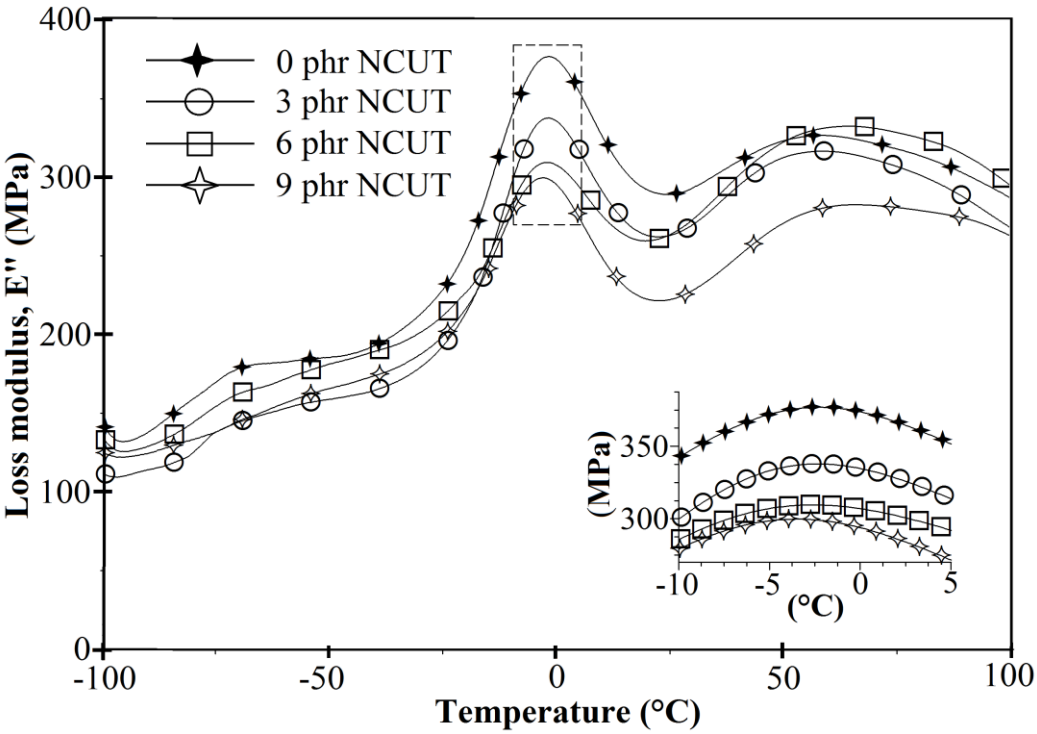

Appendix 4.18: The loss modulus curves of PP/G45 hybrid composites with different NCUT contents

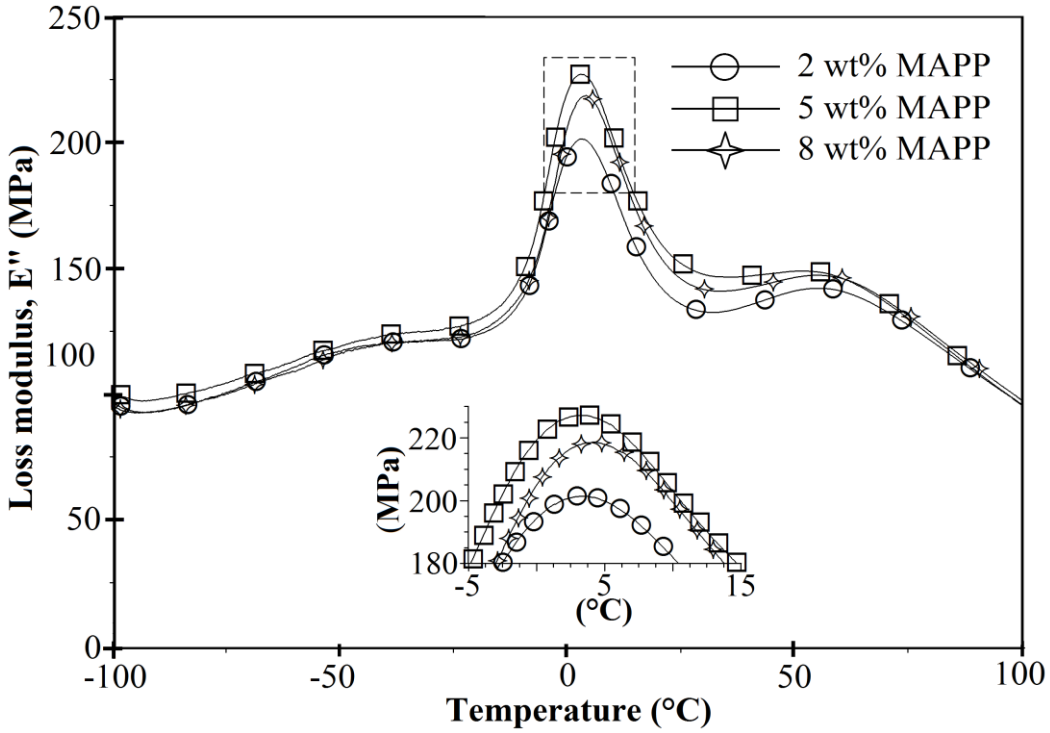

Appendix 4.19: The loss modulus curves of PP/G15/NCST2 hybrid composites with different MAPP contents

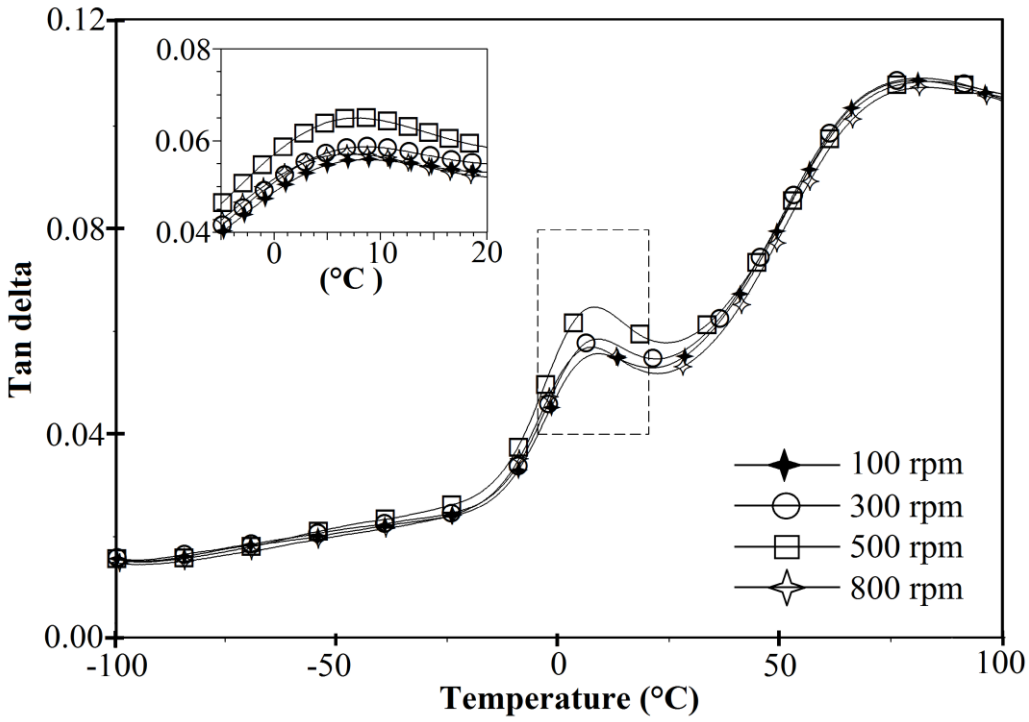

Appendix 4.20: The *tan δ* curves of PP/NCST2 nanocomposites at different screw speeds

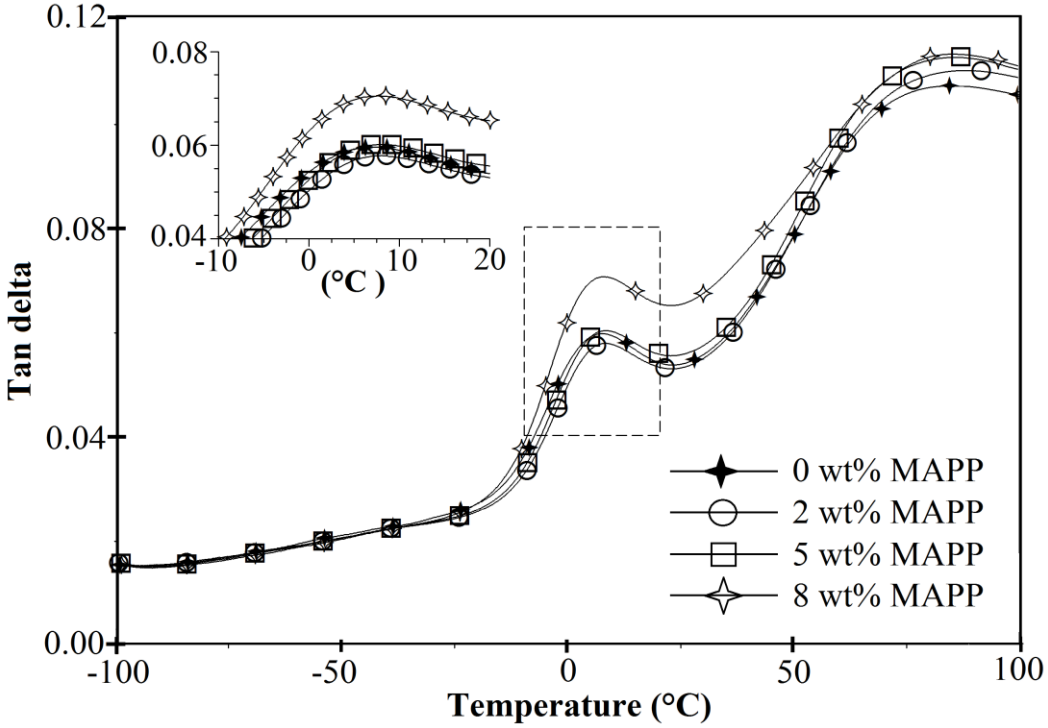

Appendix 4.21: The *tan δ* curves of PP/NCST2 nanocomposites with different MAPP contents

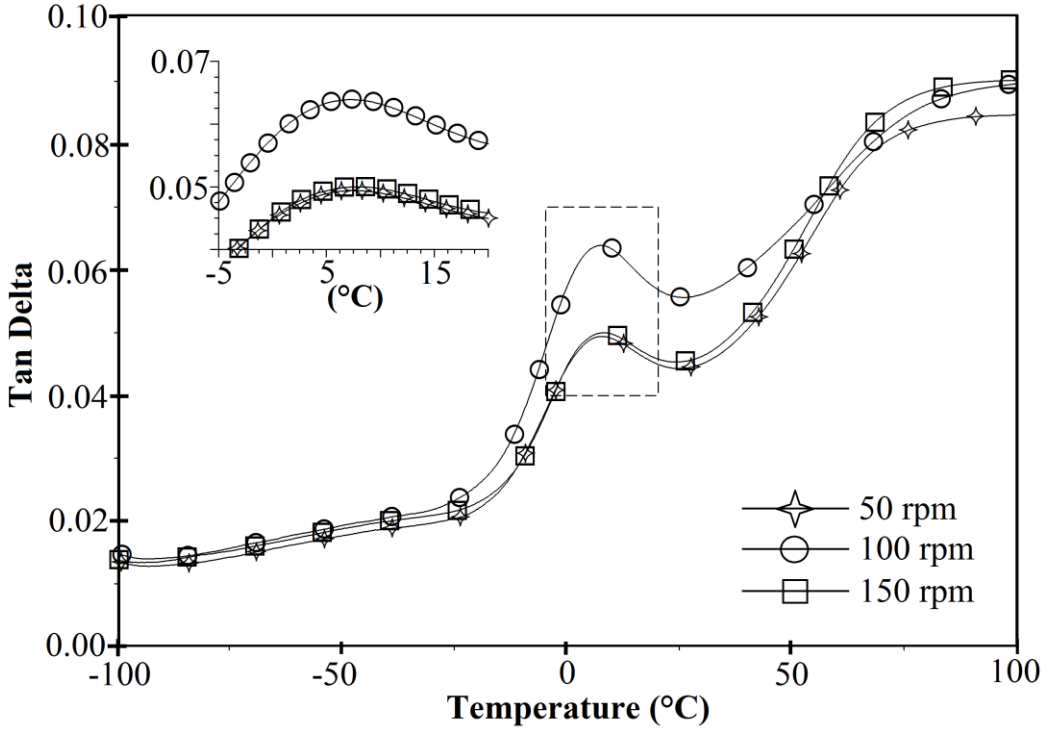

Appendix 4.22: The *tan δ* curves of glass fibre composites at different screw speeds

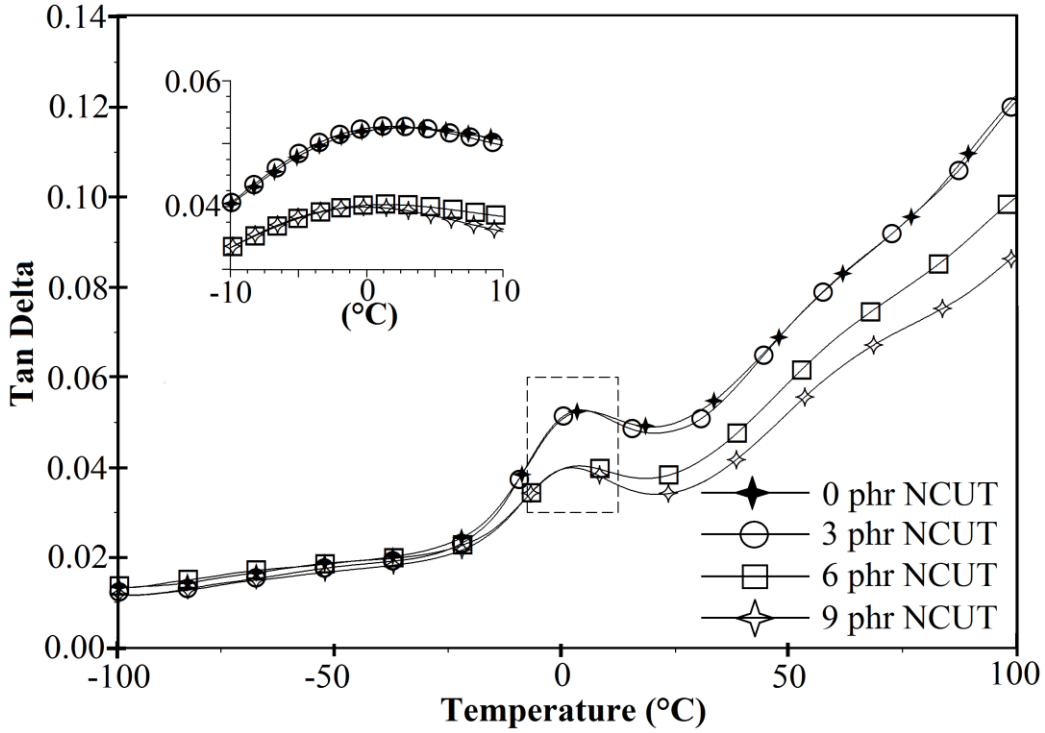

Appendix 4.23: The *tan δ* curves of PP/G30 hybrid composites with different NCUT contents

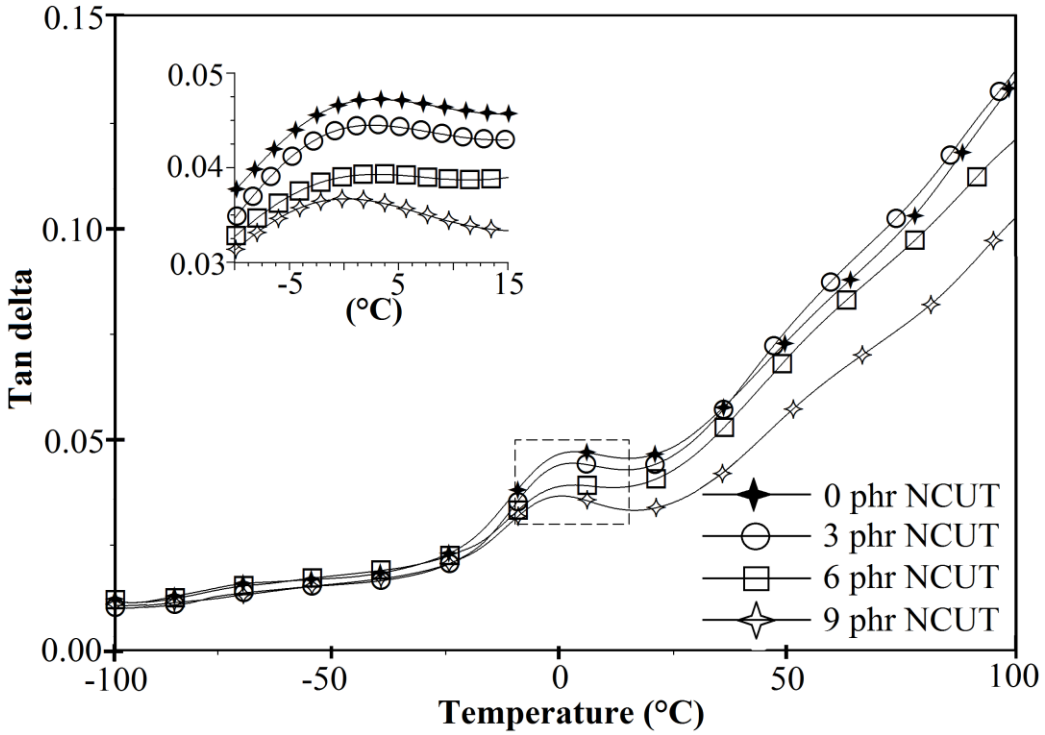

Appendix 4.24: The *tan δ* curves of PP/45 hybrid composites with different NCUT contents

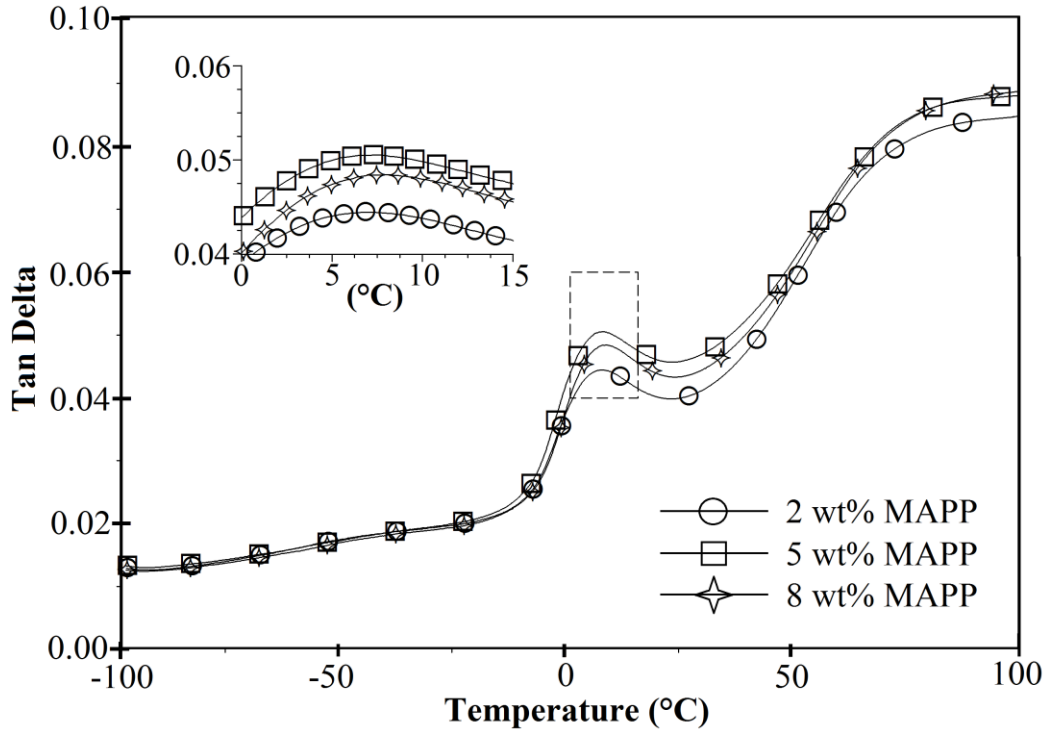

Appendix 4.25: The *tan δ* curves of PP/G15/NCST2 hybrid composites with different MAPP contents

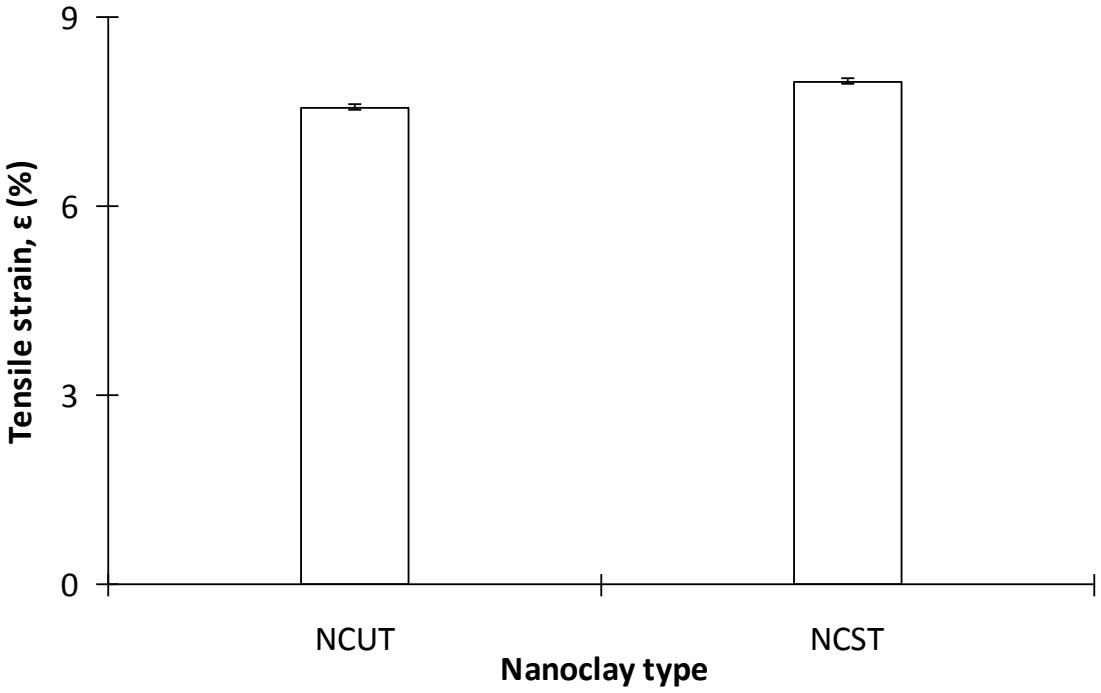

Appendix 4.26: Tensile strain of nanocomposites with untreated and treated nanoclays

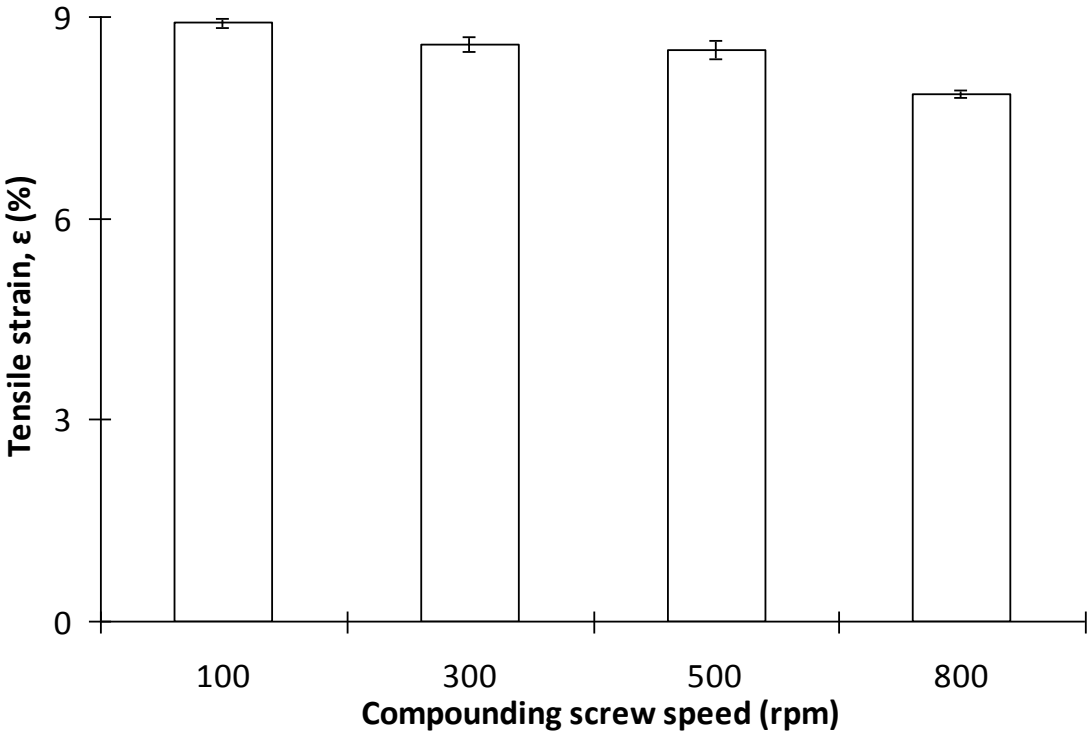

Appendix 4.27: Tensile strain of PP/NCST2 nanocomposites at different screw speeds

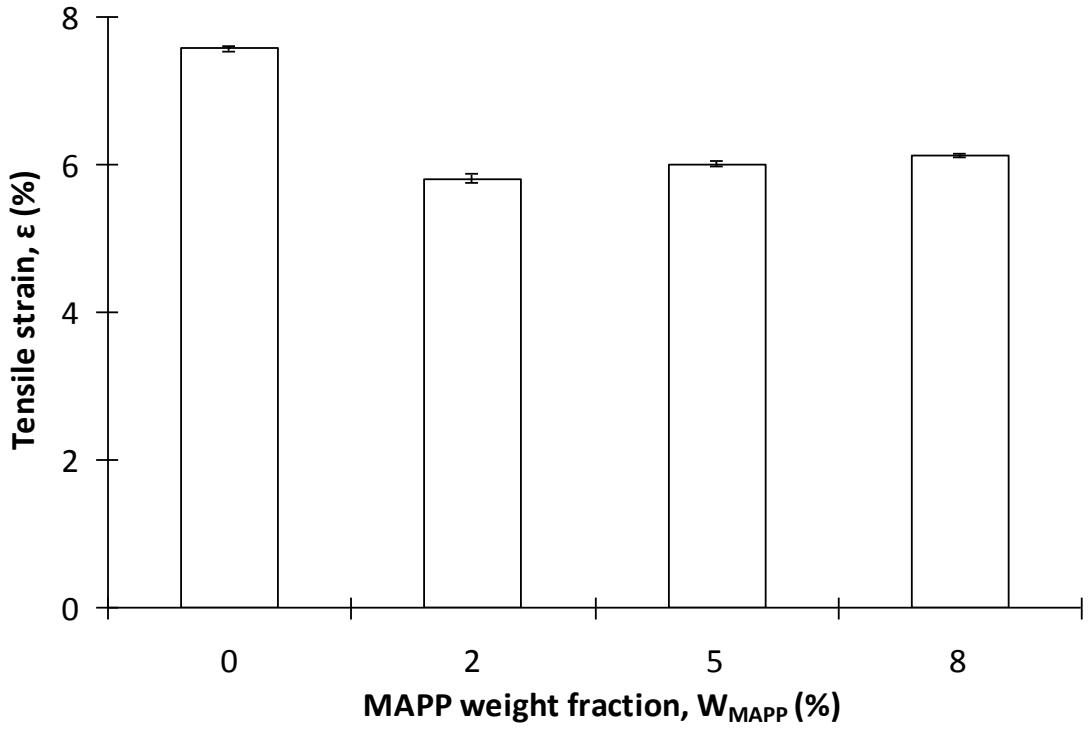

Appendix 4.28: Tensile strain of PP/NCUT6 nanocomposites with different MAPP contents

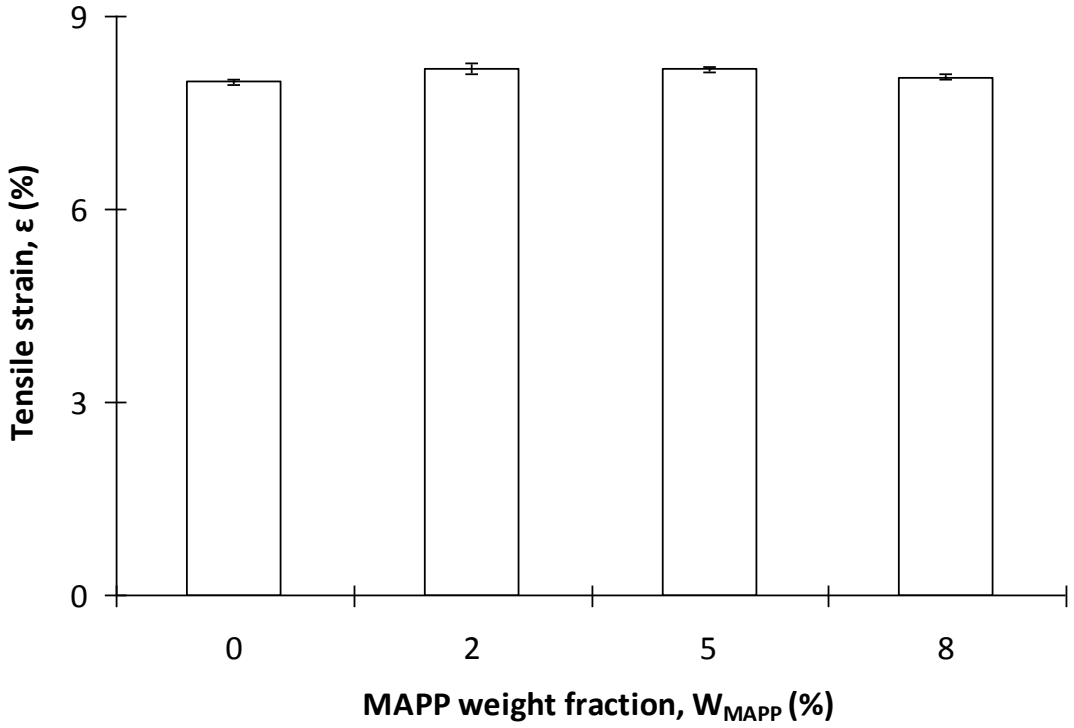

Appendix 4.29: Tensile strain of PP/NCST2 nanocomposites with different MAPP contents

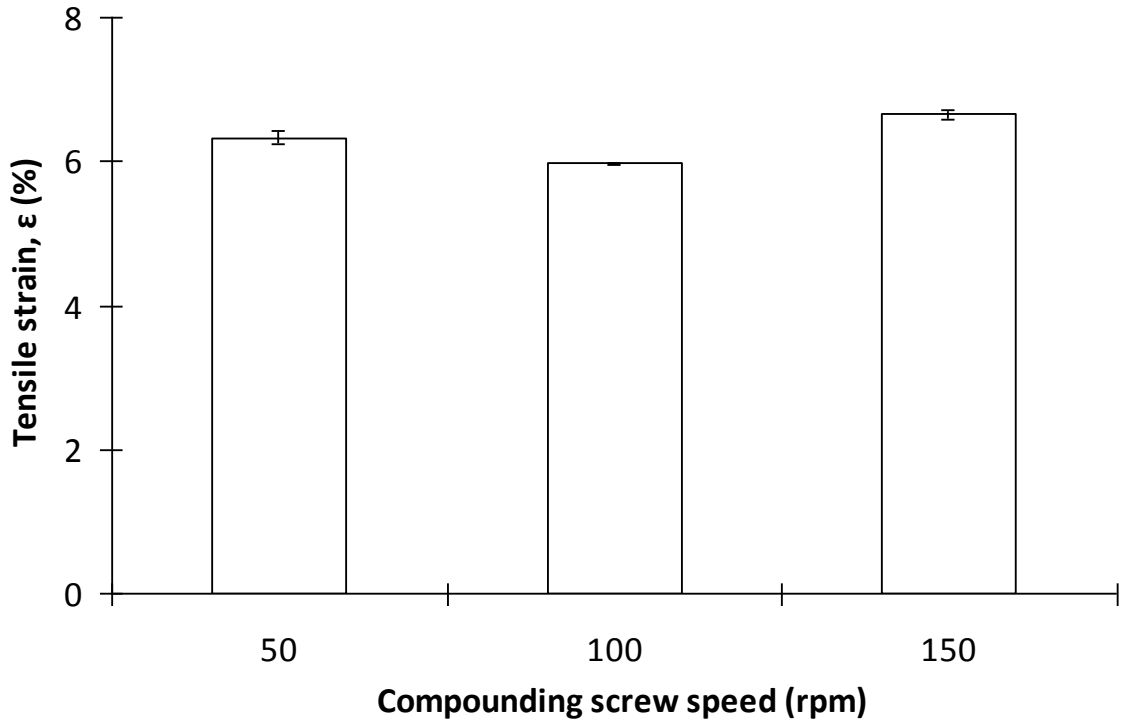

Appendix 4.30: Tensile strain of glass fibre composites at different screw speeds

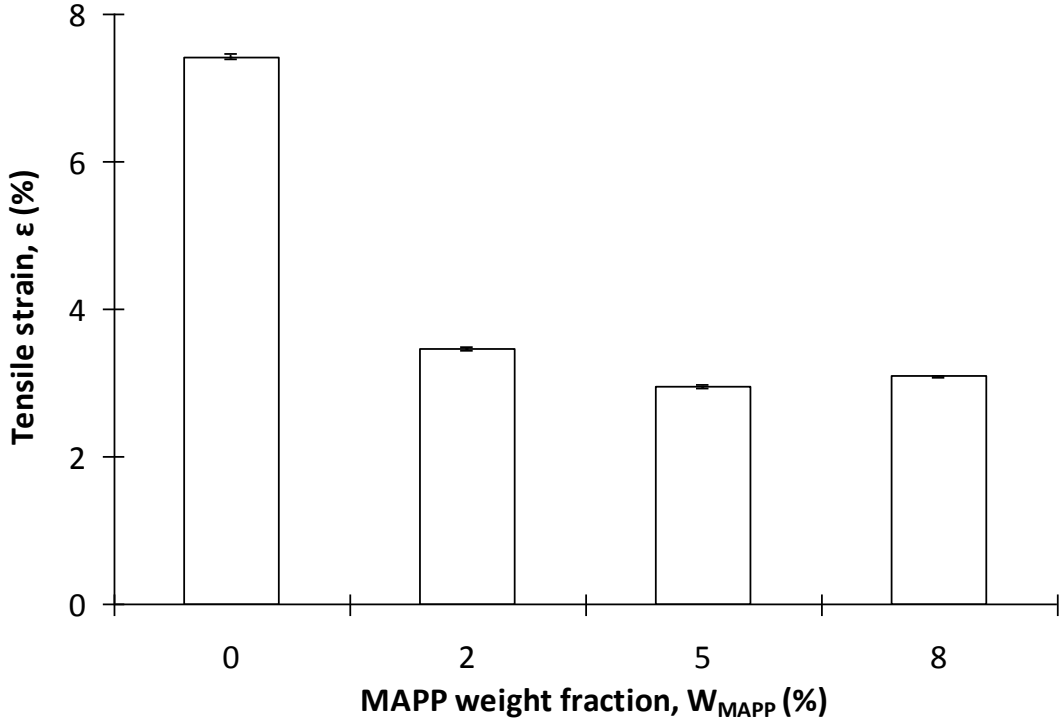

Appendix 4.31: Tensile strain of PP/GF15 composites with different MAPP contents

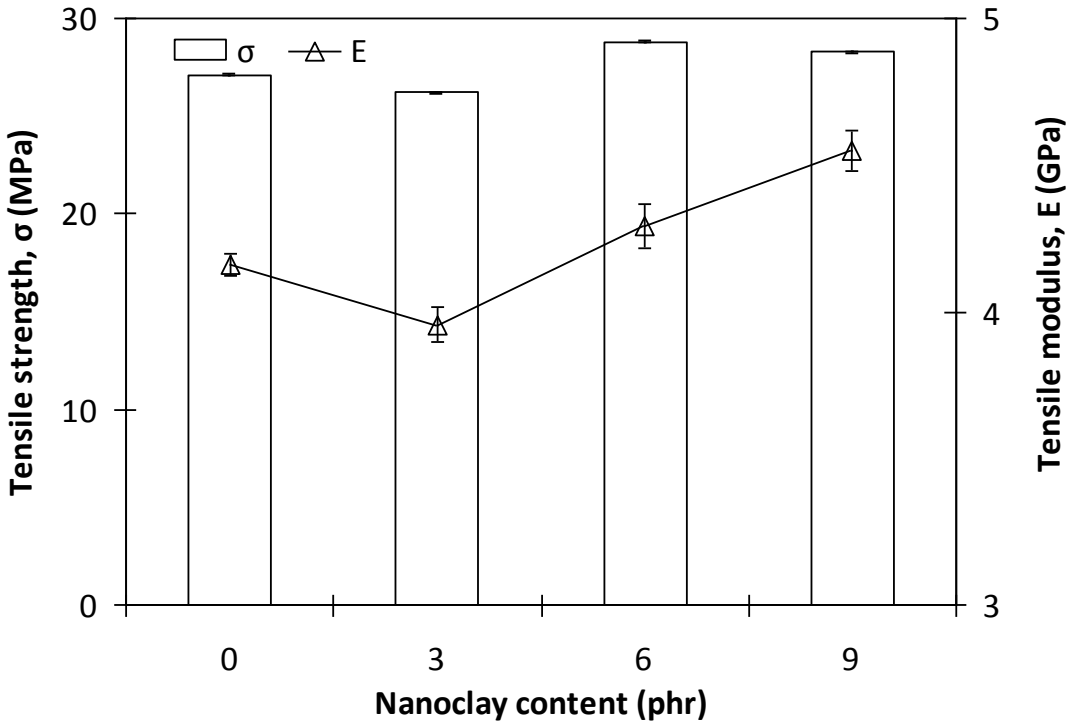

Appendix 4.32: Tensile strength and tensile modulus of PP/G30 hybrid composites with different NCUT contents

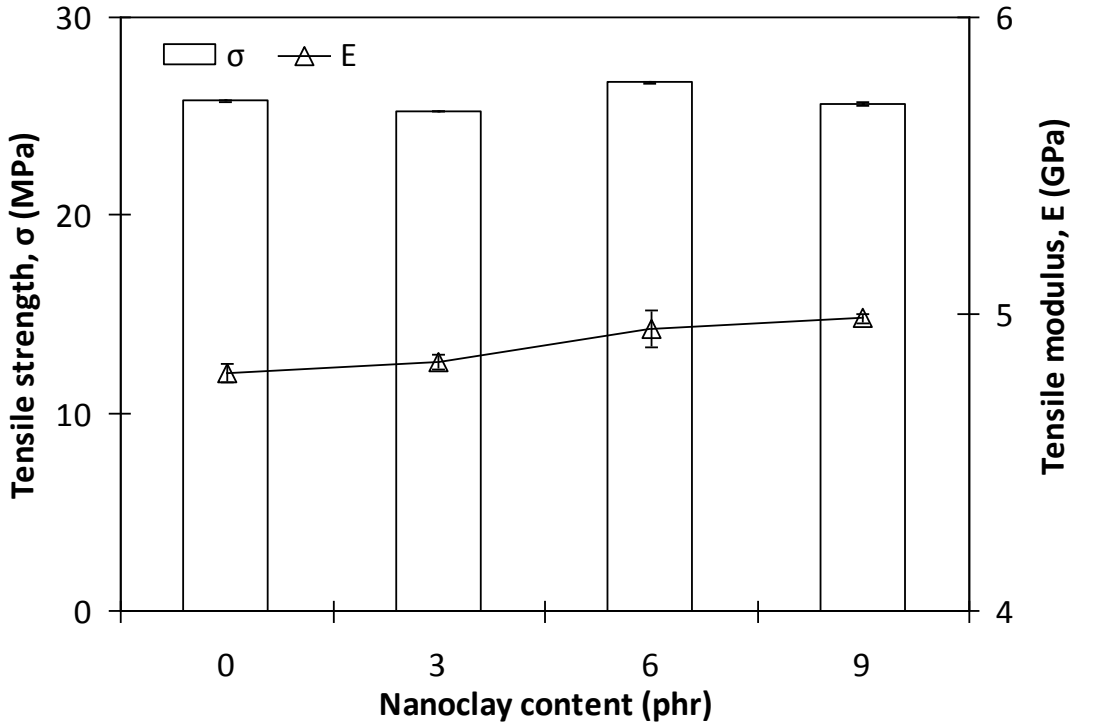

Appendix 4.33: Tensile strength and tensile modulus of PP/G45 hybrid composites with different NCUT contents

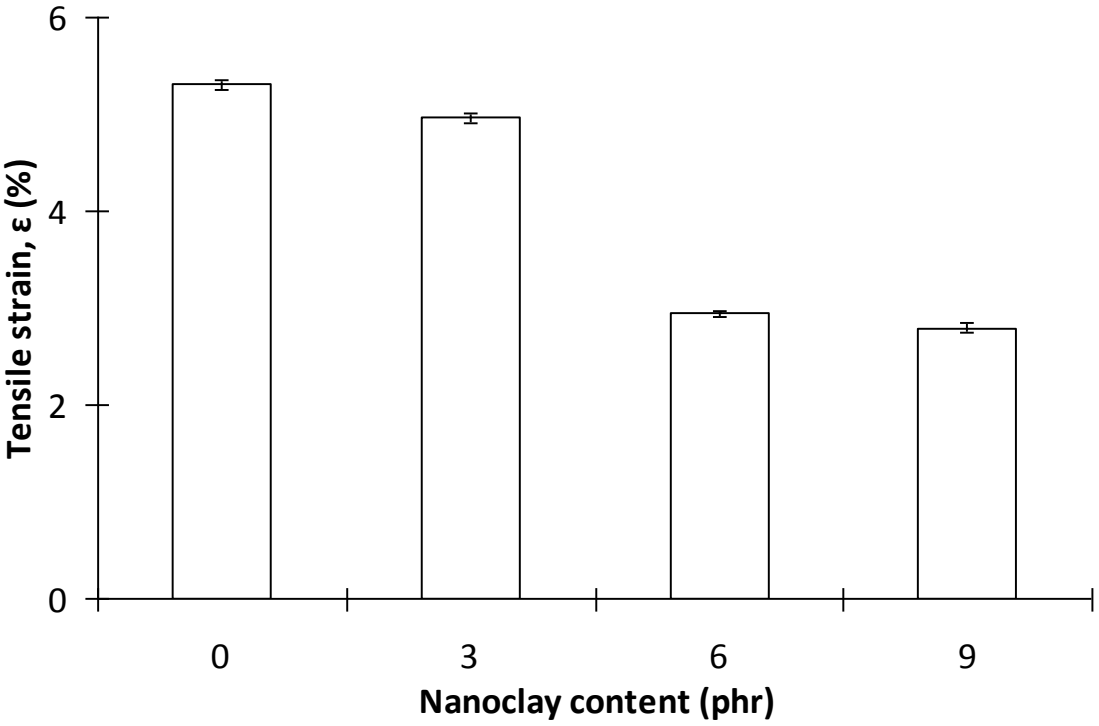

Appendix 4.34: Tensile strain of PP/G30 hybrid composites with different NCUT contents

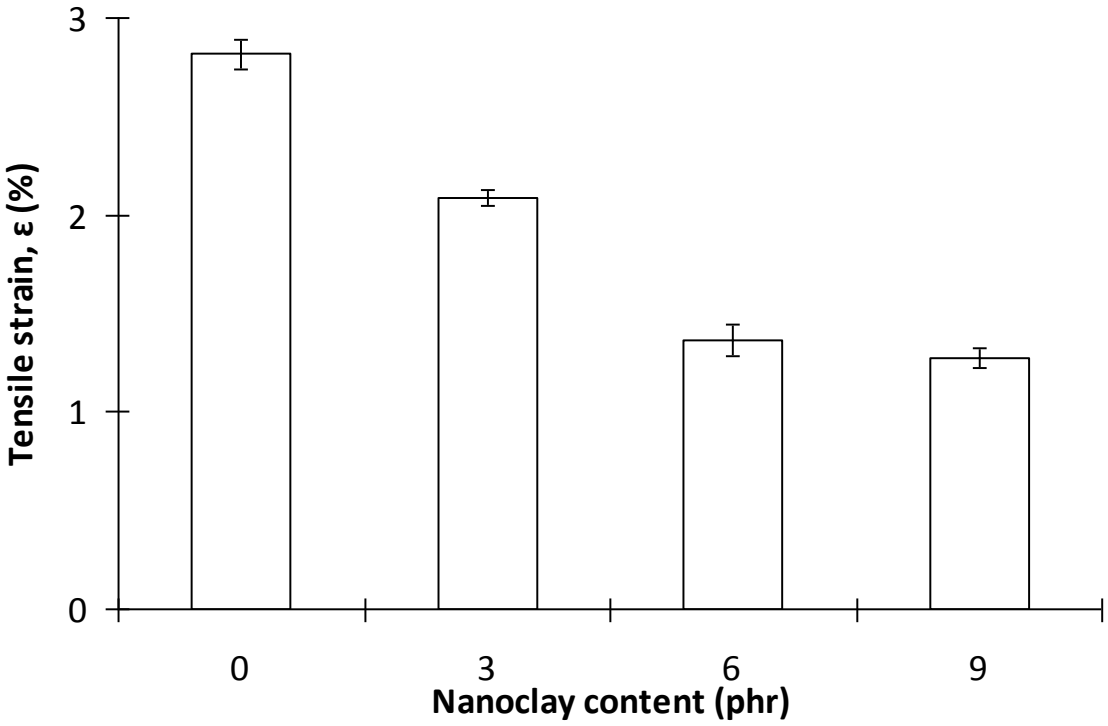

Appendix 4.35: Tensile strain of PP/G45 hybrid composites with different NCUT contents

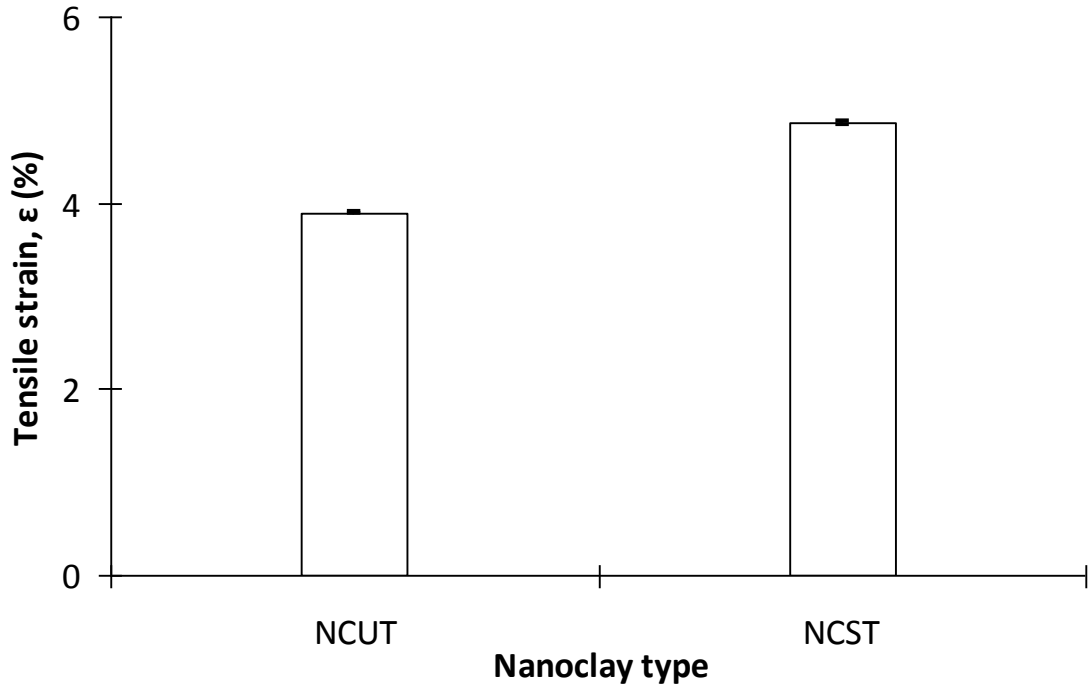

Appendix 4.36: Tensile strain of (PP:C5)/G15 hybrid composites with treated and untreated nanoclays

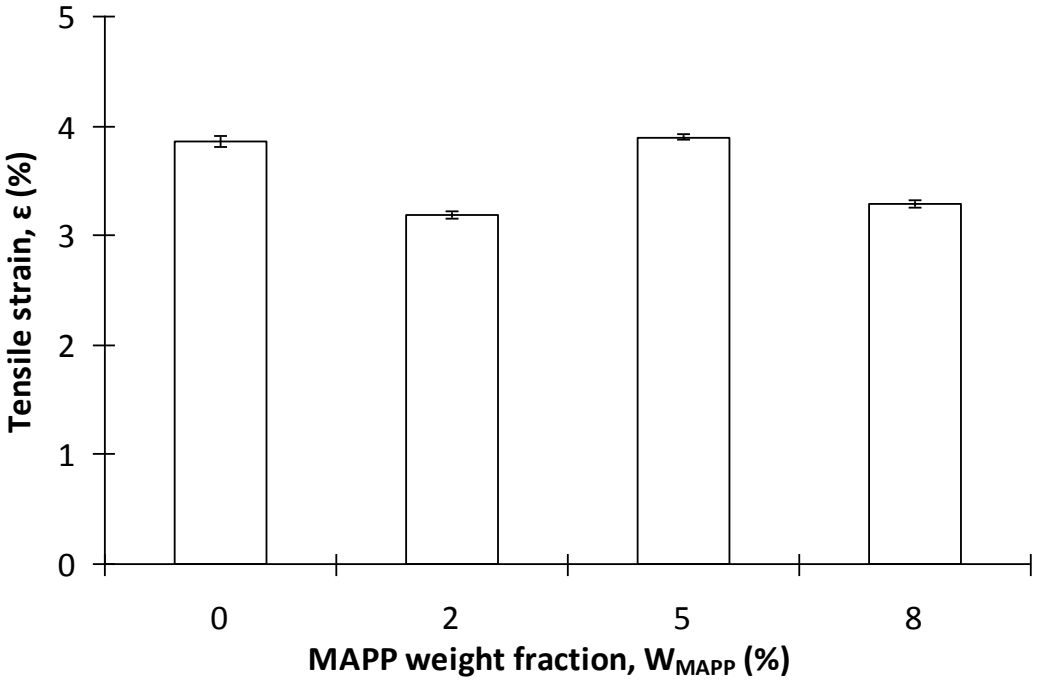

Appendix 4.37: Tensile strain of PP/G15/NCUT6 hybrid composites with different MAPP contents

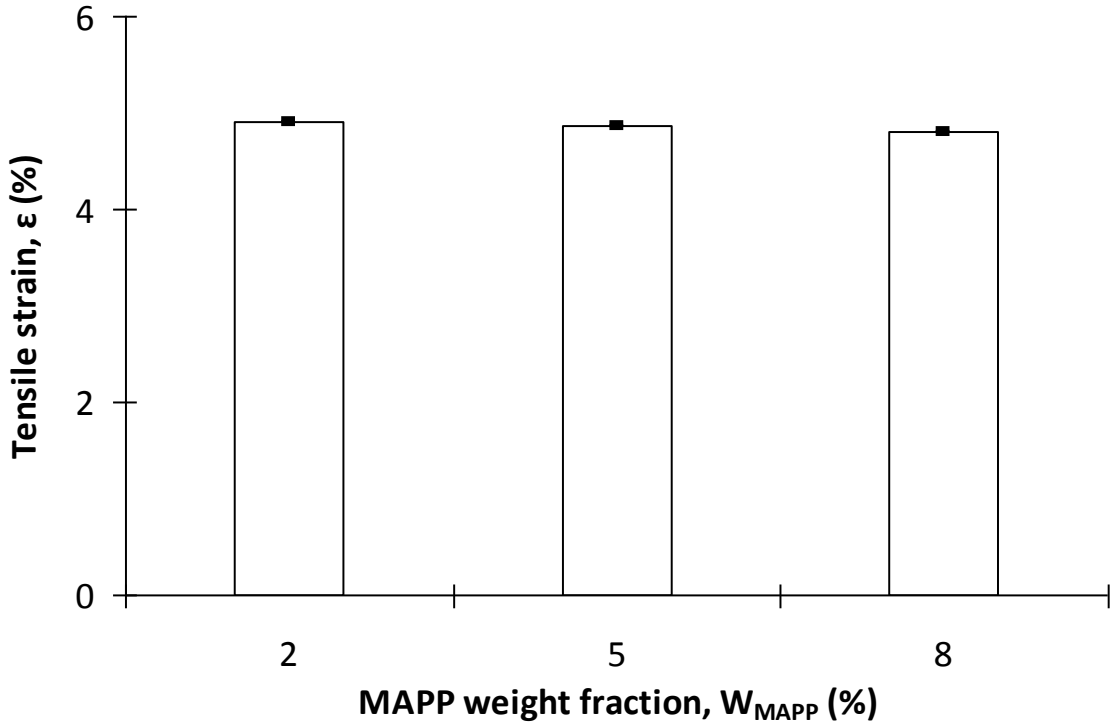

Appendix 4.38: Tensile strain of PP/G15/NCST2 hybrid composites with different MAPP contents

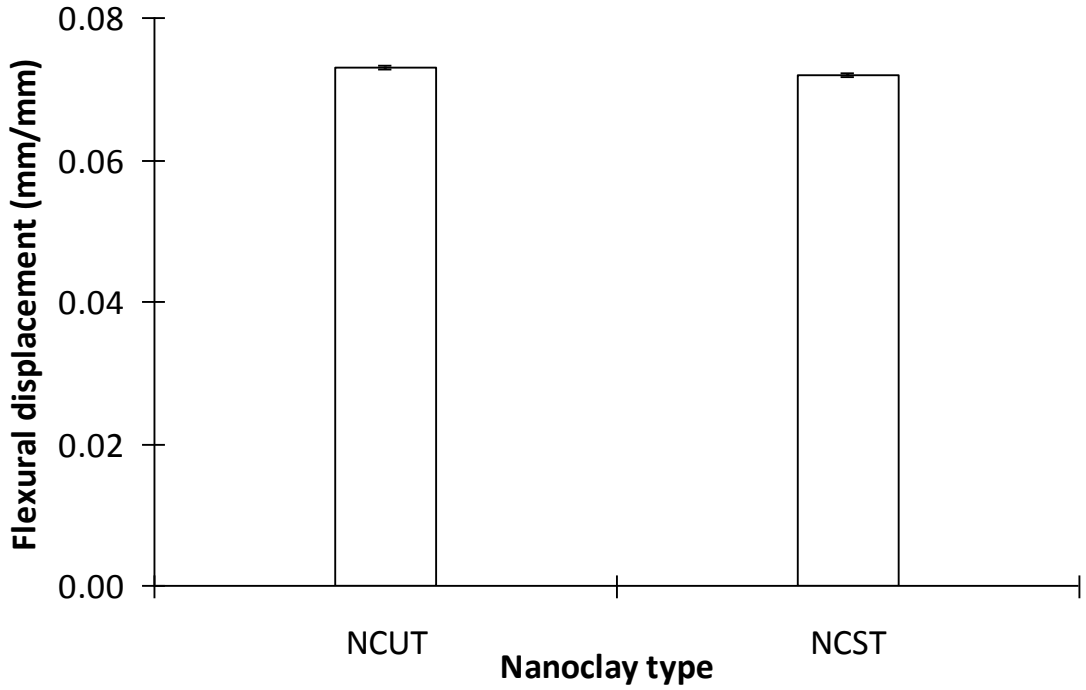

Appendix 4.39: Flexural displacement of nanocomposites with untreated and treated nanoclays

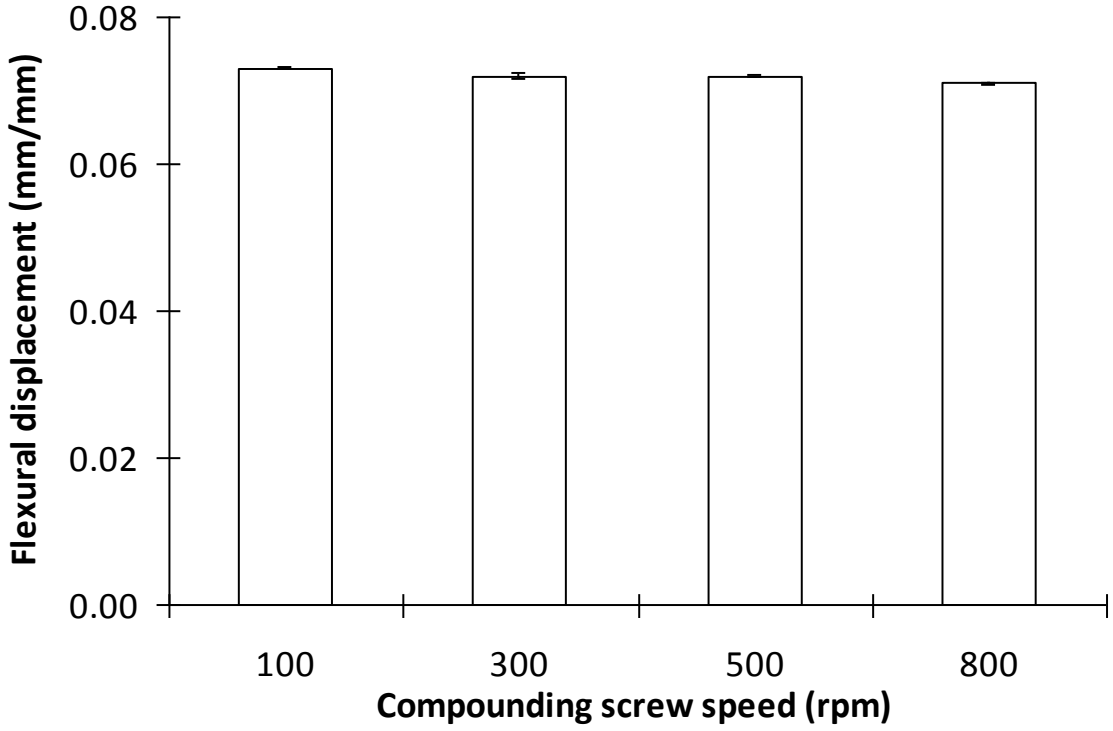

Appendix 4.40: Flexural displacement of PP/NCST2 nanocomposites at different screw speeds

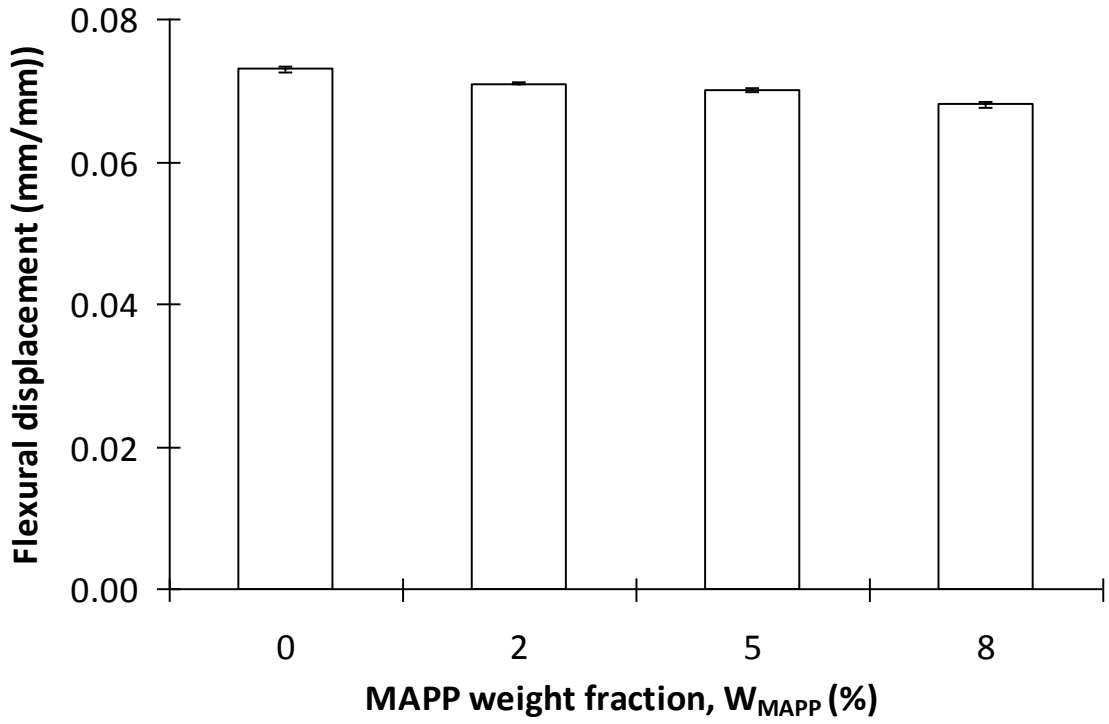

Appendix 4.41: Flexural displacement of PP/NCUT6 nanocomposites with different MAPP contents

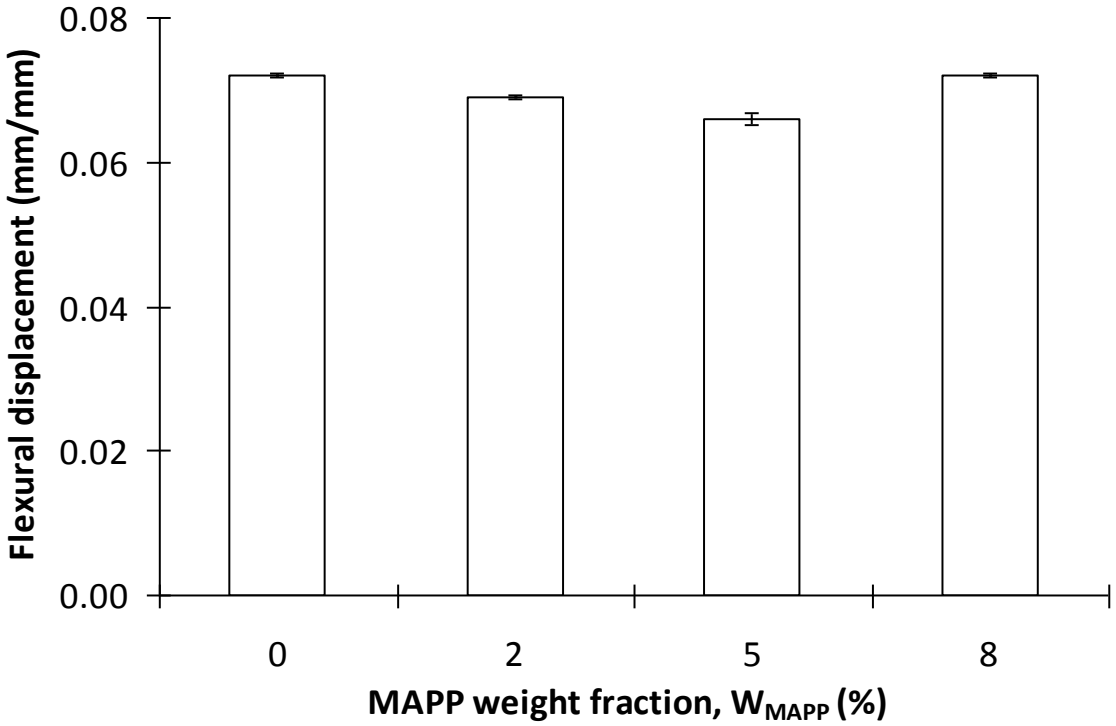

Appendix 4.42: Flexural displacement of PP/NCST2 nanocomposites with different MAPP contents

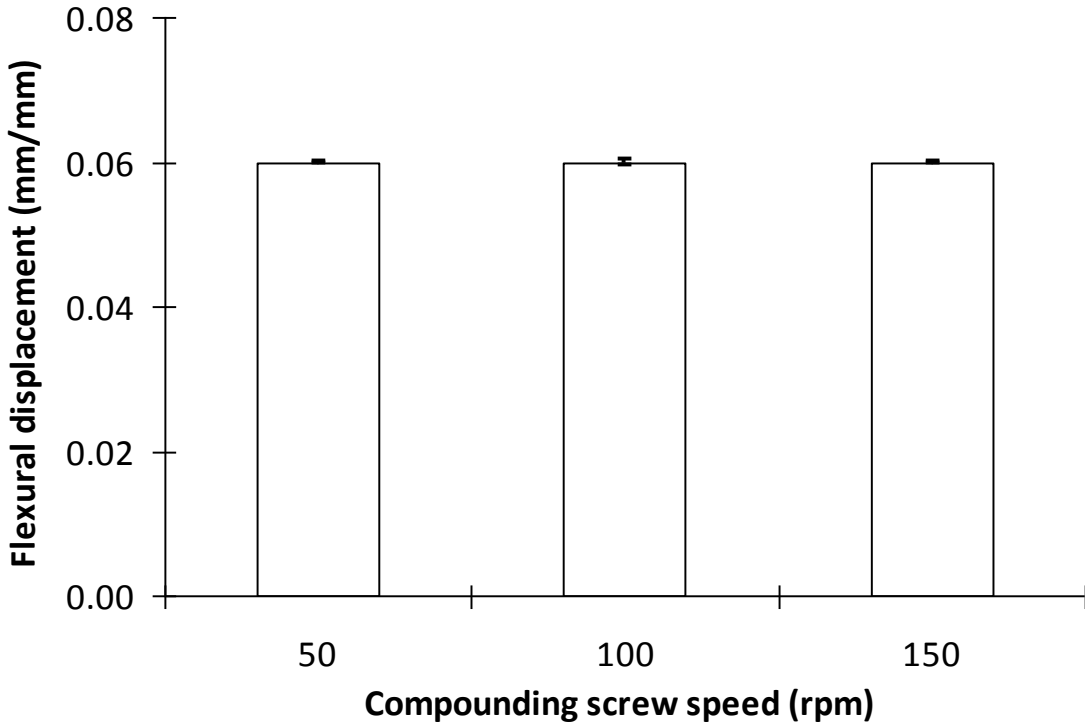

Appendix 4.43: Flexural displacement of PP/GF composites at different screw speeds

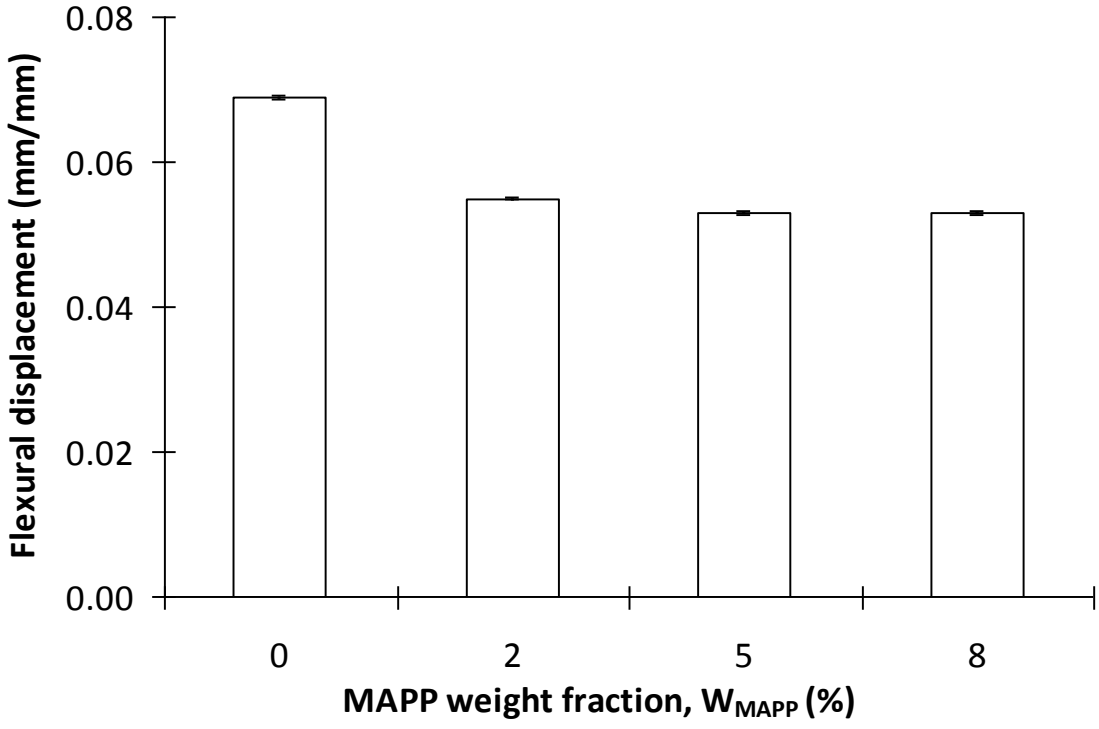

Appendix 4.44: Flexural displacement of PP/GF15 composites with different MAPP contents

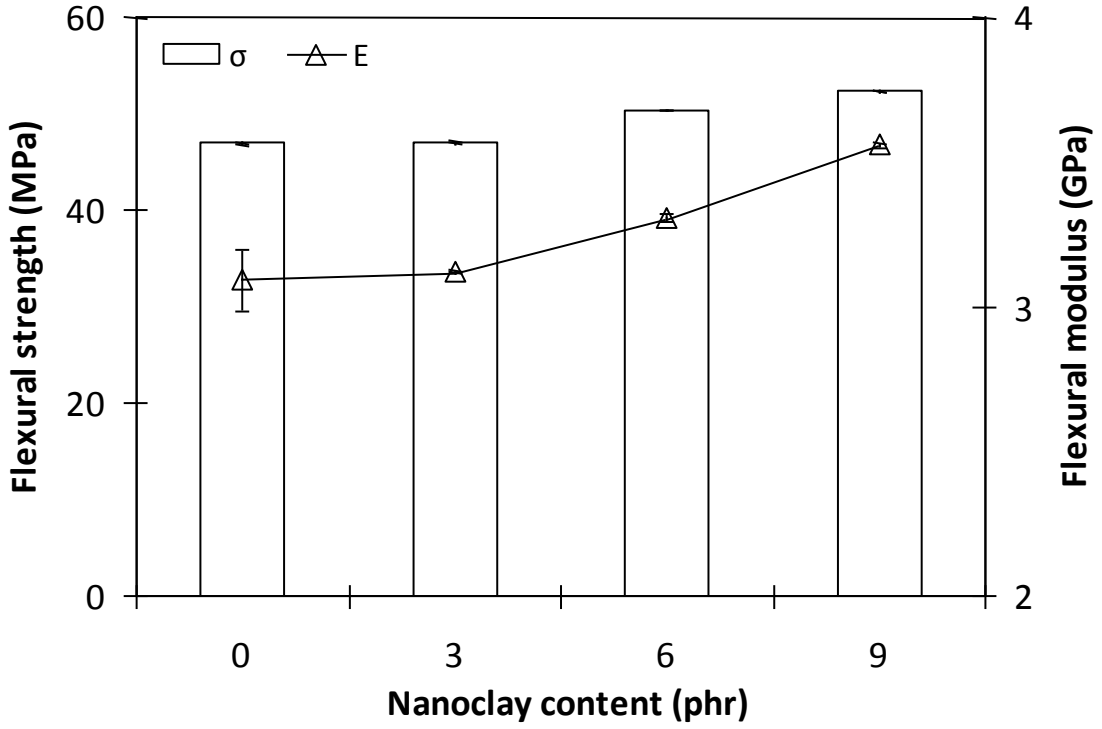

Appendix 4.45: Flexural strength and flexural modulus of PP/G30 hybrid composites with different NCUT contents

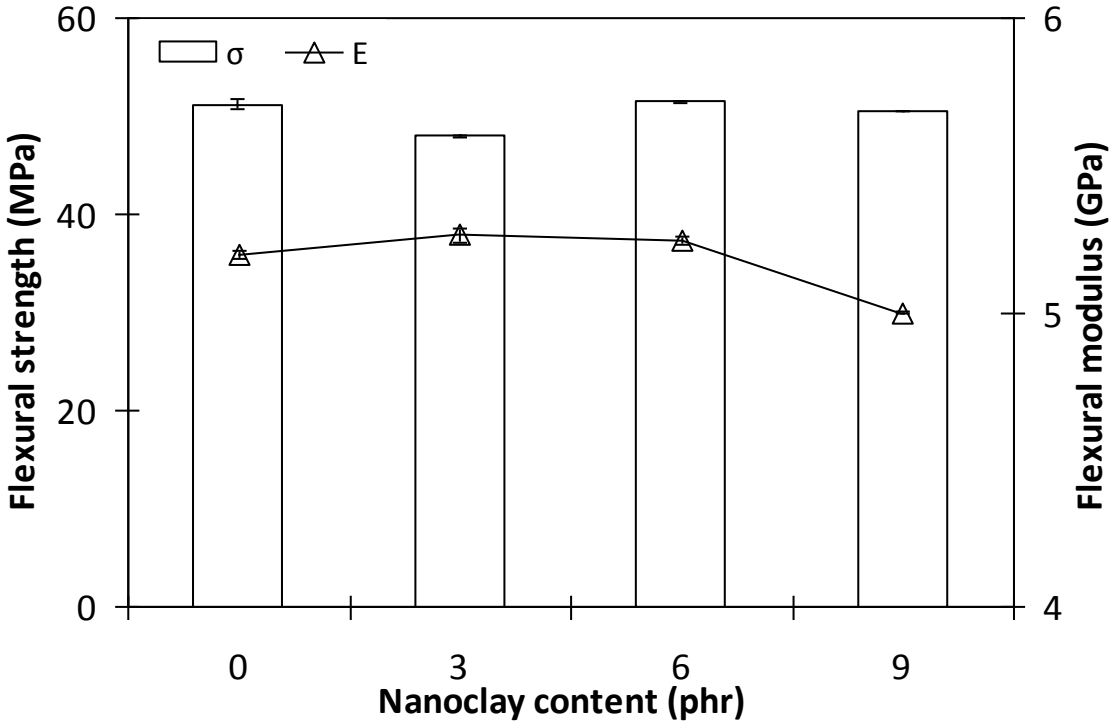

Appendix 4.46: Flexural strength and flexural modulus of PP/G45 hybrid composites with different NCUT contents

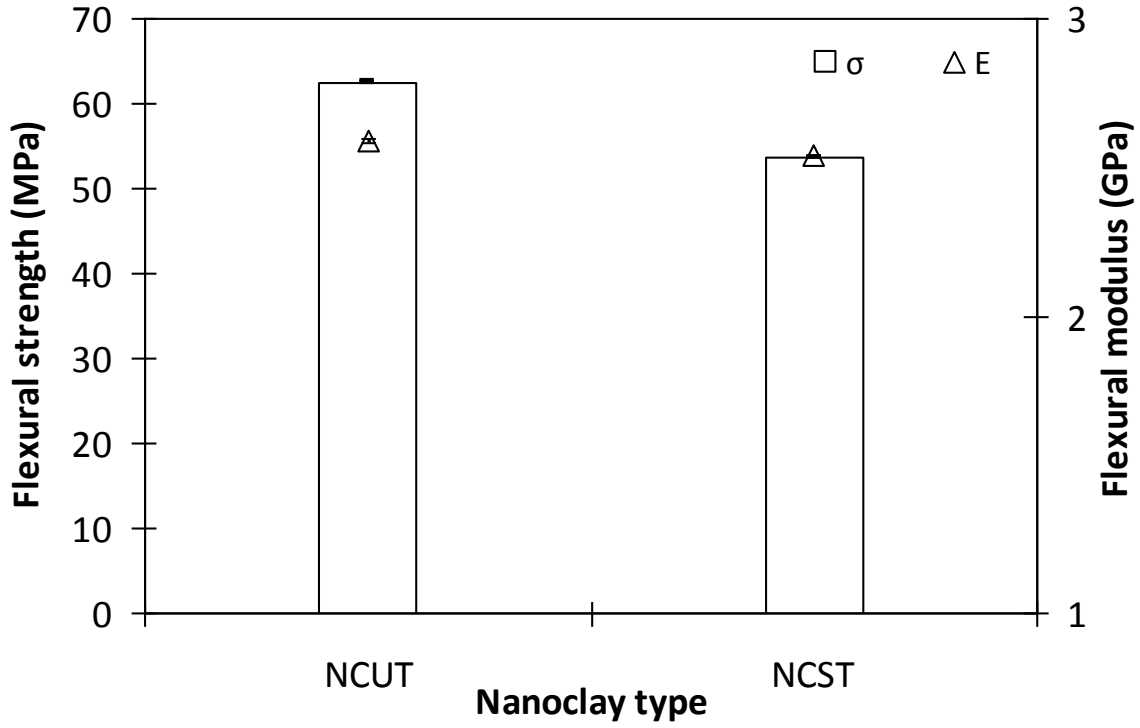

Appendix 4.47: Flexural strength and flexural modulus of (PP:C5)/G15 hybrid composites with treated and untreated nanoclays

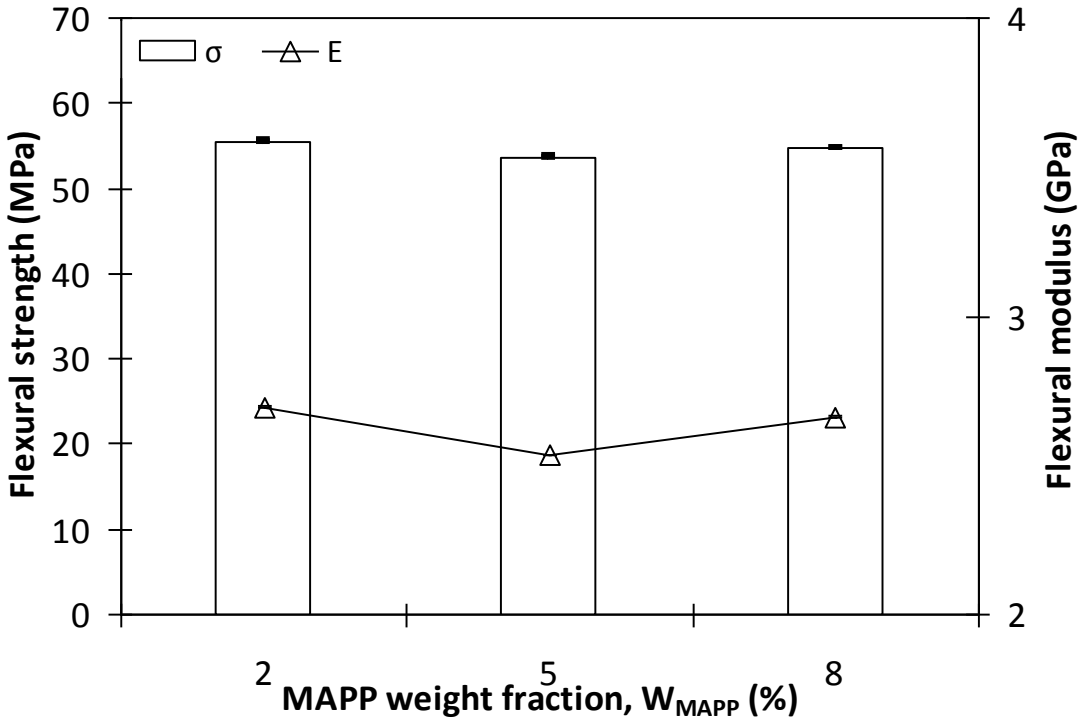

Appendix 4.48: Flexural strength and flexural modulus of PP/G15/NCST2 hybrid composites with different MAPP contents

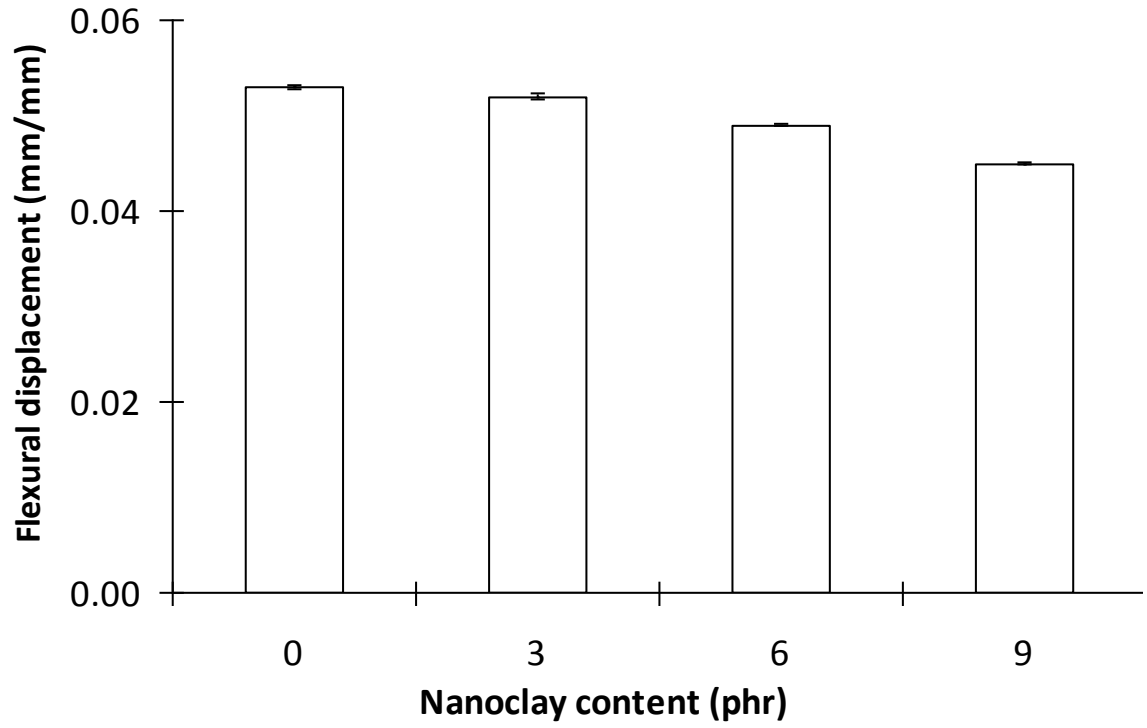

Appendix 4.49: Flexural displacement of PP/G30 hybrid composites with different NCUT contents

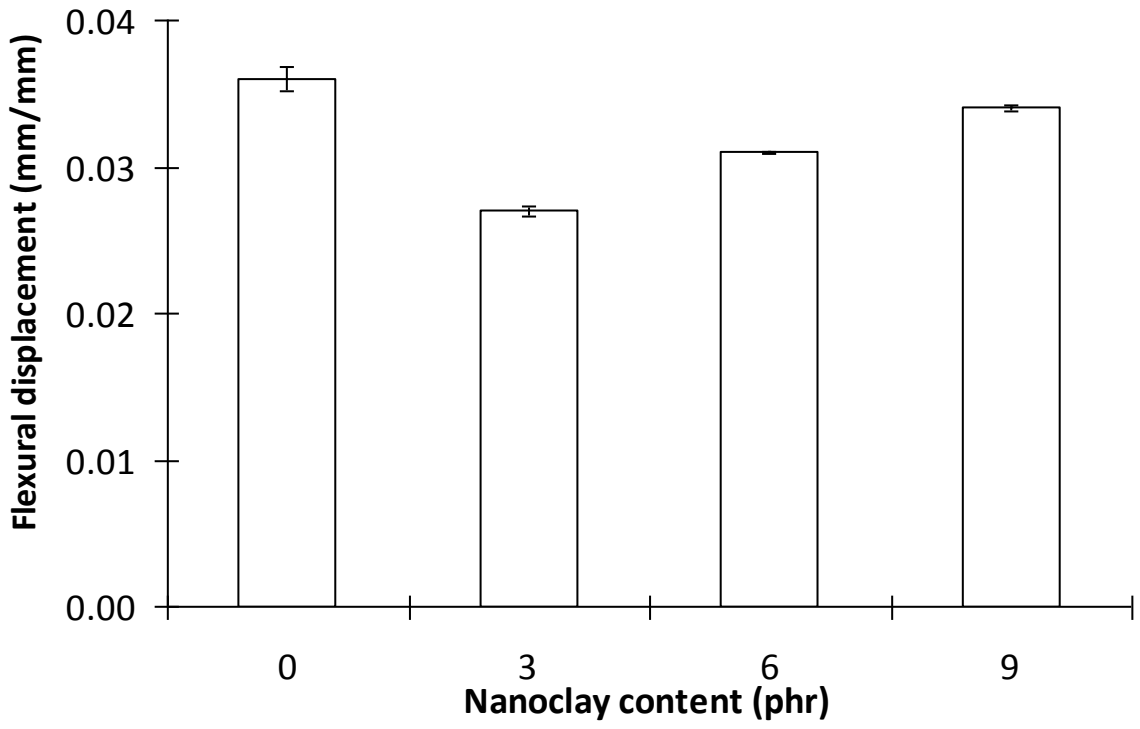

Appendix 4.50: Flexural displacement of PP/G45 hybrid composites with different NCUT contents

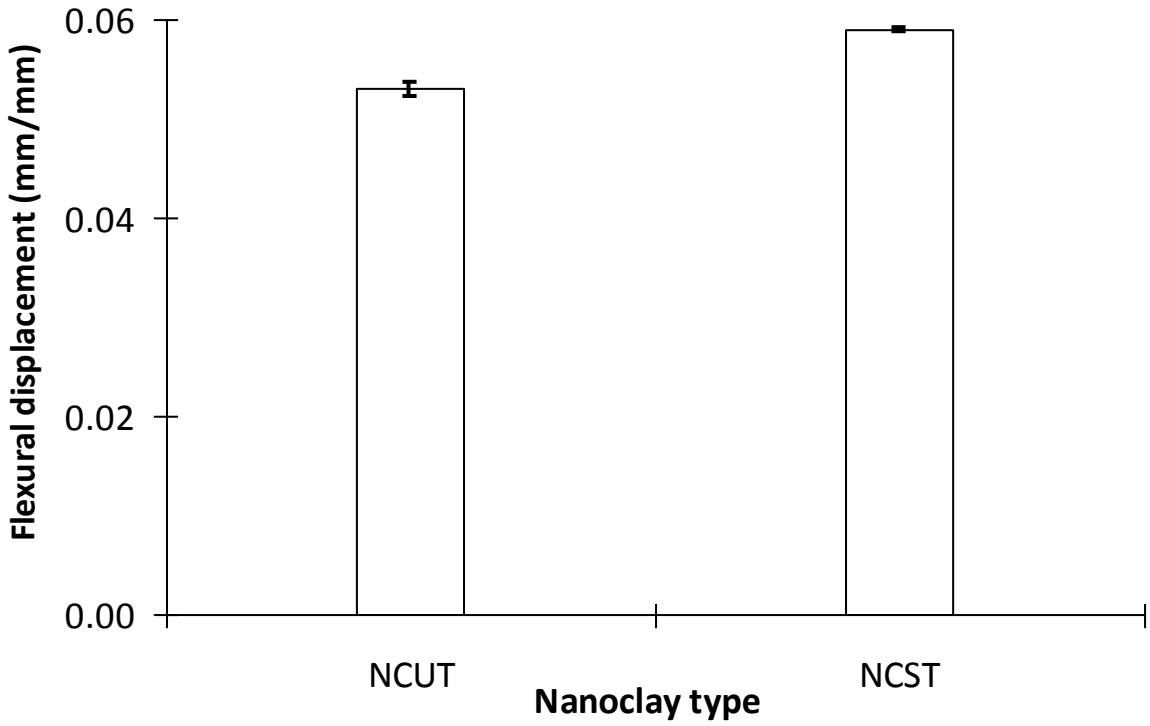

Appendix 4.51: Flexural displacement of (PP:C5)/G15 hybrid composites with treated and untreated nanoclays

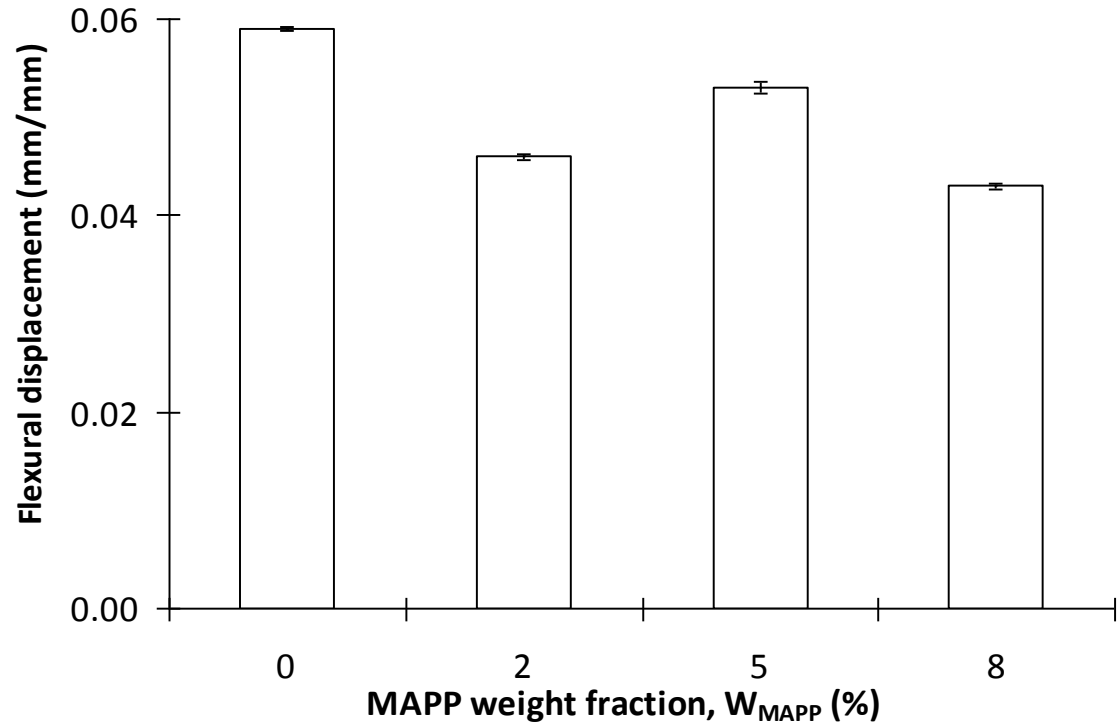

Appendix 4.52: Flexural displacement of PP/G15/NCUT6 hybrid composites with different MAPP contents

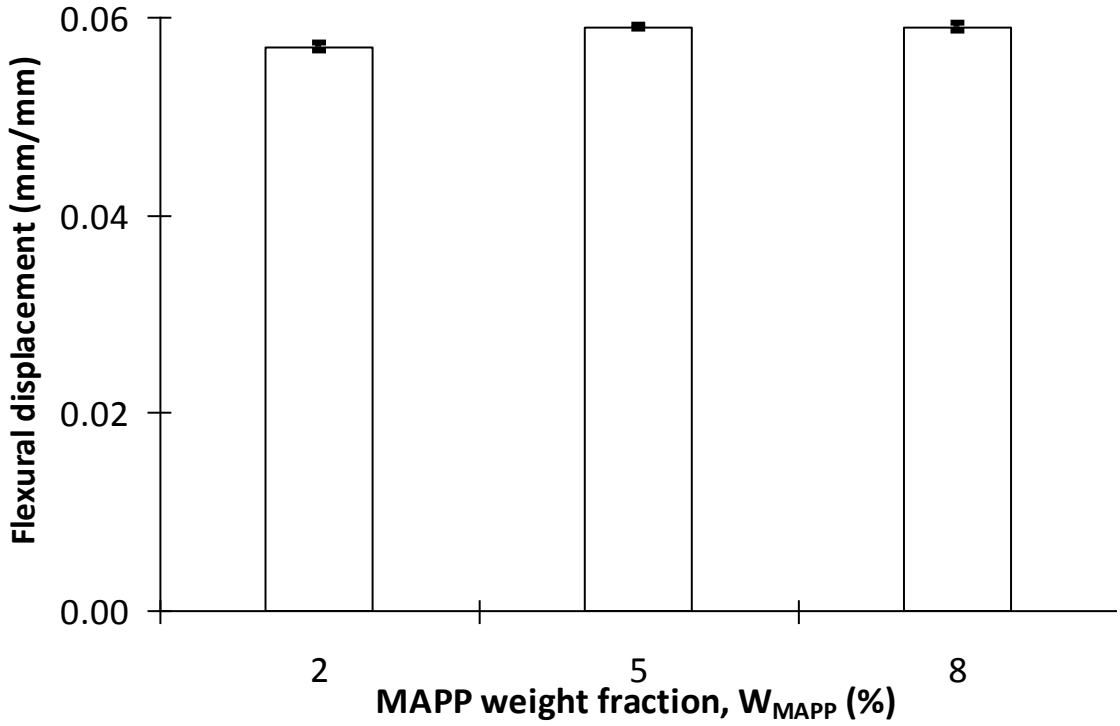

Appendix 4.53: Flexural displacement of PP/G15/NCST2 hybrid composites with different MAPP contents

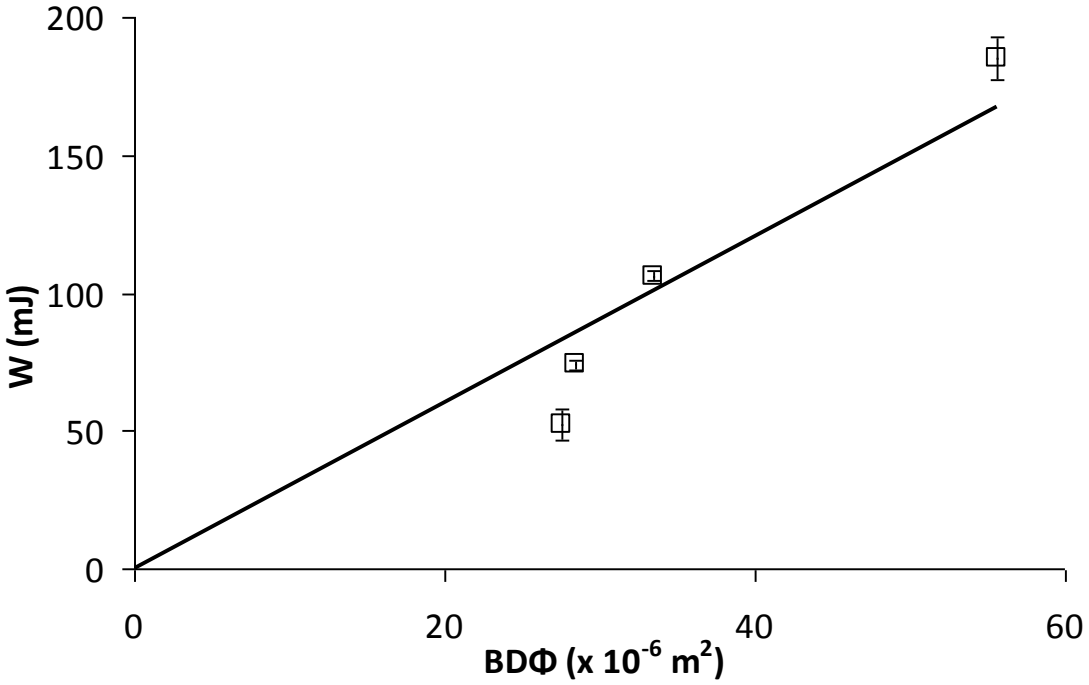

Appendix 4.54: Plot of *W* as a function of *BDΦ* of the PP/NCUT3 nanocomposites

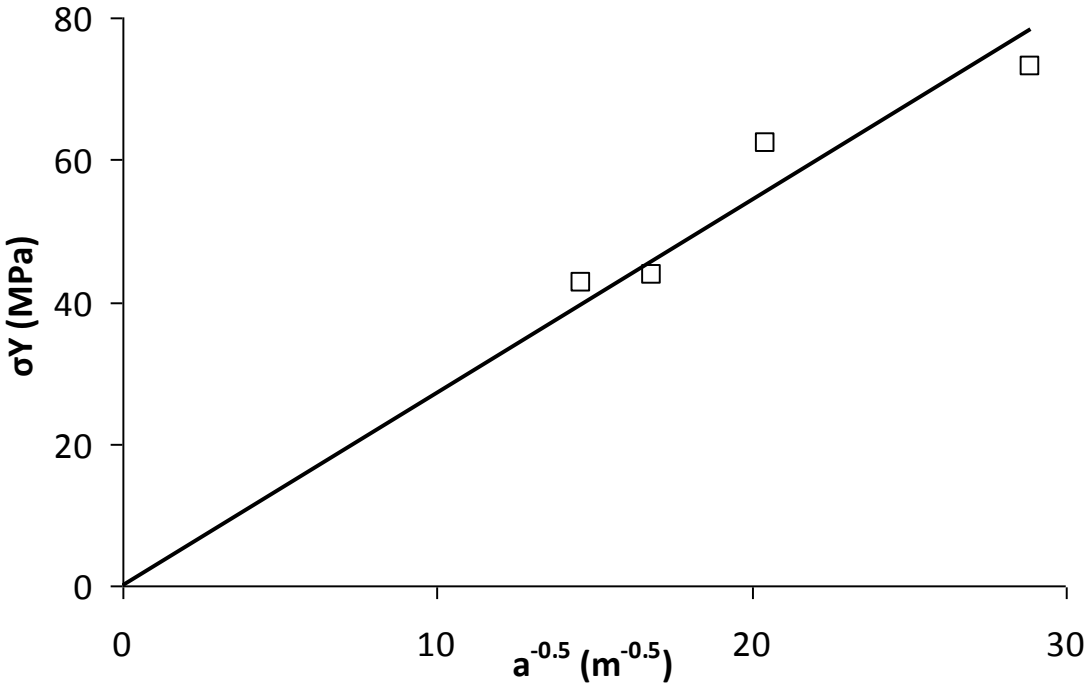

Appendix 4.55: Plot of σY as a function of $a^{-0.5}$ of the PP/NCUT3 nanocomposites

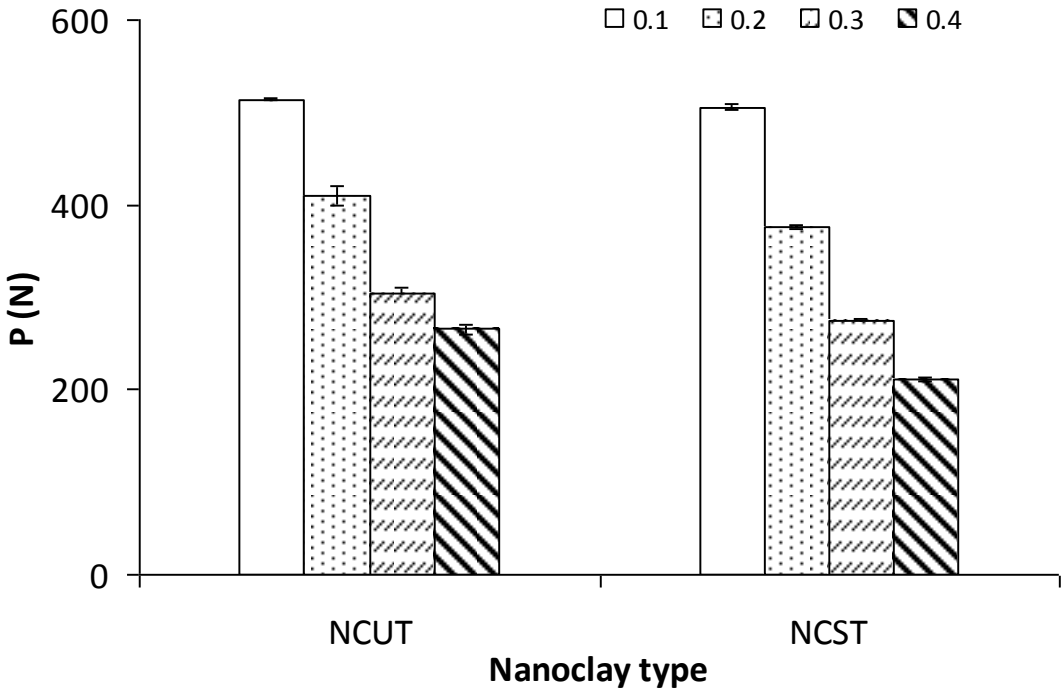

Appendix 4.56: Peak load (*P*) of nanocomposites with untreated and treated nanoclays

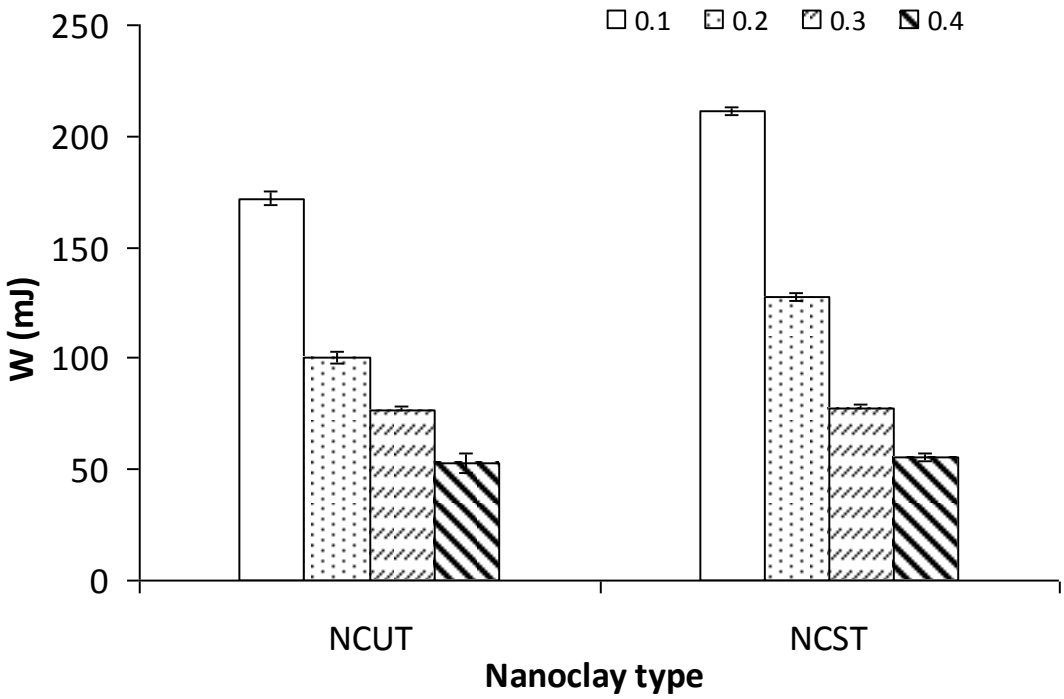

Appendix 4.57: Fracture energy (*W*) of nanocomposites with untreated and treated nanoclays

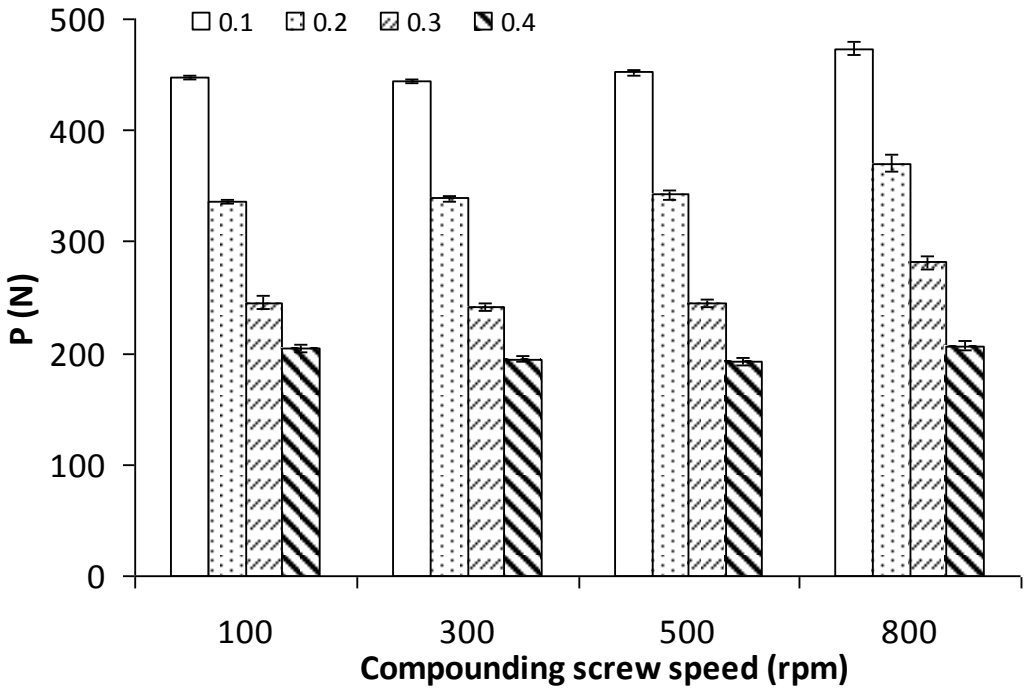

Appendix 4.58: Peak load (*P*) of PP/NCST2 nanocomposites at different screw speeds

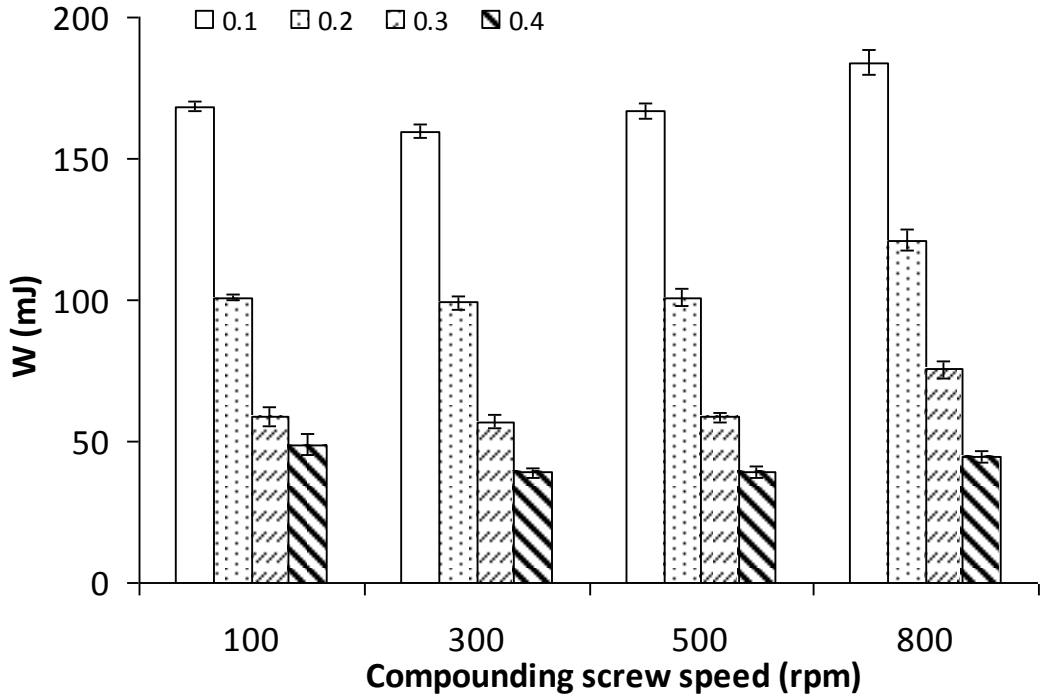

Appendix 4.59: Fracture energy (*W*) of PP/NCST2 nanocomposites at different screw speeds

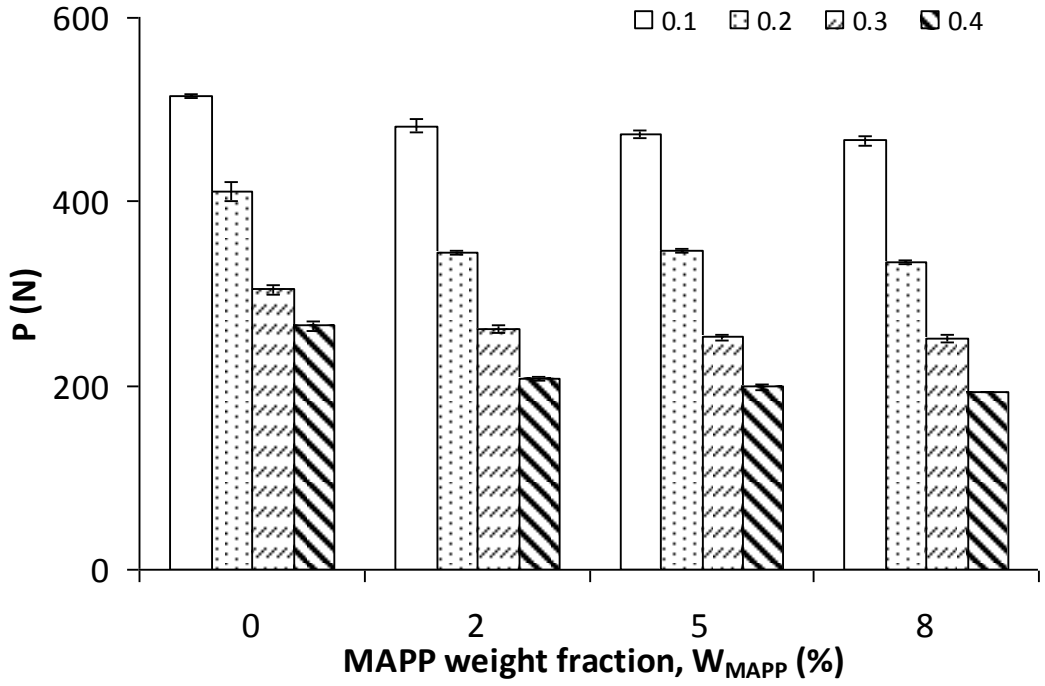

Appendix 4.60: Peak load (*P*) of PP/NCUT6 nanocomposites with different MAPP contents

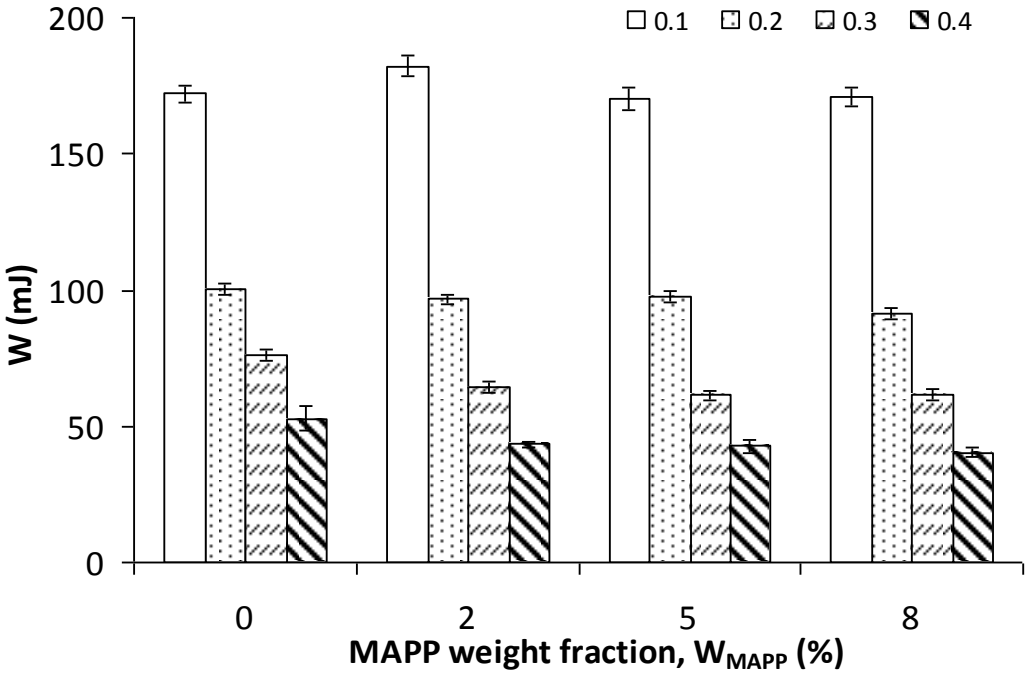

Appendix 4.61: Fracture energy (*W*) of PP/NCUT6 nanocomposites with different MAPP contents

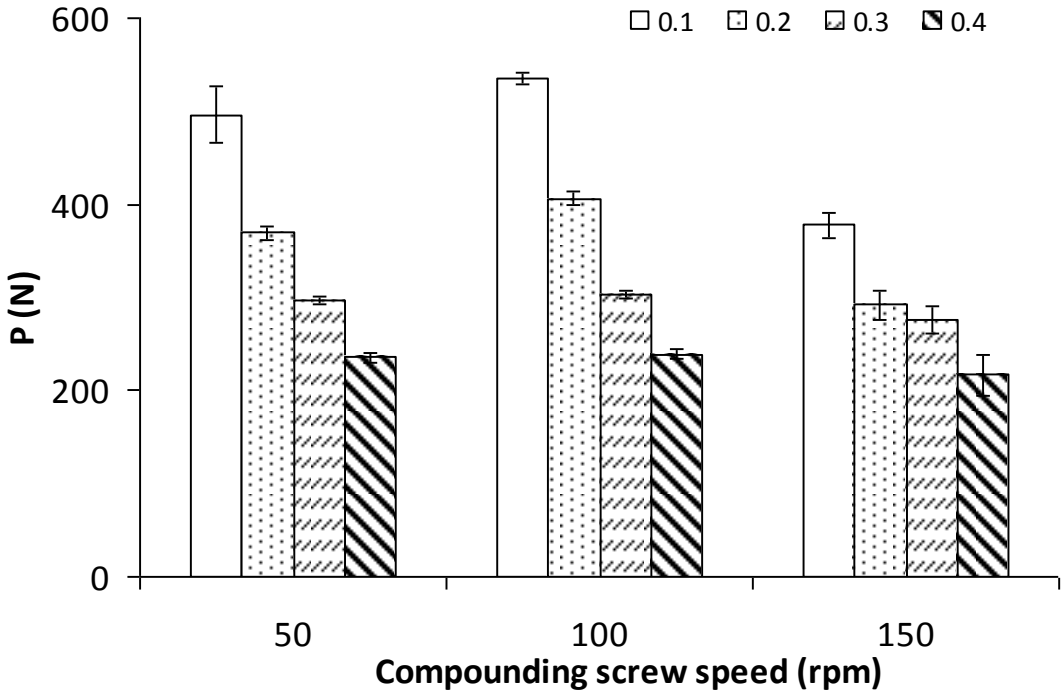

Appendix 4.62: Peak load (*P*) of glass fibre composites at different screw speeds

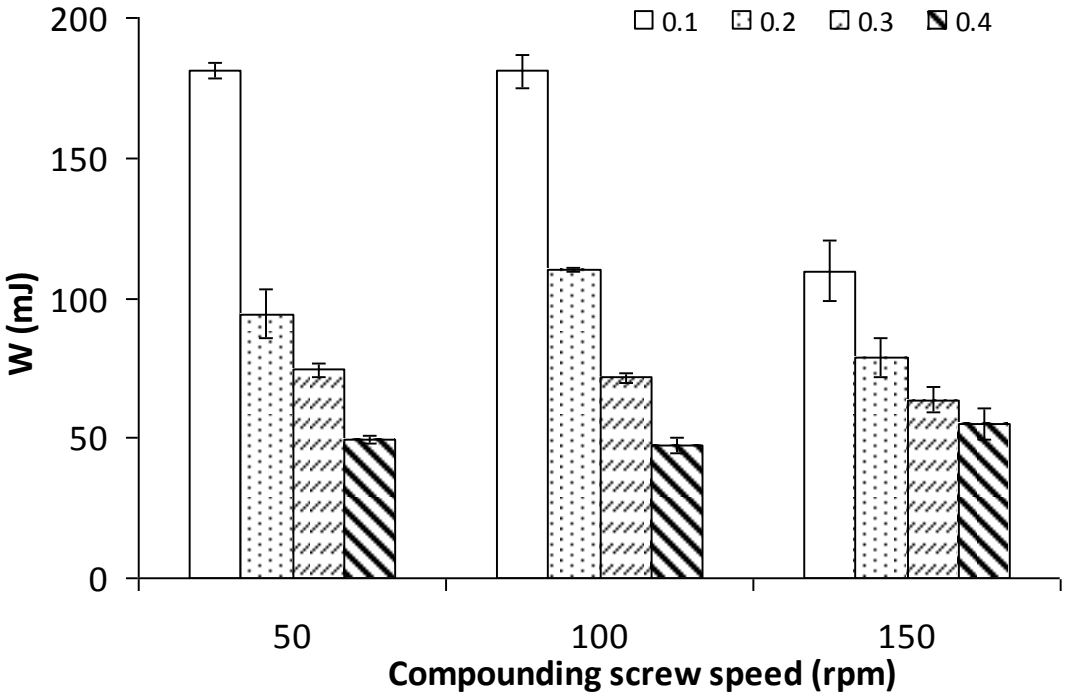

Appendix 4.63: Fracture energy (*W*) of glass fibre composites at different screw speeds

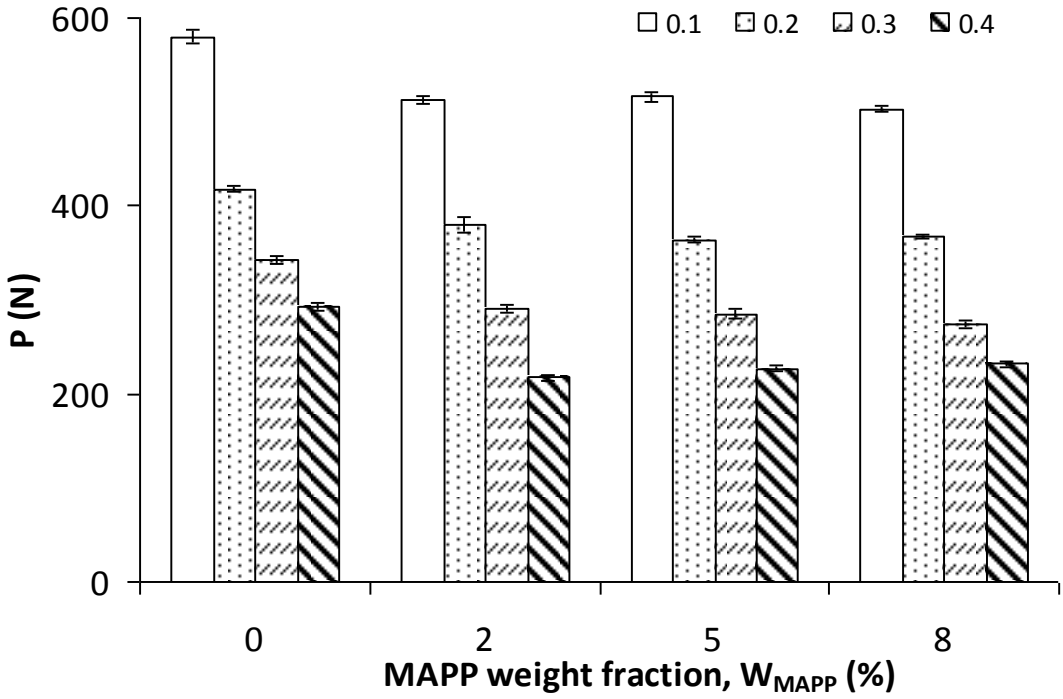

Appendix 4.64: Peak load (*P*) of PP/GF15 composites with different MAPP contents

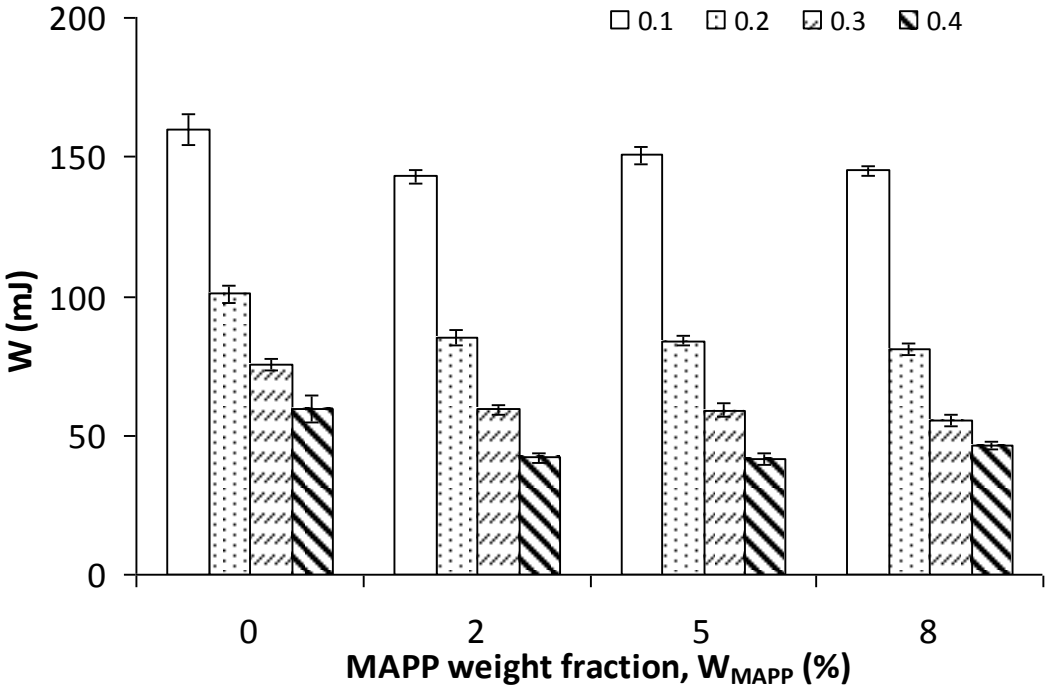

Appendix 4.65: Fracture energy (*W*) of PP/GF15 composites with different MAPP contents

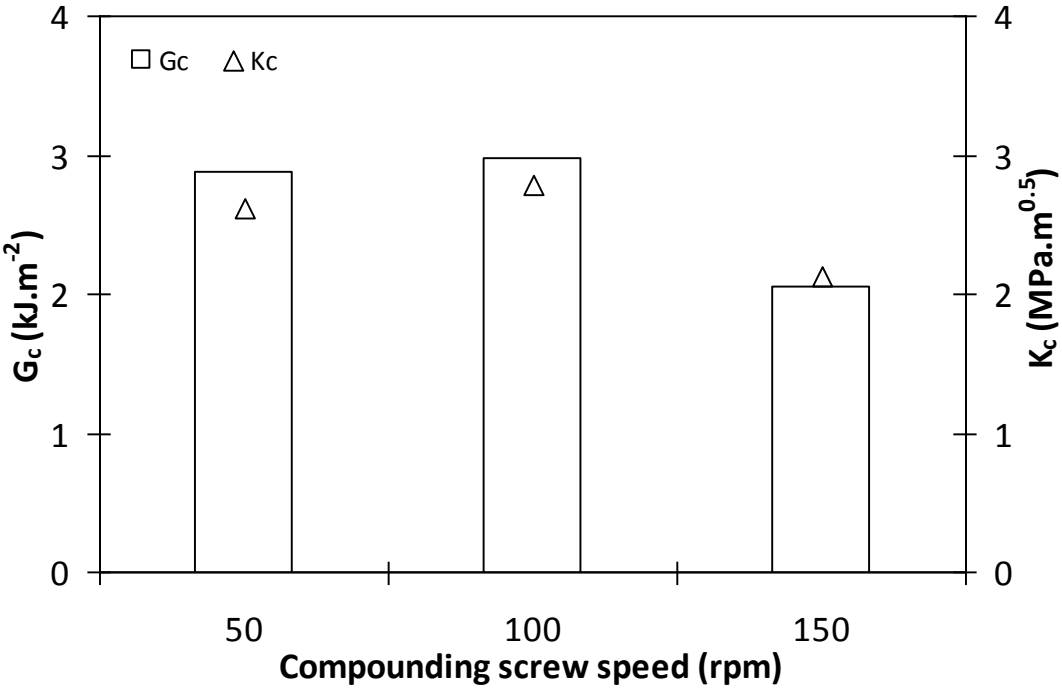

Appendix 4.66: G_c and K_c of PP/GF composites at different screw speeds

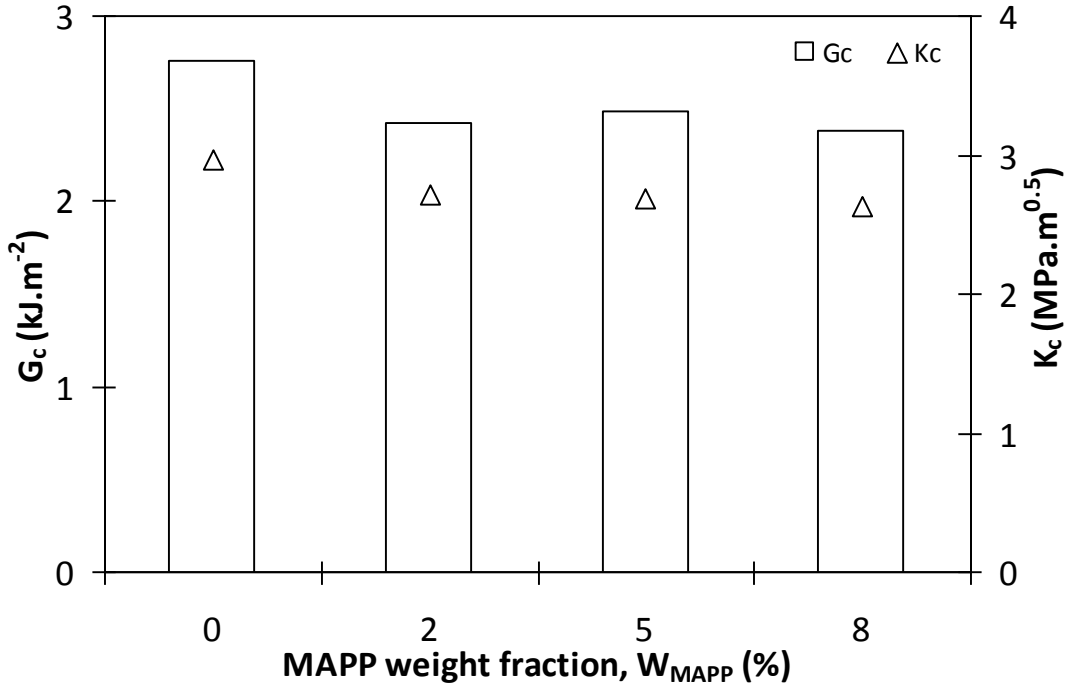

Appendix 4.67: G_c and K_c of PP/GF15 composites with different MAPP contents

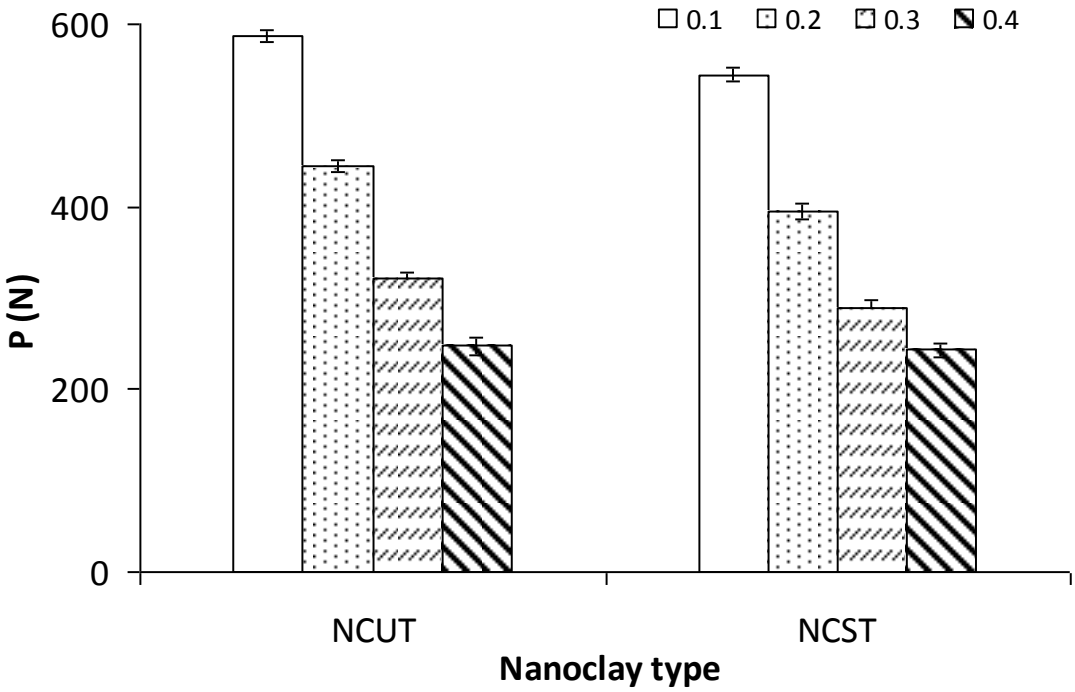

Appendix 4.68: Peak load (*P*) of (PP:C5)/G15 hybrid composites with treated and untreated nanoclays

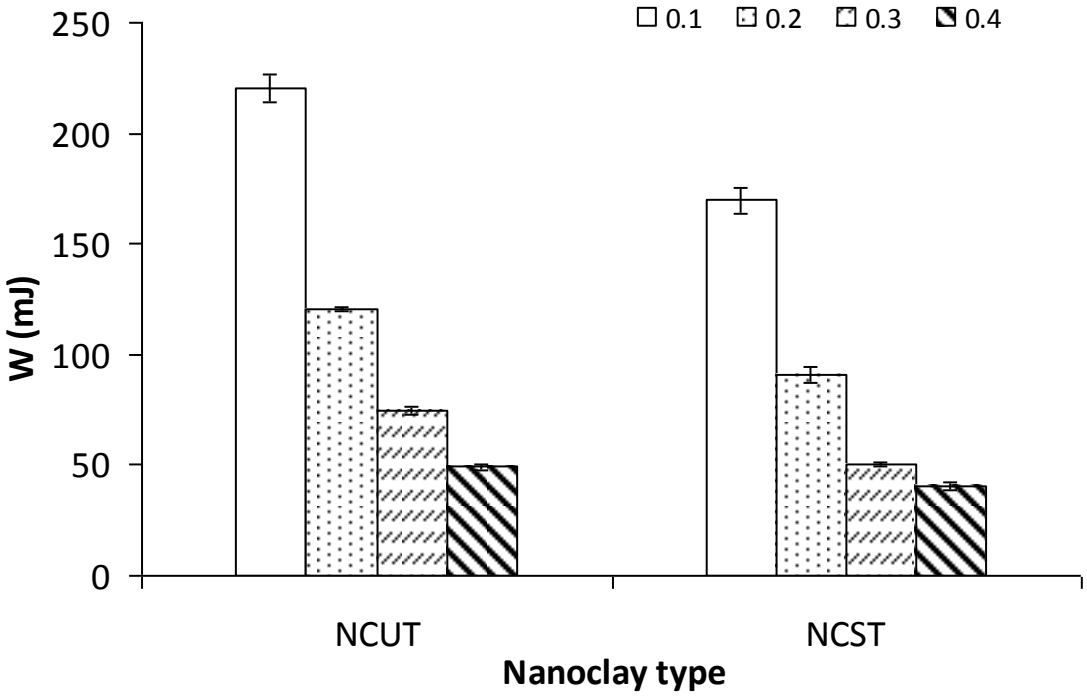

Appendix 4.69: Fracture energy (*W*) of (PP:C5)/G15 hybrid composites with treated and untreated nanoclays

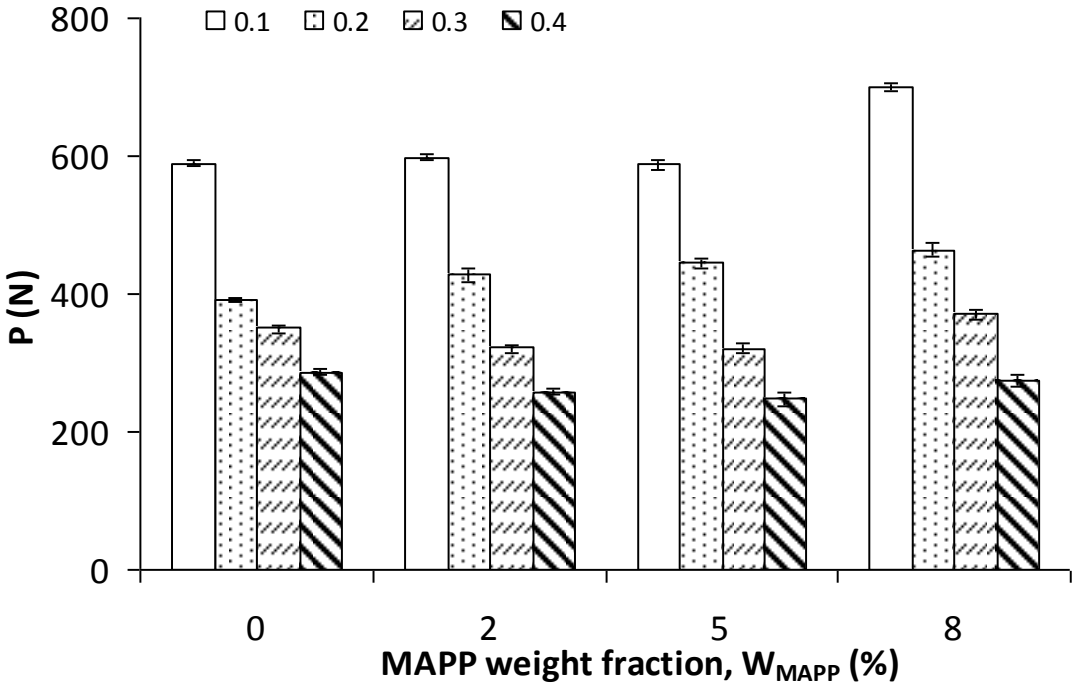

Appendix 4.70: Peak load (*P*) of PP/G15/NCUT6 hybrid composites with different MAPP contents

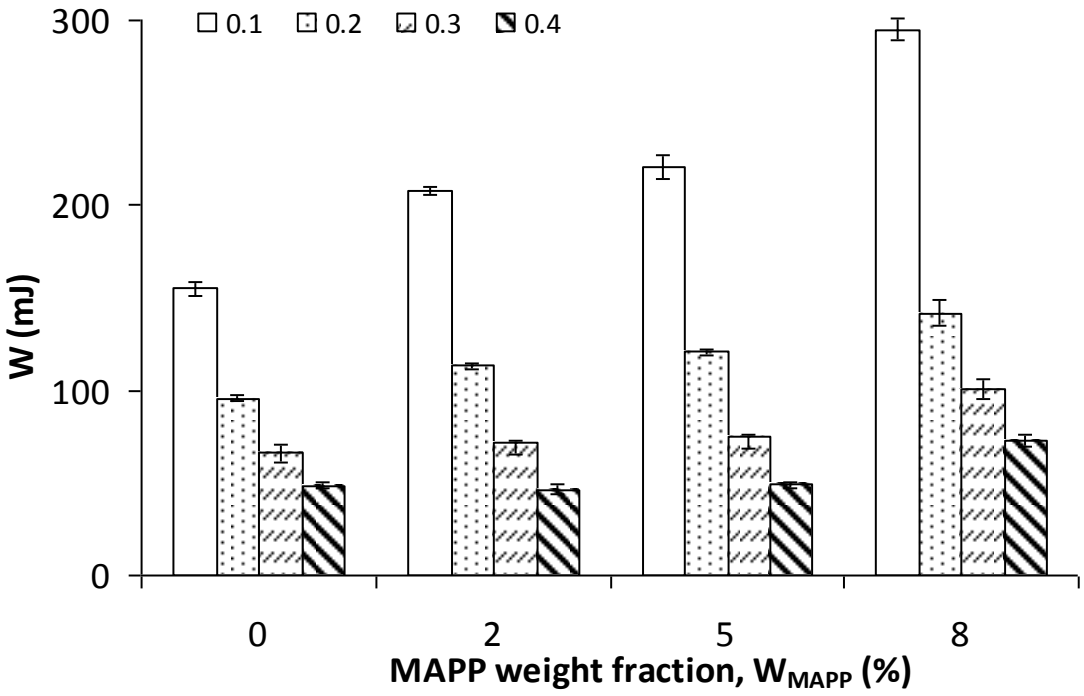

Appendix 4.71: Fracture energy (*W*) of PP/G15/NCUT6 hybrid composites with different MAPP contents

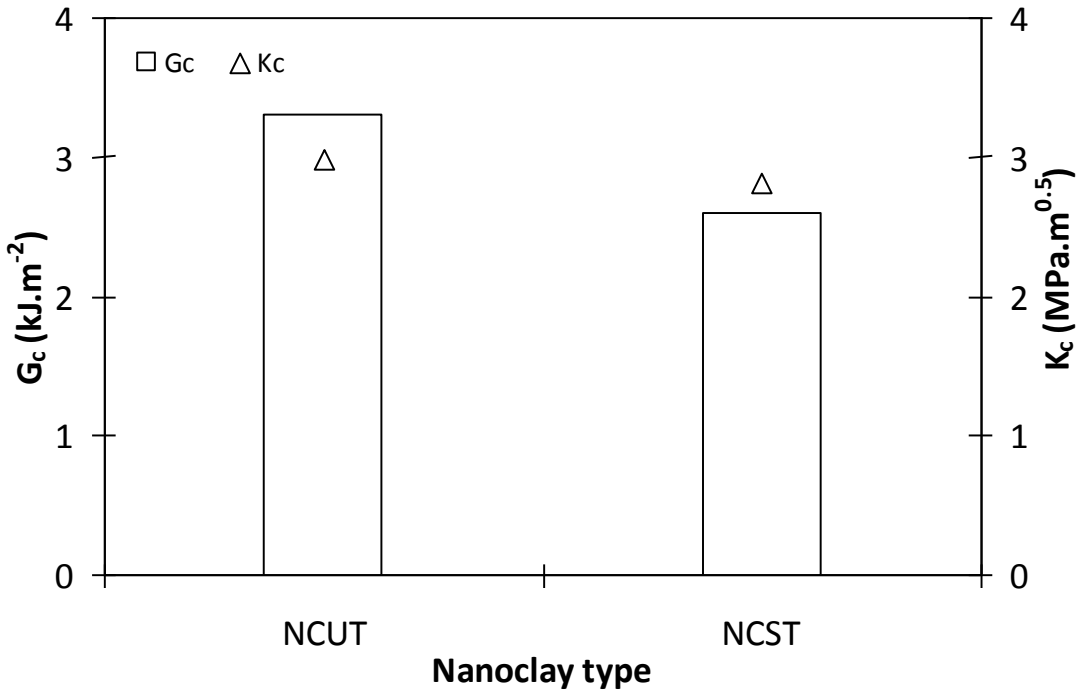

Appendix 4.72: G_c and K_c of (PP:C5)/G15 hybrid composites with treated and untreated nanoclays

RESEARCH OUTPUT

Publications:

Normasmira A. R., Hassan A., Yahya R. and Lafia-Araga R. A. Impact properties of glass-fiber/polypropylene composites: The influence of fiber loading, specimen geometry and test temperature. *Fibers and Polymers* 2013, Accepted. (*ISI-Cited Publication*)

Normasmira A. R., A Hassan, Yahya R. and Lafia-Araga R. A. Glass fiber and nanoclay reinforced polypropylene composites: Morphological, thermal and mechanical properties. *Sains Malaysiana* 2013;42(4):537-546. (*ISI-Cited Publication*)

Normasmira A. R., Hassan A., Yahya R., Lafia-Araga R. A. and Hornsby P. R. Polypropylene/glass fiber/nanoclay hybrid composites: Morphological, thermal, dynamic mechanical and impact behaviors. *Journal of Reinforced Plastics and Composites* 2012;31(18):1247-1257. (*ISI-Cited Publication*)

Normasmira A. R., Hassan A., Yahya R., Lafia-Araga R. A. and Hornsby P. R. Micro-structural, thermal and mechanical properties of injection-molded glass-fiber/nanoclay/polypropylene composites. *Journal of Reinforced Plastics and Composites* 2012;31(4):269-281. (*ISI-Cited Publication*)

Hassan A., Normasmira A. R. and Yahya R. Extrusion and injection-molding of glass fiber/MAPP/polypropylene: Effect of coupling agent on DSC, DMA and mechanical properties. *Journal of Reinforced Plastics and Composites* 2011;30(14):1223-1232. (*ISI-Cited Publication*)

Normasmira A. R., Hassan A., Yahya R. and Lafia-Araga R. A. Melt mixed of polypropylene/glass fibre/nanoclay hybrid composites: The effect of compatibiliser on morphological, thermal and dynamic mechanical behaviours Composites. *Journal of Reinforced Plastics and Composites*, Submitted. (*ISI*)

Proceedings:

Normasmira A. R., Hassan A., Yahya R. and Lafia-Araga R. A. Glass fiber and nanoclay reinforced polypropylene composites: A study of the morphological, thermal and dynamic mechanical behaviors. Proceeding of The Asian International Conference on Materials, Minerals and Polymer 2012 (MAMIP 2012), Penang, Malaysia, 23 – 24 March 2012.

Hassan A., Normasmira A. R. and Yahya R. Extrusion and injection-molding of glass-fiber/MAPP/polypropylene: Effect of coupling agent on DSC, DMA and mechanical properties. Proceeding of The Asian International Conference on Materials, Minerals and Polymer 2012 (MAMIP 2012), Penang, Malaysia, 23 – 24 March 2012.

Normasmira A. R., Hassan A. and Yahya R. Processing, micro-structural, thermal and mechanical properties of glass fiber/nanoclay/polypropylene composites. Proceeding of Malaysia Polymer International Conference 2011 (MPIC 2011), Putrajaya, Malaysia, 18 – 20 October 2011.

Conferences:

Yahya R., Normasmira A. R., Hassan A. Melt mixed of polypropylene/glass fibre/nanoclay hybrid composites: The effect of compatibiliser on morphological, thermal and dynamic mechanical behaviours. Eurofillers 2013, 25 – 29 August 2013, Bratislava, Slovakia. (International)

Normasmira A. R., Hassan A., Yahya R. and Lafia-Araga R. A. Glass fiber and nanoclay reinforced polypropylene composites: A study of the morphological, thermal and dynamic mechanical behaviors. The Asian International Conference on Materials, Minerals and Polymer 2012 (MAMIP 2012), 23 – 24 March 2012, School of Materials and Mineral Resources Engineering, Universiti Sains Malaysia. (International)

Hassan A., Normasmira A. R. and Yahya R. Extrusion and injection-molding of glass-fiber/MAPP/polypropylene: Effect of coupling agent on DSC, DMA and mechanical properties. The Asian International Conference on Materials, Minerals and Polymer 2012 (MAMIP 2012), 23 – 24 March 2012, University Sains Malaysia. (International)

Normasmira A. R., Hassan A., Yahya R. and Lafia-Araga R. A. Processing, micro-structural, thermal and mechanical properties of glass fiber/nanoclay/polypropylene composites. Malaysia Polymer International Conference 2011 (MPIC 2011), 18 – 20 October 2011, Polymer Research Center, Universiti Kebangsaan Malaysia. (International)